

**CHARACTERIZATION OF SOFT X-RAY UNDULATOR
FOR THE SIAM PHOTON SOURCE**

Thananchai Dasri

A Thesis Submitted in Partial Fulfillment of the Requirements for

the Degree of Doctor of Philosophy in Physics

Suranaree University of Technology

Academic Year 2008

การศึกษาคุณสมบัติของอันดูลเตอร์รังสีเอ็กซ์พลังงานต่ำ
สำหรับเครื่องกำเนิดแสงสยาม

นายธัญชัย ดาศรี

วิทยานิพนธ์นี้เป็นส่วนหนึ่งของการศึกษาตามหลักสูตรปริญญาวิทยาศาสตรดุษฎีบัณฑิต
สาขาวิชาฟิสิกส์
มหาวิทยาลัยเทคโนโลยีสุรนารี
ปีการศึกษา 2551

CHARACTERIZATION OF SOFT X-RAY UNDULATOR FOR THE SIAM PHOTON SOURCE

Suranaree University of Technology has approved this thesis submitted in partial fulfillment of the requirements for the Degree of Doctor of Philosophy.

Thesis Examining Committee

(Assoc. Prof. Dr. Chinorat Kobdaj)

Chairperson

(Asst. Prof. Dr. Supagorn Rugmai)

Member (Thesis Advisor)

(Prof. Dr. Prasart Suebka)

Member

(Asst. Prof. Dr. Prayoon Songsiriritthigul)

Member

(Asst. Prof. Dr. Chitnarong Sirisathitkul)

Member

(Asst. Prof. Dr. Chitrlada Thongbai)

Member

(Prof. Dr. Pairote Sattayatham)

Vice Rector for Academic Affairs

(Assoc. Prof. Dr. Prapan Manyum)

Dean of Institute of Science

ชัญญชัช ดาศรี : การศึกษาคุณสมบัติของอันคูเลเตอร์รังสีเอ็กซ์พลังงานต่ำสำหรับ
เครื่องกำเนิดแสงสยาม (CHARACTERIZATION OF SOFT X-RAY UNDULATOR
FOR THE SIAM PHOTON SOURCE) อาจารย์ที่ปรึกษา : ผู้ช่วยศาสตราจารย์ ดร.
ศุภกร รักใหม่, 197 หน้า.

ได้ศึกษาสนามแม่เหล็กของอันคูเลเตอร์ เพื่อให้ทราบค่าความผิดเพี้ยนของสนามแม่เหล็ก
อันคูเลเตอร์ และผลกระทบที่จะมีต่อลำอิเล็กตรอนในวงกักเก็บอิเล็กตรอนของเครื่องกำเนิดแสง
สยาม เพื่อให้ได้ค่าสนามแม่เหล็กในแต่ละตำแหน่งภายในอันคูเลเตอร์ที่ต้องการ จึงได้สร้าง
เครื่องมือที่มีระบบความแม่นยำสูงสำหรับติดตั้งหัวอ่านสนามแม่เหล็กฮอลล์ นอกจากนั้นได้วัดค่า
field integral ด้วยวิธี flipping coil คือการหมุนเส้นลวดตัดสนามแม่เหล็กของอันคูเลเตอร์ ค่าสนาม
แม่เหล็กได้ทำการวัดที่ขนาดช่องว่างระหว่างแม่เหล็กของอันคูเลเตอร์ต่างๆ กัน ที่ขนาดช่องว่าง
หนึ่งๆ วัดที่ตำแหน่งในแนวขวางต่างๆ กัน และวัดตลอดความยาวของอันคูเลเตอร์ ส่วนการวัด
field integral วัดได้ทั้งองค์ประกอบในแนวราบและแนวตั้งฉาก ค่าสนามแม่เหล็กที่ได้ นำไปใช้
คำนวณตำแหน่งและมุมของอิเล็กตรอนภายในอันคูเลเตอร์ ใช้สร้างแบบจำลองแม่เหล็กเพื่อคำนวณ
ค่า tune shifts ของลำอิเล็กตรอน และสุดท้ายคือใช้ประมาณปริมาณความเข้มแสงซินโครตรอนที่
ผลิตจากอันคูเลเตอร์ โดยดูจากความต่างของระยะทางที่อิเล็กตรอนที่เคลื่อนที่ได้ ในแต่ละคาบ ส่วน
ค่า field integral ใช้คำนวณองค์ประกอบของสนามแม่เหล็กที่ผลิตจากอันคูเลเตอร์ องค์ประกอบ
ของแม่เหล็กสองขั้วใช้คำนวณตำแหน่งและมุมของอิเล็กตรอน ที่ตำแหน่งปลายของอันคูเลเตอร์
คำนวณผลขององค์ประกอบของแม่เหล็กสี่ขั้วที่มีต่อค่า betatron tune ของลำอิเล็กตรอน และ
คำนวณผลขององค์ประกอบของแม่เหล็กหกขั้วที่มีต่อค่า chromaticity ในที่สุดแล้วการวิเคราะห์
สนามแม่เหล็ก ทำให้สามารถหาวิธีการชดเชยผลกระทบของอันคูเลเตอร์ต่อลำอิเล็กตรอนได้ นั่นคือ
ตำแหน่งและมุมของอิเล็กตรอนที่เปลี่ยนไปจากเส้นทางที่ออกแบบไว้ ชดเชยโดยใช้สนามแม่เหล็ก
สองขั้วซึ่งสร้างจากขดลวดยาวรูปสี่เหลี่ยม ร่วมกับแม่เหล็กสองขั้วที่ติดตั้งก่อนและหลังอันคูเลเตอร์
tune shifts ของลำอิเล็กตรอน ชดเชยโดยใช้แม่เหล็กสี่ขั้วสองคู่ที่ปลายทั้งสองข้างของอันคูเลเตอร์
ความผิดเพี้ยนของค่า chromaticity ชดเชยโดยสมาชิกแม่เหล็กหกขั้วในวงกักเก็บอิเล็กตรอน

สาขาวิชาฟิสิกส์

ปีการศึกษา 2551

ลายมือชื่อนักศึกษา _____

ลายมือชื่ออาจารย์ที่ปรึกษา _____

THANANCHAI DASRI : CHARACTERIZATION OF SOFT X-RAY

UNDULATOR FOR THE SIAM PHOTON SOURCE. THESIS

ADVISOR : ASST. PROF. SUPAGORN RUGMAI, Ph.D. 197 PP.

INSERTION DEVICE/UNDULATOR/SOFT X-RAYS

Magnetic fields of the soft x-ray undulator, named U60, were characterized to estimate field errors and perturbations of the device on the electron beam in the storage ring of the Siam Photon Source. High precision magnetic field measurement system has been constructed to enable magnetic field mapping of the device using Hall probe scans. Field integral measurements are carried out using a flipping coil system. The magnetic fields were measured at various undulator gaps and horizontal positions. Magnetic field measurement results were used to calculate angles and trajectories of an electron inside the device. They were also used to model the undulator magnetic structure in order to calculate the linear perturbation on the storage ring beam dynamics. Phase errors are calculated to estimate quality of the synchrotron radiation emitted from the device. The measured field integrals were used to calculate integrated multipole field components. The dipole field component was used to estimate the deviated angle and position of an electron at the exit of the device. The quadrupole field component was used to calculate effects of field errors on the betatron tune. The sextupole field component was used to calculate effects on chromaticities. Finally, compensation schemes were obtained from the magnetic field analyses. A long coil system was simulated and constructed to compensate electron trajectory, together with steering magnets. Tune shift compensation by a pair of

quadrupoles and chromaticity compensation by two families of the sextupole magnets were simulated.

School of Physics

Academic Year 2008

Student's Signature_____

Advisor's Signature_____

ACKNOWLEDGMENTS

I am grateful to my thesis advisor, Asst. Prof. Dr. Supagorn Rugmai, for his valuable advices, comments for my thesis, for kindness, and suggestions about positive thinking. I am also very thankful Prof. Dr. Prasart Suebka, Asst. Prof. Dr. Chinorat Kobdaj, Asst. Prof. Dr. Prayoon Songsiriritthigul, Asst. Prof. Dr. Chitnarong Sirisathitkul and Asst. Prof. Dr. Chitrlada Thongbai for valuable advices, comments for my thesis.

I am thankful to all members in Siam Photon Laboratory. First, I would like to thank Mr. Supachai Prawanta, Mr. Apichai Kwankasem, Mr. Sarayut Siriwattanapitoon Mr. Nawin Juthong, Mr. Natawut Suradet, Mr. Visitchai Sooksrimuang and Mr. Pichit Kaewbutta for the Hall probe bench installation and controlled software, second, Mr. Sarayut Siriwattanapitoon Mr. Winit Chachai and Mr. Piyawat Pruekthaisong for the Flipping coil bench installation and design, third, Mr. Supan Boonsuya, Tanet Panuwattanawong and Mr. Piyawat Pruekthaisong for long coil magnet installation and design, Miss Porntip Sutmuang and Asst. Prof. Dr. Supagorn Rugmai for tune shifts and COD experimental data.

I would like to thank Nongkhai Campus, Khon Kaen University, Synchrotron Light Research Institute (Public Organization) and Suranaree University of Technology for financial support.

Last, but certainly not least, it is my pleasure to thank my beloved family for their support, believe, and encouragement.

Thananchai Dasri

CONTENTS

	Page
ABSTRACT IN THAI	IV
ABSTRACT IN ENGLISH	V
ACKNOWLEDGEMENTS	VII
CONTENTS	VIII
LIST OF TABLES	XI
LIST OF FIGURES	XII
LIST OF ABBREVIATIONS	XXII
CHAPTER	
I INTRODUCTION	1
1.1 Motivations	1
1.2 Insertion Devices for Synchrotron Light Source	3
1.3 The Siam Photon Source	10
II THEORY OF UNDULATOR	19
2.1 Radiation from an Ideal Undulator	19
2.1.1 The Wiggler Strength	19
2.1.2 Electron Dynamics	21
2.1.3 The Undulator Equation	27
2.1.4 Frequency Spectrum of the Undulator Radiation	30
2.1.5 The On-Axis Spectral Photon Flux of Undulator Radiation	39

CONTENTS (Continued)

	Page
2.2 Magnetic Field Errors of Undulators	40
2.2.1 The Phase Error.....	41
2.2.2 The Spectral Photon Flux with Phase Error.....	43
2.3 Theories of Magnetic Field Measurements.....	44
2.3.1 Magnetic Field Mapping.....	44
2.3.2 First Field Integral Measurements by Flipping Coil.....	45
2.3.3 Second Field Integral Measurements by Flipping Coil	51
III DESIGN OF SOFT X-RAY UNDULATOR FOR SPS.....	56
3.1 Magnetic Structure.....	56
3.2 Simulation of Magnetic Field Error.....	62
IV MAGNETIC FIELD MEASUREMENTS OF U60.....	69
4.1 Magnetic Field Mapping.....	69
4.1.1 The Hall Probe Installation.....	69
4.1.2 The Field Mapping Measurement.....	73
4.2 Field Integral Measurements.....	73
4.2.1 The Flipping Coil System Installation.....	73
4.2.2 First Field Integral Measurements.....	78
4.2.3 Second Field Integral Measurements.....	81
4.3 The Results of the Field Measurements.....	81
4.3.1 Field Distribution Measurements.....	81
4.3.2 Integrated U60 Undulator Magnetic Field Measurements.....	89

CONTENTS (Continued)

		Page
V	ANALYSES OF MAGNETIC FIELD MEASUREMENT RESULTS	102
	5.1 Electron Trajectory Inside the U60.....	102
	5.2 Phase Error	107
	5.3 Effects on Closed Orbit Distortion	111
	5.3.1 Effects on the Betatron Tunes and Betatron Function	116
	5.4 Higher Order Perturbations.....	12
VI	COMPENSATION OF FIELD ERRORS.....	128
	6.1 Correction of Trajectory.....	128
	6.2 Compensation of Orbit Distortion.....	135
	6.3 Compensation of Tune Shift	145
	6.4 Correction of Chromaticity	149
VII	CONCLUSIONS	153
	REFERENCES	155
	APPENDICES	162
	CURRICULUM VITAE.....	170

LIST OF TABLES

Table	Page
1.1 Summary of SPS storage ring's main parameters.....	13
1.2 Parameters for the U60 undulator of the SPS	17
3.1 Parameters of the designing undulator.....	62
4.1 Various undulator gaps and coordinates to measure the U60 field	73
4.2 Multipole field components at gap of 26.5 mm.....	96
4.3 Multipole field components at gap of 40 mm.....	96
4.4 Multipole field components at gap of 65 mm.....	96
6.1 The relation between undulator gap and compensated current.....	134
6.2 The relation between undulator gap and applied current for vertical correction coil.....	142
6.3 The relation between undulator gap and applied current for horizontal correction coil.....	143
6.4 The relation between undulator gap and applied current for tune shifts compensation.....	147
6.5 The relation between undulator gap and applied current for chromaticities compensation.....	151

LIST OF FIGURES

Figure	Page
1.1 Flux density as a function of photon energy emitted by electron beam of 100 mA and energy of 1.2 GeV from the bending magnet (10°) in the SPS storage ring	5
1.2 Flux density as a function of a photon energy from the wavelength shifter of the SPS. Electron beam current is 100 mA . The bending magnet spectrum is also shown for comparison	7
1.3 A magnetic structure of (a) planar undulator (b) planar-helical undulator. An arrow presenting in each magnet block indicates direction of magnetization	8
1.4 Flux density as function of a photon energy, up to the 5 th harmonic, emitted by electron beam of 100 mA and energy of 1.2 GeV as move through the U60 undulator, compared with the bending magnet and wavelength shifter spectrum	9
1.5 The SPS accelerator layout	11
1.6 Phase space ellipse	13
1.7 β function of the SPS storage ring.....	14
1.8 Alpha function of the SPS storage ring.....	14
1.9 Gamma function of the SPS storage ring.....	15
1.10 The dispersion function of the SPS storage ring.....	15

LIST OF FIGURES (Continued)

Figure	Page
1.11	U60 undulator of the SPS..... 16
2.1	Particle trajectories in an elliptical undulator, with $\lambda_u = 60$ mm , $N = 10$, $K_x = 0.5$ and $K_x = 1.5$ for small elliptical orbit; $K_x = 1$ and $K_x = 3$ for large elliptical orbit, observed in the (a) laboratory system, (b) moving system, (c) moving system in $x^* z^*$ plane and (d) moving system in $x^* y^*$ plane..... 26
2.2	Electron path inside an undulator..... 27
2.3	Fundamental wavelength as a function of a wiggler strength and the observation angle for 1.2 GeV electron beam and a 60 mm period length..... 29
2.4	An electron motion inside undulator for the analysis of undulator radiation..... 30
2.5	The linewidth of the radiation as a function of Q , plotted with periods $N = 5$ (widest graph) $N = 10$ (middle graph) and $N = 41$ (narrowest graph)..... 36
2.6	Trajectory of an electron in a imperfect periodic field $B_y(z)$ 41
2.7	The reduction of ratio photon flux as a function of harmonic number for various rms phase error 44

LIST OF FIGURES (Continued)

Figure	Page
2.8	The coil configuration for measuring the first field integral. a) side view along the longitudinal axis and b) side view of the coil along the transverse axis ($\vec{n} = +\hat{x}$) 46
2.9	The procedure for measuring ε'_y . a) is the start of the procedure. First flips the coil from 0° to 180° (b-c), next flip the coil from 180° to 360° (c-d). The coil is then flipped back from 0° to -180° (e- f) and it is finally flipped from -180° to -360° (f-g)..... 48
2.10	The procedure to measure ε'_x . The coil is started with configuration in 2.11a. First, the coil is flipped from 90° to 270° (b-c). Next, it is flipped from 270° to 450° (d-e). Later, the coil is flipped back from 90° to -270° (e-f). Finally, it is flipped from -270° to -450° (f-g) 50
2.11	The coil configuration to measure the second field integral. (a) side view along the longitudinal axis and (b) side view of the coil along the transverse axis ($\vec{n} = +\hat{x}$) 52
3.1	The relation between the radiated fundamental photon energy at the 1.2 GeV beam energy, the magnetic peak field and the period length 57
3.2	The structure of planar undulator. The arrow in the magnet blocks indicate the direction of the magnetization 58
3.3	The permanent rectangular magnet with magnetization in arbitrary direction..... 58

LIST OF FIGURES (Continued)

Figure	Page
3.4	The peak field as function of period length. The thick line is simulated peak magnetic field from assembly of magnet blocks and the thin line is theoretical calculation for the fundamental energy of 30 eV 60
3.5	The peak field as function of (a) block length and (b) block height, simulated at the gap of 20 mm. The optimums of the magnet length and magnet height are 100 and 62 mm, respectively..... 61
3.6	Simulated on-axis U60 field at 20 mm gap (a) vertical field (b) horizontal field..... 63
3.7	The calculated trajectory of an electron in the ideal undulator..... 64
3.8	The magnetization vector of a magnet block..... 65
3.9	The simulated horizontal fields for the cases: $\left \frac{\Delta B_r}{B_r} \right \leq 5\%$, $ \Delta\theta \leq 5^\circ$, and $\left \frac{\Delta B_r}{B_r} \right \leq 1\%$, $ \Delta\theta \leq 1^\circ$, and the ideal device (lies on x -axis) 66
3.10	The simulated vertical fields for the cases: (a) $\left \frac{\Delta B_r}{B_r} \right \leq 1\%$, $ \Delta\theta \leq 1^\circ$ and (b) $\left \frac{\Delta B_r}{B_r} \right \leq 5\%$, $ \Delta\theta \leq 5^\circ$ 67
3.11	The trajectory of an electron calculated from the simulated fields 68
4.1	Schematic drawing of the bench for Hall probe installation..... 69
4.2	The steps of the Hall probe installation..... 71

LIST OF FIGURES (Continued)

Figure	Page
4.3	The schematic view of (a) find the horizontal center (b) find the vertical center and (c) ready to map the field by Hall Probe 72
4.4	The flipping coil for the field integral measurement: (a) the components of the flipping coil to obtain the signal and (b) picture the real device... 74
4.5	The drawing of the coil support structure, fixed on the rotator plate..... 75
4.6	Schematic of Butterworth low pass Filters 76
4.7	User interface panel for flipping coil measurement code 77
4.8	Side view of the measurement of the horizontal first field integral. (a) the starting of measurement, $\hat{n} = \hat{x}$. (b) after clockwise flip by 180° , $\hat{n} = -\hat{x}$. (c) after clockwise flip to 360° , $\hat{n} = \hat{x}$ 78
4.9	Side view of the measurement of the vertical first field integral. (a) the starting of measurement, $\hat{n} = \hat{y}$ (b) after clockwise flip by 180° , $\hat{n} = -\hat{y}$ (c) after clockwise flip to 360° $\hat{n} = \hat{y}$ 80
4.10	Schematic of coil configuration for second field integral measurement 81
4.11	Undulator magnetic field at the gap of 26.5 mm 83
4.12	Undulator magnetic field at the both edges of the undulator: (a) at the entrance (b) at the exit of the device 84

LIST OF FIGURES (Continued)

Figure	Page
4.13 Undulator magnetic field at the both edges of the undulator (Δ) including the field obtained from exponential fitting (-): (a) at the entrance (b) at the exit of the device. The equations, shown in the graphs, are fitting equations	85
4.14 Undulator magnetic fields at the gap of (a) 26.5 mm, (b) 40 mm and (c) 65 mm	86
4.15 Peak magnetic field as a function of undulator gap. The error bars are statistical errors.	87
4.16 Wiggler strength as a function of undulator gap	87
4.17 Peak field as a function of horizontal position, x , at the undulator gap of (a) 26.5 mm (b) 40 mm and (c) 65 mm.....	88
4.18 Photon energy as a function of undulator gap at the first (diamond), third (circle), fifth (square), and seventh (triangle) harmonic.....	89
4.19 Integrated signal of the vertical field of the gap 26.5 mm at $x = 0$: (a) flip from 0° to 180° (b) flip from 180° to 360°	91
4.20 Integrated signal of horizontal field of gap 26.5 mm at $x = 0$: (a) flip from 90° to 270° (b) flip from 270° to 450°	92
4.21 First field integrals as a function of horizontal position at 26.5 mm: (a) horizontal component and (b) vertical component. Lines are multipole fits	93

LIST OF FIGURES (Continued)

Figure	Page
4.22	First field integrals as a function of horizontal position at 40 mm: (a) horizontal component and (b) vertical component. Lines are multipole fits 94
4.23	First field integrals as a function of horizontal position at 65 mm: (a) horizontal component and (b) vertical component. Lines are multipole fits 95
4.24	Field components as a function of gap: (a) dipole (b) quadrupole (c) sextupole and (d) octupole component 98
4.25	Measured signal of the second vertical field integral as function of time: (a) flip from 90° to 270° (b) flip from 270° to 450° 99
4.26	Measured signal of the second vertical field integral: (a) flip from 0° to 180° (b) flip from 180° to 360° 100
4.27	Second field integral as function of gap: (a) horizontal and (b) vertical component 101
5.1	Electron angles at 26.5 and 40 mm gap 105
5.2	Electron trajectories at 26.5, 40, 65 and 70 mm gap 105
5.3	Polynomial fits to the second field integrals 106
5.4	The quadratic coefficients of the second field integral at various gaps 106
5.5	Result of eliminating the quadratic component from the second field integral at the gap of 26.5 mm 107

LIST OF FIGURES (Continued)

Figure	Page
5.6 Shows the phase errors as function of a pole number.....	108
5.7 The rms phase error as function of the undulator gap	109
5.8 The relative flux intensities of the U60 undulator radiation as function of the gap for various harmonics	110
5.9 The percentage of the obtained flux intensities of undulator radiation as function of harmonic number	110
5.10 Deviated angle of an electron at the exit of the undulator as function of gap.....	112
5.11 Off-axis position of an electron at the exit of the undulator	112
5.12 Calculated horizontal COD as function of a BPM numbe.....	114
5.13 Calculated vertical COD as function of a BPM number.....	114
5.14 Compared COD between the experimental prediction and COD measurement. (a) horizontal COD and (b) vertical COD.....	115
5.15 The location of the U60 in the SPS storage ring	119
5.16 Rectangular dipole model	120
5.17 Shows the tunes shift as function as of the undulator gap	120
5.18 The quadrupole component as function of the undulator gap	121
5.19 The quadrupole strength as function of the undulator gap	121
5.20 The tunes shift due to the undulator field error.....	122
5.21 The vertical tune shift due to the U60 undulator that is summation of intrinsic field and field error.....	122

LIST OF FIGURES (Continued)

Figure	Page
5.22	The tunes shift from the measurement when (a) close the undulator gap of 26.5 mm and (b) open the undulator gap, marked by the ellipticities. The device shifts the vertical betatron tune by 0.0064.....
	123
5.23	The betatron function of (a) without undulator (b) with the undulator at gap of 26.5 mm. The thin lines are β_x and thick lines are β_y
	124
5.24	The sextupole component as function of the undulator gap.....
	127
5.25	The sextupole strength as function of the undulator gap
	127
5.26	Chromaticity due to phase error as function of the undulator gap
	128
6.1	The geometry of the two-turn rectangular coil, (a) top view and (b) side view. The dash line is the position of the evaluated field
	130
6.2	The rectangular coil field measurement by Hall probe scan.....
	130
6.3	(a) The example of the long coil field. And (b) The second field integral calculated from the measured field at various applied currents
	131
6.4	The relation between the quadratic component and the applied current. The dashed line and thin line are respectively obtained from the polynomial fits of the second field integral of the calculated and measured fields
	132
6.5	The relation between quadratic component as function of the undulator gap.....
	133

LIST OF FIGURES (Continued)

Figure	Page
6.6	The relation between compensated current and undulator gap for correcting of an electron trajectory. Solid line is polynomial fit.....
	135
6.7	(a) The layout of the corrector magnet (C_1, C_2) in the U60 undulator straight section. (b) The layout for the deviated angle and position of the electron calculation (top view)
	136
6.8	Deviated angle must be corrected by (a) corrector magnet C_1 and (b) corrector magnet C_2
	140
6.9	Compensated magnetic field generated by (a) corrector magnet C_1 and (b) corrector magnet C_2
	141
6.10	The applied currents of (a) corrector magnet C_1 and (b) corrector magnet C_2
	144
6.11	Position of the U60 undulator in the SLRI storage ring. It is located between QF12 and QF13
	146
6.12	Compensated quadrupole strength as a function of the undulator gap.....
	146
6.13	Compensated currents as a function of the undulator gap for compensating tune shifts Solid lines present polynomial fit.....
	148
6.14	The required sextupole strength as function of the undulator gap
	151
6.15	The compensated current as function of the undulator gap (a) SF and (b) SD magnets.....
	152

LIST OF ABBREVIATIONS

a	(1) electron acceleration, (2) dipole component
A	ampere
AT	Accelerator Toolbox
α	(1) fine structure($\approx \frac{1}{137.036}$), (2) twiss parameter
b	quadrupole component
B_n	normal magnetic field component
B_x	horizontal magnetic field
B_y	vertical magnetic field
B_0	peak magnetic field
B_r	remanent field
$\frac{\Delta B_r}{B_r}$	deviated of the remanent field
β	(1) twiss parameter, (2) relative velocity($=\frac{v}{c}$)
$\bar{\beta}_z$	average of a relative longitudinal velocity
c	(1) speed of light in a vaccuum($=2.99792458(1)\times 10^8$ m/s), (2) sextupole component
cm	centimeter
°C	degree Celcius

LIST OF ABBREVIATIONS (Continued)

d	(1) distance between two adjacent wavefronts, (2) Hall plate thickness
D	coil width
DBA	Double Bend Achromat
$\frac{d^2W}{d\Omega d\omega}$	angular distribution of the radiation emitted by electron
$d\Omega$	solid angle(= $2\pi\sigma_{rms}^2$)
δ	phase function
δ_{real}	phase function in each period in real device
δ_{avg}	average of phase function
Δ	closed orbit distortion
$\Delta\delta$	phase error
$\frac{\Delta\omega}{\omega}$	frequency bandwidth
$\Delta\theta$	deviated polar angle of the magnetization direction
$\Delta\phi$	deviated azimuthal angle of the magnetization direction
Δt	time step
Δx	changed horizontal position of electron
$\Delta x'$	changed horizontal deflection angle
Δy	deviated vertical position
$\Delta y'$	changed vertical angle

LIST OF ABBREVIATIONS (Continued)

<i>et al.</i>	et alia (and other)
eV	electron-Volt
E	energy
ε	emittance of electron beam
ε_0	permittivity of free space
ε_1	fundamental energy
ε_x	horizontal emittance
ε_y	vertical emittance
ε'	integrated voltage
f	Mayer f -function
F	force
Φ	magnetic flux
GeV	gigaelectron-volts
γ	(1) relativistic factor($=\frac{E}{m_0c^2}$), (2) twiss parameter
h	Planck constant
\hbar	reduced Planck constant or Dirac constant ($= h/2\pi$)
<i>i.e.</i>	id est (that is)
I	electron beam current
I_x	horizontal first field integral
I_y	vertical first field integral

LIST OF ABBREVIATIONS (Continued)

II_x	horizontal second field integral
II_y	vertical second field integral
J	Bessel function
k_B	Boltzmann constant ($\sim 1.38 \times 10^{-23} \text{ J K}^{-1}$)
k	(1) wave vector, (2) harmonic number
k_{sp}	special sextupole strength
k_{sex}	sextupole strength
k_u	undulator wave vector ($= \frac{2\pi}{\lambda_u}$)
keV	kiloelectron volts
kW	kilowatts
K	wiggler strength
K_y	vertical focusing strength of undulator
$K_{\frac{1}{2}}, K_{\frac{2}{3}}$	modified Bessel function of the second kind
Kg	Kilogram
l_{sp}	special sextupole length
l_h	effective of dipole length
L	(1) undulator length, (2) coil length
λ_u	periods length of undulator magnetic field
λ_1	fundamental radiated wavelength

LIST OF ABBREVIATIONS (Continued)

mA	miliampere
m_e	electron mass
mm	millimeter
m/s	meter per seconds
M	magnetization
M_C	One-turn transfer matrix
$M_{F,eff}$	undulator transfer matrix
MeV	megaelectron volt
MHz	megahertz
μ_0	permeability of free space($=4\pi \times 10^{-7} \frac{N}{A^2}$)
μ_y	vertical phase advance
n	harmonic number of undulator radiation
nm	nanometer
N	number of magnetic field periods
NdFeB	Neodymium Iron Boron magnet
η_x	horizontal dispersion function
η_y	vertical dispersion function
PPM	planar permanent magnet
π	pi ($=22/7$)
$\pi\epsilon$	ellipse area in phase space
ψ	vertical observation angle

LIST OF ABBREVIATIONS (Continued)

ξ_x	horizontal chromaticity
ξ_y	vertical chromaticity
QD	defocusing quadrupole magnet
QF	focusing quadrupole magnet
q	electric charge
r	electron position
<i>rad</i>	radian
R_H	Hall coefficient of the material
RF	Radio frequency
ρ	bending radius
ρ_h	curvature radius
ρ_0	bending radius
ρ^{-1}	bending strength
s	(1) second, (2) longitudinal coordinate
SD	defocusing sextupole magnet
SPS	Siam Photon Source
SF	focusing sextupole magnet
σ_{rms}	rms opening angle
σ_ϕ	rms phase error
t	time
T	tesla

LIST OF ABBREVIATIONS (Continued)

θ	horizontal observation angle
Θ	maximum deflection angle
U60	undulator of 60 mm of periods length
v	electron velocity
V	induced voltage
ν_x	horizontal betatron tune
ν_y	vertical betatron tune
W/m ²	Watt per square meter
ω	photon frequency
ω_c	critical frequency
X	magnet block width
x'	horizontal deflection angle
Y	magnet block height
y'	vertical deflection angle
Z	magnet block length

CHAPTER I

INTRODUCTION

1.1 Motivations

The Siam Photon Source (SPS) is designed to contain four long straight sections, each with the length of 5.2 meters for installation of insertion devices. Superior characteristics of synchrotron light from insertion devices will enable the SPS to better serve various research fields. An undulator is one of such insertion devices. A soft x-ray undulator, named U60, is the first insertion device to be installed in the SPS storage ring. It is a Planar Permanent Magnet (PPM) undulator. It consists of magnet blocks of alternating polarity that repetitively bend electron beam back and forth. The magnetic structure is designed to deflect electron with the angle, the angle between electron trajectory and undulator axis, less than $\frac{1}{\gamma}$, where γ is the relativistic factor. So, synchrotron radiation emitted from each turn adds coherently, resulting in high intensity of undulator radiation. The intensity is proportional to the square of the number of periods. In addition, the opening angle at any given wavelength of the radiation is decreased by \sqrt{N} , where N is the number of magnetic periods. Therefore, the undulator radiation is emitted in a narrow cone. However, characteristics of synchrotron light from real undulators are different from ideal

devices. This fact arises from magnetic field errors of real undulators (Bobbs et al., 1994; Kennedy, Cover, and Slater, 1990; Alp and Viccaro, 1988; Kinkaid, 1985; Kinkaid, 1990; Walker, 1993). The magnetic field errors affect interference condition of the undulator radiation, resulting in the degradation of undulator spectra. These effects on interference condition can be investigated via rms field error, or phase error.

The field errors also give rise to perturbation of electron beam in the storage ring. Ideally, the electron beam should exit from an undulator with the same transverse angle and position as it enters. This condition is equivalent to zero field integrals of the undulator. However, unavoidable field errors of real undulators make this condition impossible. These nonzero field integrals will give rise to closed orbit distortion of the electron beam in the storage ring. Therefore, the undulator field must be measured and analyzed. The most common method of undulator field distribution measurements is the magnetic field mapping by Hall probes. The field integrals can be measured by flipping coil method. The measurements can also provide integrated nonlinear terms of undulator magnetic field.

Apart from perturbing the orbit the undulator also gives a tune shift of the electron beam in the storage ring. This tune shift arises from both internal characteristic of the undulator itself and the field errors. Too large tune shift can lead to instability of the electron beam. Moreover, the undulator magnetic field may also have nonlinear terms, especially the sextupole term, which may also give rise to instability. Effects of these perturbations therefore have to be studied carefully, in order to be compensated to make the storage ring operational after installation of the undulator. Different techniques and magnetic components are required to compensate

each type of perturbations (Rugmai, 2005; Walker and Diviacco, 1994; Yonehara, Kasuga, Hasumoto, and Kinoshita, 1998).

1.2 Insertion Devices for Synchrotron Light Source

Synchrotron radiation is the electromagnetic radiation emitted when a charged particle is accelerated, i.e. constraint to move in curved paths by a magnetic field. The most common synchrotron light source is a bending magnet. For the bending magnet radiation, the radiated spectral photon flux within a certain frequency bandwidth $\Delta\omega$ is given by

$$\frac{dF}{d\Omega} = \frac{d^2W}{d\Omega d\omega} \frac{I}{e\hbar} \frac{\Delta\omega}{\omega}, \quad (1.1)$$

where $\frac{d^2W}{d\Omega d\omega}$ is given by (Duke, 2004; Schwinger, 1949; Winick, 1994)

$$\frac{d^2W}{d\Omega d\omega} = \frac{3}{4} \frac{\alpha\gamma^2}{\pi^2} \left(\frac{\omega}{\omega_c}\right)^2 (1 + \gamma^2\psi^2)^2 \left[K_{\frac{2}{3}}^2(\xi) + \frac{\gamma^2\psi^2}{1 + \gamma^2\psi^2} K_{\frac{1}{3}}^2(\xi) \right], \quad (1.2)$$

where

$$\xi = \frac{1}{2} \frac{\omega}{\omega_c} (1 + \gamma^2\psi^2)^{\frac{3}{2}}, \quad (1.3)$$

and $\alpha = \frac{q^2}{4\pi\epsilon_0\hbar c} \approx \frac{1}{137.036}$ is the fine-structure constant. ψ is the observation angle

in vertical direction, perpendicular to the storage ring plane, $\frac{\Delta\omega}{\omega}$ is the frequency

bandwidth. I is the electron beam current, ω is photon frequency and ω_c is critical

frequency, defined to be the frequency which the argument ξ in Equation (1.3)

becomes $\frac{1}{2}$. The first term in Eq. (1.2), dependent on $K_{\frac{2}{3}}^2$, is the synchrotron

radiation having planar polarization, i.e. polarization being in the storage ring plane. The second term, dependent on K_1^2 , is the synchrotron radiation having vertical polarization, i.e. perpendicular to the storage ring plane. On the beam axis ($\psi = 0$), only the planar polarized synchrotron light is produced. For the observation angles above or below the beam orbit, elliptically polarized radiation is produced. Moreover, the modified Bessel function starts to fall off rapidly when argument $\xi = \frac{1}{2}$. At this point, one important parameter is defined, called critical frequency. In Equation (1.3) for $\xi = \frac{1}{2}$ and observing angle $\psi = 0$, the critical frequency is therefore obtained as

$$\omega_c = \frac{3}{2} \frac{c}{\rho} \gamma^3 = 3.37 \times 10^8 \frac{E^3 [\text{GeV}]}{\rho [\text{m}]} . \quad (1.4)$$

And the critical photon energy, $\varepsilon_c = \hbar \omega_c$, is given by

$$\varepsilon_c [\text{KeV}] = 2.218 \frac{E^3 [\text{GeV}]}{\rho [\text{T}]} = 0.665 B [\text{T}] E^2 [\text{GeV}] . \quad (1.5)$$

For example, the photon flux density generated by the SPS bending magnet at 1.2 GeV beam energy, calculated by the program SPECTRA (Tanaka and Kitamura, 2001), is shown in the Figure 1.1. The critical photon energy radiated by the bending magnet is 1.38 keV. This critical photon energy implies the photon energy range which will have enough radiation flux for experiments.

However, some experiments require higher intensity at higher photon energy than that obtained from the bending magnet. New synchrotron light sources must be considered to produce synchrotron light with required properties.

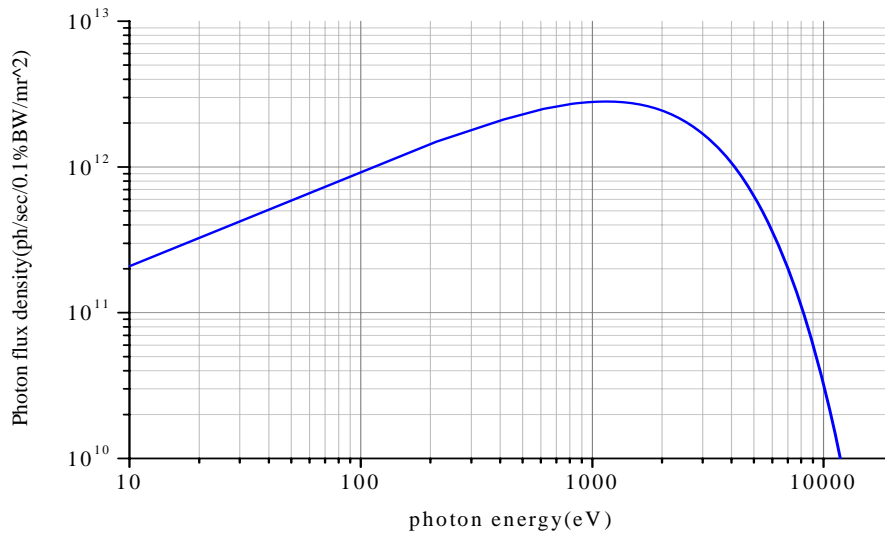


Figure 1.1 Photon flux density as a function of photon energy emitted by electron beam of 100 mA and energy of 1.2 GeV from the bending magnet (10° of detected angle) in the SPS storage ring.

Modern synchrotron light sources are designed to have straight sections in the storage rings. For example, the SPS contains long 4-straight sections, 5.2 meters each. These straight sections are provided for installation of synchrotron light sources called insertion device. There are two classes of insertion device. One is a wiggler and the other is an undulator. This classification is based on the value of the so-called wiggler strength K , defined by

$$K = 0.934B_0\lambda_u, \quad (1.6)$$

where λ_u is the period length of magnetic field in cm and B_0 is the magnetic peak field in tesla. An undulator has a low K , theoretically $K \ll 1$, whereas a wiggler has a large K , theoretically $K \gg 1$.

A wiggler has a magnetic structure consisting of series of dipole magnets with alternating polarity. The main purpose of a wiggler is to shift the synchrotron light

spectrum to hard X-ray region. The wiggler field is therefore higher than bending magnet. The simplest form of a wiggler consists of superconducting magnets with three magnetic poles. This is called a wavelength shifter. The central pole with strong field is used as a source of radiation. Two side poles with weaker field at the entrance and exit are used for compensation of orbit distortion of electron beam, i.e. to satisfy zero first and second field integrals,

$$I_y(z) = \int_{z'=0}^{z'=z} B_y(z') dz' = 0, \quad (1.7)$$

$$J_y(z) = \int_{z'=0}^{z'=z} \int_{z''=0}^{z''=z'} B_y(z'') dz'' dz' = 0. \quad (1.8)$$

For example, the wavelength shifter of the SPS has the central pole with a peak field of 6.4 T, while two side poles produce 3.7 T (Klysubun, Rugmai, Kwankasem, Klysubun, and Prawatsri, 2007). The wavelength shifter of the J. Bennett Johnston, Sr., Center for Advanced Microstructures and Devices (CAMD) has the central pole with the peak field of 7 T, while two side poles produce 1.65 T (Borovikov et al., 1998). The more common wiggler type is called multipole wiggler. It consists of many poles with alternating polarity. Each pole produces a high magnetic field. The magnetic structure is also satisfied (1.7) and (1.8). For example, the magnetic structure for symmetric configuration with an odd number of main poles should have magnetic structure like $\frac{1}{2}, -1, 1, -1, \dots, -1, \frac{1}{2}$, where the numbers indicate longitudinal pole size with 1 meaning full-size pole. The magnetic structure for an asymmetric configuration with having an even number of main pole have a structure like $\frac{1}{4}, -\frac{3}{4}, 1, -1, \dots, -1, -\frac{3}{4}, \frac{1}{4}$ (Mezentsev, 2005). For example, the superconducting multipole

wiggler having 63 poles with 2 T peak field, is installed in the Canadian Light Source storage ring (Khrushev et al., 2007), the 47-pole 3.5 T superconducting wiggler is installed in Max-Lab (Wallen, LeBlanc, and Eriksson, 2001). The photon flux radiated from a wiggler is $2N$ times of that radiated from a bending magnet, where N is number of pole. The spectrum from the wavelength shifter of the SPS is shown in Figure 1.2 calculated using SPECTRA (Tanaka and Kitamura, 2001). The critical energy of the device using the relation (1.5) is 6.13 keV. In the direction making an angle θ with the wiggler axis, the critical energy is also roughly given by (Elleume, 1991)

$$\varepsilon_c(\theta) = \varepsilon_c(\theta = 0) \sqrt{1 - \frac{\theta\gamma}{K}}, \quad (1.9)$$

where $\gamma = 1957E[\text{GeV}]$ and $\varepsilon_c(\theta = 0)$ is defined in (1.5).

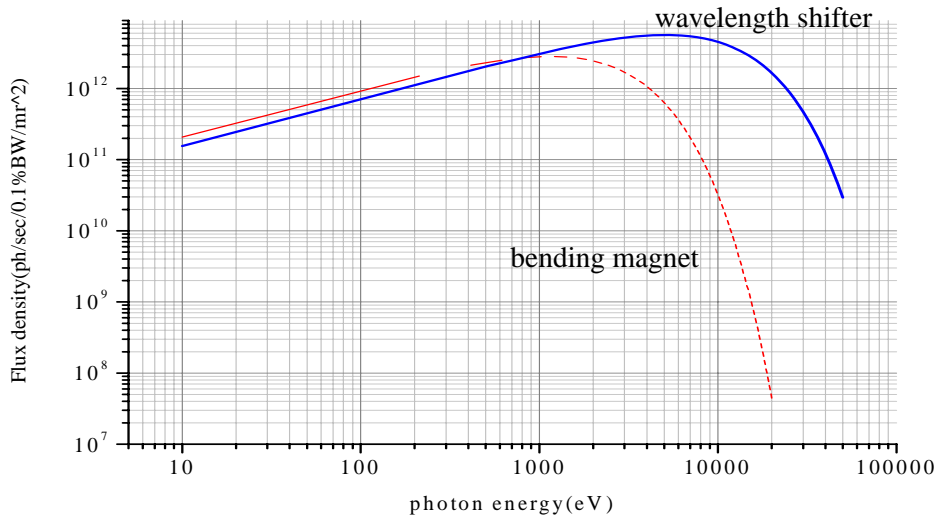


Figure 1.2 Flux density as a function of a photon energy from the wavelength shifter of the SPS, electron beam current of 100 mA. The bending magnet spectrum is also shown for comparison.

Undulators are the other class of insertion devices. It consists of series of dipole magnet with alternating polarity, similar to a wiggler. The magnet structure also satisfies the condition (1.7) and (1.8). However, the undulator radiation differs from the wiggler and bending magnet radiation. Undulator radiation is a result of the interference that occurs from the radiation emitted by an electron moving in a periodic field. Emission angle of undulator radiation is in the order of $\frac{1}{\gamma}$. A planar undulator is an undulator, which the electron trajectory is only in one plane. The polarization of undulator radiation is therefore in that plane. The device consists of two magnet arrays symmetrically positioned above and below the electron beam axis, shown in Figure 1.3a. The device produces a sinusoidal magnetic field in the vertical direction. For example, the U60 undulator of the SPS (Rugmai et al., 2007; Dasri, Siri wattanapaitoon, Chachai, and Rugmai, 2007) will be discussed in the section 1.4.

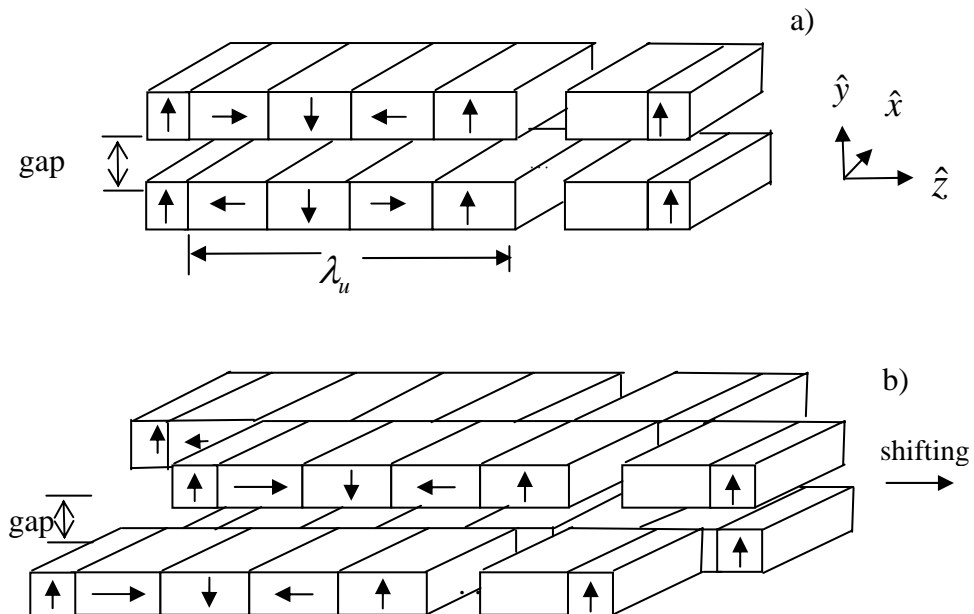


Figure 1.3 A magnetic structure of (a) planar undulator (b) planar-helical undulator.

An arrow presenting in each magnet block indicates direction of magnetization.

The flux density radiated from U60 undulator is shown in Figure 1.4. More detailed theory of an undulator will be discussed in chapter II. Figure 1.3 also shows a series of harmonics of U60 spectrum. The clearly spectrum shows that the flux density, within some specific energy range, produced from the U60 undulator is higher than that from the bending magnet and wavelength shifter. This higher intensity results from the constructive interference of synchrotron light emitted by electron beam moving through each magnetic pole of the undulator.

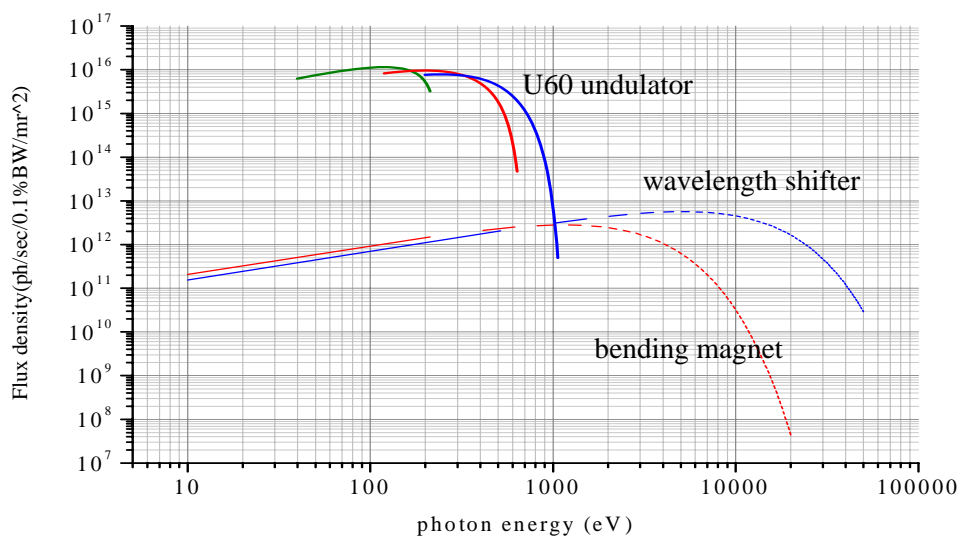


Figure 1.4 Flux density as function of a photon energy, up to the 5th harmonic, emitted by a 1.2 GeV electron beam of 100 mA through the U60 undulator, compared with the bending magnet and wavelength shifter spectrum.

The other type is an elliptical or a helical undulator. An example of such device is the Apple-II undulator proposed by Sasaki (Sasaki, 1994). This device consists of four magnet arrays of Halbach-type positioned above and below the

electron beam axis shown in Figure. 1.3b. The lower-front and upper-back are fixed in space. The upper-front and lower-back can be shifted. By shifting, the magnitude of magnetic fields in the two vertical planes can be inversely changed, i.e. one plane increases and another decreases. So, users can select the type of polarization, i.e. linear, elliptical or circular polarized. For example, the 6 cm period Apple-II type elliptically polarized undulator is installed at Pohang Accelerator Laboratory (Kim, Lee, Suh, Jung, Park, Kim, and Bak, 2001).

1.3 The Siam Photon Source

The layout of the SPS is shown in Figure. 1.5 (<http://www.slri.or.th>). It consists of a 40 MeV linear accelerator (linac), a 1 GeV booster synchrotron and a 1.2 GeV storage ring. The linac consists of two accelerating tubes, each with the length of 2.3 meters. Electrons are generated from thermionic electron gun, bunched into short electron bunches and accelerated along a linear path to a nominal energy of 40 MeV. The electron bunches are then transported through the low energy beam transport line (LBT) into the booster synchrotron. The booster synchrotron has a six fold symmetric lattice. The lattice structure is FODO (Focus-none-Defocus-none). The magnet system contains 12 bending magnets, 18 quadrupole magnets and 6 steering magnets. The bending magnet radius is 3.03 meters, with the maximum magnetic field of 1.1 T. It has a circumference of 43.19 meters and harmonic number of 17. The RF frequency used is 118.080 MHz. The electrons are eventually extracted to move along the high energy beam transport line (HBT) and injected into the storage ring at 1 GeV. The electron beam is then ramped up in the storage ring to the final energy of 1.2 GeV.

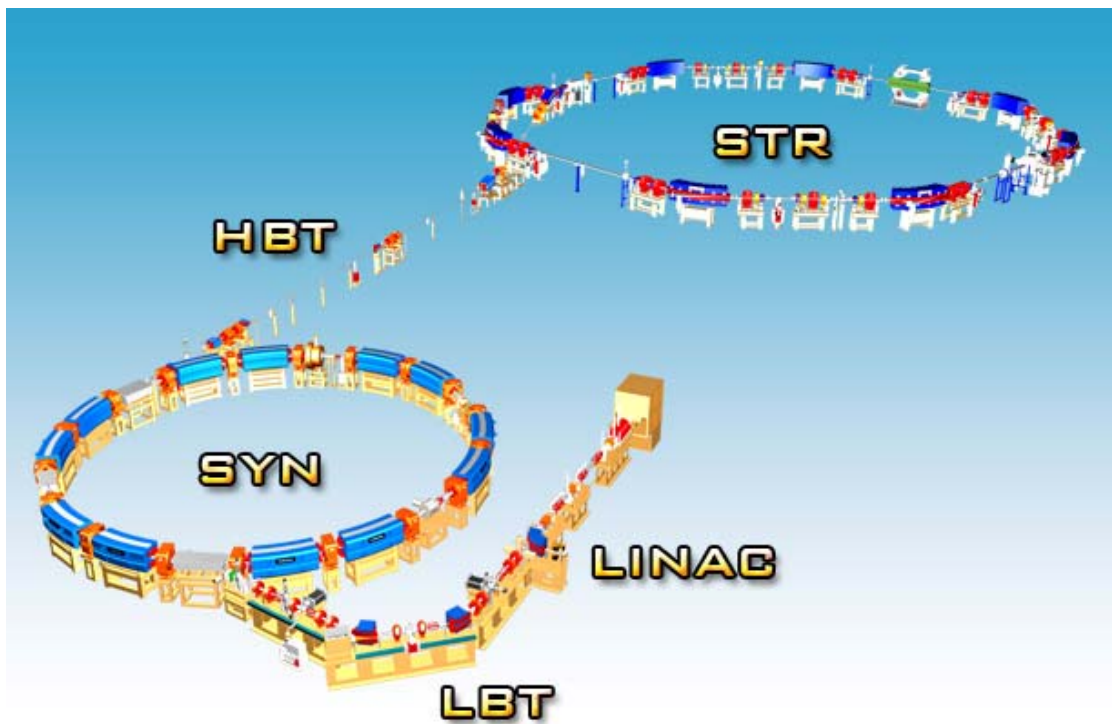


Figure 1.5 The SPS accelerator layout (<http://www.slri.or.th>).

The main parameters of the storage ring are listed in Table 1.1. The original designed beam energy of the storage ring is 1.0 GeV. Currently, the storage ring is operated at the beam energy of 1.2 GeV (Rugmai et al., 2007).

Table 1.1 Summary of SPS storage ring's main parameters.

Parameters	Data
Operating beam energy	1.0 GeV-1.2 GeV
Circumference	81.3 m
Length of straight section	5.2 m x 4
Lattice	Double Bend Achromat (DBA)
Lattice symmetry	Four fold
Nominal electron beam current	150 mA
RF frequency	118.080 MHz
Harmonic number	32
Natural chromaticity; ξ_x, ξ_y	-7.96; -6.45
Betatron tune; ν_x, ν_y	4.75; 2.82
Natural emittance	64 nm. rad
Momentum compaction factor	0.0241
Number bending magnet	8
Bending magnetic field	1.2-1.4 T
Bending radius	2.78
Energy loss per turn from bending magnet	65.98 keV
Total radiated power from bending magnet	6.598 kW

For an electron moving in a storage ring, if the position and angle of electrons at any point in a storage ring are mapped into the phase space (x, x') , the phase space ellipse with area of $\pi\varepsilon$ is obtained, as shown in Figure 1.6. The equation of the ellipse at a given location s , can be written as

$$x(s)^2 + \left(\frac{2\alpha_s x'(s)}{\gamma_s}\right)x'(s) + \left(\frac{\beta_s x'(s)^2 - \varepsilon}{\gamma_s}\right) = 0. \quad (1.10)$$

The ellipse shape changes along the beam path s . This ellipse is related to the twiss parameters, β , α and γ . These parameters are related to the maximum amplitude and angle of the oscillation, at a given location s (Courant, Corant, and Snyder, 1958):

$$x_{\max}(s), y_{\max}(s) = \sqrt{\varepsilon_{x,y}(s)\beta_{x,y}(s)}, \quad (1.11)$$

$$x'_{\max}(s), y'_{\max}(s) = \sqrt{\frac{\varepsilon_{x,y}(s)}{\beta_{x,y}(s)}}. \quad (1.12)$$

The SPS storage ring twiss parameters, calculated using Accelerator Toolbox (Terebilo, 2001), are shown in the Figure 1.7, 1.8 and 1.9. Figure 1.10 shows dispersion functions (η_x and η_y) of the SPS storage ring. The dispersion function is introduced as a result of the fact that the energy of the electrons differ from the nominal energy.

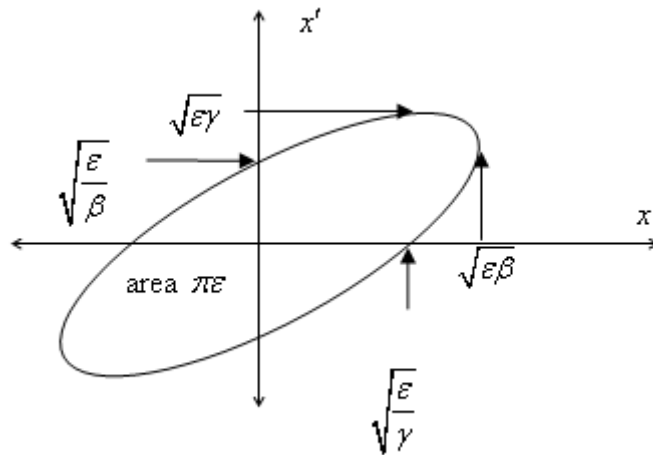


Figure 1.6 Phase space ellipse.

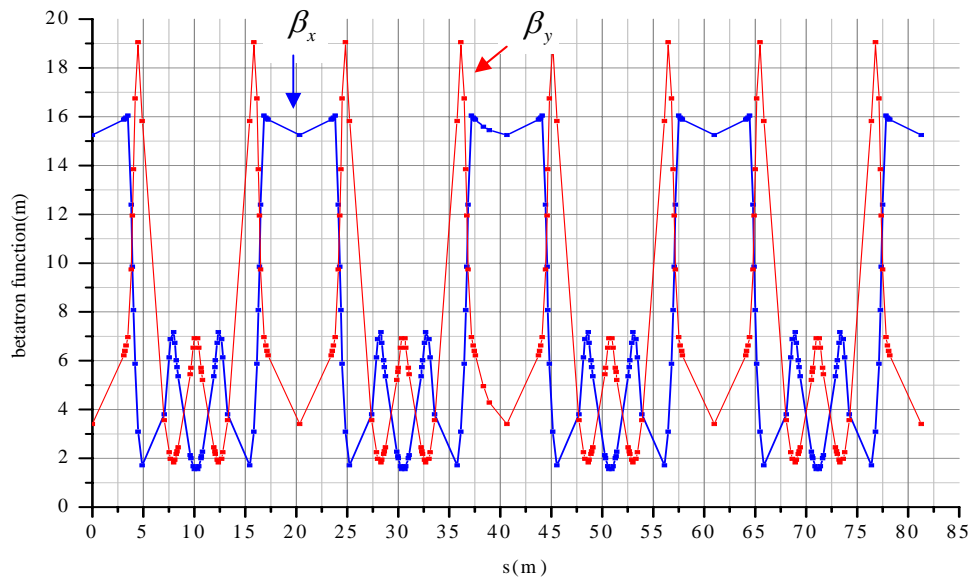


Figure 1.7 β function of the SPS storage ring.

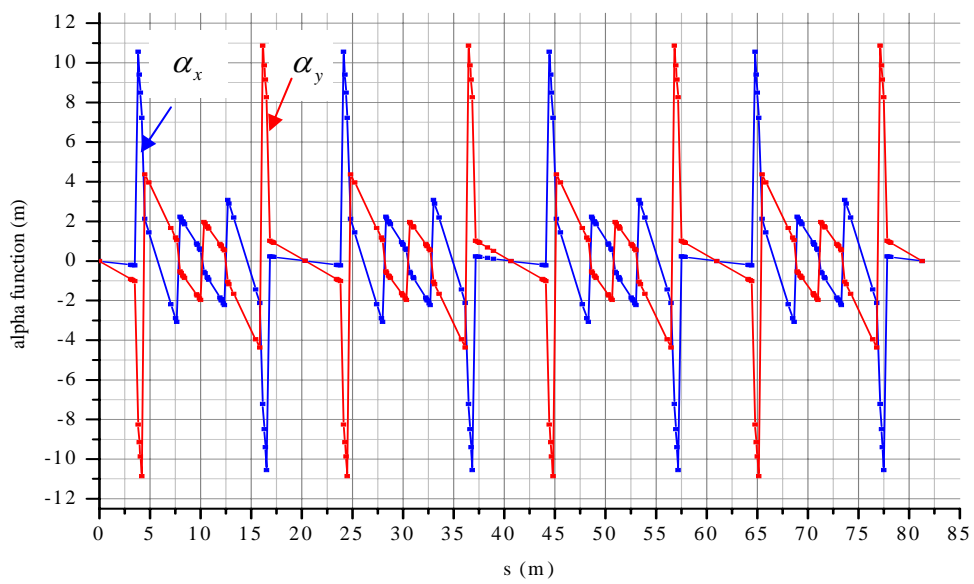


Figure 1.8 Alpha function of the SPS storage ring.

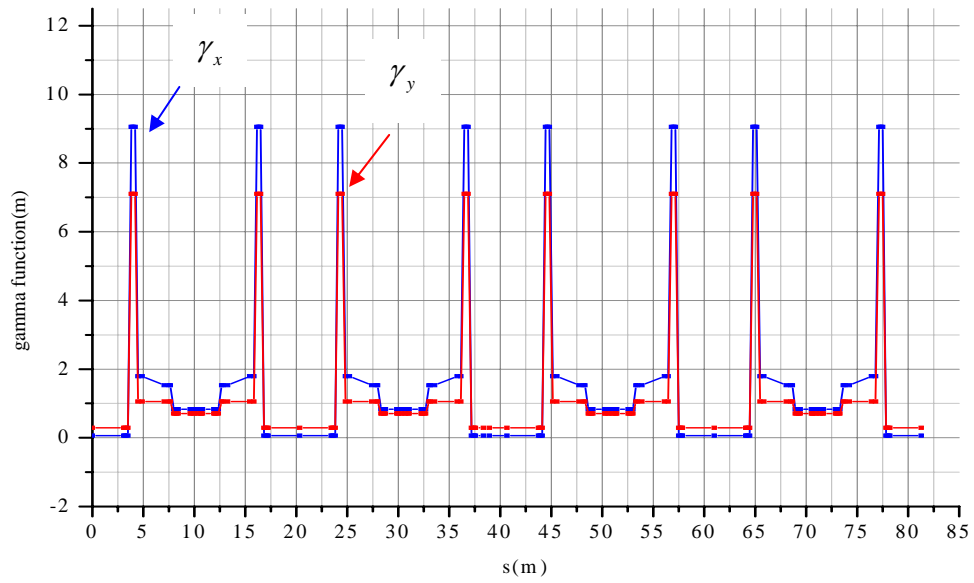


Figure 1.9 Gamma function of the SPS storage ring.

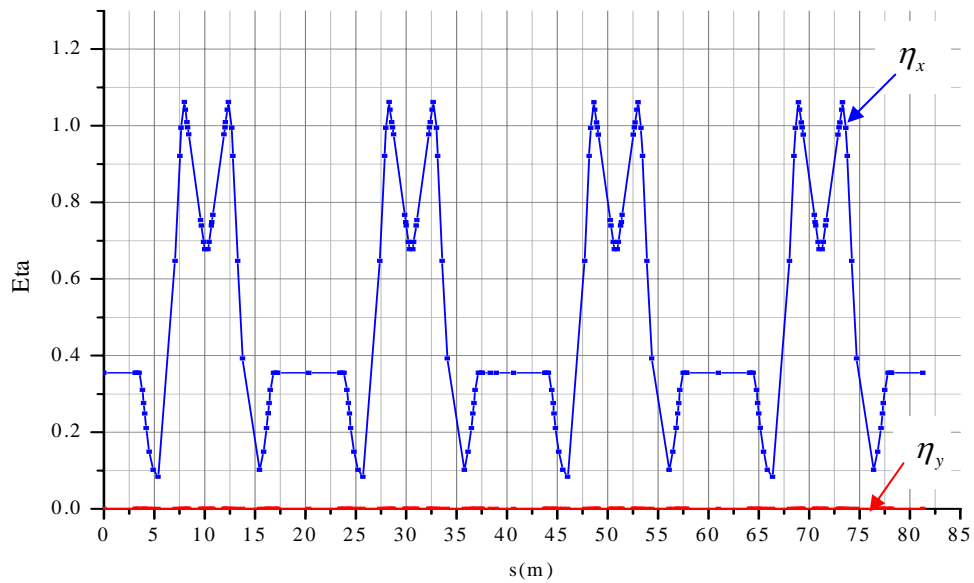


Figure 1.10 The dispersion function of the SPS storage ring.

1.4 The U60 Undulator

The U60 undulator of the SPS is designed to produce intense soft-x-rays. It is a permanent magnet planar undulator containing 41 magnetic periods, with 60 mm period length. The total length of the undulator was designed to be 2520 mm, which will occupy approximately half the space in one of the straight sections. It was constructed by Danfysik. Main parameters and a photograph of the U60 undulator are shown in Table 1.2 and Figure 1.11, respectively.



Figure 1.11 U60 undulator of the SPS.

Table 1.2 Parameters for the U60 undulator of the SPS.

Parameters	Data
ConFigureuration	PPM, symmetric
Period length	60 mm
Minimum gap	26 mm
Maximum gap	≥ 200
Length of magnet assemblies	2510 mm
Number of full size periods	40.5
Number of full size poles	81
Total number of poles	83
Magnetic material of vertical block	VACODUM 745 TP
Average remanence magnetic field (Br)	1.38 T
Magnetic material of horizontal block	VACODUM 655 TP
Average Br	1.23 T
Full size magnet block	38×96×15 mm
Magnetic flux density at minimum gap:	
Average B_0	0.5730 T
Average wiggler strength (K)	3.21
Minimum photon energy	37.03 eV
(26 mm gap, 1.2 GeV beam)	
Transverse roll-off at 26 mm gap:	
$x = \pm 5$ mm	0.072%
$x = \pm 10$ mm	0.31%

For the beam service, the SPS currently has three operational beamlines: Photoemission spectroscopy (BL-4), X-ray Lithography (BL-6) and X-ray Absorption Spectroscopy (BL-8). Synchrotron light used by all beamlines is generated by the bending magnets with synchrotron radiation critical energy of 1.34 keV at 1.2 GeV of electron beam energy. A few more beamlines are now under construction. These include a soft x-ray beamline which will utilize synchrotron radiation from a soft x-ray undulator U60.

CHAPTER II

THEORY OF UNDULATOR

In this chapter, theories related to undulator radiation and magnetic field measurements are discussed. These are divided into four parts, i.e. radiation from an ideal undulator, effects of field errors on the radiation, perturbations on storage ring and theories of magnetic field measurements.

2.1 Radiation from an Ideal Undulator

2.1.1 The Wiggler Strength

Before discussing the radiation from undulators, the important parameter called the wiggler strength must be defined. To satisfy the condition that when an insertion device is inserted into the storage ring, the electron beam must move out of the device with the same orbit as it enters. And by assuming that the net deflection orbit of electron is zero, the field integral must be zero.

$$\int_{-\infty}^{\infty} B_y(y=0, z) dz = 0. \quad (2.1)$$

For an ideal undulator, the magnetic field is approximated as

$$B_y(z) = B_o \sin(k_u z). \quad (2.2)$$

Here, B_0 is the peak magnetic field, $0 \leq z \leq N\lambda_u$, and $k_u = \frac{2\pi}{\lambda_u}$, where λ_u is the undulator magnetic period. A charged particle of mass γm_0 moving in the field \vec{B} will be acted upon by the Lorentz force

$$\gamma m_0 \frac{d^2 \vec{r}}{dt^2} = q(\vec{v} \times \vec{B}), \quad (2.3)$$

where q is the electric charge of the particle, $\gamma = \frac{E}{m_0 c^2}$ ($\gamma = 2345.1$ for electron energy $E = 1.2$ GeV) and $\vec{v} = \vec{v}_x + \vec{v}_z$ is velocity of an electron. By using (2.3), we obtain

$$\frac{dx}{dz} = \frac{qB_0}{\gamma m_0 c k_u} \cos(k_u z). \quad (2.4)$$

Therefore, the maximum deflection angle of the particle in the undulator field can be found as

$$\Theta = \left(\frac{dx}{dz} \right)_{\max} = \frac{eB_0}{\gamma m_0 c k_u}. \quad (2.5)$$

We therefore obtain the parameter characterizing the insertion device which is called the wiggler strength. It is defined as

$$K = \gamma \Theta = \frac{qB_0}{m_0 c k_u},$$

or

$$K = \frac{q\lambda_u B_0}{2\pi m_0 c} = 93.4 B_0 [\text{T}] \lambda_u [\text{m}]. \quad (2.6)$$

K is small for undulators. Theoretically K should be much less than 1, but in practice K may be maximum around 1 or even higher, e.g. the U60 undulator has maximum $K = 3.07$. In the case of $K = 1$ the angle becomes

$$\Theta = \frac{1}{\gamma},$$

which is the natural emission angle of the synchrotron radiation. For very small K , the radiation from each turn of an electron motion then added coherently, resulting in very high intensity of radiation.

2.1.2 Electron Dynamics

Since radiation characteristics depend upon the motion of the charged particle, a general case of undulators will be discussed, i.e. an elliptical undulator. The ideal device has perfectly sinusoidal fields in the two transverse planes, with phase difference of $\frac{\pi}{2}$. The longitudinal field is zero. These fields will cover all types of undulators. The fields in both transverse planes, B_x and B_y , with amplitudes B_{x0} and B_{y0} , respectively, are given by

$$\begin{aligned} B_x(z) &= B_{x0} \cos(k_u z), \\ B_y(z) &= B_{y0} \sin(k_u z). \end{aligned} \quad (2.7)$$

Inserting these fields and velocity $\vec{v} = \vec{v}_x + \vec{v}_y + \vec{v}_z$ in (2.3), we obtain the equation of motions as

$$\begin{aligned} \ddot{x} &= -\dot{z} \frac{q}{\gamma m_o} B_y(z), \\ \ddot{y} &= \dot{z} \frac{q}{\gamma m_o} B_x(z), \\ \ddot{z} &= \frac{q}{\gamma m_o} (\dot{x} B_y(z) - \dot{y} B_x(z)). \end{aligned} \quad (2.8)$$

The expressions in x and y components can be integrated to give the velocities in the transverse direction as

$$\begin{aligned}\dot{x} &= \frac{cK_y}{\gamma} \cos(k_u z), \\ \dot{y} &= \frac{cK_x}{\gamma} \sin(k_u z).\end{aligned}\tag{2.9}$$

In relativistic forms, these are

$$\begin{aligned}\beta_x &= \frac{K_y}{\gamma} \cos(k_u z), \\ \beta_y &= \frac{K_x}{\gamma} \sin(k_u z).\end{aligned}\tag{2.10}$$

The longitudinal velocity can be evaluated by using the relation

$$\beta_z = (\beta^2 - \beta_x^2 - \beta_y^2)^{\frac{1}{2}}.\tag{2.11}$$

Substituting β_x and β_y and using $(1+x)^m = 1 + mx + \frac{m(m-1)x^2}{2!} + \dots$, then

$$\beta_z \approx \beta \left(1 - \frac{1}{2\beta^2\gamma^2} (K_y^2 \cos^2(k_u z) + K_x^2 \sin^2(k_u z)) \right).$$

Because $\cos^2(x) = \frac{1}{2}(1 + \cos(2x))$, therefore

$$\begin{aligned}\beta_z &\approx \beta \left(1 - \frac{1}{4\beta^2\gamma^2} (K_y^2 (\cos(2k_u z) + 1) + K_x^2 (1 - \cos(2k_u z))) \right), \\ \beta_z &= \beta \left(1 - \frac{1}{4\beta^2\gamma^2} (K_x^2 + K_y^2) - \frac{1}{4\beta^2\gamma^2} (K_y^2 \cos(2k_u z) - K_x^2 \cos(2k_u z)) \right).\end{aligned}$$

This expression now can be written in the form

$$\beta_z = \bar{\beta}_z + \frac{1}{4\beta\gamma^2} (K_x^2 - K_y^2) \cos(2k_u z).\tag{2.12}$$

The formation of (2.12) consists of the time dependent velocity oscillation and the average longitudinal velocity $\bar{\beta}_z$ which is defined as

$$\bar{\beta}_z = \beta \left(1 - \frac{1}{4\beta^2\gamma^2} (K_x^2 + K_y^2) \right). \quad (2.13)$$

Because the wiggler strength $K \ll \gamma$, $\bar{\beta}_z$ therefore can be approximated as

$\bar{\beta}_z = \beta \left(1 - \frac{K^2}{4\gamma^2} \right) \approx \beta$. We now can express the term $k_u z$ as a function of time, $\omega_u t$

$$k_u z \approx k_u c \bar{\beta}_z t \approx \frac{2\pi\beta c}{\lambda_u} t = \omega_u t$$

Eventually, we obtain the components of the velocity as

$$\dot{x} = \frac{cK_y}{\gamma} \cos(\omega_u t),$$

$$\dot{y} = \frac{cK_x}{\gamma} \sin(\omega_u t),$$

$$\dot{z} = \bar{\beta}_z c + \frac{c}{4\beta\gamma^2} (K_x^2 - K_y^2) \cos(2\omega_u t).$$

Integrating these expressions gives

$$x = \frac{cK_y}{\gamma\omega_u} \sin(\omega_u t),$$

$$y = -\frac{cK_x}{\gamma\omega_u} \cos(\omega_u t),$$

$$z = \bar{\beta}_z ct + \frac{c}{8\beta\omega_u\gamma^2} (K_x^2 - K_y^2) \sin(2\omega_u t). \quad (2.14)$$

These expressions are the positions of an electron inside an elliptical undulator at time t , observed in the laboratory system. We will therefore see the particle trajectory as shown in Figure 2.1a. However, from the Lorentz transformation $x^* = x$, $y^* = y$ and

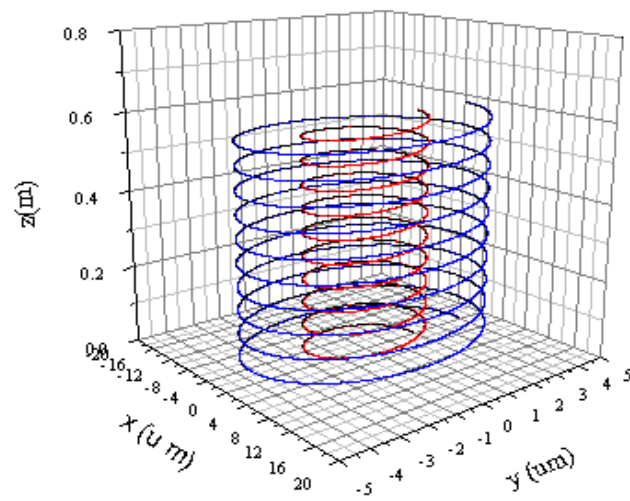
$z^* = \gamma(z - \bar{\beta}_z ct)$, the trajectory equations of a charged particle in the moving system are then

$$x^*(t) = \frac{K_y c}{\omega_u \gamma} \sin(\omega_u t),$$

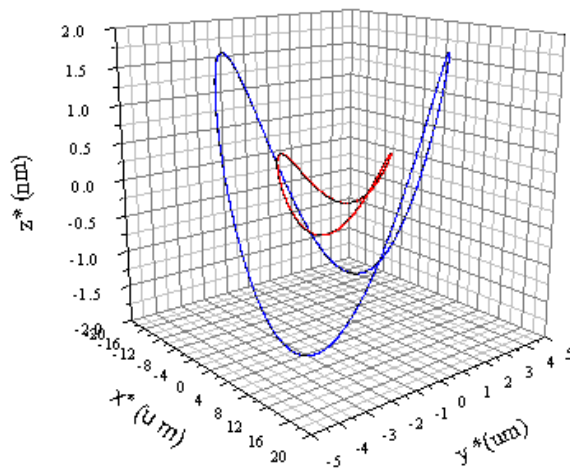
$$y^* = \frac{c K_x}{\gamma \omega_u} \sin(\omega_u t),$$

$$z^* = -\frac{c}{8\beta\omega_u\gamma^2} (K_x^2 - K_y^2) \sin(2\omega_u t).$$

The trajectories are now illustrated in Figure 2.1b-2.1d. In Figure 2.1b the trajectory is shown in 3D. For 2D trajectory, it processes the motion with “8” shape in x^*z^* plane. The smaller orbit is for the smaller wiggler strength K_i , where $i = x, y$. However, for large $K_x^2 - K_y^2$ the longitudinal amplitude grows quadratically, whereas the transverse amplitude is proportional to K_i . For the 2D trajectory in x^*y^* plan, the trajectory has elliptical shape, as illustrated in Figure 2.1d.

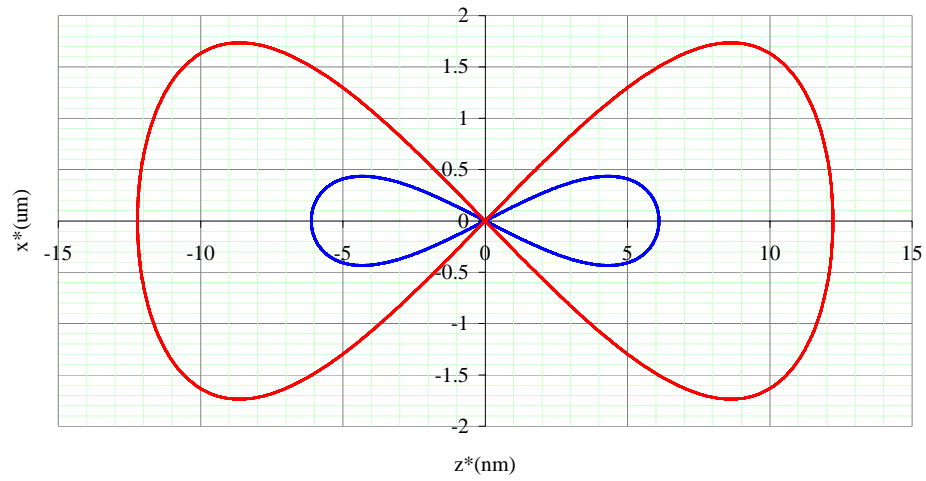


(a)

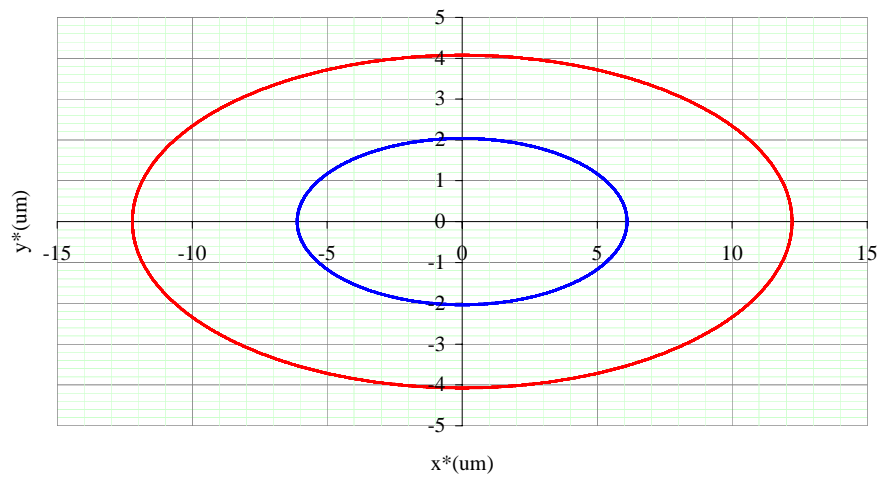


(b)

Figure 2.1 Particle trajectories in an elliptical undulator, with $\lambda_u = 60\text{mm}$, $N = 10$, $K_x = 0.5$ and $K_y = 1.5$ for small elliptical orbit; $K_x = 1$ and $K_y = 3$ for large elliptical orbit, observed in the (a) laboratory system, (b) moving system, (c) moving system in $x^* z^*$ plane and (d) moving system in $x^* y^*$ plane.



(c)



(d)

Figure 2.1 (Continued) Particle trajectories in an elliptical undulator, with $\lambda_u = 60\text{mm}$, $N = 10$, $K_x = 0.5$ and $K_y = 1.5$ for small elliptical orbit; $K_x = 1$ and $K_y = 3$ for large elliptical orbit, observed in the (a) laboratory system, (b) moving system, (c) moving system in $x^* z^*$ plane and (d) moving system in $x^* y^*$ plane.

We have the information of electron motion now. Next, we will employ them to find the radiation spectrum emitted by this electron.

2.1.3 The Undulator Equation

Figure 2.2 shows an electron trajectory inside an undulator (Wiedemann, 1995). At point A, it emits the synchrotron light. Later time τ , it moves to point B and emits the synchrotron light. The synchrotron light emitted at point A travels the distance S_{ph} before the emission at point B, where θ is the emitted angle. The distance d between two wavefronts is then expressed as

$$d = S_{ph} - \lambda_u \cos \theta$$

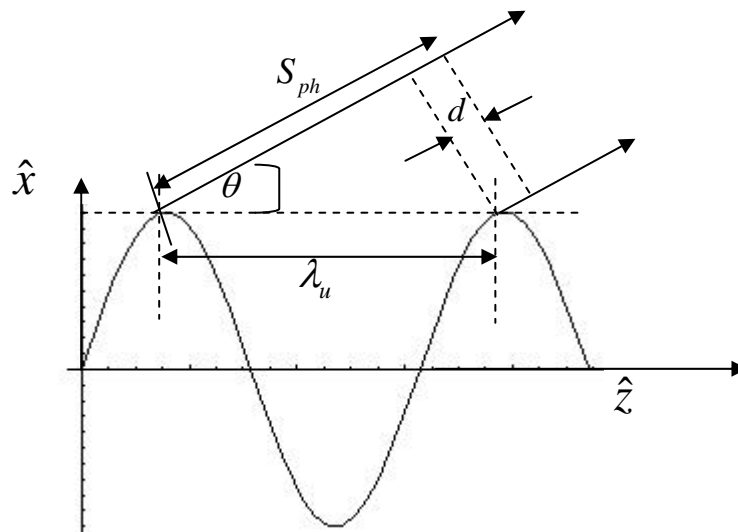


Figure 2.2 Electron path inside an undulator.

Constructive interference will occur, if the distance d is a whole number of wavelengths, $n\lambda_n$. So, we obtain

$$n\lambda_n = \lambda_u \left[\frac{1}{\bar{\beta}_z} - \cos \theta \right].$$

By substituting $\bar{\beta}_z$, defined in (2.13), this expression is then given by

$$\lambda_n = \frac{\lambda_u}{n} \left[\left[\beta \left(1 - \frac{K^2}{4\beta^2 \gamma^2} \right) \right]^{-1} - \cos \theta \right],$$

where $K^2 = K_x^2 + K_y^2$. By using binomial expansion, this equation becomes

$$\lambda_n = \frac{\lambda_u}{2n\gamma^2} \left[1 + \frac{K^2}{2} + \gamma^2 \theta^2 \right]. \quad (2.15)$$

The emitted photon energy is then given by

$$\varepsilon_n [eV] = 9.498n \frac{(E[GeV])^2}{\lambda_u [m] \left(1 + \frac{K^2}{2} + \gamma^2 \theta^2 \right)}. \quad (2.16)$$

The (2.15) is the radiated wavelength of an undulator. It depends on the observation angle, wiggler strength and the electron beam energy. In practice, an undulator is installed in a storage ring that services the synchrotron light for many users at fixed beam energy. The radiated wavelength tuning can be done by changing the wiggler strength. This tuning is achieved by opening and closing the undulator gap. The observation angle is also fixed while service the synchrotron light for the users. The relation between the radiated wavelength, K and θ is illustrated in Figure 2.3. For $n = 1$, the fundamental wavelength, λ_1 , of undulator radiation is obtained. This relates to the fundamental frequency, ω_1 . The fundamental frequency is the minimum frequency at which the undulator radiation from each turn interferes constructively.

We can see that (2.15) is the Doppler effect. When we observe at the $\theta = 0$ and off-

axis, the Doppler factor is respectively $1 + \frac{K^2}{2}$ and $1 + \frac{K^2}{2} + \gamma^2 \theta^2$. For the observed

angle of $\theta = 0$, $\lambda_u = 60$ mm and electron beam energy of 1.2 GeV, the on-axis fundamental wavelength is approximately 5.45 nm. The larger observed angle the

frequency appears red-shifted. And the wavelength increases rapidly for $\theta > \frac{1}{\gamma}$.

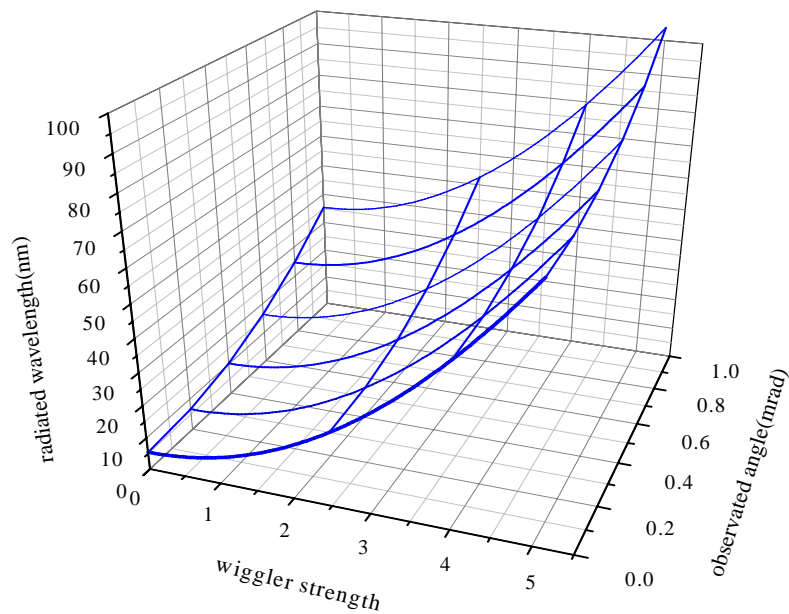


Figure 2.3 Fundamental wavelength as a function of a wiggler strength and the observation angle for 1.2 GeV electron beam and a 60 mm period length.

2.1.4 Frequency Spectrum of the Undulator Radiation

The energy radiated per unit frequency interval per unit solid angle by an electron passing through the undulator with period length λ_u consisting of N periods can be expressed as

$$\frac{d^2W}{d\omega d\Omega} = \frac{e^2 \omega^2}{16\pi^3 c \varepsilon_0} \left| \int_{\frac{\pi N}{\omega_u}}^{\frac{\pi N}{\omega_u}} (\hat{n} \times \hat{n} \times \vec{\beta}) e^{i\omega(t - \frac{\hat{n} \cdot \vec{r}(t)}{c})} dt \right|^2, \quad (2.17)$$

where \hat{n} is a unit vector pointing to the observer and $\vec{\beta}$ is $\frac{\vec{v}}{c}$, where c is the speed of light. ε_0 is the permittivity of free space and $\vec{r}(t)$ is the electron's position vector. The process is illustrated in Figure 2.4.

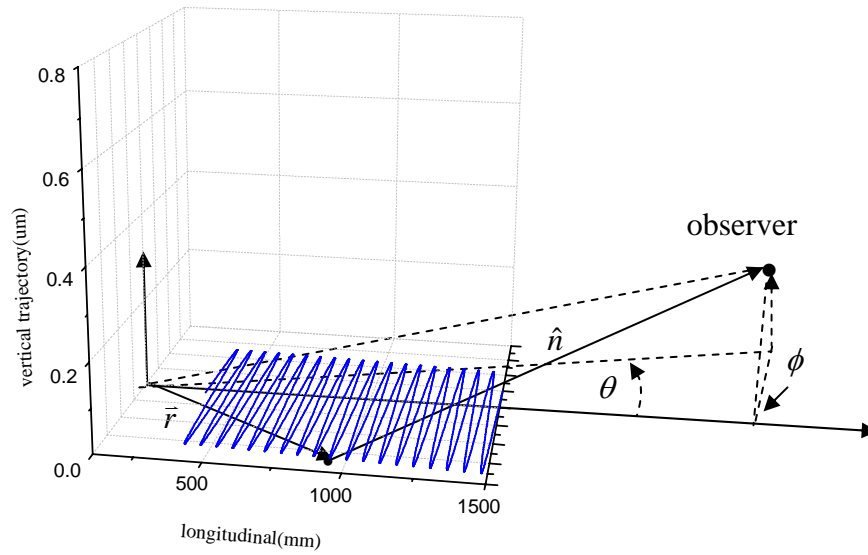


Figure 2.4 An electron motion inside undulator for the analysis of undulator radiation.

The term $\hat{n} \times \hat{n} \times \bar{\beta}$ can be found as

$$\hat{n} \times \hat{n} \times \bar{\beta} = (\beta_z \theta \cos \phi - \beta_x) \hat{x} + (\beta_z \theta \sin \phi - \beta_y) \hat{y} + (\beta_x \theta \cos \phi + \beta_y \theta \sin \phi) \hat{z},$$

where the unit vector \hat{n} , pointing from the particle to the observer, is defined as

$$\hat{n} = \sin \theta \cos \phi \hat{x} + \sin \theta \sin \phi \hat{y} + \cos \theta \hat{z}. \quad (2.18)$$

By assuming that $\beta_x \ll \beta_z$, $\beta_y \ll \beta_z$ and $\beta_z \approx 1$, this gives

$$\hat{n} \times \hat{n} \times \bar{\beta} = (\theta \cos \phi - \beta_x) \hat{x} + (\theta \sin \phi - \beta_y) \hat{y}, \quad (2.19)$$

where β_x and β_y are defined in (2.10). The electron trajectory (2.14) is

$$\begin{aligned} \bar{r}(t) = & \frac{cK_y}{\gamma\omega_u} \sin(\omega_u t) \hat{x} - \frac{cK_x}{\gamma\omega_u} \cos(\omega_u t) \hat{y} + \\ & [\bar{\beta}_z ct + \frac{c}{8\beta\omega_u\gamma^2} (K_x^2 - K_y^2) \sin(2\omega_u t)] \hat{z}. \end{aligned} \quad (2.20)$$

The exponent can then be expressed as

$$\begin{aligned} \omega(t - \frac{\hat{n} \cdot \bar{r}}{c}) = & \frac{\omega}{\omega_1} [\omega_u t - \frac{\omega_1}{\omega_u} \frac{\theta K_y}{\gamma} \cos \phi \sin(\omega_u t) + \frac{\omega_1}{\omega_u} \frac{\theta K_x}{\gamma} \sin \phi \cos(\omega_u t) \\ & + \frac{\omega_1}{\omega_u} (\frac{K_y^2 - K_x^2}{8\beta\gamma^2} \sin(2\omega_u t))]. \end{aligned}$$

This complicated expression can be simplified using the following relation

$$\omega(t - \frac{\hat{n} \cdot \bar{r}}{c}) = \frac{\omega}{\omega_1} [\omega_u t - X \sin(\omega_u t - \Phi) + Y \sin(2\omega_u t)], \quad (2.21)$$

where

$$\begin{aligned} X = & [A^2 + B^2]^{\frac{1}{2}}, \\ A = & \frac{\omega_1}{\omega_u} \theta \frac{K_x}{\gamma} \sin \phi, \\ B = & \frac{\omega_1}{\omega_u} \theta \frac{K_y}{\gamma} \cos \phi, \end{aligned}$$

$$Y = \frac{\omega_1}{\omega_u} \left[\frac{K_x^2 - K_y^2}{8\beta\gamma^2} \right]^{\frac{1}{2}},$$

and

$$\tan \Phi = \frac{A}{B}.$$

By using Bessel functions

$$e^{ix \sin \theta} = \sum_{q=-\infty}^{\infty} J_q(x) e^{iq\theta}, \quad (2.22)$$

the phase (2.22) can be then rewritten as

$$\exp\left[i\omega\left(t - \frac{\hat{n} \cdot \vec{r}}{c}\right)\right] = \exp[ik\omega_u t] \exp[-iX \sin(\omega_u t - \Phi)] \exp[+iY \sin(2\omega_u t)],$$

or

$$\exp\left[i\omega\left(t - \frac{\hat{n} \cdot \vec{r}}{c}\right)\right] = \sum_{p=-\infty}^{\infty} J_p(X) \sum_{p'=-\infty}^{\infty} J_{p'}(Y) e^{i(k\omega_u t - p(\omega_u t - \Phi) + p'(2\omega_u t))},$$

Substituting these equations into the energy spectrum (2.17) gives

$$\frac{d^2W}{d\omega d\Omega} = \frac{e^2 \omega^2}{16\pi^3 c \epsilon_0} \left| \int_{-\frac{\pi N}{\omega_u}}^{\frac{\pi N}{\omega_u}} (\hat{x}(\theta \cos \phi - \beta_x) + \hat{y}(\theta \sin \phi - \beta_y)) \sum_{p=-\infty}^{\infty} J_p(X) \sum_{p'=-\infty}^{\infty} J_{p'}(Y) e^{iQ\omega_u t} e^{i(p\Phi)} dt \right|^2, \quad (2.23)$$

where $Q = k - p + 2p'$, $k = \frac{\omega}{\omega_1}$. The time-independent term $e^{i(p\Phi)}$ is canceled by its

complex conjugate. Therefore, only the time-dependent term is carried out. That is

$$\int_{-\frac{\pi N}{\omega_u}}^{\frac{\pi N}{\omega_u}} (\hat{x}(\theta \cos \phi - \beta_x) + \hat{y}(\theta \sin \phi - \beta_y)) \left(\sum_{p=-\infty}^{\infty} J_p(X) \sum_{p'=-\infty}^{\infty} J_{p'}(Y) \right) e^{iQ\omega_u t} dt. \quad (2.24)$$

By using

$$\int_{-b}^b \exp(ia\omega t) dt = \frac{2 \sin(ab\omega)}{a\omega},$$

and

$$\int_{-b}^b \cos(\omega t) \exp(ia\omega t) dt = \frac{\sin((a+1)b\omega)}{(a+1)\omega} + \frac{\sin((a-1)b\omega)}{(a-1)\omega},$$

and substituting β_x and β_y in (2.24), the horizontal component therefore is given by

$$\begin{aligned} & \frac{\frac{\pi N}{\omega_u}}{\frac{\pi N}{\omega_u}} \int_{\frac{\omega_u}{\omega_u}}^{\frac{\omega_u}{\omega_u}} (\theta \cos \phi + \frac{K_y}{\gamma} \cos(\omega_u t)) \left(\sum_{p=-\infty}^{\infty} J_p(X) \sum_{p'=-\infty}^{\infty} J_{p'}(Y) \right) e^{iQ\omega_u t} dt = 2A_0 \left(\sum_{p=-\infty}^{\infty} J_p(X) \sum_{p'=-\infty}^{\infty} J_{p'}(Y) \frac{\sin(\pi QN)}{Q\omega_u} \right) \\ & + A_1 \left(\sum_{p=-\infty}^{\infty} J_p(X) \sum_{p'=-\infty}^{\infty} J_{p'}(Y) \left(\frac{\sin(Q+1)\pi N}{(Q+1)\omega_u} + \frac{\sin(Q-1)\pi N}{(Q-1)\omega_u} \right) \right), \end{aligned} \quad (2.25)$$

where $A_0 = \theta \cos \phi$ and $A_1 = \frac{K_y}{\gamma}$. The vertical component is given by

$$\begin{aligned} & \frac{\frac{\pi N}{\omega_u}}{\frac{\pi N}{\omega_u}} \int_{\frac{\omega_u}{\omega_u}}^{\frac{\omega_u}{\omega_u}} (\theta \sin \phi - \frac{K_x}{\gamma} \cos(\omega_u t + \psi)) \left(\sum_{p=-\infty}^{\infty} J_p(X) \sum_{p'=-\infty}^{\infty} J_{p'}(Y) \right) e^{iQ\omega_u t} dt = \\ & 2B_0 \left(\sum_{p=-\infty}^{\infty} J_p(X) \sum_{p'=-\infty}^{\infty} J_{p'}(Y) \frac{\sin(\pi QN)}{Q\omega_u} \right) - B_1 \left(\sum_{p=-\infty}^{\infty} J_p(X) \sum_{p'=-\infty}^{\infty} J_{p'}(Y) \left(\frac{\sin(Q+1)\pi N}{(Q+1)\omega_u} + \frac{\sin(Q-1)\pi N}{(Q-1)\omega_u} \right) \right), \end{aligned} \quad (2.26)$$

where $B_0 = \theta \sin \phi$ and $B_1 = \frac{K_x \cos \psi}{\gamma}$. By substituting (2.25) and (2.26) into (2.23),

the undulator radiation spectrum is eventually given by

$$\begin{aligned} \frac{d^2W}{d\omega d\Omega} &= \frac{e^2 \omega^2 N^2}{4\pi c \epsilon_0 \omega_u^2} \left| \hat{x} \left(A_0 \sum_{p=-\infty}^{\infty} J_p(X) \sum_{p'=-\infty}^{\infty} J_{p'}(Y) \frac{\sin(\pi QN)}{\pi N Q} \right. \right. \\ & \quad \left. \left. + A_1 \sum_{p=-\infty}^{\infty} J_p(X) \sum_{p'=-\infty}^{\infty} J_{p'}(Y) \frac{1}{2} \left(\frac{\sin(Q+1)\pi N}{\pi N(Q+1)} + \frac{\sin(Q-1)\pi N}{\pi N(Q-1)} \right) \right) \right. \\ & \quad \left. + \hat{y} \left(B_0 \sum_{p=-\infty}^{\infty} J_p(X) \sum_{p'=-\infty}^{\infty} J_{p'}(Y) \frac{\sin(\pi QN)}{\pi N Q} \right. \right. \end{aligned}$$

$$-B_1 \sum_{p=-\infty}^{\infty} J_p(X) \sum_{p'=-\infty}^{\infty} J_{p'}(Y) \frac{1}{2} \left(\frac{\sin(Q+1)\pi N}{\pi N(Q+1)} + \frac{\sin(Q-1)\pi N}{\pi N(Q-1)} \right) \Bigg|^2.$$

(2.27)

This expression (2.27) contains the components that correspond to radiation polarized in horizontal plane, denoted by unit vector \hat{x} , and in vertical plane, denoted by unit vector \hat{y} . The $\frac{\sin(\pi Q N)}{\pi Q N}$ and $\frac{\sin((Q \pm 1)\pi N)}{(Q \pm 1)\pi N}$ factors represent the linewidth of the radiation. It is the result of the interference between successive periods of N periods. The expression (2.27) can be expressed in a simpler form. Firstly, by defining

$$P_{Q+j} = \frac{\sin \pi N(Q+j)}{\pi N(Q+j)}, \quad j = 0, \pm 1. \quad (2.28)$$

We know that the function $\frac{\sin x}{x}$ is maximum when $x \rightarrow 0$. Therefore, the P_Q and

P_{Q+j} factors are respectively maximum at

$$\omega = (p - 2p')\omega_1,$$

$$\omega = (p - 2p' - j)\omega_1. \quad (2.29)$$

That is

$$k = p - 2p',$$

$$k = p - 2p' - j. \quad (2.30)$$

The factor $Q + j$ can be therefore replaced by Q_k , where

$$Q_k = \frac{\omega}{\omega_1} - k = \frac{\Delta\omega_k}{\omega_1}. \quad (2.31)$$

The factor P_k is then given by

$$P_k = \frac{\sin \pi N Q_k}{\pi N Q_k}. \quad (2.32)$$

Secondly, the polarization modes at k^{th} harmonics in the horizontal and vertical planes are assigned to $A_{\sigma k}$ and $A_{\pi k}$, respectively. The undulator spectrum for the k^{th} harmonic from (2.27) eventually is obtained

$$\frac{d^2 W_k}{d\omega d\Omega} = \frac{e^2 \omega_k^2 N^2}{4\pi c \epsilon_0 \omega_u^2} P_k^2 |A_{\sigma k}, A_{\pi k}|^2, \quad (2.33)$$

where $A_{\sigma k}$, $A_{\pi k}$ and S_j are respectively defined as

$$A_{\sigma k} = A_0 S_0 + \frac{A_1}{2} (S_{+1} + S_{-1}),$$

$$A_{\pi k} = B_0 S_0 - \frac{B_1}{2} (S_{+1} + S_{-1}),$$

$$S_j = \sum_{p'=-\infty}^{\infty} J_{k+2p'+j}(X) J_{p'}(Y), \quad (2.34)$$

The factor P_k^2 with various undulator periods is illustrated in Figure 2.5. The graph shows that the undulator with more periods ($N = 41$) produces radiation with narrower linewidth. So, the more sharp peak will be produced when the number of the number of magnetic period, N , is increased. Moreover, the undulator radiation spectrum is proportional to the square of number magnetic periods.

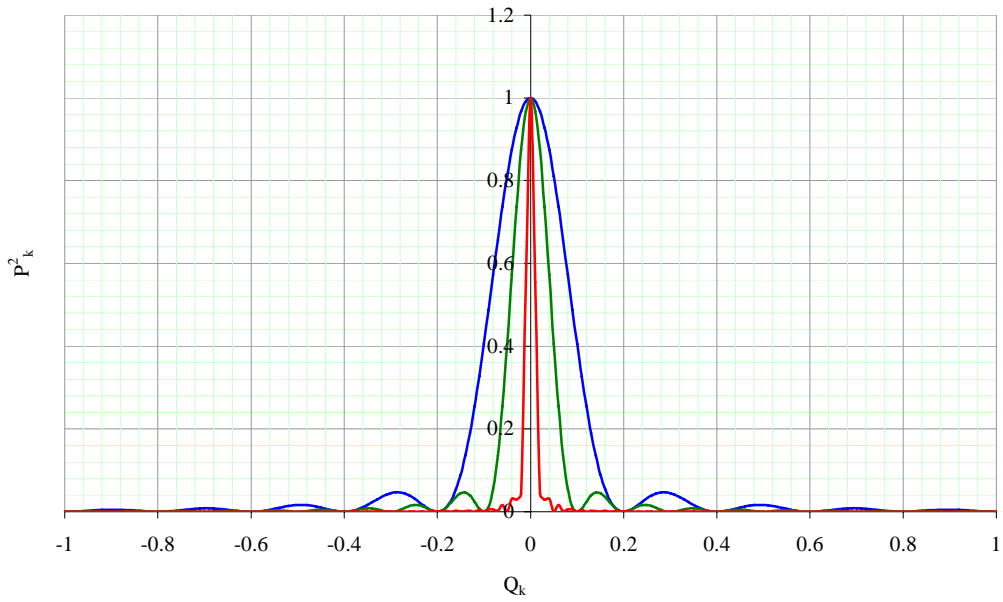


Figure 2.5 The linewidth of the radiation as a function of Q , plotted with periods $N = 5$ (widest graph) $N = 10$ (middle graph) and $N = 41$ (narrowest graph).

The spectrum of the undulator radiation is then obtained by summing over all the harmonics,

$$\frac{d^2W}{d\omega d\Omega} = \sum_k \frac{d^2W_k}{d\omega d\Omega}. \quad (2.35)$$

The radiation produced in the forward direction now will be discussed.

A_0 , B_0 and X are zero in this case. Because the property of the Bessel function,

$$J_{k+2p'+j}(0) = \begin{cases} 1, & k+2p'+j=0, \\ 0, & k+2p'+j \neq 0. \end{cases}$$

The spectrum expressed in (2.35) is non-zero only when

$$p' = -\frac{k+j}{2}. \quad (2.36)$$

By substitution p' into the expression S_j , this gives

$$S_j = J_{\frac{k+j}{2}}(Y). \quad (2.37)$$

By substituting S_j into $A_{\sigma k}$ and $A_{\pi k}$ and using the identity $J_{-n} = (-1)^n J_n$, these give

$$\begin{aligned} A_{\sigma k} &= \frac{A_1}{2} (J_{\frac{k-1}{2}}(Y) - J_{\frac{k+1}{2}}(Y)), \\ A_{\pi k} &= \frac{B_1}{2} (J_{\frac{k+1}{2}}(Y) - J_{\frac{k-1}{2}}(Y)). \end{aligned} \quad (2.38)$$

Due to the integral order of the Bessel functions, the index k must be restricted to odd numbers and thus there are no even harmonics observed on-axis.

For the planar undulator, the wiggler strength in horizontal component, K_x , is zero. The energy spectrum for the k^{th} harmonic is therefore reduced to

$$\frac{d^2 W_k}{d\omega d\Omega} = \frac{e^2 \omega_k^2 N^2}{4\pi c \epsilon_0 \omega_u^2} P_k^2 |A_{\sigma k}|^2,$$

or

$$\frac{d^2 W_k}{d\omega d\Omega} = \frac{e^2 \omega_k^2 N^2}{4\pi c \epsilon_0 \omega_u^2} P_k^2 \left(\frac{K_y}{2\gamma}\right)^2 \left| J_{\frac{k-1}{2}}(Y) - J_{\frac{k+1}{2}}(Y) \right|^2, \quad (2.39)$$

where Y is reduced to $Y = \frac{kK_y^2}{4(1 + \frac{K_y^2}{2})}$.

The linewidth function P_k in (2.32) is first zero, i.e. destructive interference first occur, when the bandwidth $\frac{\Delta\omega_k}{\omega_1} = \frac{1}{N}$. Therefore the bandwidth of the k^{th} harmonic of the radiation at frequency ω_k is then

$$\frac{\Delta\omega_k}{\omega_k} = \frac{1}{kN}. \quad (2.40)$$

For example, a typical undulator with 41 periods would have a bandwidth of around 2.43% at the first harmonic.

At the angle θ , the frequency is changed by

$$\Delta\omega_k = \omega(\theta) - \omega_k,$$

where

$$\omega(\theta) = \frac{2k\gamma^2\omega_u}{1 + \frac{K^2}{2} + \gamma^2\theta^2}, \quad (2.41)$$

and

$$\omega_k = \frac{2k\gamma^2\omega_u}{1 + \frac{K^2}{2}}.$$

The frequency, $\omega(\theta)$, can be rewritten in form of $\Delta\omega_k$ and ω_k :

$$\omega(\theta) = \omega_k \left(\frac{\Delta\omega_k}{\omega_k} + 1 \right).$$

By substituting $\frac{\Delta\omega_k}{\omega_k}$ from (2.41) we obtain

$$\omega(\theta) = \omega_k \left(1 + \frac{1}{kN} \right).$$

Later, by substituting this expression into (2.42), we finally obtain the angle at which the intensity falls to zero,

$$\theta = \frac{1}{\gamma} \sqrt{\frac{1 + \frac{K^2}{2}}{1 + kN}}.$$

For an undulator consisting of a large number of magnetic periods, kN , this gives

$$\theta \approx \frac{1}{\gamma} \sqrt{\frac{1 + \frac{K^2}{2}}{kN}} = \sqrt{\frac{2\lambda}{N\lambda_u}}. \quad (2.42)$$

The rms opening angle is defined as

$$\theta_1^2 = 2\sigma_{rms}^2,$$

where θ_1 is the angle at which $\sin x = 0$ for the first time. The rms opening angle is therefore given by

$$\sigma_{rms} \approx \frac{1}{\gamma} \sqrt{\frac{1 + \frac{K^2}{2}}{2kN}}. \quad (2.43)$$

Eq. (2.44) shows that the undulator radiation becomes more collimated as the number of magnetic periods and harmonic number increase. This expression will be employed to calculate the total flux of undulator radiation.

2.1.5 The On-axis Spectral Photon Flux of Undulator Radiation

We have now the frequency distribution of the undulator radiation. However, the photon flux distribution is more useful for the user. The photon flux distribution will therefore be discussed next. Since we know the number of photon is the photon energy divided by energy of one photon, $\hbar\omega$. The photon flux, the number of photons per unit time, for the k^{th} harmonic of synchrotron radiation emitted by the electron beam with the beam current I is given by

$$\frac{d^2F_k}{d\omega d\Omega} = \frac{I}{e} \frac{1}{\hbar\omega} \frac{d^2W_k}{d\omega d\Omega}. \quad (2.44)$$

Since the synchrotron radiation received by the user is not exactly monochromatic, but has a small bandwidth around the required frequency. The on-axis photon flux is therefore

$$\left. \frac{dF_k}{d\Omega} \right|_{\theta=0} = \frac{I}{eh} \frac{\Delta\omega}{\omega} \left. \frac{d^2W_k}{d\omega d\Omega} \right|_{\theta=0}. \quad (2.45)$$

Due to the synchrotron light radiated from an undulator is collimated, the total photon flux can be evaluated inside solid angle $d\Omega = 2\pi\sigma_{rms}^2$. The total flux is eventually given by

$$F_k|_{\theta=0} = \frac{d^2W_k}{d\omega d\Omega}|_{\theta=0} = \frac{I\pi}{Ne\hbar} \frac{\Delta\omega}{\omega} \frac{(1 + \frac{K^2}{2})}{k}. \quad (2.46)$$

2.2 Magnetic Field Errors of Undulators

The spectrum of undulator radiation from an ideal undulator has been derived in the previous section. However, in practice a perfect device cannot be realized. Magnetic field errors in the device always exist. Therefore, the generated magnetic field is not quite a perfect sinusoidal field. The errors affect the undulator radiation. In this section the magnetic field errors and their influence on the undulator radiation will be discussed.

2.2.1 The Phase Error

While an electron is moving inside a real undulator, it is acted to move with different path length in each period. This effect is called “phase error”. In Figure 2.6, an electron moves through a periodic field $\vec{B}_y(z)$, generated by a real device. This field is assumed such that it is not perfectly sinusoidal.

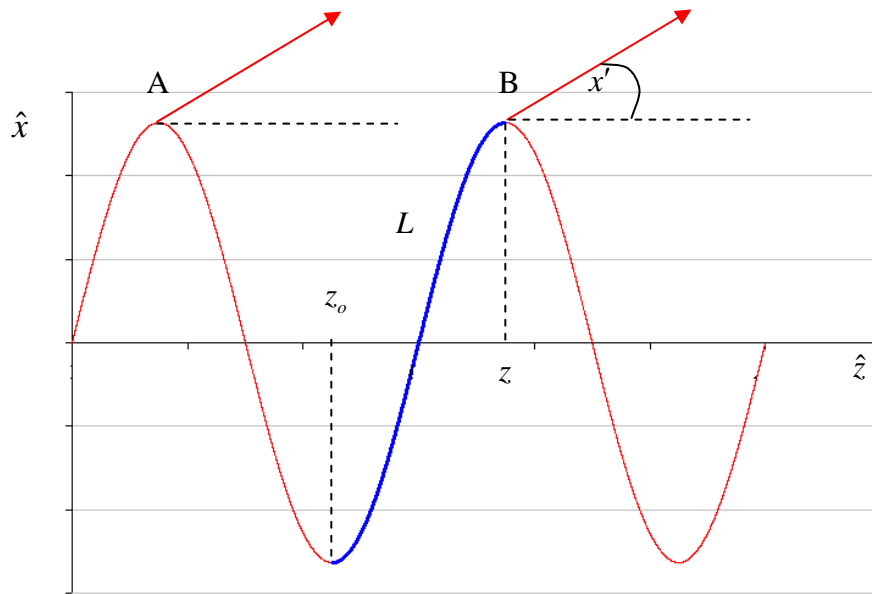


Figure 2.6 Trajectory of an electron in a imperfect periodic field $B_y(z)$.

In Figure 2.6, an electron moves with the path length, dL , that can be expressed as

$$dL = (dx^2 + dz^2)^{\frac{1}{2}},$$

where dx and dz are respectively the distance elements in horizontal and longitudinal direction. When the electron moves from z_0 to z , the distance can be written as

$$L = \int_{z=z_0}^{z=z} [1 + x'^2]^{\frac{1}{2}} dz.$$

By using the polynomial expansion, this equation gives

$$L = \int_{z=z_0}^{z=z} \left(1 + \frac{x'^2}{2}\right) dz,$$

$$L \cong (z - z_0) + \int_{z=z_0}^{z=z} \frac{x'^2}{2} dz,$$

where $x'(z)$ is the deflection angle evaluated from the equation of motion which can be found by

$$x'(z) = \frac{0.3}{E[\text{GeV}]} I_y(z), \quad (2.47)$$

where $I_y(z)$ is the first field integral. It is defined as

$$I_y(z) = \int_{z'=0}^{z'=z} B_y(z') dz'. \quad (2.48)$$

The phase function at point z with respect to point z_o is defined by (Diviacco, Walker, 1988)

$$\delta(z) = \frac{2\pi}{\lambda} \left[\frac{L}{\beta} - (z - z_o) \right],$$

where λ is the wavelength of the undulator radiation. By substituting L , this gives

$$\delta(z) = \frac{2\pi}{\lambda} \left[\frac{(z - z_o)}{\beta} + \frac{\int_{z=z_o}^{z=z} \frac{x'^2}{2} dz}{\beta} - (z - z_o) \right],$$

$$\delta(z) = \frac{2\pi}{\lambda} \left[(z - z_o) \left(\frac{1 - \beta}{\beta} \right) + \frac{1}{\beta} \int_{z=z_o}^{z=z} \frac{x'^2}{2} dz \right].$$

For $\beta \approx 1$, $1 - \beta$ can be approximated as

$$1 - \beta = \frac{(1 - \beta)(1 + \beta)}{(1 + \beta)} = \frac{(1 - \beta^2)}{(1 + \beta)} = \frac{1}{\gamma^2(1 + \beta)},$$

$$1 - \beta \approx \frac{1}{2\gamma^2}.$$

Finally, the phase function can be written as

$$\delta(z) = \frac{2\pi}{\lambda} \left[\frac{(z - z_o)}{2\gamma^2} + \int_{z=z_o}^{z=z} \frac{x'^2}{2} dz \right]. \quad (2.49)$$

If the phase function in each period is calculated, the average can be found. Therefore, by subtracting the average, the phase error can be calculated (Diviacco and Walker, 1996). That is

$$\Delta\delta = \delta_{real} - \delta_{avg}, \quad (2.50)$$

where δ_{real} and δ_{avg} are phase function in each period in real device and the average of them, respectively. In an ideal undulator, the phase function of all periods are the same. That means the phase error of an ideal device is zero.

2.2.2 The Spectral Photon Flux with Phase Error

The phase error naturally affects the quality of undulator radiation. The reduction in undulator radiation due to the phase error (Diviacco and Walker, 1996) can be calculated by

$$F_k|_{real} = \left(\frac{d^2W_k}{d\omega d\Omega} \right) \Big|_{ideal} e^{-(k\sigma_\phi)^2} \frac{I\pi}{Ne\hbar} \frac{\Delta\omega}{\omega} \frac{(1 + \frac{K^2}{2})}{k}, \quad (2.51)$$

where σ_ϕ is the rms phase error and k is the harmonic number. The ratios of photon flux as a function of harmonic number for various rms phase errors are illustrated in Figure 2.7. The on-axis spectrum can be calculated using the following approximation (Shih and Caponi, 1982; Walker, 1993) :

$$\frac{d^2W_k}{d\omega d\Omega} = \frac{e^2\omega_k^2}{16\pi^3 c^3 \epsilon_0} \left| \int_{-\infty}^{\infty} x' e^{i\delta} dz \right|^2, \quad (2.52)$$

where δ is the phase function and $x'(z)$ is the deflection angle of an electron as moving inside an undulator, defined in (2.47).

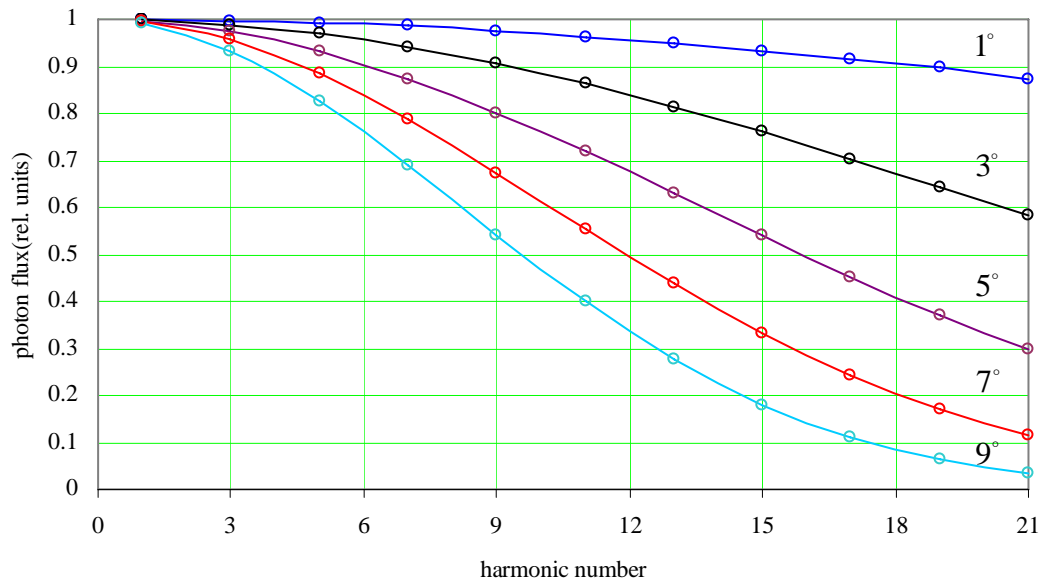


Figure 2.7 The reduction of ratio photon flux as a function of harmonic number for various rms phase error.

2.3 Theories of Magnetic Field Measurements

2.3.1 Magnetic Field Mapping

Magnetic field mapping is carried out by Hall Probe scanning. The field value is obtained by Hall effect. This is the production of the electric field in a current carrying crystal when it is acted on by a magnetic field. The electric field, current and magnetic field are mutually orthogonal. The resultant voltage is given by

$$V_H = \frac{R_H}{d} IB_n, \quad (2.53)$$

where R_H is the Hall coefficient of the material, d is the plate thickness and I is the current and B_n is the normal component of magnetic field.

2.3.2 First Field Integral Measurements by Flipping Coil

The basic expression of the magnetic flux Φ due to magnetic field, \vec{B} , passing through the element area $d\vec{s}$ is given by

$$\Phi = N \int_s \vec{B} \cdot \vec{n} ds,$$

where N is the number of turns in the coil and \vec{n} is normal vector, defined as

$$\vec{n} = \sin \theta \hat{x} + \cos \theta \hat{y}.$$

The undulator magnetic field, \vec{B} , is given by

$$\vec{B} = B_x \hat{x} + B_y \hat{y}.$$

By substituting \vec{n} and \vec{B} , the magnetic flux thus becomes

$$\Phi = N \int_s B_y ds \cos \theta + N \int_s B_x ds \sin \theta,$$

$$\Phi = \Phi_x + \Phi_y,$$

where Φ_x and Φ_y are defined as

$$\Phi_y = N \int_s B_y ds \cos \theta,$$

$$\Phi_x = N \int_s B_x ds \sin \theta.$$

When the magnetic flux varies with time, the induced voltage V is generated. The relation can be written by

$$V = -\frac{d\Phi}{dt} = -\frac{d\Phi_x}{dt} - \frac{d\Phi_y}{dt}.$$

The mathematical expression for obtaining the first field integral will now be derived. From the definition of the first field integral, the coil must be formed

in the rectangular shape. The coil is therefore formed with dimension $L \times D$, shown in Figure 2.8b.

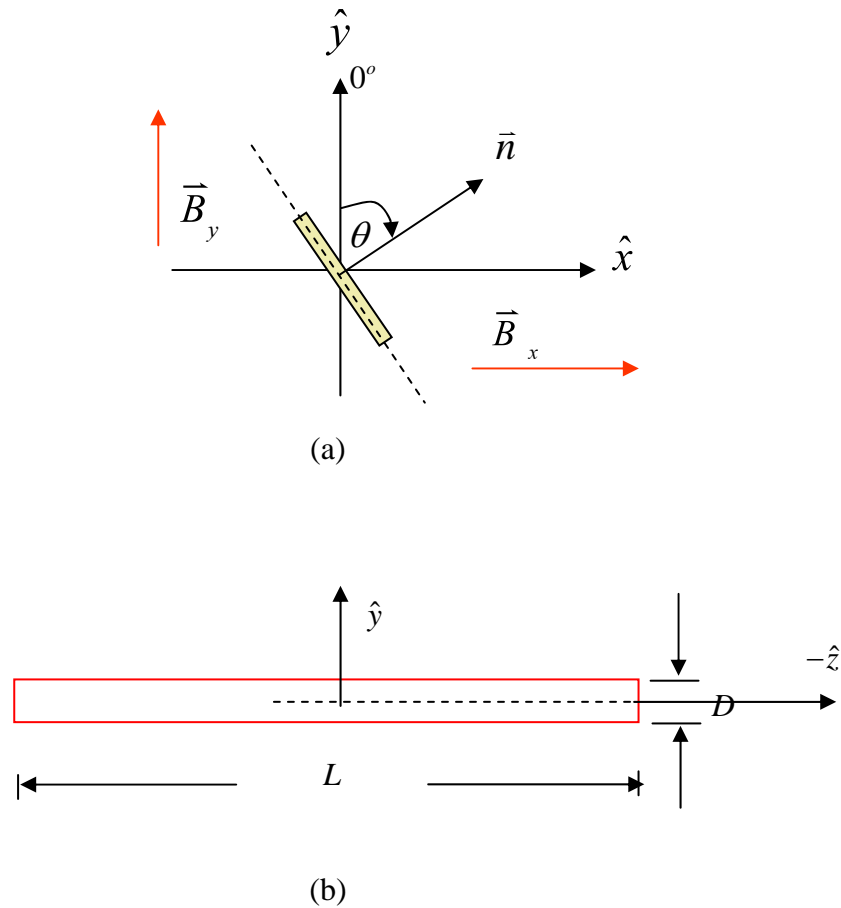


Figure 2.8 The coil configuration for measuring the first field integral. a) side view along the longitudinal axis and b) side view of the coil along the transverse axis ($\vec{n} = +\hat{x}$).

By substituting the magnetic flux into the induced voltage equation, the result becomes

$$V = -ND \left[\left(\int_{z=0}^L B_y(z) dz \right) \left(-\sin \theta \frac{d\theta}{dt} \right) + \left(\int_{z=0}^L B_x(z) dz \right) \left(\cos \theta \frac{d\theta}{dt} \right) \right],$$

$$V = -ND[I_y(-\sin \theta \frac{d\theta}{dt}) + I_x(\cos \theta \frac{d\theta}{dt})].$$

By flipping the coil from θ_i at time t_i to θ_f at time t_f , the integrated voltage, ε' , will therefore be obtained:

$$\varepsilon' = \frac{\int_{t_i}^{t_f} V dt}{ND} = I_y \int_{\theta_i}^{\theta_f} \sin \theta d\theta - I_x \int_{\theta_i}^{\theta_f} \cos \theta d\theta,$$

$$\varepsilon' = I_y[-\cos \theta]_{\theta_i}^{\theta_f} + I_x[-\sin \theta]_{\theta_i}^{\theta_f},$$

$$\varepsilon' = \varepsilon'_y + \varepsilon'_x,$$

where ε'_y and ε'_x are defined as

$$\varepsilon'_y = I_y[-\cos \theta]_{\theta_i}^{\theta_f}, \quad (2.54)$$

$$\varepsilon'_x = I_x[-\sin \theta]_{\theta_i}^{\theta_f}. \quad (2.55)$$

ε'_y in (2.54) will be first measured. By starting with the vector \vec{n} in direction of \hat{y} ($\theta = 0^\circ$), the coil is then flipped from 0° to 180° and next it is flipped from 180° to 360° . Later, it is reversely flipped from 0° to -180° and it is finally flipped from -180° to -360° . These procedures are illustrated in Figure 2.9.

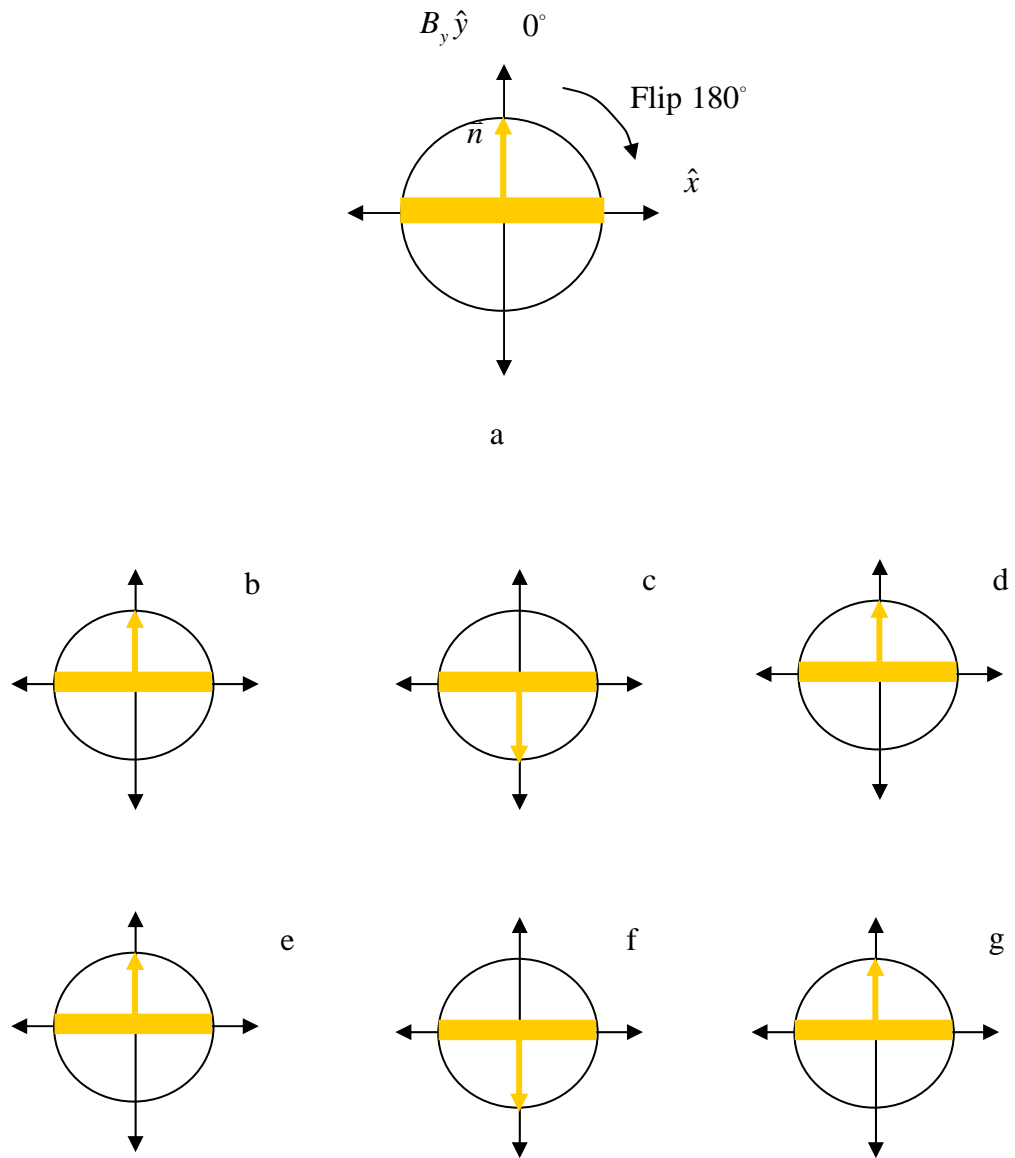


Figure 2.9 The procedure for measuring ε'_y . a) is the start of the procedure. First flips the coil from 0° to 180° (b-c), next flip the coil from 180° to 360° (c-d). The coil is then flipped back from 0° to -180° (e- f) and it is finally flipped from -180° to -360° (f-g).

Flipping the coil from 0° to 180° gives

$$\varepsilon'_{y,1} = 2I_y + I_d, \quad (2.56)$$

where I_d is the zero field offset. Next, flipping the coil from 180° to 360° gives

$$\varepsilon'_{y,2} = -2I_y + I_d. \quad (2.57)$$

Next, the coil is flipped back from 0° to -180° . This procedure gives

$$\varepsilon'_{y,3} = 2I_y + I_d. \quad (2.58)$$

Finally, the coil is flipped from -180° to -360° . This procedure gives

$$\varepsilon'_{y,4} = -2I_y + I_d. \quad (2.59)$$

Making subtraction (2.56) with (2.57) and (2.58) with (2.59) give vertical first field integrals as

$$I_{y,1} = \frac{\varepsilon'_{y,1} - \varepsilon'_{y,2}}{4} \quad (2.60)$$

$$I_{y,2} = \frac{\varepsilon'_{y,3} - \varepsilon'_{y,4}}{4} \quad (2.61)$$

The averaged vertical field integral are evaluated by making repeated measurement.

For measuring the ε'_x in (2.55), the coil starts at $\theta = 90^\circ$ ($\vec{n} = \hat{x}$), shown in Figure 2.10a. The procedure for measuring the ε'_x is illustrated in Figure 2.10b-2.10g.

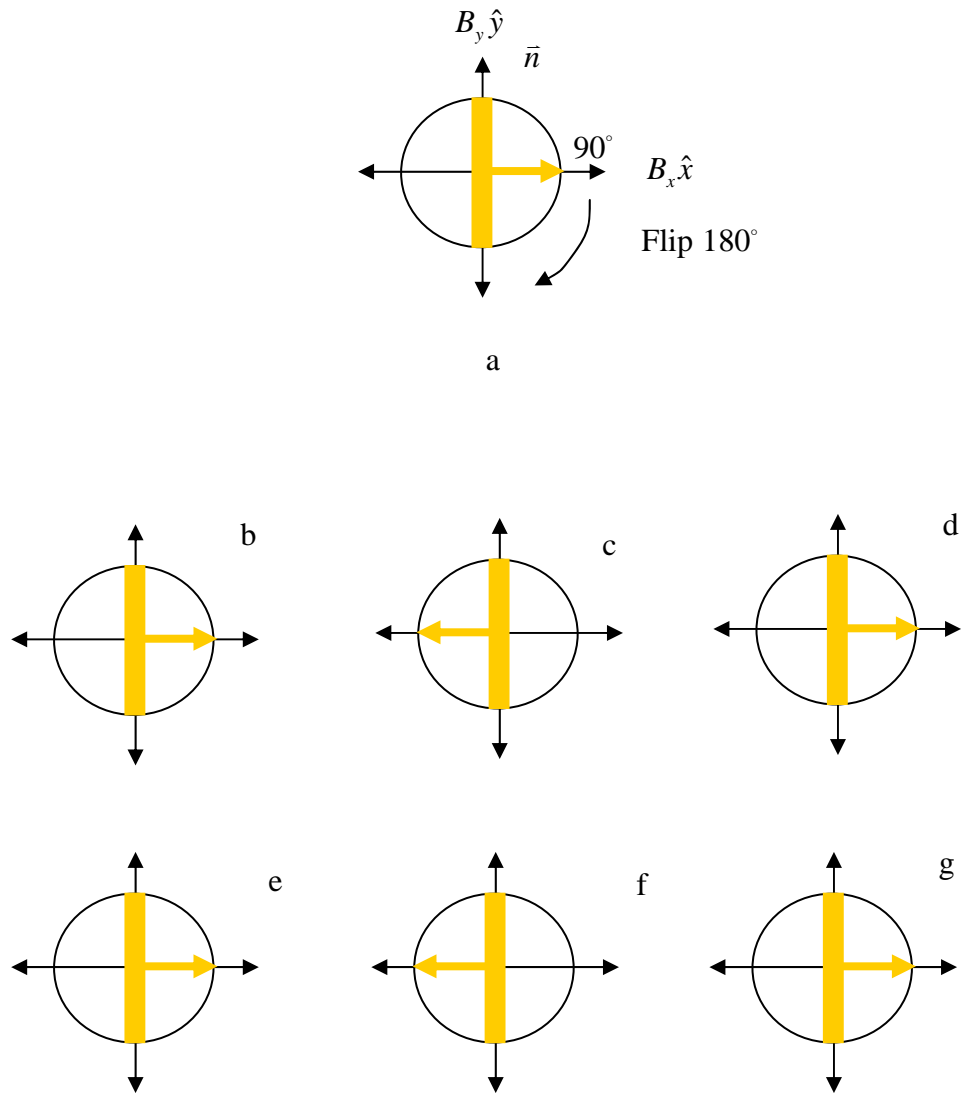


Figure 2.10 The procedure to measure ε'_x . The coil is started with configuration in 2.11a. First, the coil is flipped from 90° to 270° (b-c). Next, it is flipped from 270° to 450° (d-e). Later, the coil is flipped back from 90° to -270° (e-f). Finally, it is flipped from -270° to -450° (f-g).

For measuring ε'_x in Figure 2.10, the coil is first flipped from 90° to 270° (Figure 2.10b-c.). This procedure gives

$$\varepsilon'_{x,1} = 2I_x + I_d. \quad (2.62)$$

The coil is then flipped from 270° to 450° (Figure 2.10d-e). This procedure gives

$$\varepsilon'_{x,2} = -2I_x + I_d. \quad (2.63)$$

Next, it is flipped back from 90° to -270° (Figure 2.10e-f). This procedure gives

$$\varepsilon'_{x,3} = 2I_x + I_d. \quad (2.64)$$

Finally, it is flipped from -270° to -450° (Figure 2.10f-g). This procedure gives

$$\varepsilon'_{x,4} = -2I_x + I_d. \quad (2.65)$$

Making subtraction (2.62) with (2.63) and (2.64) with (2.65) thus give the vertical first field integral as

$$I_{x,1} = \frac{\varepsilon'_{x,1} - \varepsilon'_{x,2}}{4}, \quad (2.66)$$

$$I_{x,2} = \frac{\varepsilon'_{x,3} - \varepsilon'_{x,4}}{4}. \quad (2.67)$$

Similarly, the averaged horizontal field integral are obtained by making repeated measurements.

2.3.3 Second Field Integral Measurements by Flipping Coil

In this section the mathematical expression for obtaining the second field integral will be derived. Before measuring the second field integral, the coil must be formed in the 8-shape configuration. The schematic view is shown in Figure 2.11.

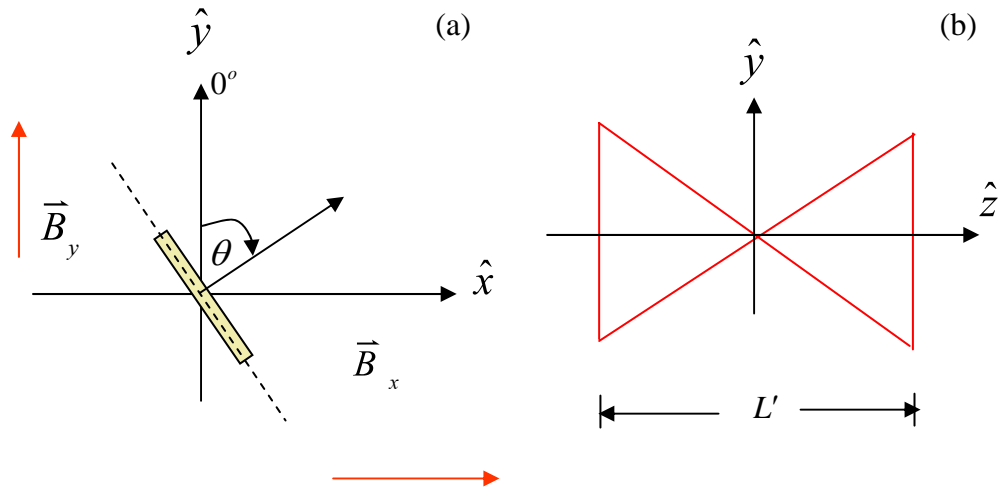


Figure 2.11 The coil configuration to measure the second field integral. (a) side view along the longitudinal axis and (b) side view of the coil along the transverse axis ($\vec{n} = +\hat{x}$).

To obtain the second field integral, we will go back to the equation for the magnetic flux:

$$\Phi = N \int_S B_y ds \cos \theta + N \int_S B_x ds \sin \theta.$$

Making substitution to the modified elementary area ds , the magnetic flux can therefore be written as

$$\Phi = \frac{2ND}{L'} \left[\int_{z=0}^{z=L'} B_y(z) z dz \cos \theta + \int_{z=0}^{z=L'} B_x(z) z dz \sin \theta \right],$$

$$\Phi = \Phi_x + \Phi_y,$$

where $\Phi_y = \frac{2ND}{L'} \int_{z=0}^{z=L'} B_y(z) z dz \cos \theta$ and $\Phi_x = \frac{2ND}{L'} \int_{z=0}^{z=L'} B_x(z) z dz \sin \theta$.

Integrating by part the term $\int_{z=0}^{L'} B_i(z)zdz$ then gives

$$\int_{z=0}^{L'} B_i(z)zdz = \frac{L'}{2} \int_{z=0}^{L'} B_i(z)dz - \int_{z''=0}^{L'} \int_{z'=0}^{z''} B_i(z')dz'dz'',$$

$$\int_{z=0}^{L'} B_i(z)zdz = \frac{L'}{2} I_i - II_i,$$

where $i = x$ or y . Magnetic flux is eventually obtained in the form

$$\Phi = \frac{2ND}{L'} \left[\frac{L'}{2} (I_y - II_y) \cos \theta + \frac{L'}{2} (I_x - II_x) \sin \theta \right].$$

By substituting the magnetic flux into the induced voltage equation, we will then obtain

$$V = -\frac{d\Phi}{dt} = -\frac{ND}{L'} \left[\frac{L'}{2} (I_y - II_y) (-\sin \theta \frac{d\theta}{dt}) + \frac{L'}{2} (I_x - II_x) (\cos \theta \frac{d\theta}{dt}) \right].$$

By integrating with respect to time, this process then gives

$$\int_{t_i}^{t_f} Vdt = \frac{-2ND}{L'} \left[\left(\frac{L'}{2} I_y - II_y \right) \left(-\int_{\theta_i}^{\theta_f} \sin \theta d\theta \right) + \left(\frac{L'}{2} I_x - II_x \right) \left(\int_{\theta_i}^{\theta_f} \cos \theta d\theta \right) \right],$$

$$\int_{t_i}^{t_f} Vdt = \frac{-2ND}{L'} \left[\left(\frac{L'}{2} I_y - II_y \right) [\cos \theta]_{\theta_i}^{\theta_f} + \left(\frac{L'}{2} I_x - II_x \right) [\sin \theta]_{\theta_i}^{\theta_f} \right],$$

$$\varepsilon'' = \frac{\int_{t_i}^{t_f} Vdt}{2ND} = \left[\left(\frac{I_y}{2} - \frac{II_y}{L'} \right) [-\cos \theta]_{\theta_i}^{\theta_f} + \left(\frac{I_x}{2} - \frac{II_x}{L'} \right) [-\sin \theta]_{\theta_i}^{\theta_f} \right],$$

$$\varepsilon'' = \varepsilon_y'' + \varepsilon_x'',$$

where ε_y'' and ε_x'' are respectively the integrated values of the vertical and horizontal induced voltage, defined by

$$\varepsilon_y'' = \left(\frac{I_y}{2} - \frac{II_y}{L'} \right) [-\cos \theta]_{\theta_i}^{\theta_f}. \quad (2.68)$$

$$\varepsilon_x'' = \left(\frac{I_x}{2} - \frac{H_x}{L'}\right)[- \sin \theta]_{\theta_i}^{\theta_f}. \quad (2.69)$$

(2.68) and (2.69) will be used to evaluate the second field integrals.

First we will find ε_y'' . From (2.68), ε_y'' is obtained by flipping the coil from 0° to 180° and then from 180° to 360° . Next, the coil is flipped back from 360° to -180° and it is flipped from -180° to -360° . These procedures are the same with the ε_y' in Figure 2.9. The obtained equations then are

$$\varepsilon_{y,1}'' = 2\left(\frac{I_y}{2} - \frac{H_y}{L'}\right) + I_d, \quad (2.70)$$

$$\varepsilon_{y,2}'' = -2\left(\frac{I_y}{2} - \frac{H_y}{L'}\right) + I_d, \quad (2.71)$$

$$\varepsilon_{y,3}'' = 2\left(\frac{I_y}{2} - \frac{H_y}{L'}\right) + I_d, \quad (2.72)$$

$$\varepsilon_{y,4}'' = -2\left(\frac{I_y}{2} - \frac{H_y}{L'}\right) + I_d, \quad (2.73)$$

Making subtraction (2.70) with (2.71) and (2.72) with (2.73), the vertical second field integrals are eventually obtained as

$$H_{y,1} = L' \left(\frac{I_y}{2} - \frac{\varepsilon_{y,1}'' - \varepsilon_{y,2}''}{4} \right), \quad (2.74)$$

$$H_{y,2} = L' \left(\frac{I_y}{2} - \frac{\varepsilon_{y,3}'' - \varepsilon_{y,4}''}{4} \right). \quad (2.75)$$

Similarly, the averaged vertical second field integral are obtained by making repeated measurements.

Next we will measure ε_x'' , defined in (2.69). From the equation, ε_x'' is obtained by flipping the coil from 90° to 270° and from 270° to 90° . Next, it is flipped back from 90° to -270° and it is finally flipped from -270° to -90° . The

procedures are the same with the ε'_x , shown in the Figure 2.10. Thus the following

equations are then obtained

$$\varepsilon''_{x,1} = 2\left(\frac{I_x}{2} - \frac{II_y}{L'}\right) + I_d, \quad (2.76)$$

$$\varepsilon''_{x,2} = -2\left(\frac{I_x}{2} - \frac{II_x}{L'}\right) + I_d, \quad (2.77)$$

$$\varepsilon''_{x,3} = 2\left(\frac{I_x}{2} - \frac{II_x}{L'}\right) + I_d, \quad (2.78)$$

$$\varepsilon''_{x,4} = -2\left(\frac{I_x}{2} - \frac{II_x}{L'}\right) + I_d, \quad (2.79)$$

Making subtraction (2.76) with (2.77) and (2.78) with (2.79), the horizontal second field integrals are eventually obtained as

$$II_{x,1} = L'\left(\frac{I_x}{2} - \frac{\varepsilon''_{x,1} - \varepsilon''_{x,2}}{4}\right), \quad (2.80)$$

$$II_{x,2} = L'\left(\frac{I_x}{2} - \frac{\varepsilon''_{x,3} - \varepsilon''_{x,4}}{4}\right). \quad (2.81)$$

Similarly, the averaged horizontal second field integral are evaluated by making repeated measurements.

CHAPTER III

DESIGN OF SOFT X-RAY UNDULATOR FOR SPS

This chapter discusses the design of soft x-ray undulator for SPS. Designs of the magnetic structure, magnetic field simulation and simulated effects of field errors on electron motion are discussed.

3.1 Magnetic Structure

To determine the magnetic structure of the SPS undulator, we first consider the required photon energy range. The fundamental photon energy of undulator radiation at the on-axis, by substituting $n = 1$ in (2.16), is determined by the period length and the peak magnetic field,

$$\varepsilon_1(\text{keV}) = \frac{0.950E^2[\text{GeV}]}{(1 + \frac{K^2}{2})\lambda_u[\text{cm}]}, \quad (3.1)$$

where K is the wiggler strength, defined in (2.6). The relation is illustrated in Figure 3.1 for the 1.2 GeV electron beam energy. Because the current technology for obtaining maximum remanent field in a magnet block, hence the obtainable maximum magnetic field, is limited the photon energy is therefore determined by the period length. Moreover, the photon flux is determined by number of period, $N = \frac{L}{\lambda_u}$, which

is

limited by the length of the straight section. It is therefore clear that the main designing parameter is the period length. The optimum the period length which gives the required minimum photon energy can be found from the relation in Figure 3.1. From this fact we will consider the design of planar undulator for the SPS.

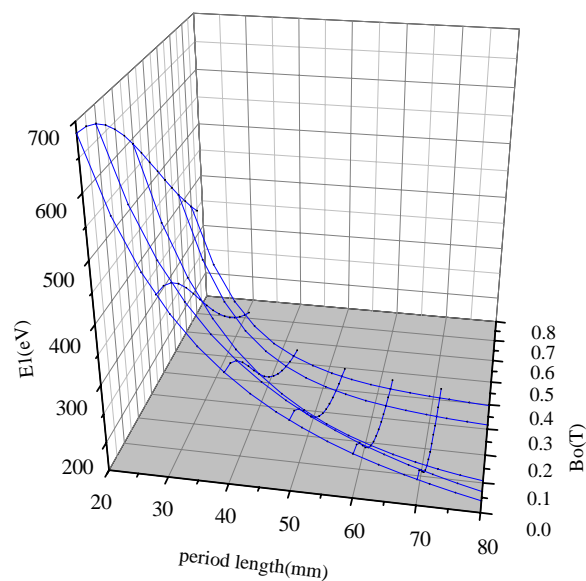


Figure 3.1 The relation between the radiated fundamental photon energy at the 1.2 GeV beam energy, the magnetic peak field and the period length.

To determine the minimum period length, the undulator field must be known. A planar undulator is constructed by the square magnet block elements arranged in the Halbach configuration (Halbach, 1981). The two end blocks are half length blocks for endfield correction. This is illustrated in Figure 3.2. The magnet block with the magnetization \vec{M} and size X , Y and Z is shown in Figure 3.3. The vertical component of the magnetic field at position (x, y, z) produced by such a magnet block

is given by (Ortega, Bazin, Deacon, Depautex, and Elleaume, 1983; Isoyama, 1989; Marechal, Chavanne, and Elleaume, 1990)

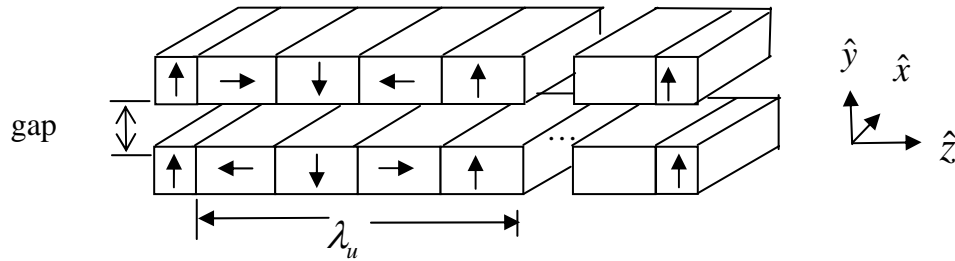


Figure 3.2 The structure of a planar undulator. The arrows in the magnet blocks indicate the direction of the magnetization.

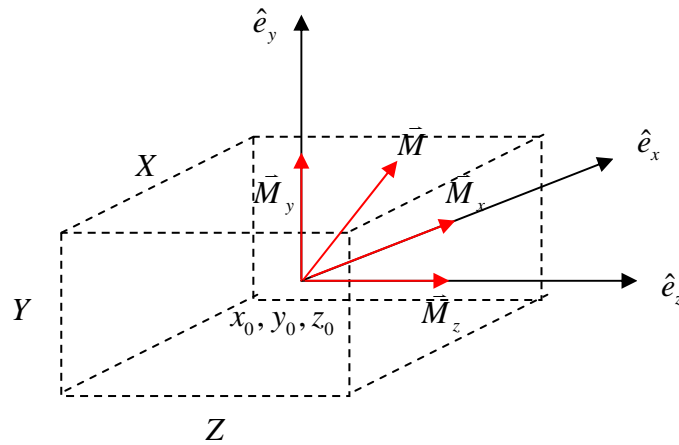


Figure 3.3 The permanent rectangular magnet with magnetization in arbitrary direction.

$$B_y(x, y, z) = [b(X, Y, Z) - b(-X, Y, Z) - b(X, -Y, Z) - b(X, Y, -Z) + b(-X, -Y, Z) + b(X, -Y, -Z) - b(-X, Y, -Z) - b(-X, -Y, -Z)].$$

(3.2)

By decomposing \vec{M} in y -component, coefficient $b(x, y, z)$ is given by

$$b(X, Y, Z) = \frac{Br_y}{4\pi} \tan^{-1} \left[\frac{(x - \frac{X}{2})(z - \frac{Z}{2})}{(y - \frac{Y}{2}) \sqrt{(\frac{X}{2} - x)^2 + (\frac{Y}{2} - y)^2 + (\frac{Z}{2} - z)^2}} \right]. \quad (3.3)$$

Decomposing \vec{M} in z -component,

$$b(X, Y, Z) = \frac{-Br_z}{4\pi} \ln \left[\frac{X}{2} - x + \sqrt{(x - \frac{X}{2})^2 + (y - \frac{Y}{2})^2 + (z - \frac{Z}{2})^2} \right]. \quad (3.4)$$

Similarly, decomposing \vec{M} in x -component,

$$b(X, Y, Z) = \frac{-Br_x}{4\pi} \ln \left[\frac{Z}{2} - z + \sqrt{(x - \frac{X}{2})^2 + (y - \frac{Y}{2})^2 + (z - \frac{Z}{2})^2} \right], \quad (3.5)$$

where Br_i is remanent field, $i = x, y, z$, and the origin of the coordinate system is at the center of the block. The undulator field can then be calculated by summing the contributions from each block. The designed planar undulator will now be constructed. The undulator length will be fixed at about 2.5 m, occupying approximately half the straight section. The size of blocks are initially set to the width of $X = 46$ mm and the height of $Y = 15$ mm. The magnet block length is determined by the period length, $z = \frac{\lambda_u}{4}$. The remanent field is fixed at 1.38 T, which is approximately the achievable maximum value for commercially available magnet blocks. The assumed minimum gap is 20 mm, determined by the operational aperture of the storage ring. The calculated field therefore can give us the peak magnetic field as function of period length and the size of magnet block. The graph in Figure 3.4 shows the relation between the peak magnetic field as a function of the undulator period length. The thin line is the theoretical relation that gives the photon energy of 30 eV. At the intercept of both lines gives the period length value of 59.6940 mm.

This period length gives the peak magnetic field of 0.6566 T. However, higher fields can be obtained if the magnet block size is increased, as illustrated in Figure 3.5. These were simulated at minimum gap. The optimum of the width and height of magnet block which give maximum peak field are 100 and 62 mm, respectively. The undulator with the parameters presented in Table 3.1 will therefore be constructed and then the magnetic error will be characterized.

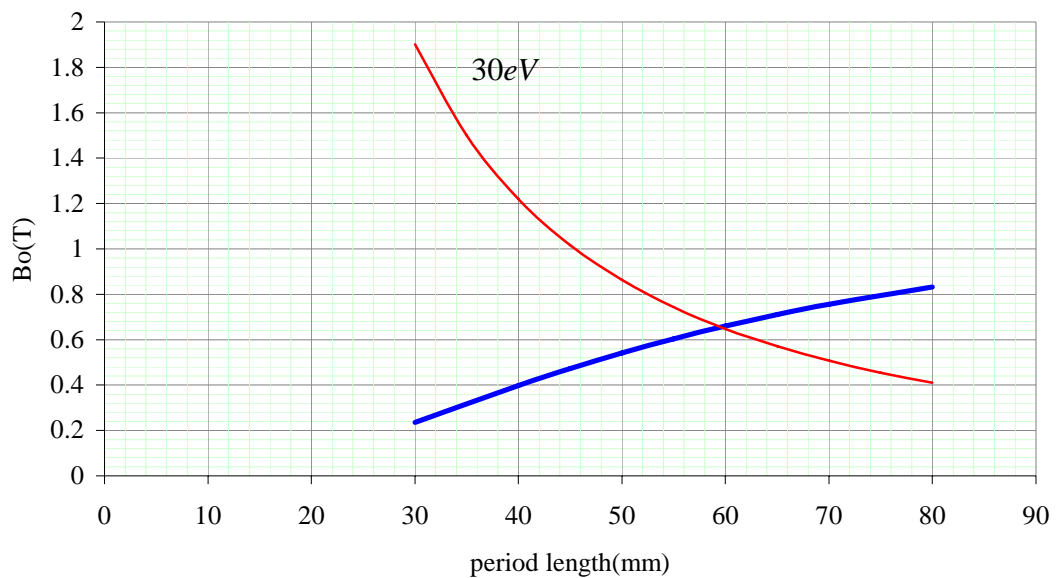
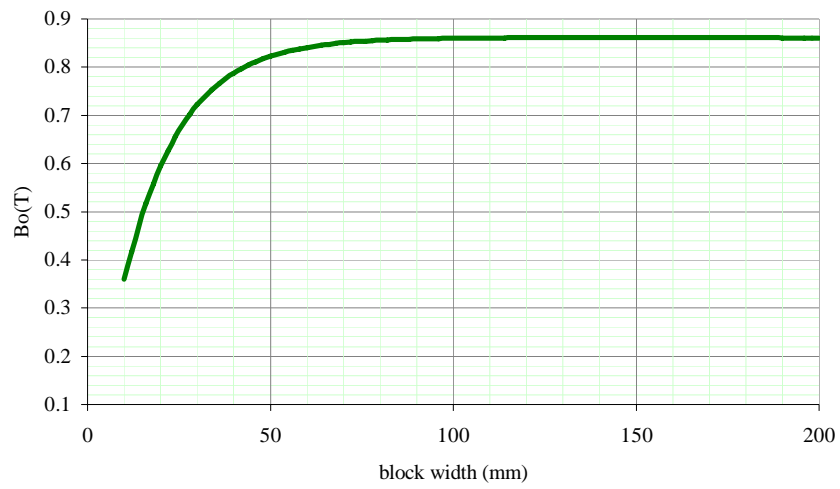
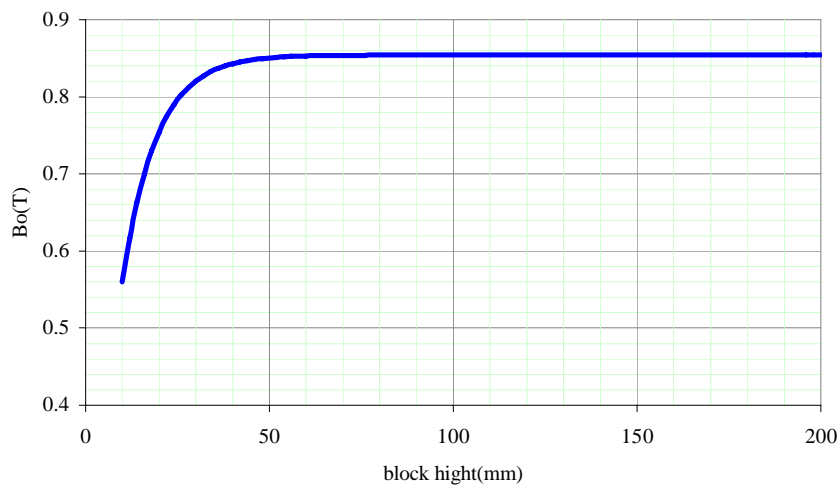


Figure 3.4 The peak field as function of period length. The thick line is simulated peak magnetic field from assembly of magnet blocks and the thin line is theoretical calculation for the fundamental energy of 30 eV .



(a)



(b)

Figure 3.5 The peak field as a function of (a) block length and (b) block height, simulated at the gap of 20 mm. The optimums of the magnet length and magnet height are 100 and 62 mm, respectively.

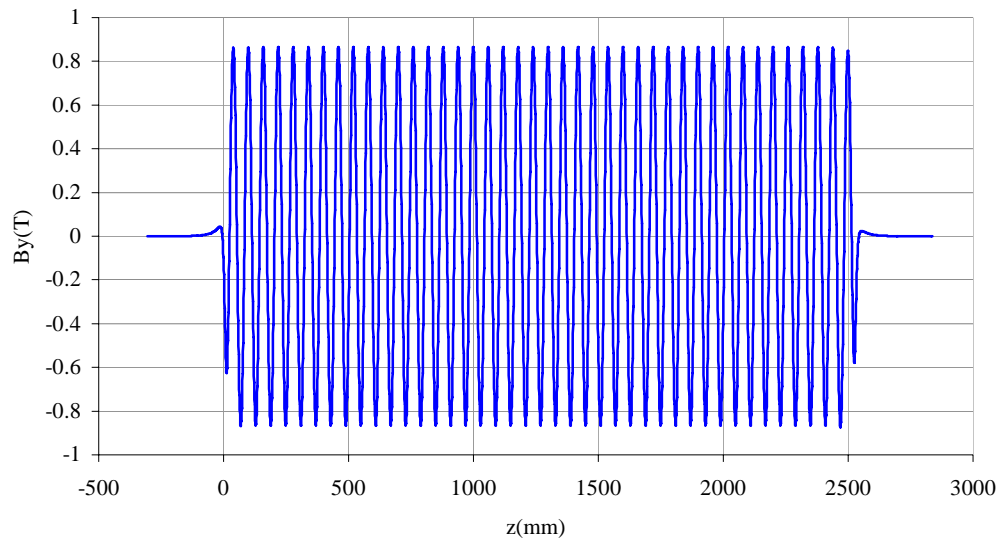
Table 3.1 Parameters of the designing undulator.

Parameters	Data
magnet material	NdFeB
maximum remanent field	1.38 T
period length	≈ 60 mm
minimum gap	20 mm
Minimum photon energy	30.00
number of periods	42
full block dimensions	100×62×15 mm

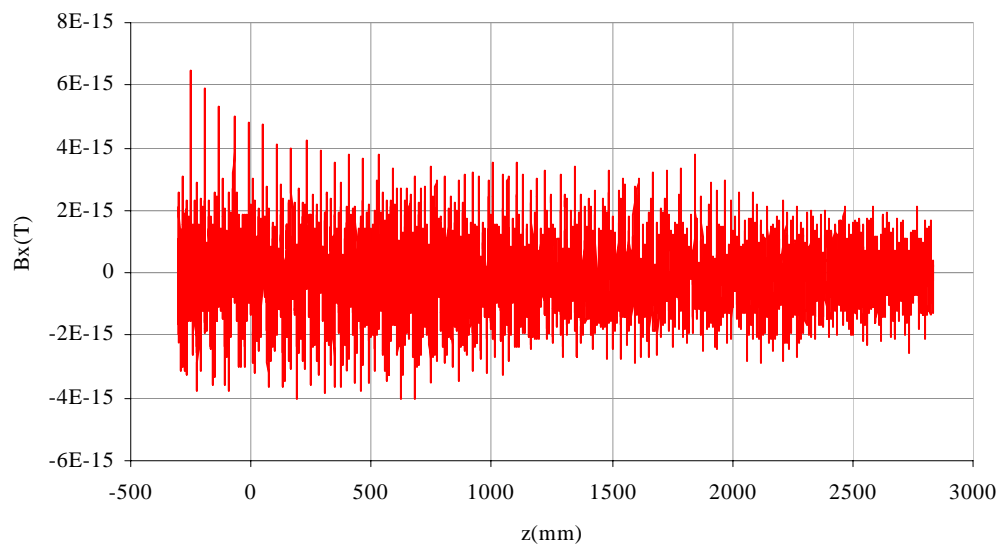
3.2 Simulation of Magnetic Field Error

As was previously mentioned, the parameters for constructing undulator were shown in Table 3.1. The magnitude and direction of magnetization in each magnet block will be considered for characterizing the undulator field error. These can be done by generating random alteration of the magnetization in the blocks.

First, we illustrate the magnetic characteristic of an ideal device. The ideal planar undulator field in both planes at the gap of 20 mm is illustrated in Figure 3.6. It can be seen that the horizontal field is negligibly small. The peak vertical magnetic field and the fundamental photon energy are respectively 0.8647 T and 17.88 eV. The electron trajectory is shown in Figure 3.7.



(a)



(b)

Figure 3.6 Simulated on-axis U60 field at 20 mm gap (a) vertical field (b) horizontal field.

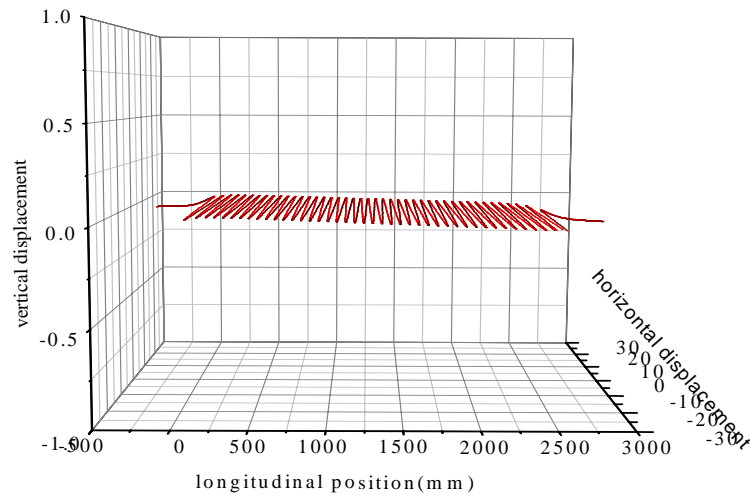


Figure 3.7 The calculated trajectory of an electron in an ideal undulator.

The magnetic field errors generated by variation of the magnetization of magnet blocks are now illustrated. Random errors of the magnitude and direction of magnetization vector in each magnet block, shown in Figure 3.8, are simulated. Two sets of random variation are performed to show effects of the errors. The first set is 1% deviation of the magnetization strength from a nominal value, $\left| \frac{\Delta B_r}{B_r} \right|, \leq 1\%$ and 1 degree deviation of the magnetization direction from a nominal magnetization axis, $|\Delta\theta| \leq 1^\circ$. The second set is $\left| \frac{\Delta B_r}{B_r} \right| \leq 5\%$ and $|\Delta\theta| \leq 5^\circ$. In both cases the azimuthal angle, $\Delta\varphi$, is randomly distributed between 0° and 360° . The calculated horizontal and vertical magnetic field results are respectively shown in Figure 3.9 and 3.10, together with that from the ideal device. The resulting electron trajectories are shown

in Figure 3.11. The errors generate significant horizontal field, the electron is therefore orbits in both planes.

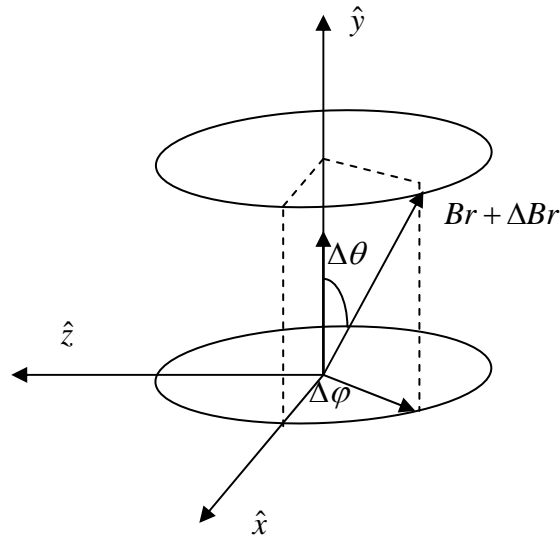


Figure 3.8 The magnetization vector of a magnet block.

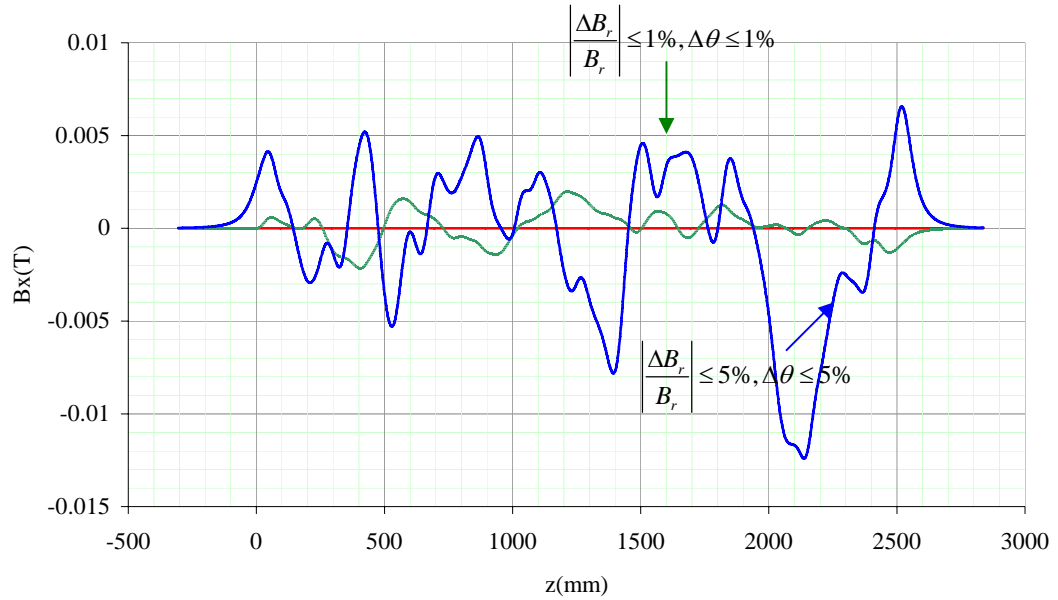
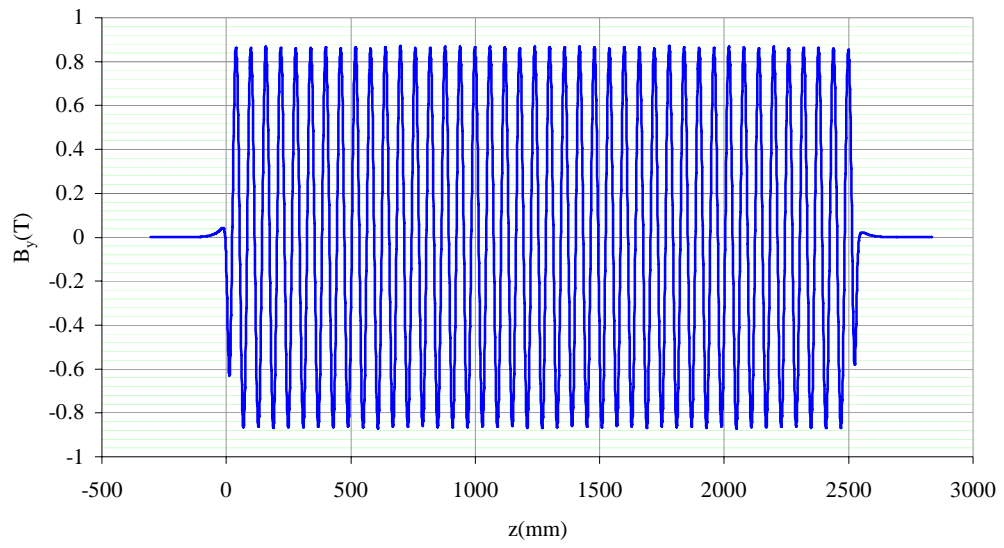
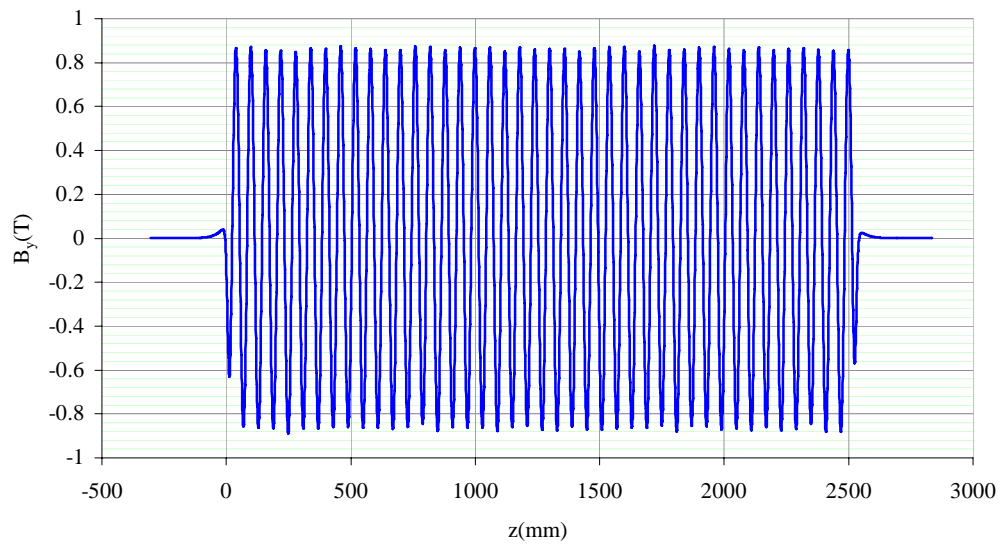


Figure 3.9 The simulated horizontal fields for the cases $\left| \frac{\Delta B_r}{B_r} \right| \leq 5\%$, $|\Delta\theta| \leq 5^\circ$, and

$$\left| \frac{\Delta B_r}{B_r} \right| \leq 1\%, |\Delta\theta| \leq 1^\circ \text{ and the ideal device (lies on } x\text{-axis).}$$



(a)



(b)

Figure 3.10 The simulated vertical fields for the cases: (a) $\left| \frac{\Delta B_r}{B_r} \right| \leq 1\%$, $|\Delta\theta| \leq 1^\circ$ and

$$(b) \left| \frac{\Delta B_r}{B_r} \right| \leq 5\%, \quad |\Delta\theta| \leq 5^\circ.$$

Moreover, the field errors affect electron beam trajectory. At the exit of the undulator, the electron is kicked out of the axis with orbit deviation of 154.87 and 2148.38 μm for the first and second error sets, respectively. Considering the phase error, the rms phase errors are generated with the values of 1.98 and 16.94 degrees for the first and second error sets, respectively. As mentioned in section 2.2.2, the phase error affects the quality of undulator radiation. The quality of undulator radiation will be rapidly reduced when the phase error is increased. The photon flux will obtain more than 90 % of the ideal undulator if the phase error is approximate 1° .

So, the maximum $\left| \frac{\Delta B_r}{B_r} \right|$ and $|\Delta\theta|$ should be respectively less than 1% and 1° .

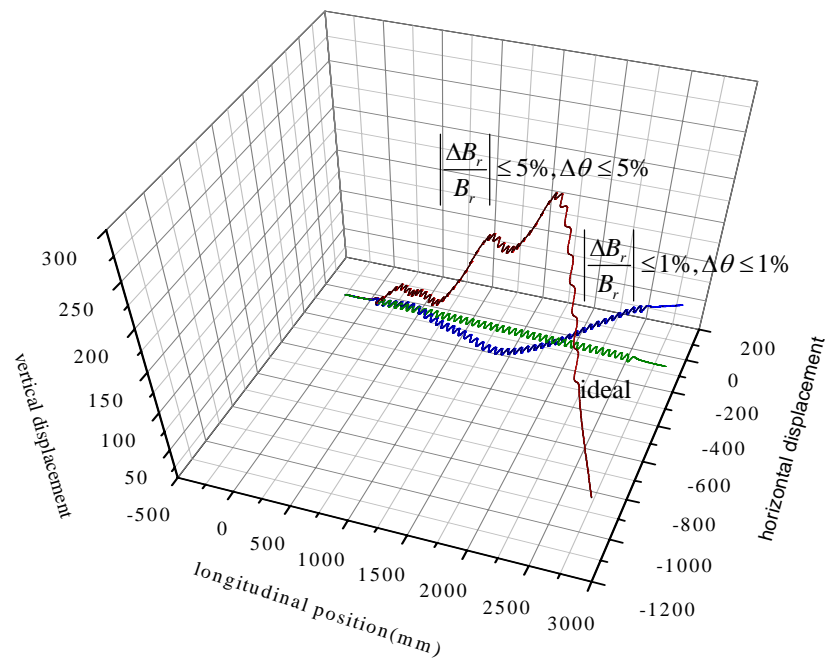


Figure 3.11 The trajectory of an electron calculated from the simulated fields.

CHAPTER IV

MAGNETIC FIELD MEASUREMENTS OF U60

This chapter will discuss the magnetic field measurements of the U60 undulator. The measurements consist of the magnetic field mapping and first and second field integral measurements. The field mapping was measured by Hall probe scan. The first and second field integral were measured by the flipping coil. The devices were designed, constructed and installed at the Siam Photon Laboratory (SPL). The details will be discussed in the following sections.

4.1 Magnetic Field Mapping

4.1.1 The Hall Probe Installation

The first technique to study the U60 field is the Hall probe scan. This technique was employed to measure the magnetic field distribution. These fields were used for calculations of the undulator radiation and its perturbation on the storage ring. The Hall probe system must therefore be designed to cover the measurements. The accuracy of the system installation must also be taken into consideration. The schematic drawing of the Hall probe system is shown in Figure 4.1. The length of the Hall probe bench is 3010 mm. The moving system was designed to move independently in 3 directions those are x (horizontal), y (vertical) and z (longitudinal). These can be done by 3 independent stepping motors. The system can

be moved to measure the field in the x and y axes ranges of 200 mm, and 2465 mm in the z axis. The positions for the field measurements are known by linear encoders. The Hall probe system in Figure 4.1 is composed of various device elements. The steps of installation therefore were carefully done. The installation is shown in Figure 4.2. The installed components were aligned by FARO Laser tracker Xi and Leica NAK2 automatic level. The standard deviation in the Hall probe positions throughout whole 3-axis lengths are within 0.025 mm (Prawanta, 2008). The systems were installed in 2004 and employed in various magnetic measurements. The system was operated via user interface by Labview software on a personal computer (PC).

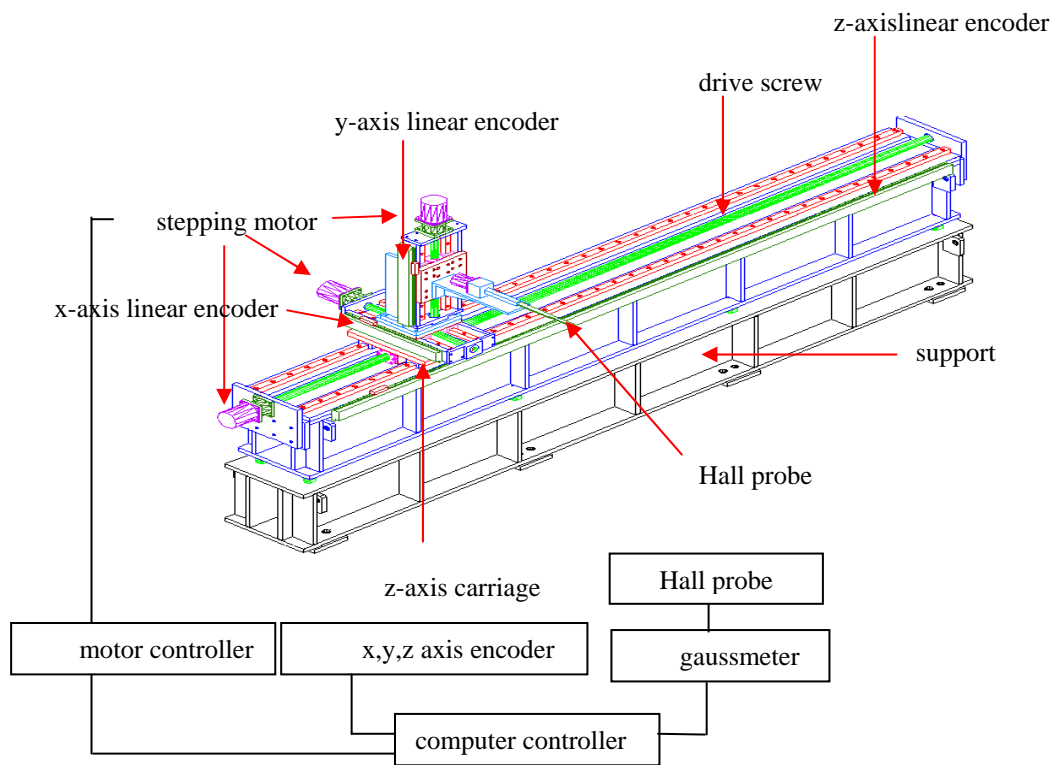


Figure 4.1 Schematic drawing of the bench for Hall probe installation.

Figure 4.2 also shows the measurement of U60 field. The U60 was aligned to certain position by referring to the bench. The center of undulator gap to measure the field must be known. This can be evaluated by using the reference marks appearing on the U60 and the Hall probe, illustrated in Figure 4.3. The mark on the U60 represents the horizontal center which was marked by the manufacturer. And the mark on center on the Hall probe can be used for finding the measured position. The center of gap in horizontal direction was known by aligning the horizontal mark of Hall probe to the mark on the U60 using Leica NAK2 automatic level. When these marks are at the same position illustrated in Figure 4.3a, the horizontal center was obtained by the linear encoders on x axis. The center in vertical direction was obtained using the edges of the U60 and horizontal mark on the probe, shown in Figure 4.3b. The horizontal mark on the probe was taken to the edge of the upper magnet, presented by position 1 in Figure 4.3b. Then this vertical position was known by linear encoder on y axis. Secondly, the probe was taken to the edge of lower magnet, represented by position 2 in Figure 3b. Then this vertical position was known. Making the subtraction of these values, the vertical direction then was known. All procedures mentioned above were managed by software on PC.



Figure 4.2 The steps of the Hall probe installation.

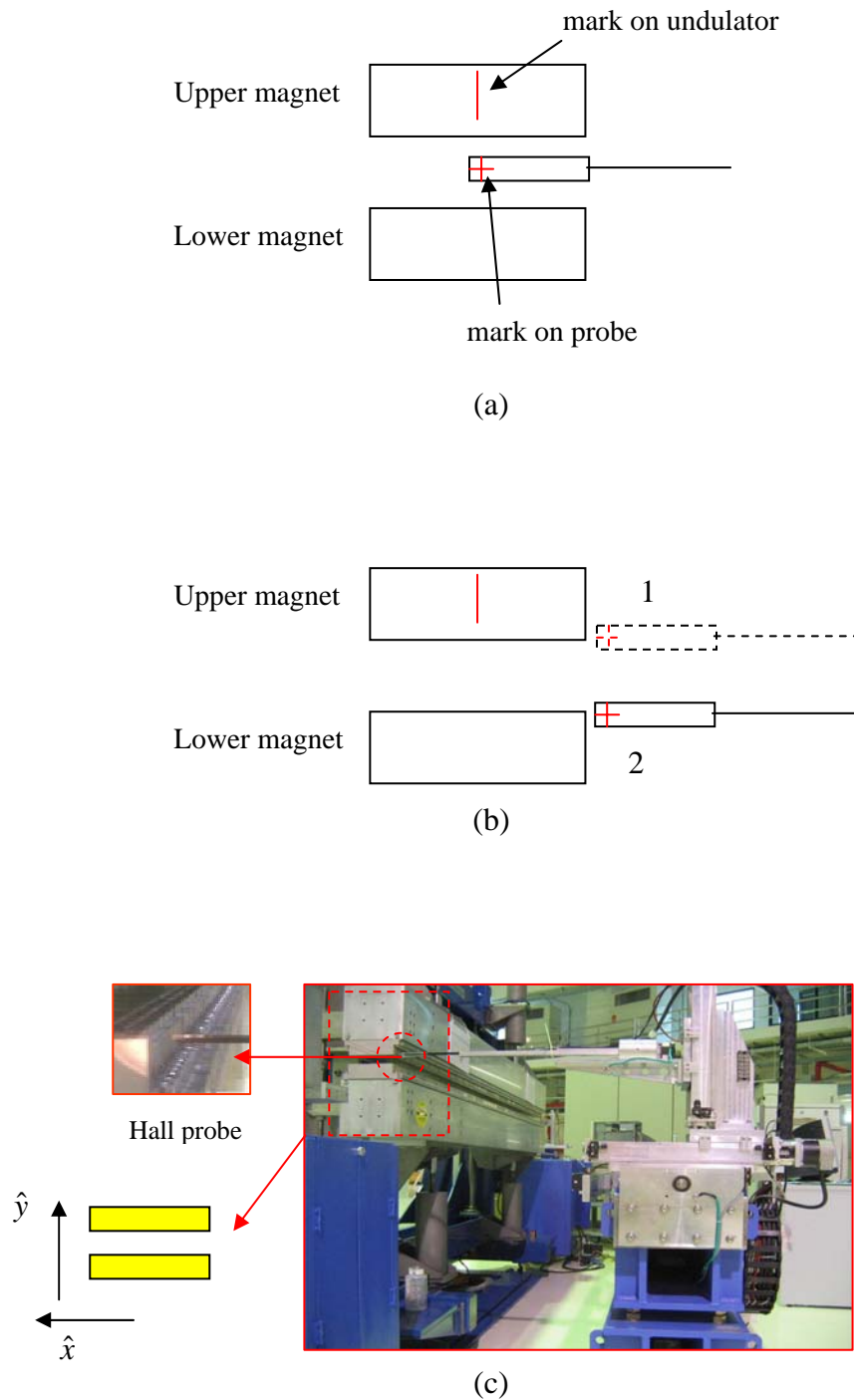


Figure 4.3 The schematic view for (a) finding the horizontal center, (b) finding the vertical center, and (c) the system ready to map the field by Hall Probe.

4.1.2 The Field Mapping Measurement

Various gaps and positions to map the field are shown in the Table 4.1. The probe ready for measurement is shown in Figure 4.3c. The fields were mapped on 1 mm interval. The measurements use the on-the-fly mode. These procedures were operated by a software on PC. The results of measurement will be presented in the next chapter.

Table 4.1 Various undulator gaps and coordinates to measure the U60 field.

Gap (mm)	Measured Coordinate	
	x (mm)	y (mm)
26.5, 30, 35, 40, 45, 50,	-25, -20, -15, -10, -5, 0, 5,	0
55, 60, 65, 70, and 75	10, 15, 20, and 25	

4.2 Field Integral Measurements

4.2.1 The flipping coil system installation

The field integral is the integrated field throughout the longitudinal undulator length. Field integrals were measured by the flipping coil. The system is shown in the Figure 4.4a. The Leica NAK2 automatic level was used to align the system. The systems were aligned with respect to the U60 undulator, shown in Figure 4.4b.

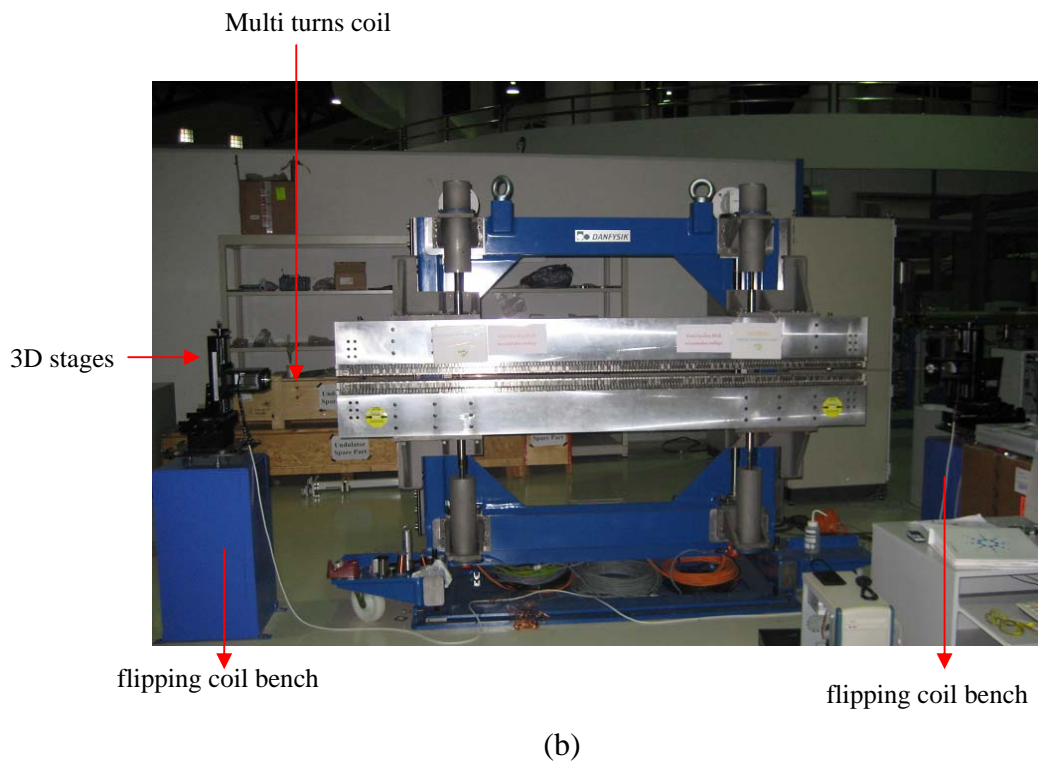
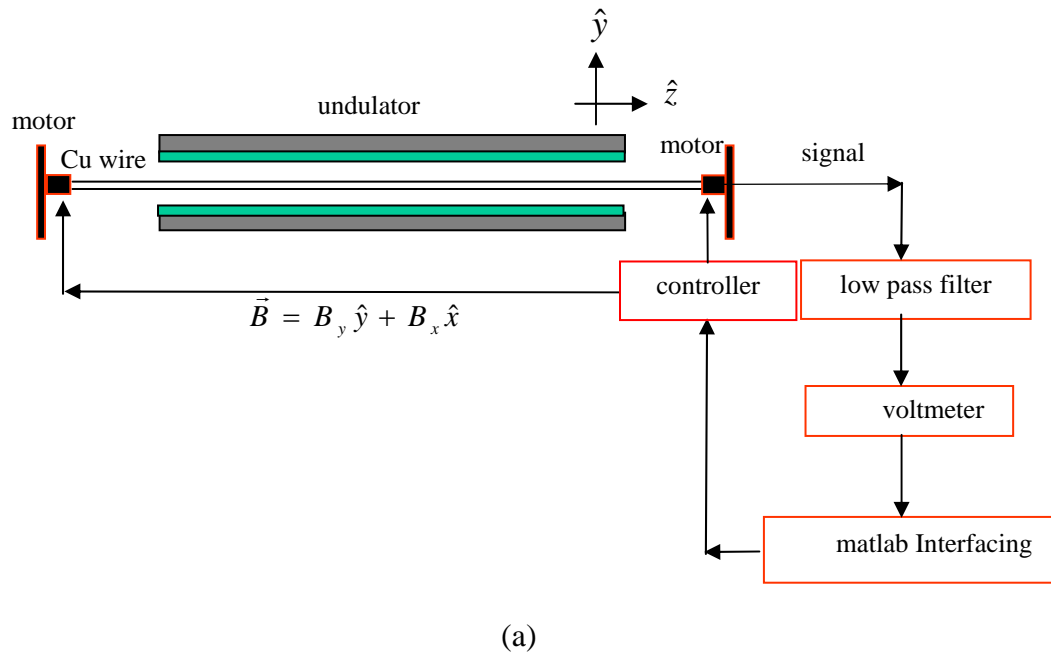


Figure 4.4 The flipping coil for the field integral measurement: (a) the components of the flipping coil to obtain the signal and (b) photograph of the real device.

The system for the field integral measurement in Figure 4.4a is composed of

- 1) The long coils make from 20 turns of copper wire with $0.7 \mu\text{m}$ diameter, 5 mm width and 3.150 meters in length. It is held by the two coil support fixed on the rotator stages, demonstrated in Figure 4.5. The rotator plates were fixed on the x-y-z stages on both sides (see Figure 4.4b). One of the z stage is movable to stretch the coil. And the two pair of x and y stages are employed to move the coil in the horizontal and vertical axis.

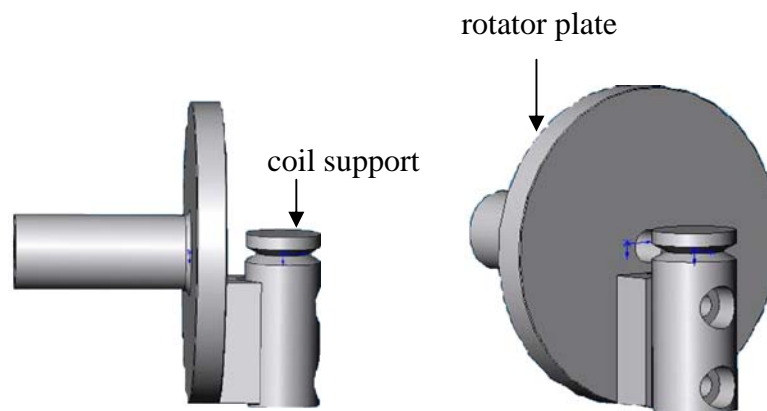


Figure 4.5 The drawing of the coil support structure, fixed on the rotator plate.

- 2) The controller was designed to store the program to control speed, direction and rotating magnitude (in the degree unit) of two-stepping motor.

- 3) The low pass signal filter was designed to eliminate the signal component with frequency higher than 5 Hz. It is successful for the elimination of high frequency noise in the measurements. The filter circuit is shown in Figure 4.6. The cut off frequency is defined as (Jacob, 1982):

$$\omega_o^2 = \frac{1}{R_1 R_2 C_1 C_2} \quad (4.1)$$

where $\omega_o = 5$ Hz, $R_1 = R_2 = 10$ k Ω , $C_1 = 4.7$ μ F and $C_2 = 2.2$ μ F. In Figure 4.6, V_{in} is the signal from the flipping coil in the U60 undulator field and V_{out} is the filtered signal.

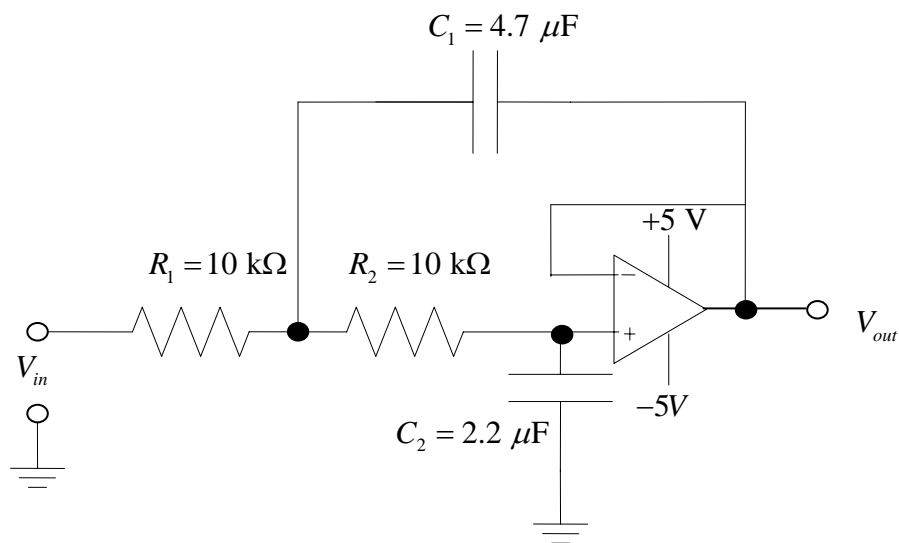


Figure 4.6 Schematic of Butterworth low pass Filters.

- 4) The HP3458A digital voltmeter is employed to read the voltage signal while the coil is flipped. It stores the signal data temporarily before

readout by the computer for the later processing. It is connected to the PC using an IEEE-488 (GPIB) card.

- 5) Matlab programming software was developed to control the systems. Figure 4.4a depicts the controlling of the software. It was designed for instruction of the controllers to control the motors, data acquisition from voltmeter and data analyses. The program therefore consists of the command to instruct the rotation motor to flip the coil, and at the same time starts reading voltage signal from the digital voltmeter. It then reads out the signal data from voltmeter memory to the PC. The user interface window consists of the panel of the obtained signal, integrated data, background and fourier transform of the signal data. In the Figure 4.7 illustrates the user interface panel for this work.

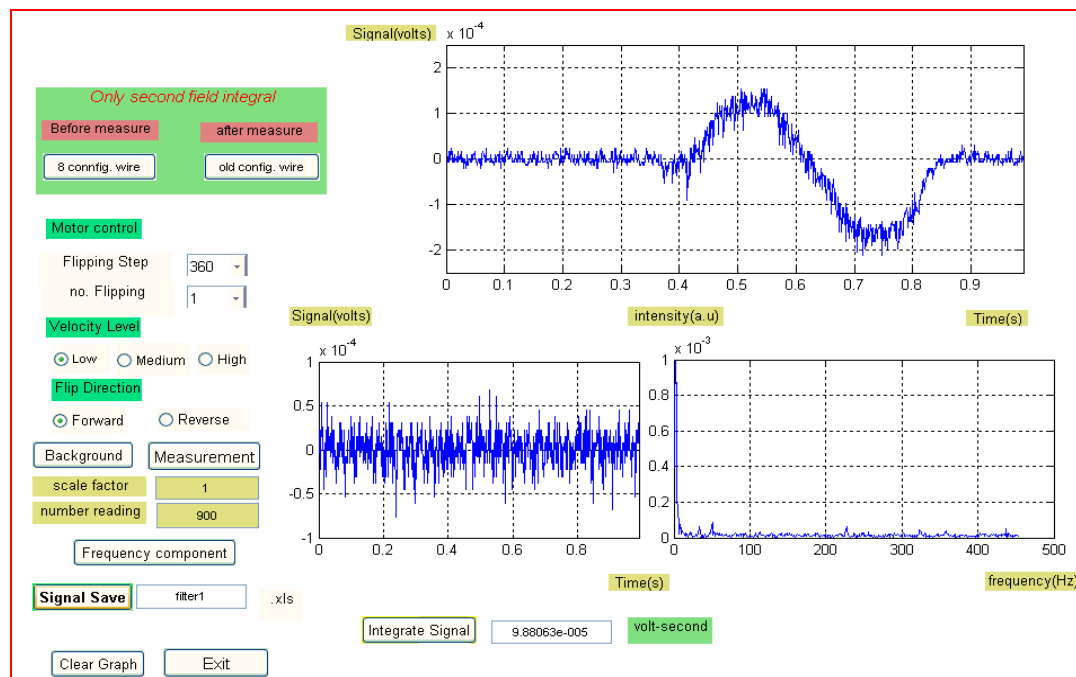


Figure 4.7 User interface panel for flipping coil measurement code.

4.2.2 First Field Integral Measurements

To measure the first field integral, the coil is configured to square shape, illustrated in the Figure 4.8. The first field integrals consist of two components which are horizontal and vertical components.

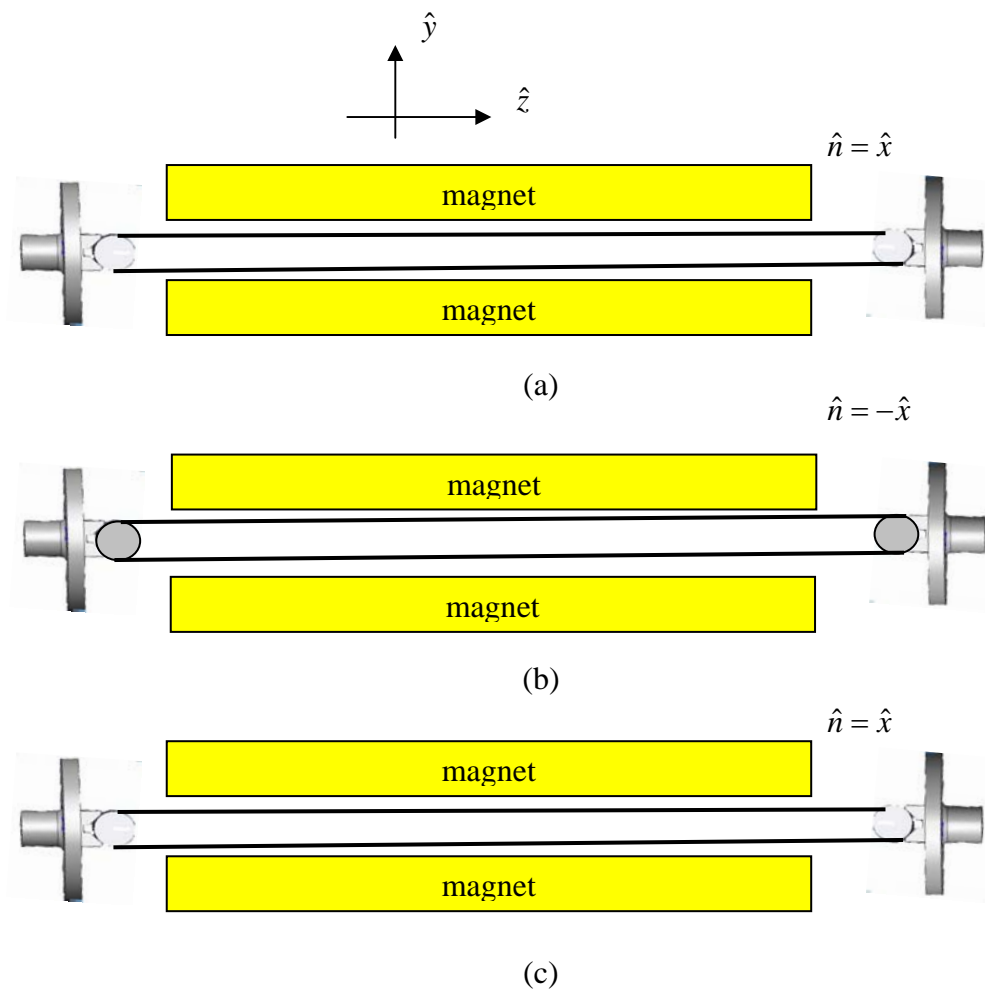


Figure 4.8 Side view of the measurement of the horizontal first field integral: (a) the starting of measurement $\hat{n} = \hat{x}$, (b) after clockwise flip by 180° $\hat{n} = -\hat{x}$ and (c) after clockwise flip to 360° , $\hat{n} = \hat{x}$.

The horizontal first field integral is illustrated in Figure 4.8. The signal voltage is obtained by flipping the coil for every 180° of angle. One flipping therefore obtains two values. The measurement is started with unit vector of the coil plane being in the direction of $+\hat{x}$ (see Figure 4.8a). The coil was then clockwise flipped to 180° (Figure 4.8b). The signal was simultaneously saved and integrated. Next, the coil was clockwise flipped to 360° (see Figure 4.8c), and the second signal data was obtained. The flipping was then reversed and another two integrated signal were obtained.

The vertical first field integral is illustrated in Figure 4.9. The signal voltage is obtained similar to that of horizontal component. The measurement is started with unit vector of the coil plane being in the direction of $+\hat{y}$ (see Figure 4.9b).

The theory of the measurements is explained in details in chapter II.

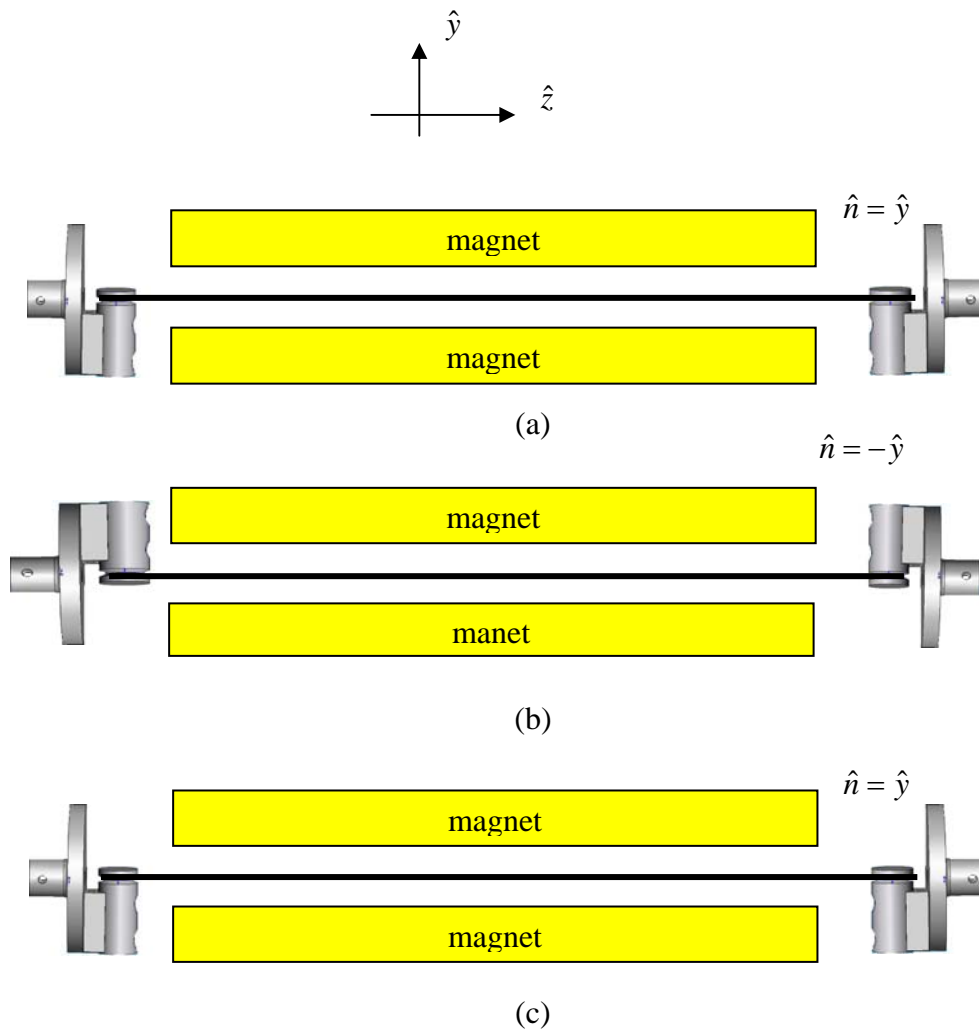


Figure 4.9 Side view of the measurement of the vertical first field integral: (a) the starting of measurement $\hat{n} = \hat{y}$, (b) after clockwise flip by 180° $\hat{n} = -\hat{y}$ and (c) after clockwise flip to 360° $\hat{n} = \hat{y}$.

4.2.3 Second Field Integral Measurements

The process to obtain the second field integral is similar with that of the first field integral. However, the configuration of the coil was changed. The coil configuration was changed from square configuration (Figure 4.8) to 8-shape configuration, illustrated in Figure 4.10. This can be done using the command in the user interface panel, shown in Figure 4.7. Then the horizontal and vertical field integrals were obtained by using the process in Figure 4.8 and 4.9, respectively. The theory of the measurements is also explained in details in chapter II.

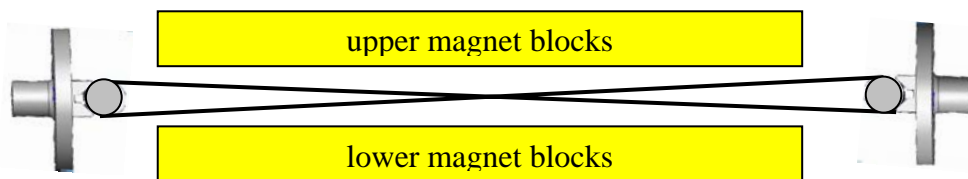


Figure 4.10 Schematic of coil configuration for second field integral measurement.

4.3 The Results of the Field Measurements

4.3.1 Field Distribution Measurements

The distribution of U60 undulator magnetic fields were measured by the Hall probe scanning. The magnetic fields at the various gaps and horizontal positions, shown in Table 4.1, were characterized. For example, the on-axis field at the undulator gap of 26.5 mm is shown in the Figure 4.11. The figure shows that the magnetic field is a sinusoidal shape with nearly constant amplitudes. Because the limit of the Hall probe bench length, the Hall probe can not scan the entire undulator

field. Clearly, at both edges of the device magnetic fields still exist. These results can be seen in Figure 4.11 and clearly for the magnified picture in Figure 4.12. The disappeared fields will result in the prediction of the involve parameters such as the angle and position of an electron. However, these disappeared fields can be generated by using a technique of exponential least square fit. The fittings are illustrated in Figure 4.13. The equation for fitting is

$$B(z) = A_0 e^{-\lambda z}, \quad (4.2)$$

where A_0 and λ are constant from the fitting. The fitting are started at the exponential decreasing position of the field, near the first or last magnetic pole. Finally, the undulator fields with zero at both edges are obtained, shown in Figure 4.13.

The undulator magnetic fields show that they consist of the 81 full poles. By averaging all these peak magnetic field, the relation between peak magnetic fields and undulator gap is obtained, shown in Figure 4.15. The graph shows that it exponentially decreases as the undulator gap increase. Later by substituting the undulator peak field, B_0 , from Figure 4.15 into the equation

$$K = 93.4 B_0 [\text{T}] \lambda_u [\text{m}],$$

where λ_u is an undulator periods length, the wiggler strength as function of the undulator gap is obtained, shown in Figure 4.16. These fields will be used to analyze the imperfection of the device including the effect on the electron in the storage ring. Figure 4.17 shows the peak field as function of the horizontal position, x . The figures show that the field is constant near the undulate axis, $|x| \leq 5$. At the minimum gap of

26.5 mm, the peak magnetic fields roll-off 0.045% and 0.019% at $x = -5$ mm and $x = +5$ mm, respectively, that within the specification (0.1%).

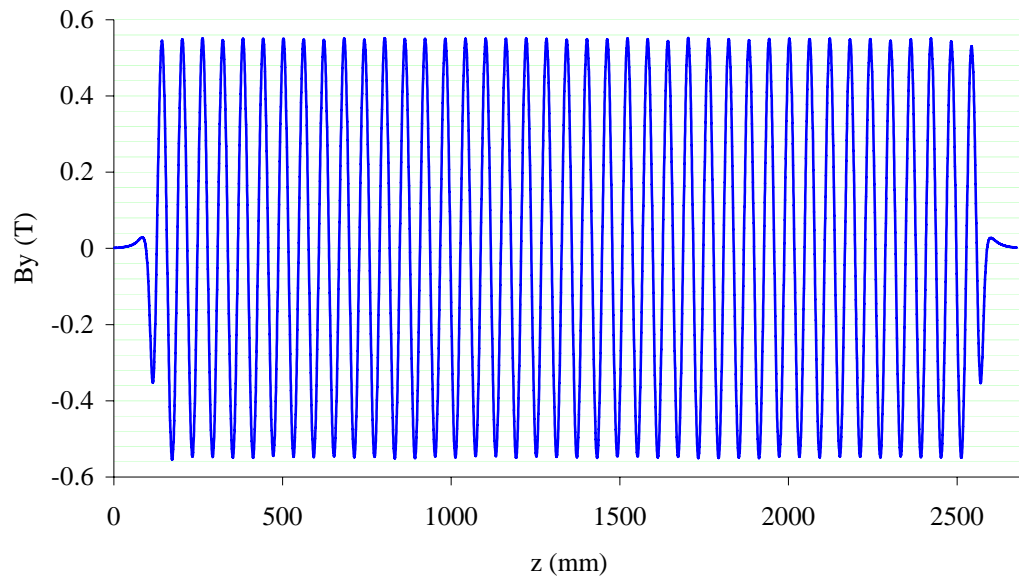
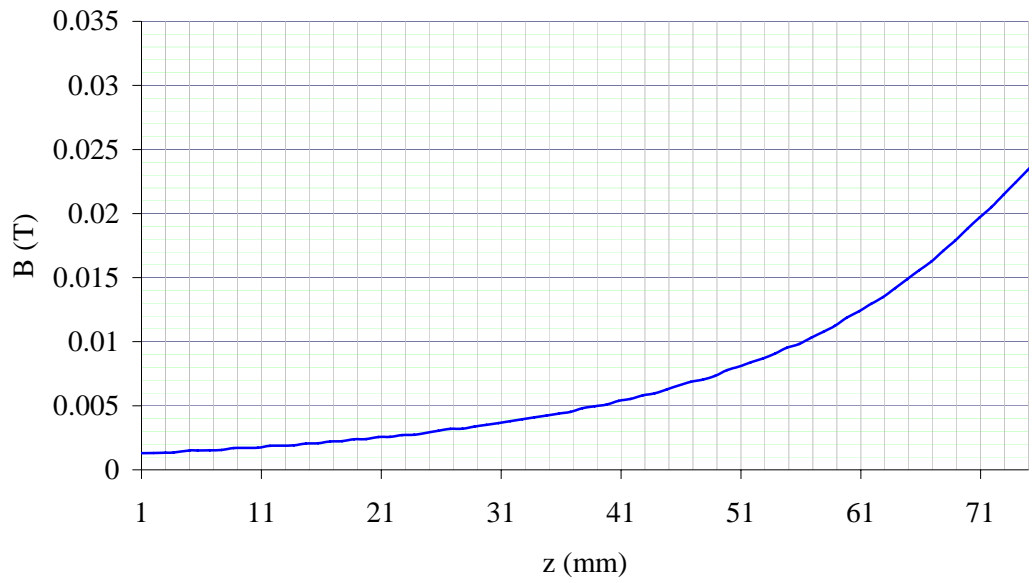
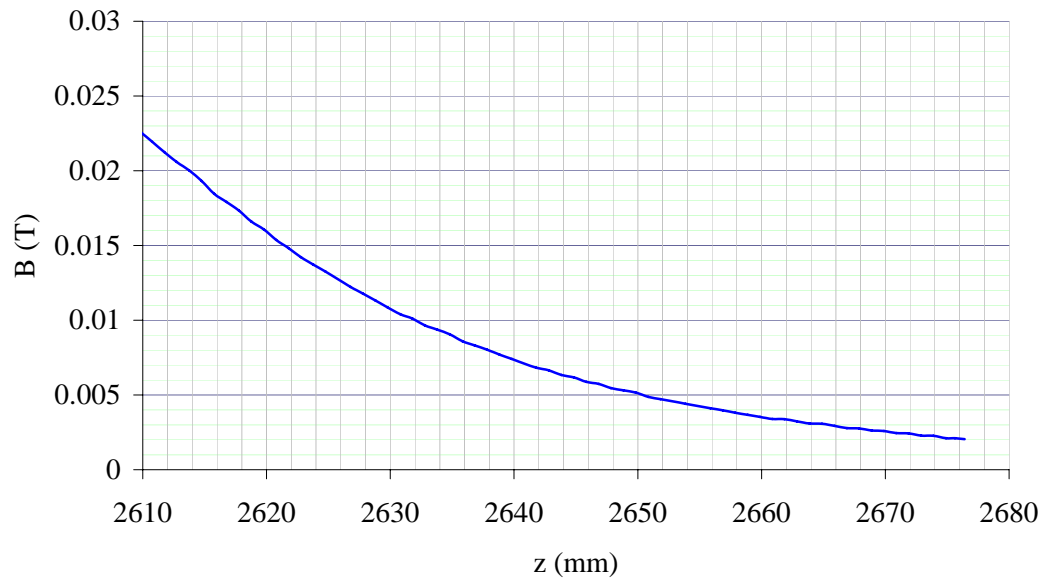


Figure 4.11 Undulator magnetic field at the gap of 26.5 mm.

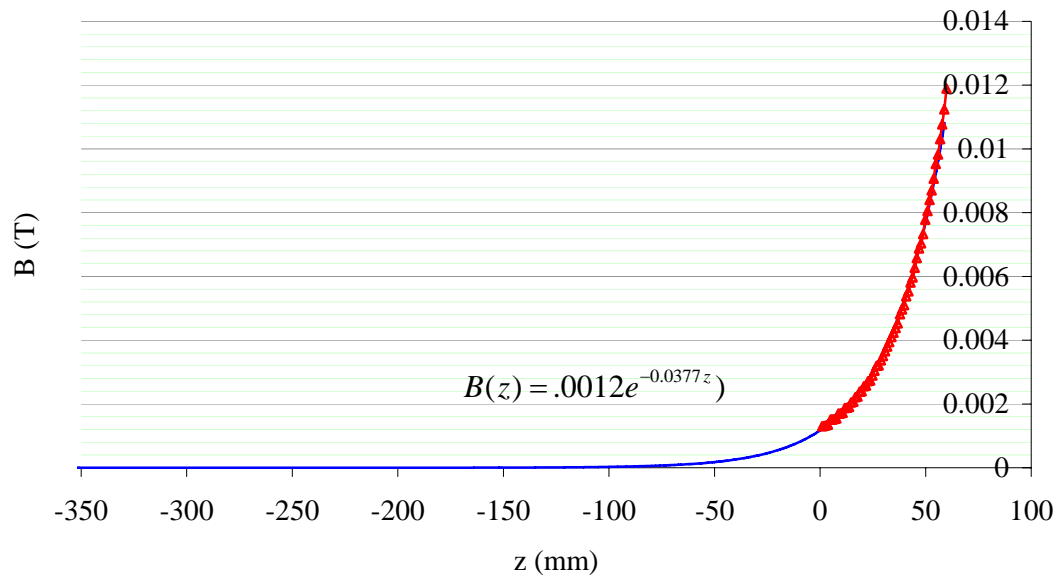


(a)

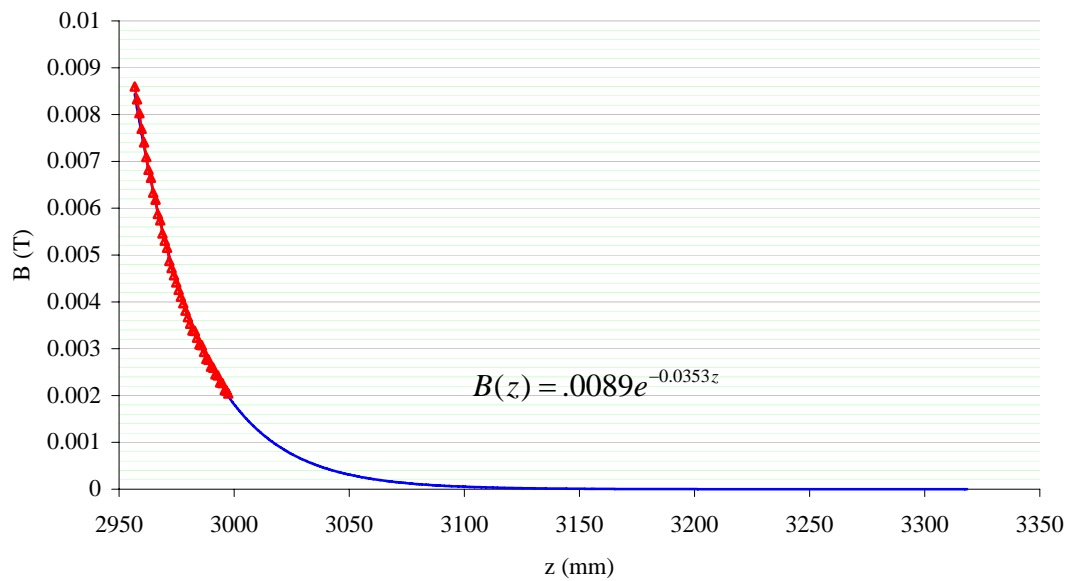


(b)

Figure 4.12 Undulator magnetic field at both edges of the undulator: (a) at the entrance, (b) at the exit of the device.



(a)



(b)

Figure 4.13 Undulator magnetic field at the both edges of the undulator (Δ) including the field obtained from exponential fitting (-): (a) at the entrance (b) at the exit of the device. The equations, shown in the graphs, are fitting equation.

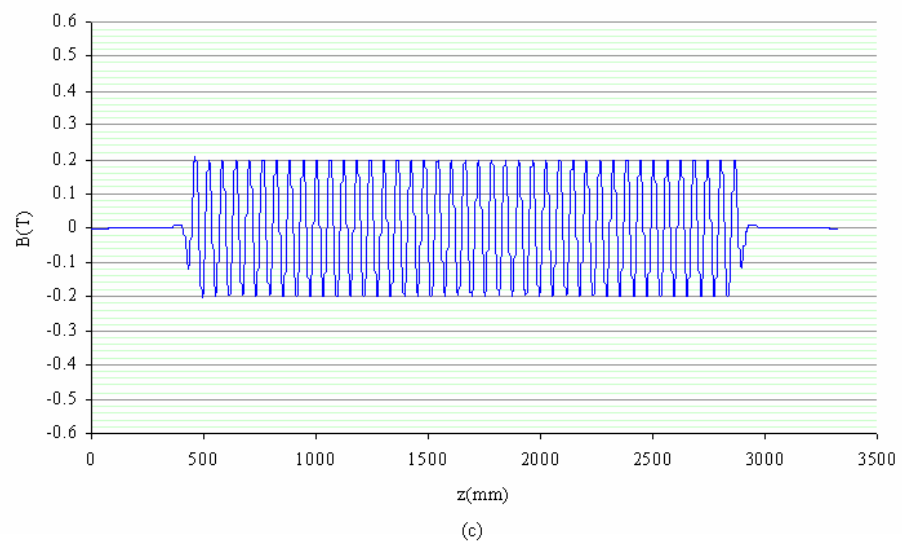
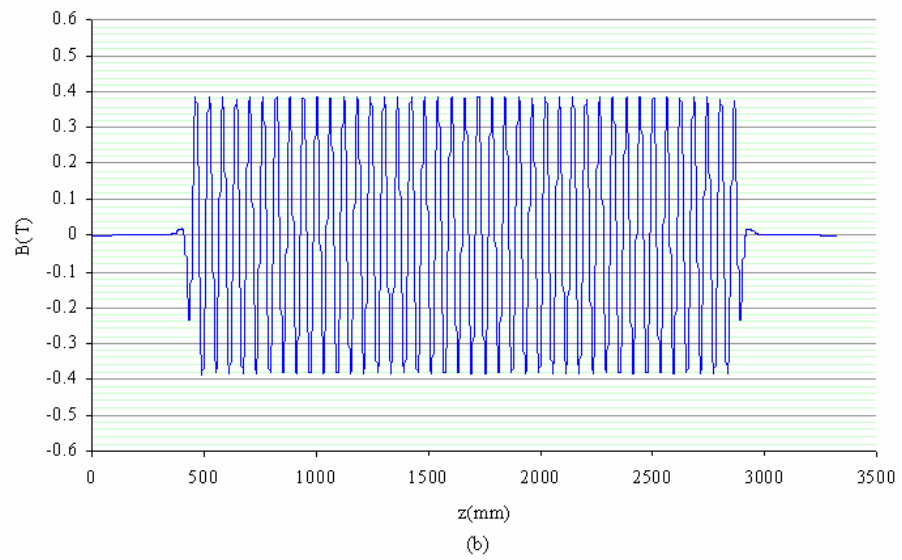
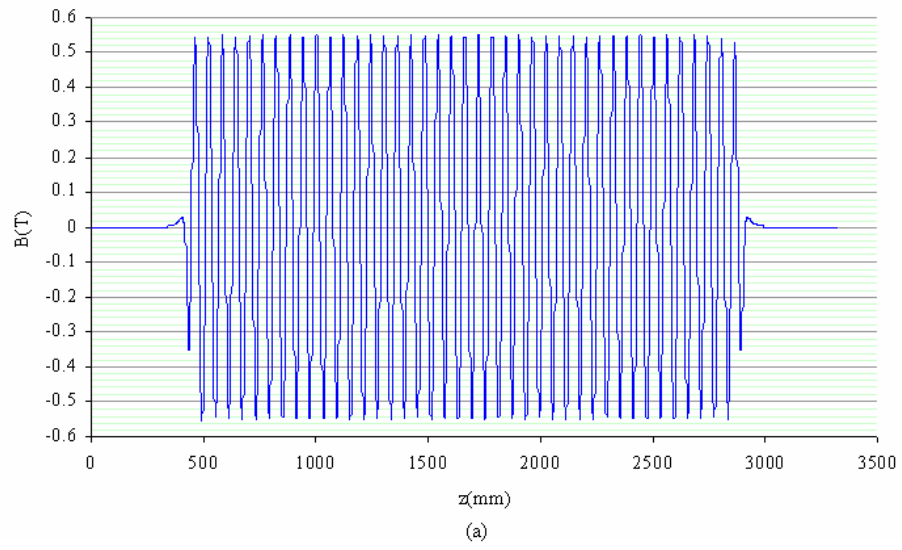


Figure 4.14 Undulator magnetic fields at the gap of (a) 26.5, (b) 40 and (c) 65 mm.

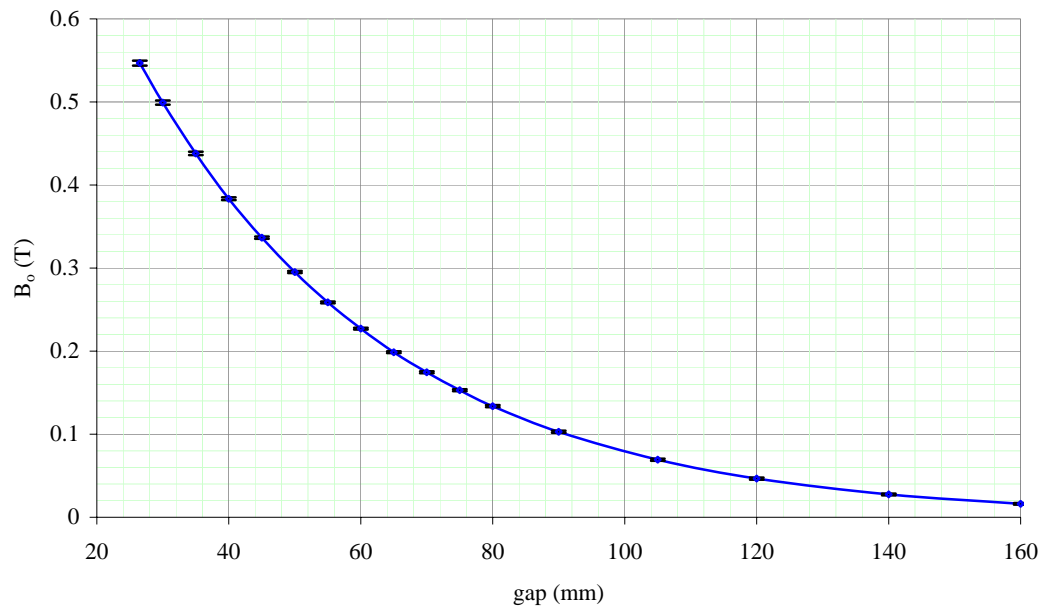


Figure 4.15 Peak magnetic field as a function of undulator gap. The error bars are statistical errors.

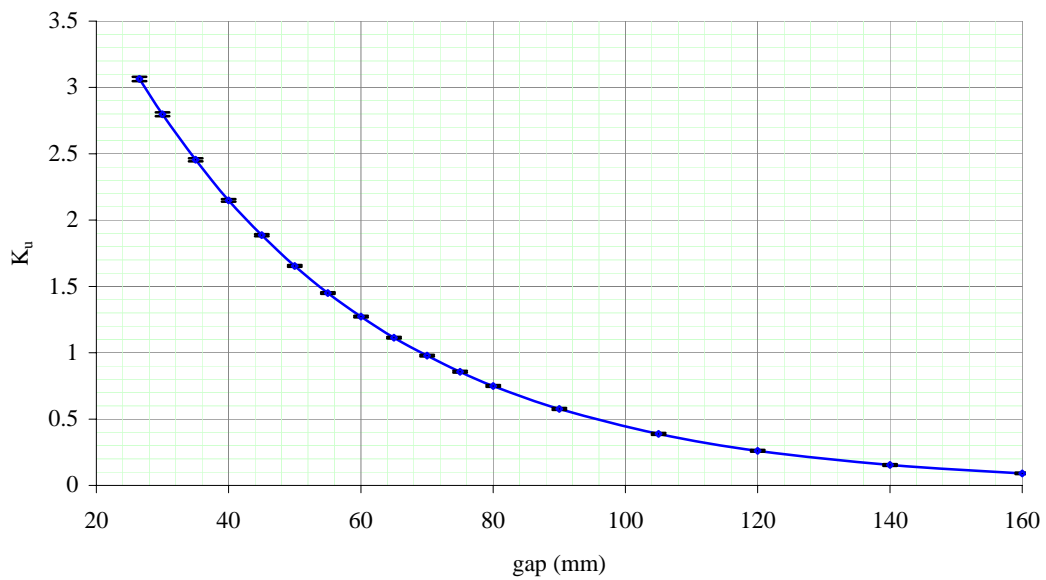


Figure 4.16 Wiggler strength as function of undulator gap.

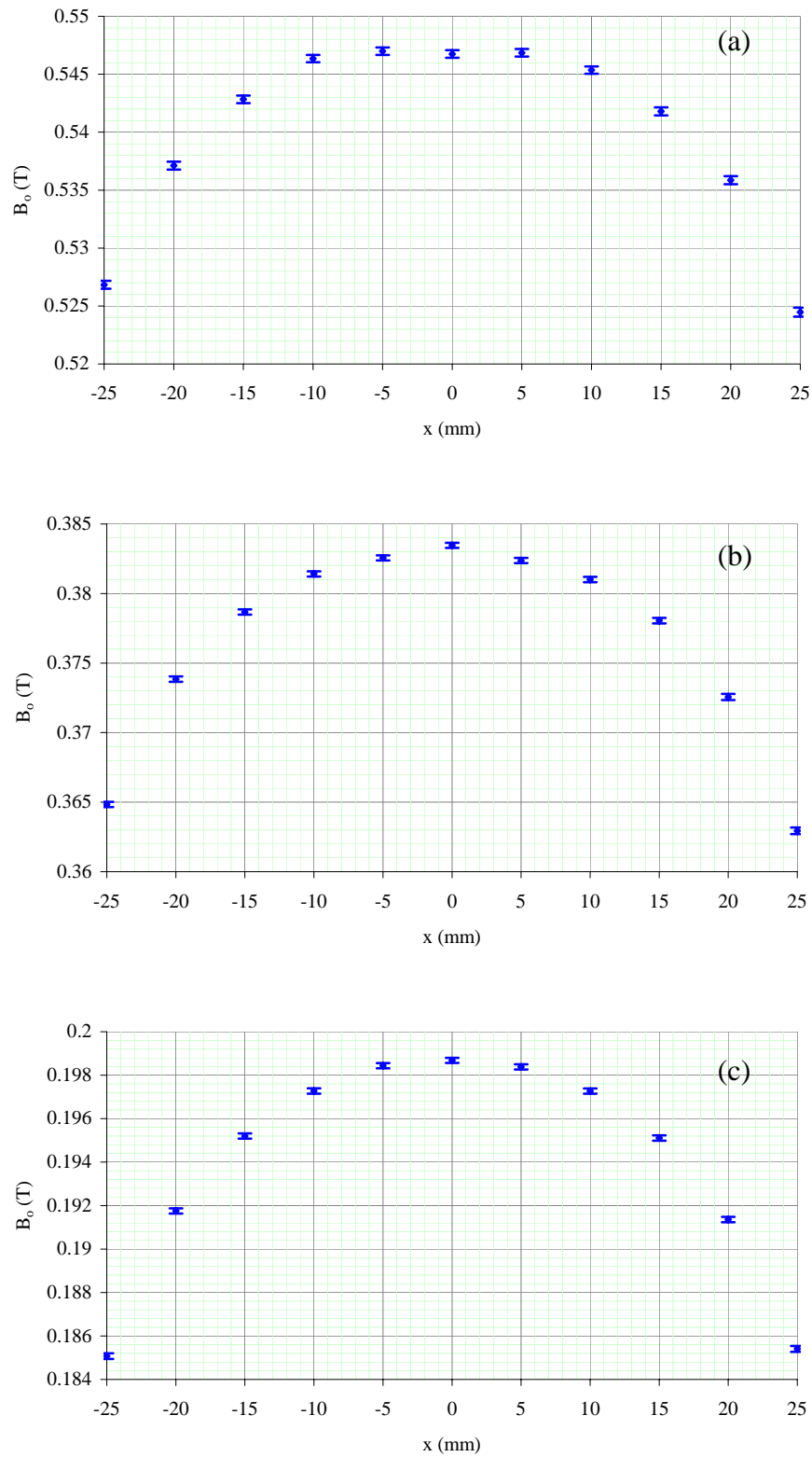


Figure 4.17 Peak field as a function of horizontal position, x , at the undulator gap of

(a) 26.5, (b) 40 and (c) 65 mm.

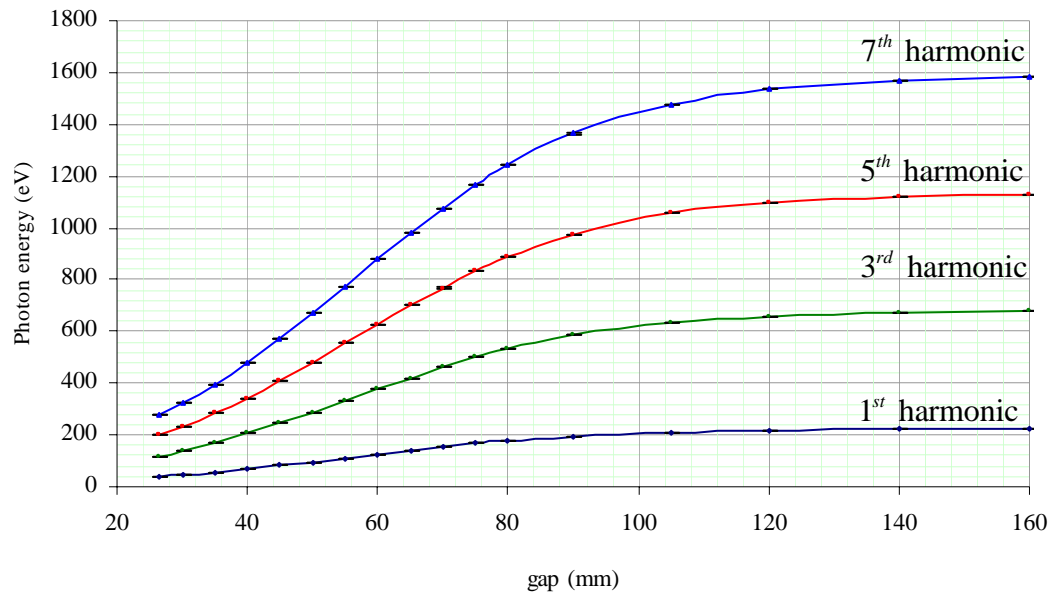


Figure 4.18 Photon energy as a function of undulator gap.

4.3.2 Integrated U60 Undulator Magnetic Field Measurements

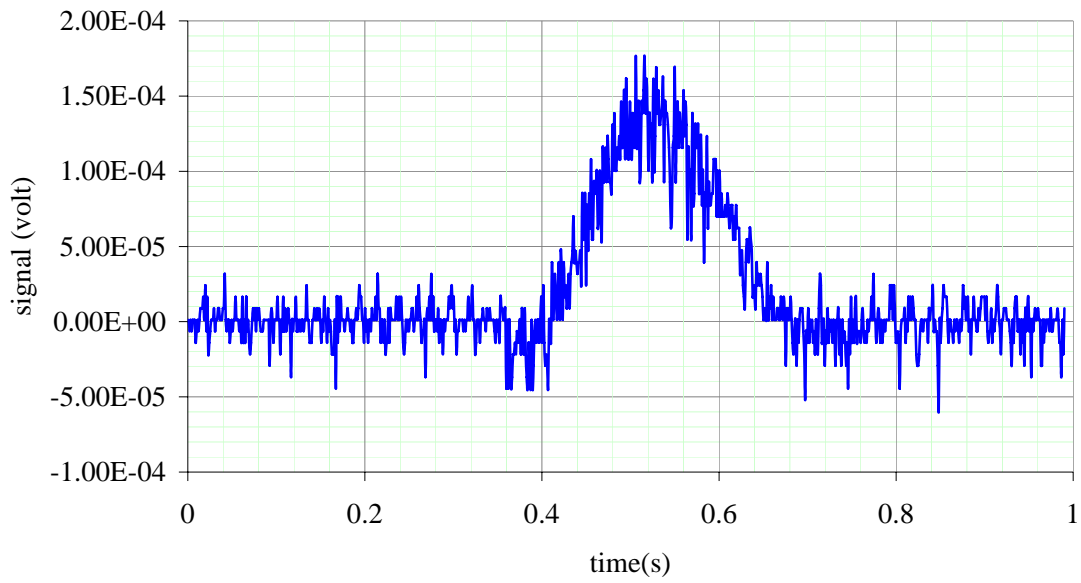
Integrated U60 undulator fields were obtained by the flipping coil, developed at the SPL. The theoretical details were mentioned in the previous section. In this section the examples of the measured results, the first field integral and then second field integral, will be shown.

For the first field integral, examples of the signals from flipping the coils in the undulator magnetic field region are shown in Figure 4.19-4.20. Figure 4.19 is the signals of the vertical field whereas the signals of the horizontal field are shown in Figure 4.20. By measuring at various horizontal positions, x , and then numerically integrating these signals, the integrated field were obtained in Figure 4.21-4.23. Later by making the multipole fits, the multipole components were obtained. These multipole fits are also shown in the Figure 4.21-4.23. And the

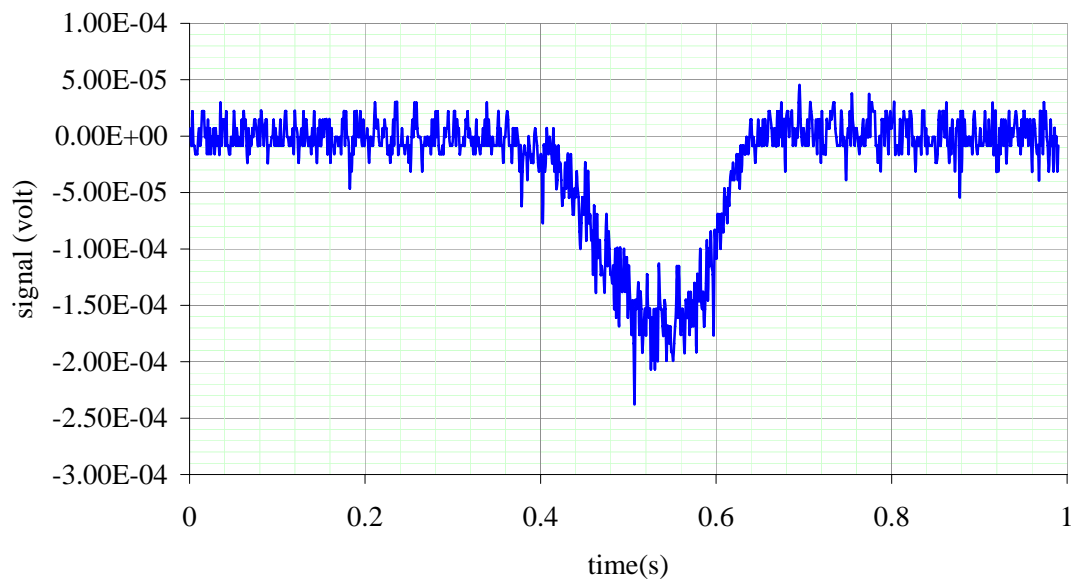
multipole field components of gap 26.5, 40 and 65 are respectively presented in Table 4.2, 4.3 and 4.4. Finally, the dipole, quadrupole, sextupole and octupole components as a function of undulator gap can be summarized in Figure 4.24a, 4.24b, 4.24c and 4.24d, respectively.

For the second field integral, the obtained signals are shown in the Figure 4.25-4.26, measured at the undulator gap of 26.5 mm. Figure 4.25 is the signal due to the vertical magnetic field, whereas Figure 4.26 is the signal due to the horizontal magnetic field. The second field integrals are only measured at the undulator axis, $x = 0$. Similarly, by integrating the obtained signal in each undulator gap the second field integrals are obtained. These results are shown in Figure 4.27. Figure 4.27a is the vertical second field integral. Figure 4.27b is the horizontal second field integral.

Now the distribution of magnetic fields and the field integrals of the U60 undulator are obtained. Next chapter these results will be used to analyze the effects of the U60 undulator on the electron beam. The distribution fields are used to calculate the electron trajectory and tune shift. The multipole components, obtained from field integral, will be used to analyze the effects of each component on the electron beam.

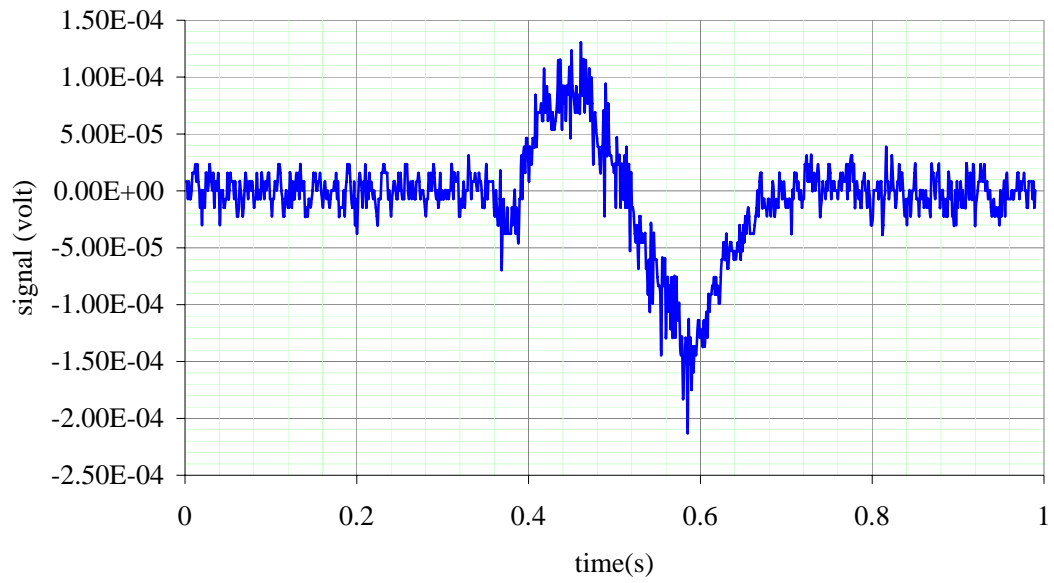


(a)

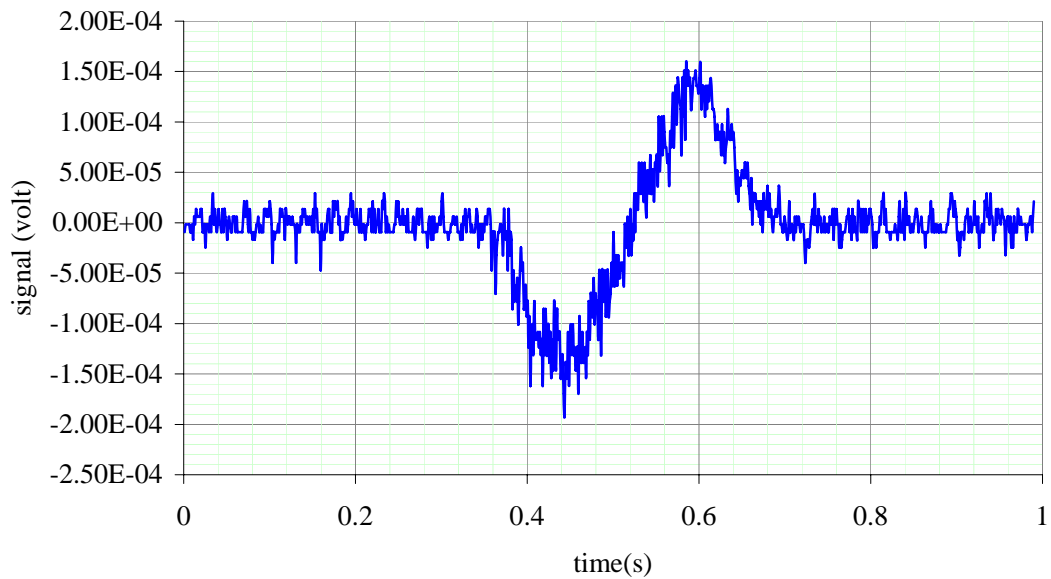


(b)

Figure 4.19 Integrated signal of the horizontal field of gap 26.5 mm at $x = 0$: (a) flip from 0° to 180° and (b) flip from 180° to 360° .

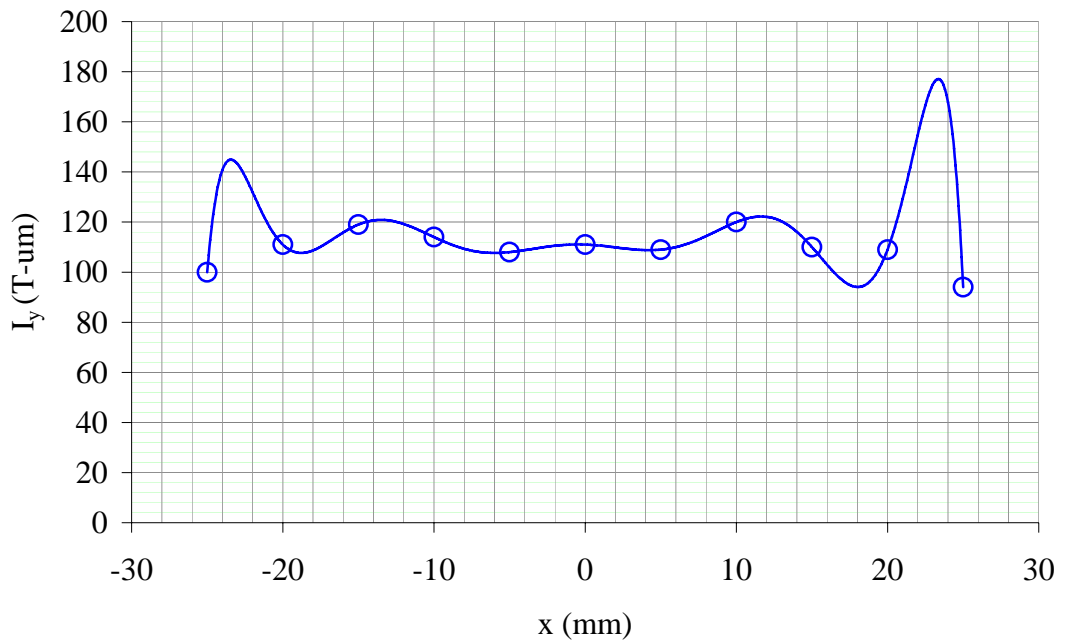


(a)

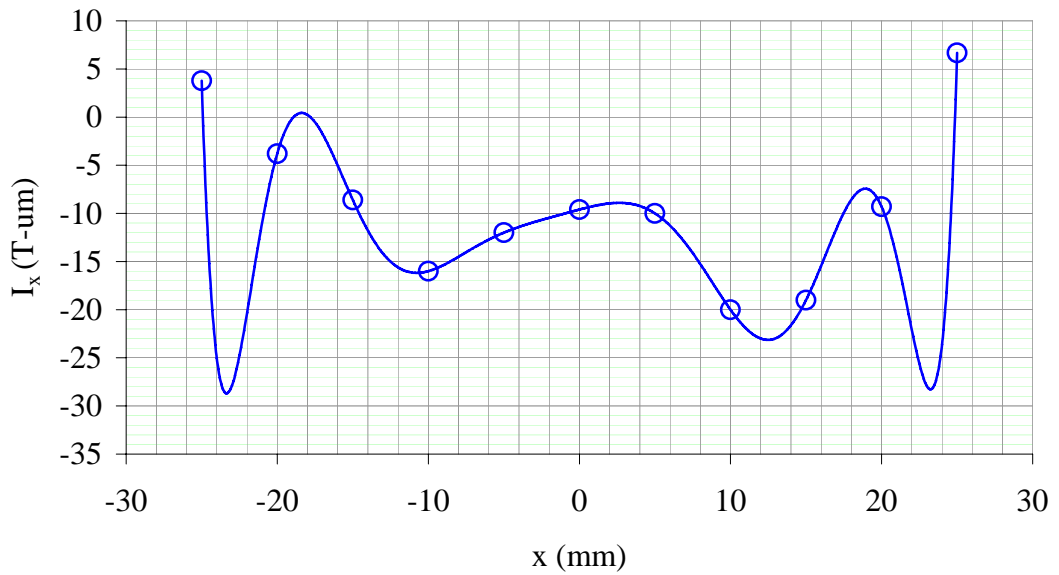


(b)

Figure 4.20 Integrated signal of horizontal field of gap 26.5 mm at $x = 0$: (a) flip from 90° to 270° and (b) flip from 270° to 450° .

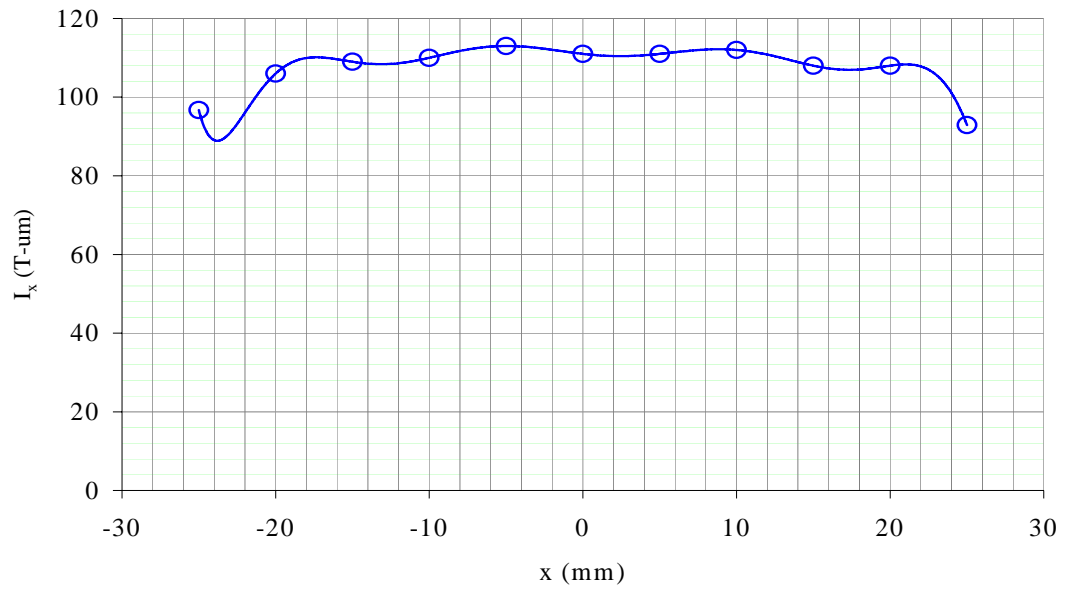


(a)

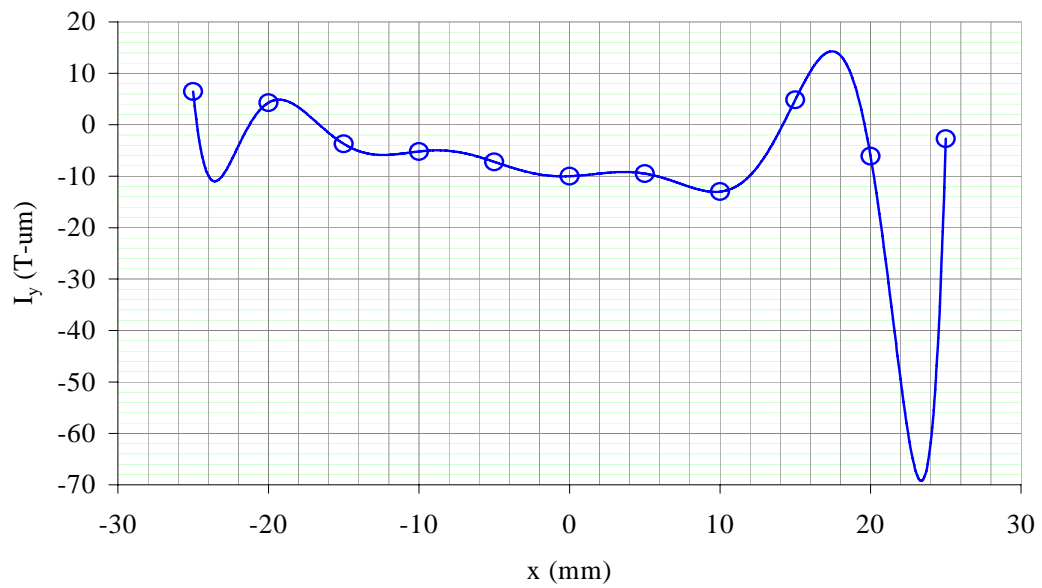


(b)

Figure 4.21 First field integrals as a function of horizontal position at the gap of 26.5 mm: (a) vertical component and (b) horizontal component. Lines are multipole fits.

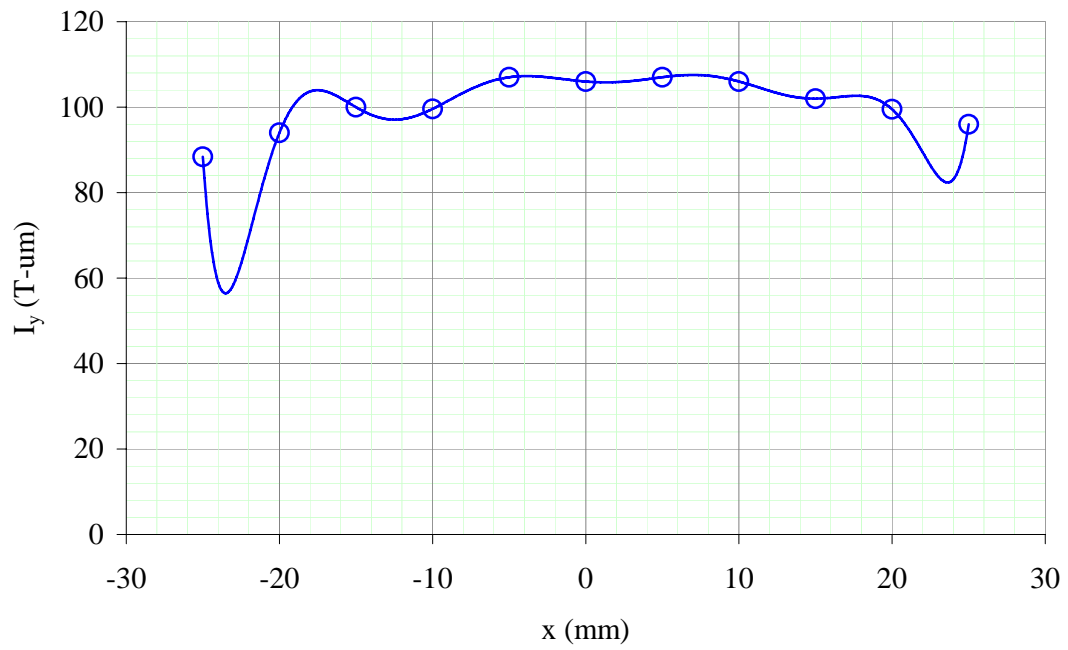


(a)

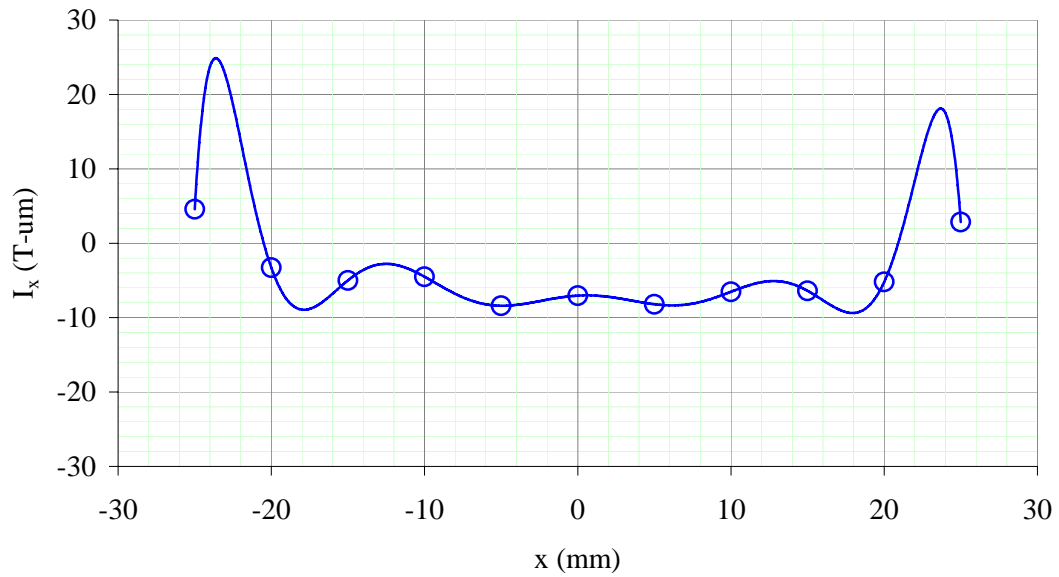


(b)

Figure 4.22 First field integrals as a function of horizontal position at 40 mm: (a) horizontal component and (b) vertical component. Lines are multipole fits.



(a)



(b)

Figure 4.23 First field integrals as a function of horizontal position at 65 mm: (a) vertical component and (b) horizontal component. Lines are multipole fits.

Table 4.2 Multipole field components at gap of 26.5 mm.

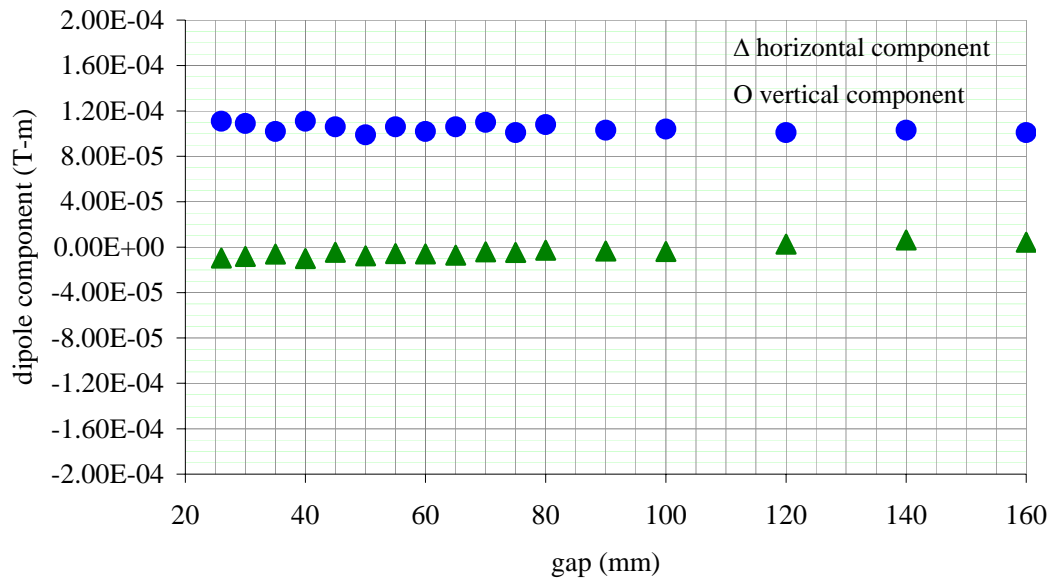
Multipole Field Components	First Field Integral		Dimension
	vertical	horizontal	
dipole	1.11×10^{-4}	-9.60×10^{-6}	T – m
quadrupole	-2.23×10^{-4}	2.77×10^{-4}	T
sextupole	-2.18×10^{-1}	-2.04×10^{-2}	T – m ⁻¹
octupole	16.4	-9.37	T – m ⁻²

Table 4.3 Multipole field components at gap of 40 mm.

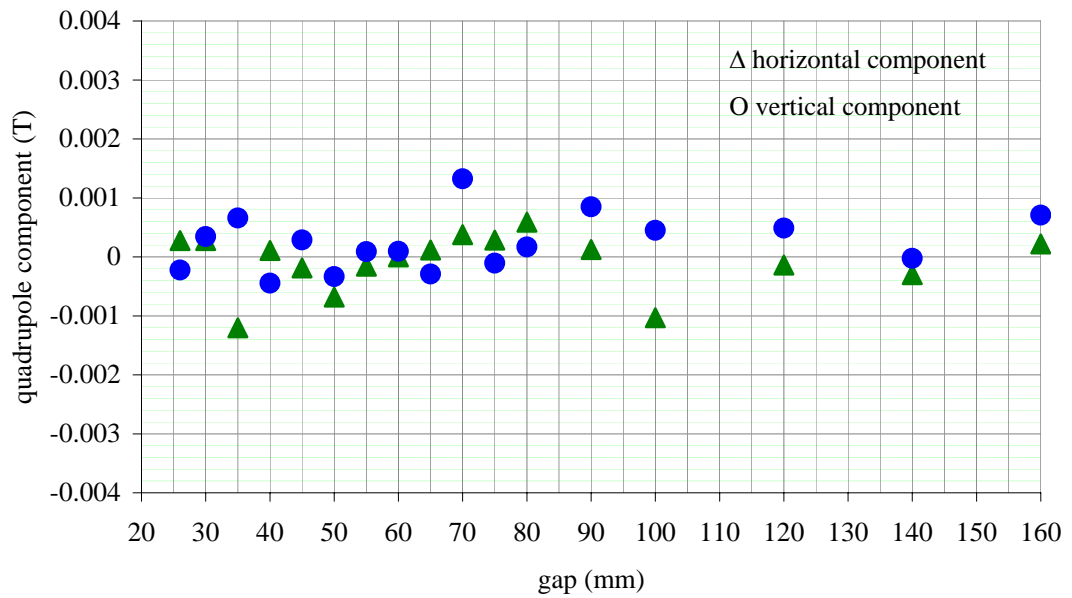
Multipole Field Components	First Field Integral		Dimension
	vertical	horizontal	
dipole	1.11×10^{-4}	-1.00×10^{-5}	T – m
quadrupole	-4.45×10^{-4}	1.09×10^{-4}	T
sextupole	6.33×10^{-2}	1.17×10^{-1}	T – m ⁻¹
octupole	11.7	-17.5	T – m ⁻²

Table 4.4 Multipole field components at gap of 65 mm.

Multipole Field Components	First Field Integral		Dimension
	vertical	horizontal	
dipole	1.06×10^{-4}	-7.04×10^{-6}	T-m
quadrupole	-2.91×10^{-4}	1.17×10^{-4}	T
sextupole	9.09×10^{-2}	-9.67×10^{-2}	T – m ⁻¹
octupole	10.4	-4.59	T – m ⁻²

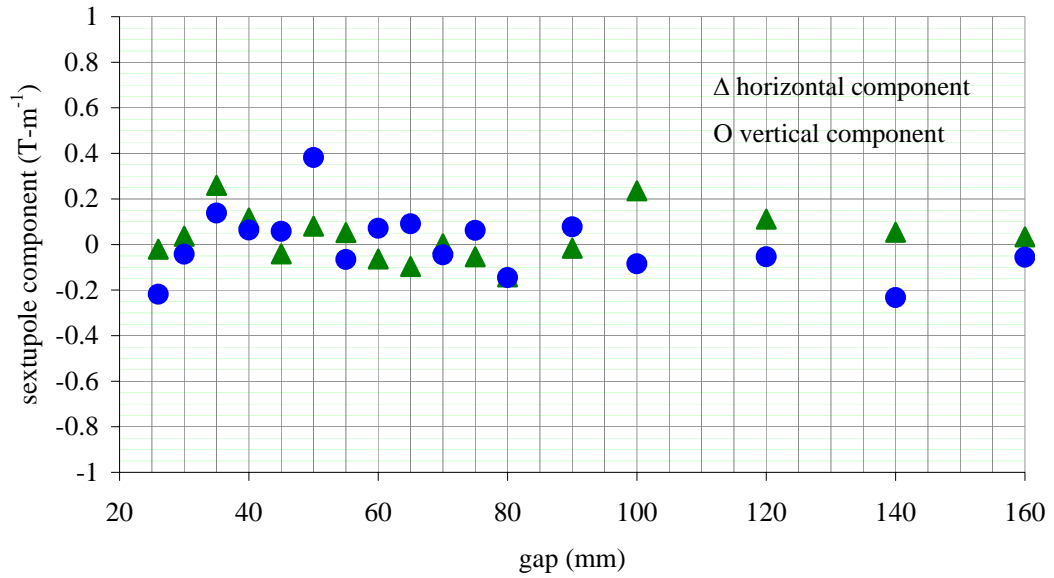


(a)

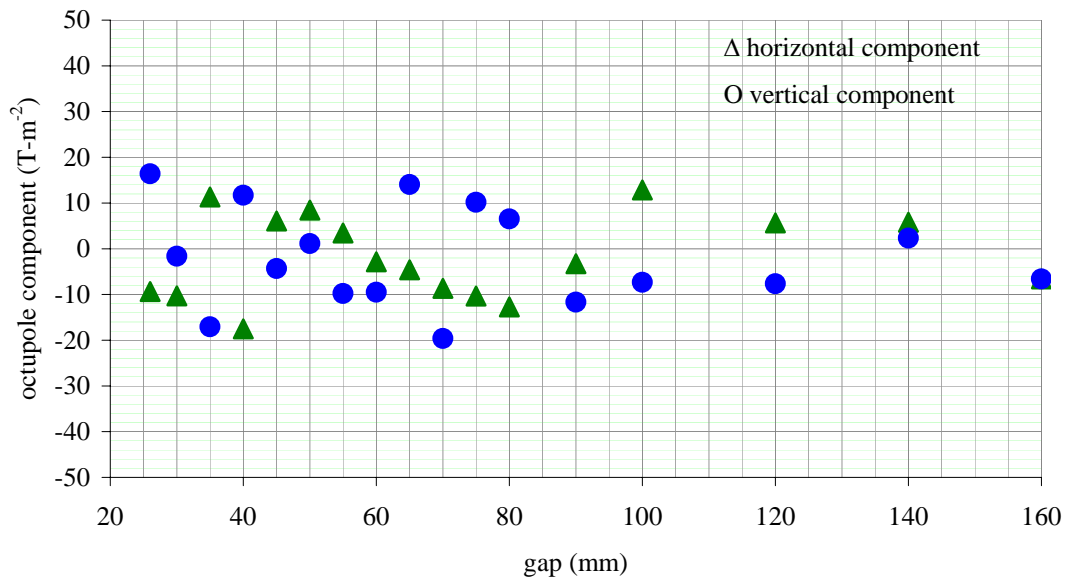


(b)

Figure 4.24 Field components as a function of gap: (a) dipole (b) quadrupole (c) sextupole and (d) octupole component.

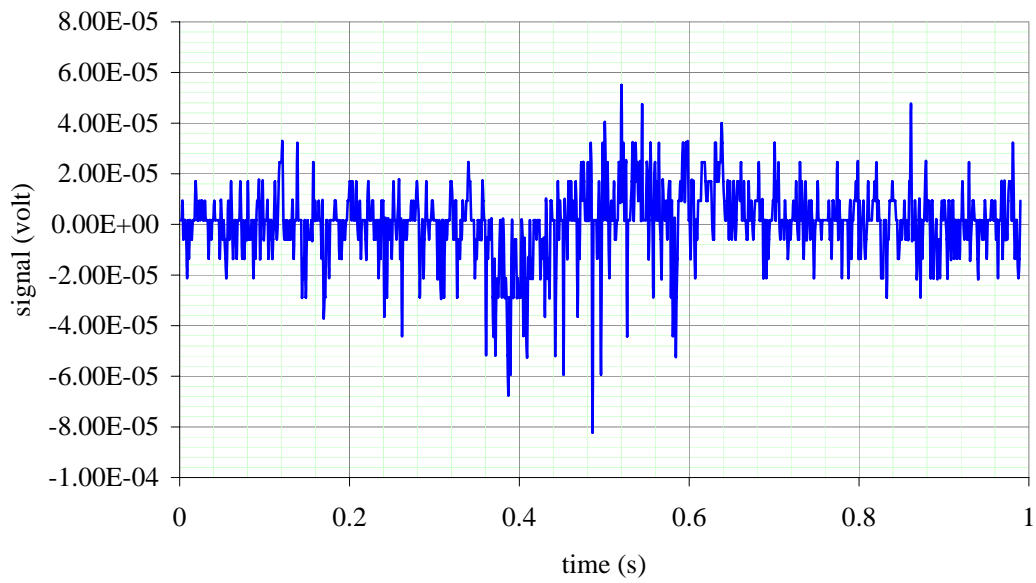


(c)

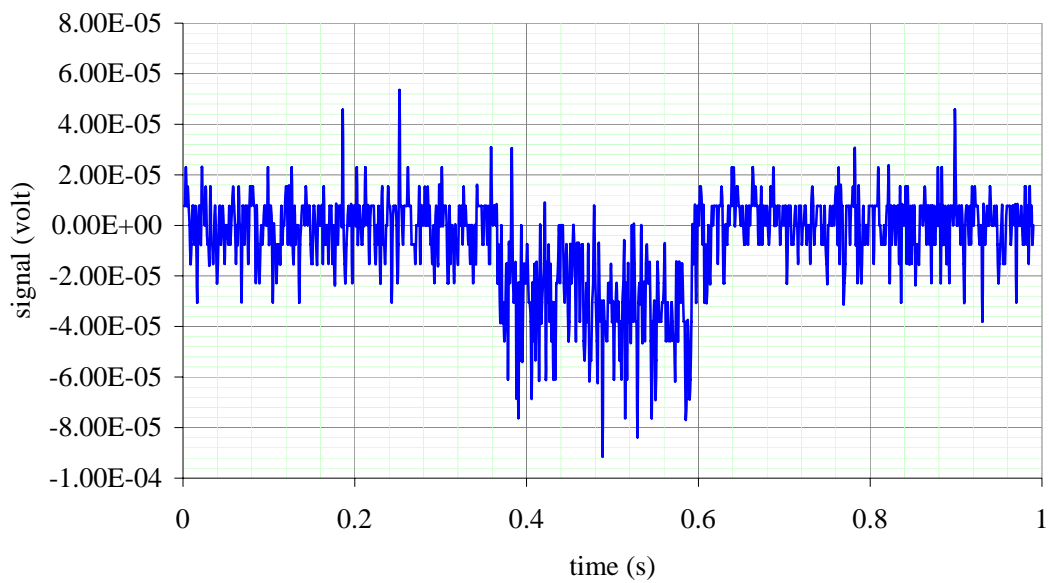


(d)

Figure 4.24 (continued) Field components as a function of gap: (a) dipole (b) quadrupole (c) sextupole and (d) octupole component.



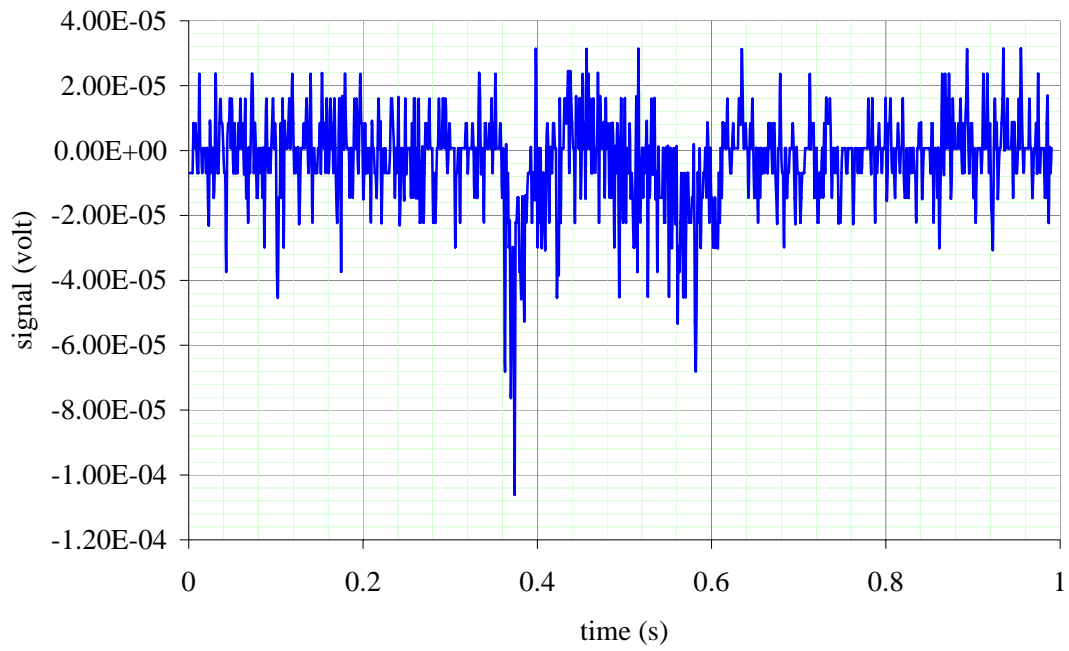
(a)



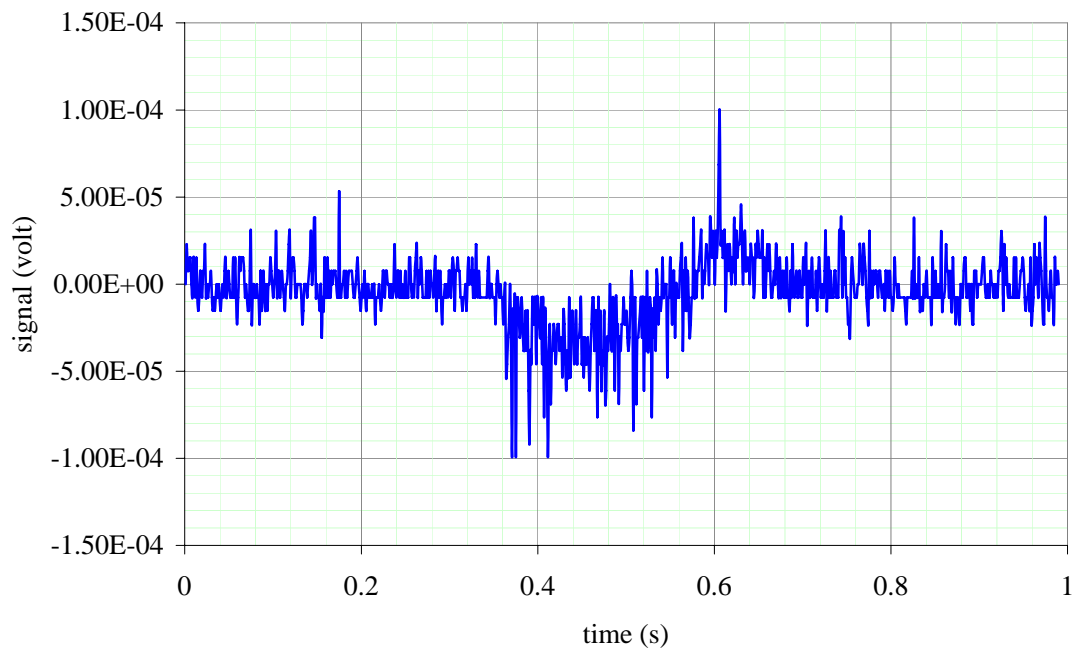
(b)

Figure 4.25 Measured signal of the second vertical field integral as function of time:

(a) flip from 0° to 180° (b) flip from 180° to 360° .

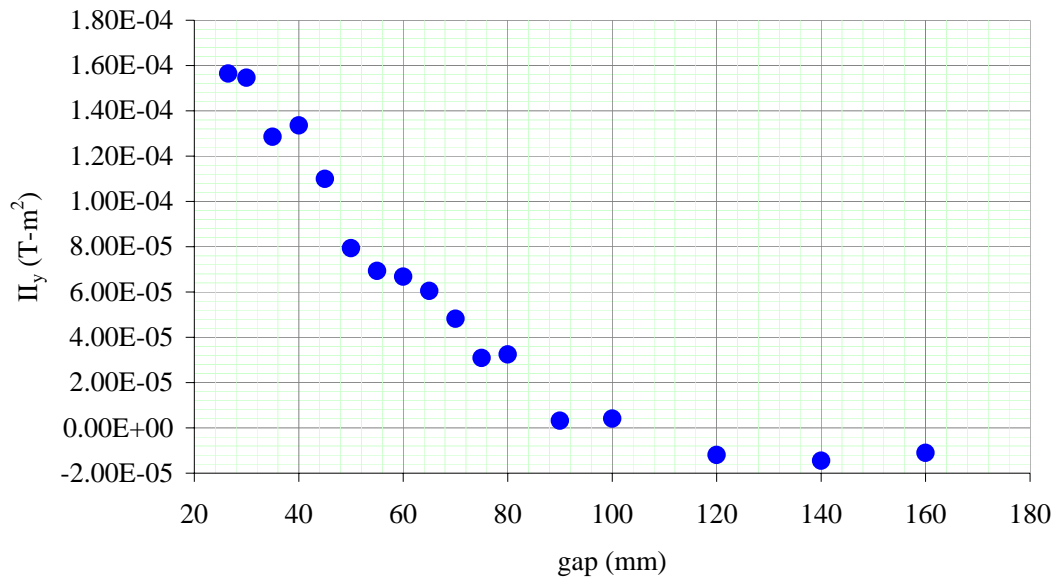


(a)

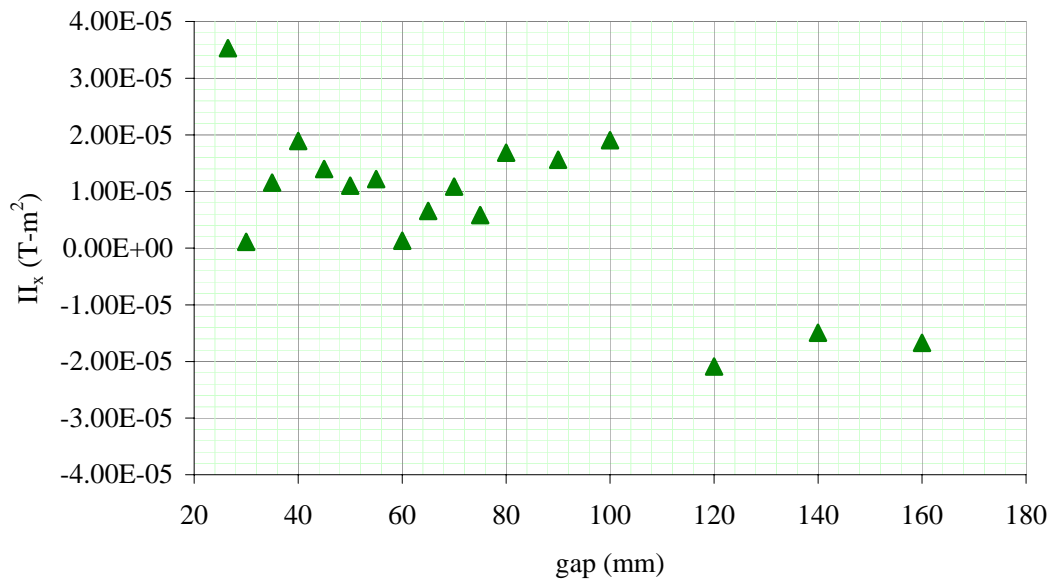


(b)

Figure 4.26 Measured signal of the second horizontal field integral: (a) flip from 90° to 270° (b) flip from 270° to 450° .



(a)



(b)

Figure 4.27 Second field integral as function of gap: (a) vertical and (b) horizontal component.

CHAPTER V

ANALYSES OF MAGNETIC FIELD MEASUREMENT

RESULTS

This chapter presents analyses of the magnetic field measurement results. The measured magnetic fields are used to analyze the effects of the U60 undulator on the electron trajectory, phase error, closed orbit distortion, betatron tune and betatron function. The multipole components are evaluated in order to investigate higher order perturbation on the electron beam.

5.1 Electron Trajectory inside the U60

As an electron moving through the U60 undulator field, it is forced to move with the sinusoidal-like trajectory. The electron motion is explained by the Lorentz force equation, presented in Equation (2.3):

$$\gamma m_o \frac{d^2 \vec{r}}{dt^2} = q(\vec{v} \times \vec{B}).$$

For the vertical magnetic field $B_y(z)$, by making the integration along the longitudinal coordinate we obtain the horizontal electron angle,

$$x'(z) = \frac{0.3}{E[GeV]} I_y(z), \quad (5.1)$$

where $I_y(z)$ is the vertical first field integral, given by

$$I_y(z) = \int_{z'=0}^{z'=z} B_y(z') dz', \quad (5.2)$$

where B_y is the vertical component of the magnetic field \vec{B} . By substituting the measured vertical magnetic field of the U60 and making the numerical integration we obtain the electron angle. The results for the 26.5 and 40 mm gap are shown in Figure 5.1. The results show that the electron beam exits the undulator with a finite angle, depending on the undulator gap. The maximum angle is 0.197 mrad at the undulator gap of 26.5 mm.

By making the integration of the electron angle in Equation (5.1), we can calculate the electron trajectory by

$$x(z) = \frac{0.3}{E[\text{GeV}]} II_y(z), \quad (5.3)$$

where $II_y(z)$ is the vertical second field integral given by

$$II_y(z) = \int_{z'=0}^{z'=z} \int_{z''=0}^{z''=z'} B_y(z'') dz'' dz' \quad (5.4)$$

By using the Equations (5.3) and (5.4) and then making numerical integration, we can then obtain the transverse position of the electron. The results are shown in Figure 5.2. The figure consists of the results that are calculated from the field obtained at the gap of 26.5, 40, 65 and 75 mm. The graphs show that the electron is gradually kicked out from the ideal orbit. The results also show that at the exit of the device the electron transverse position are not zero. The maximum position is 324.14 μm at the gap of 26.5 mm.

By using the relation in Equation (5.4), we can calculate the second field integral. The results, shown in Figure 5.3, indicate the existence of the quadratic components of the trajectory. Performing polynomial fitting up to the quadratic term,

$$H_y [\text{T} - \text{mm}^2] = a + bz + cz^2, \quad (5.5)$$

where a , b and c are the fitted coefficients, we obtain the quadratic coefficient c in the unit of T. The polynomial fits are also illustrated in Figure 5.3. The obtained quadratic coefficients at the various gaps are shown in Figure 5.4. Subtracting the quadratic term the trajectory can be brought back to undulator axis, as illustrated in Figure 5.5 for the 26.5 mm gap. This quadratic term of the trajectory is related to a constant magnetic field in the undulator. This implies that compensating this constant field the electron will be pulled back to the axis. The quadratic component elimination can be practically done by using the dipole field. The fields are produced by the long square coil. More details will be discussed in the next chapter. After the quadratic correction the electron, however, still exits the undulator with a non-zero transverse position. This orbit deviation for trajectory and angle can be corrected by steering magnets discussed in the next chapter.

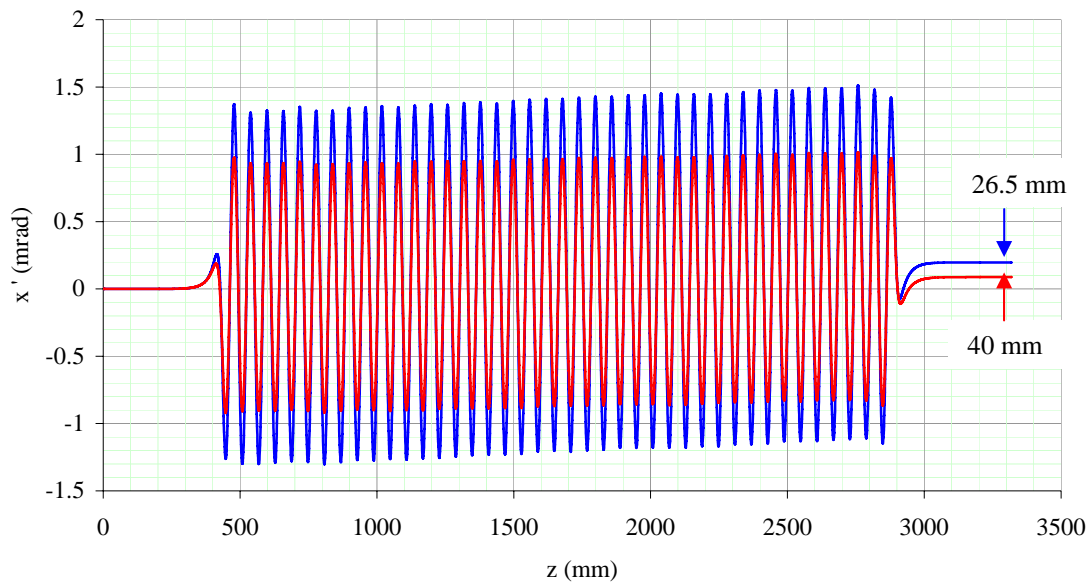


Figure 5.1 Electron angles at 26.5 and 40 mm gap.

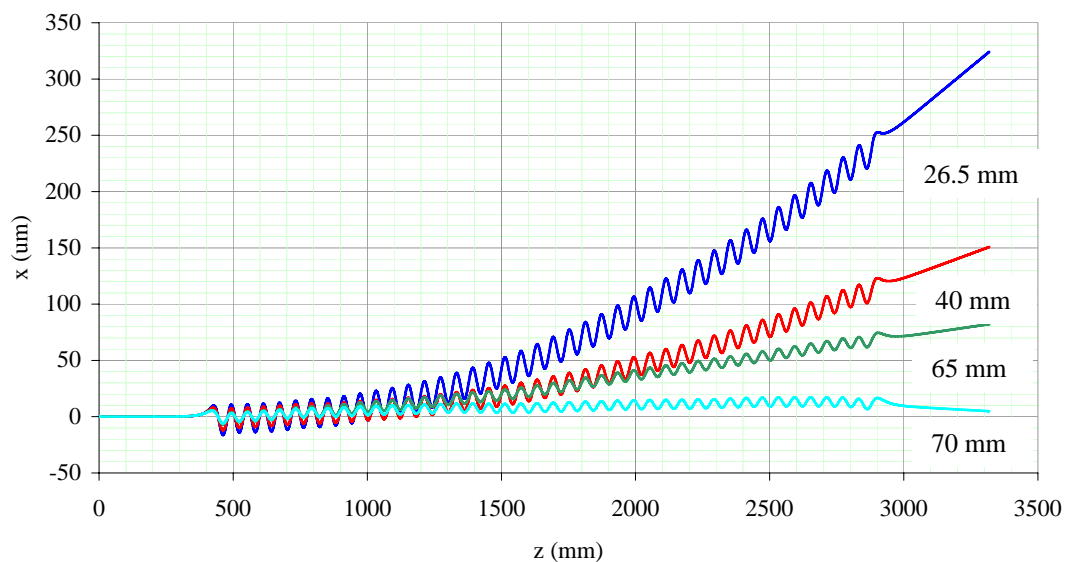


Figure 5.2 Electron trajectories at 26.5, 40, 65 and 70 mm gap.

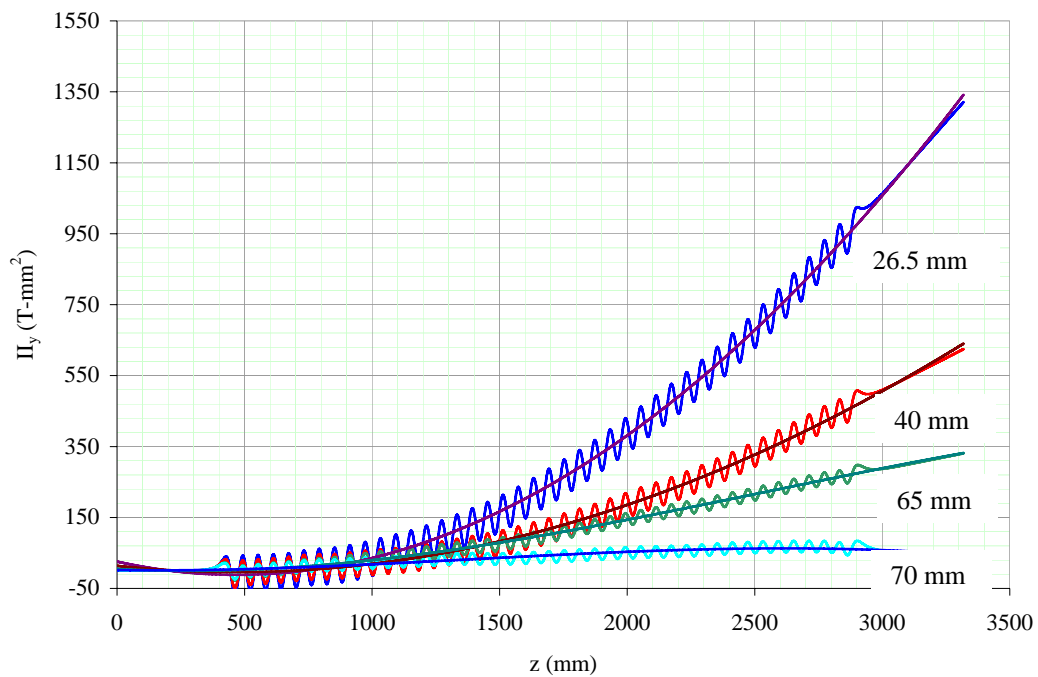


Figure 5.3 Polynomial fits to the second field integrals.

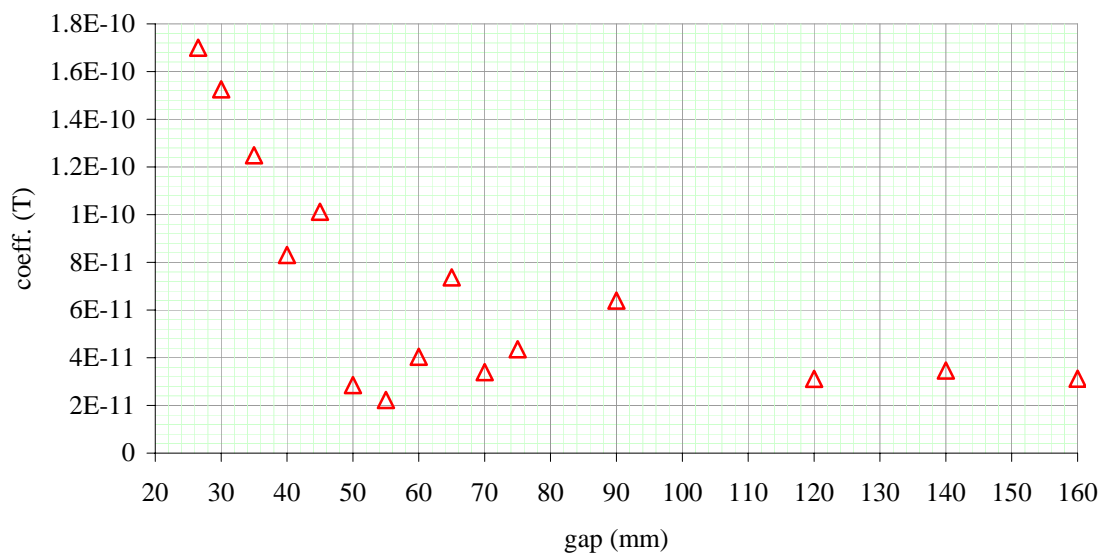


Figure 5.4 The quadratic coefficients of the second field integral at various gaps.

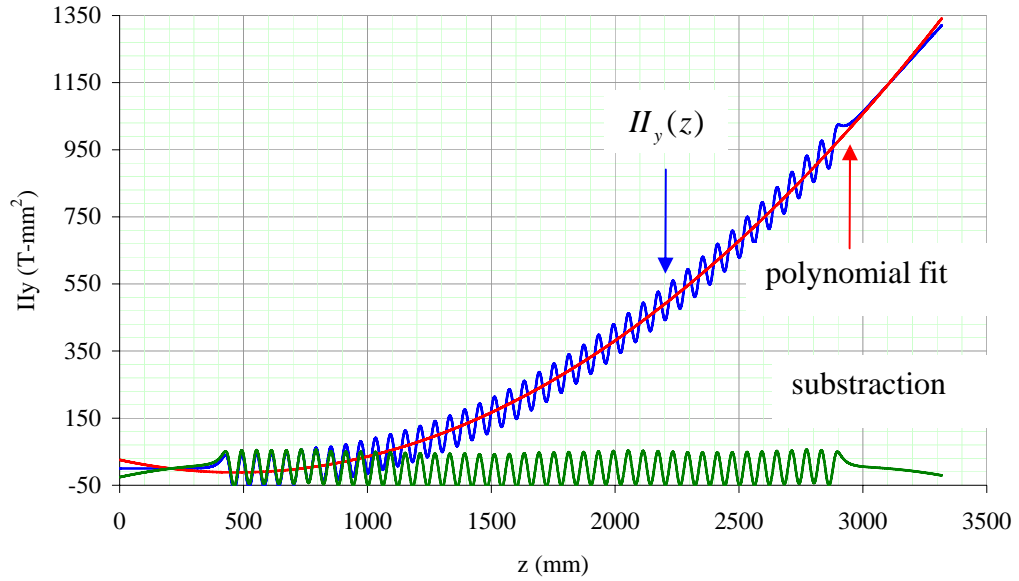


Figure 5.5 Result of eliminating the quadratic component from the second field integral at the gap of 26.5 mm.

5.2 Phase Error

The U60 undulator was designed to have 60 mm period length. However, the real device period lengths are slightly different for each magnetic period. Therefore, an electron is forced to move through the device with different distances in each period. The distance in each period subtracted by the average of all periods is the parameter called “phase error”. The phase error can be calculated by using the relation (2.50):

$$\Delta\delta = \delta_{real} - \delta_{avg}, \quad (5.6)$$

where δ_{real} is defined in (2.49):

$$\delta_{real}(z) = \frac{2\pi}{\lambda} \left[\frac{(z_f - z_0)}{2\gamma^2} + \int_{z=z_0}^{z=z_f} \frac{x'^2}{2} dz \right]. \quad (5.7)$$

Calculated phase error at the various gaps as a function of pole numbers are shown in the Figure 5.6. The rms phase error as a function of the undulator gap is shown in the Figure 5.7. The standard deviation is ± 1.02 degree. The figure shows that the rms phase errors are higher at wider gaps. The effects then result in the obtained quality of the radiation.

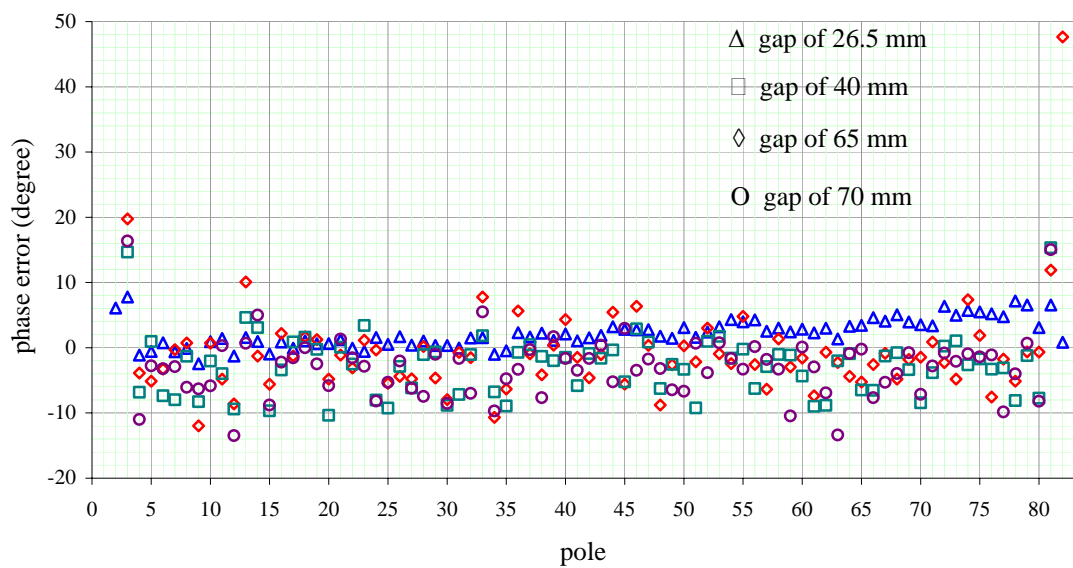


Figure 5.6 The phase errors as function of a pole number.

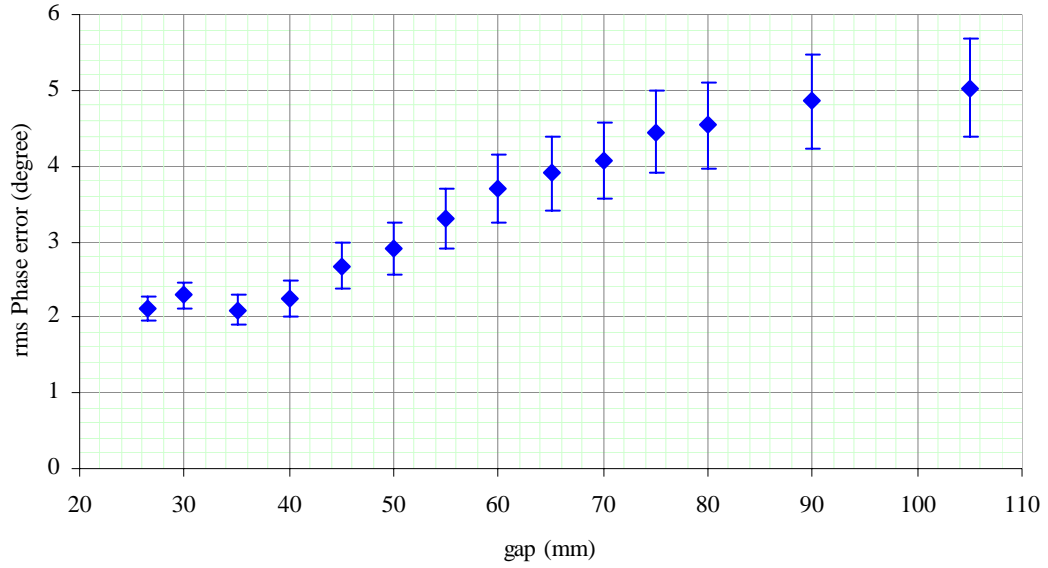


Figure 5.7 The rms phase error as function of the undulator gap. The error bars are statistical errors.

The quality of the radiations can now be predicted from the rms phase errors. The radiation intensity due to the rms phase errors can be calculated, defined in (2.51):

$$I_{real} = I_{ideal} e^{-(k\sigma_\phi)^2} \quad (5.8)$$

where I_{ideal} and I_{real} are, respectively, photon flux intensity of ideal and real devices, σ_ϕ is the rms phase error and k is a harmonic number. The percentage of the obtained flux intensities as function of gap at the 1st, 3rd, 5th and 7th harmonics are shown in Figure 5.8. We obtain the flux intensity higher than 80 % of the ideal case at the harmonic of 1st, 3rd and 5th. Figure 5.9 shows the percentage of the flux intensities at the gap of 26.5, 40, 65 and 70 mm for the of 1st, 3rd, 5th and 7th harmonics.

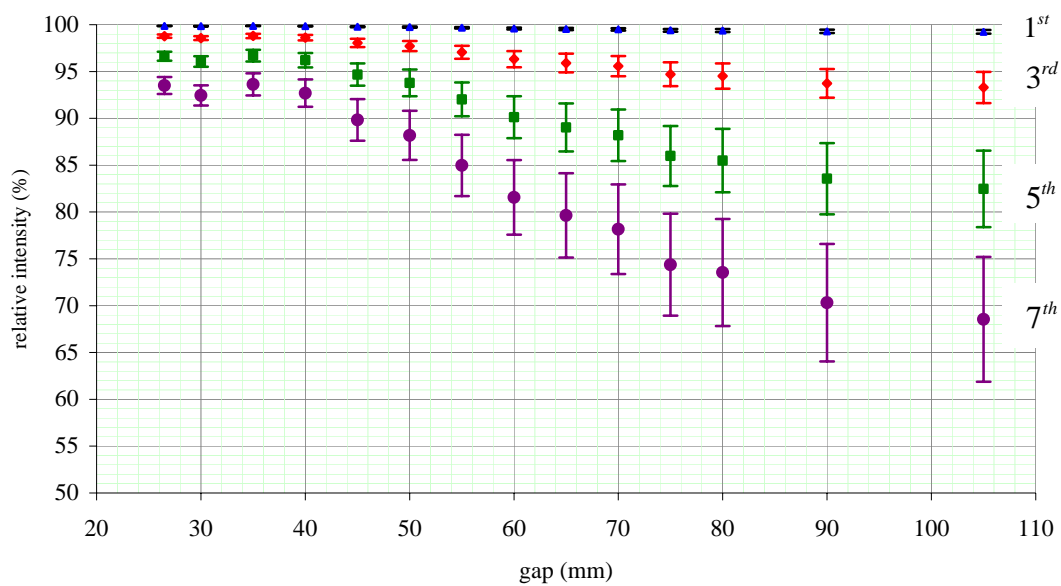


Figure 5.8 The relative flux intensities of the U60 undulator radiation as function of the gap for various harmonics.

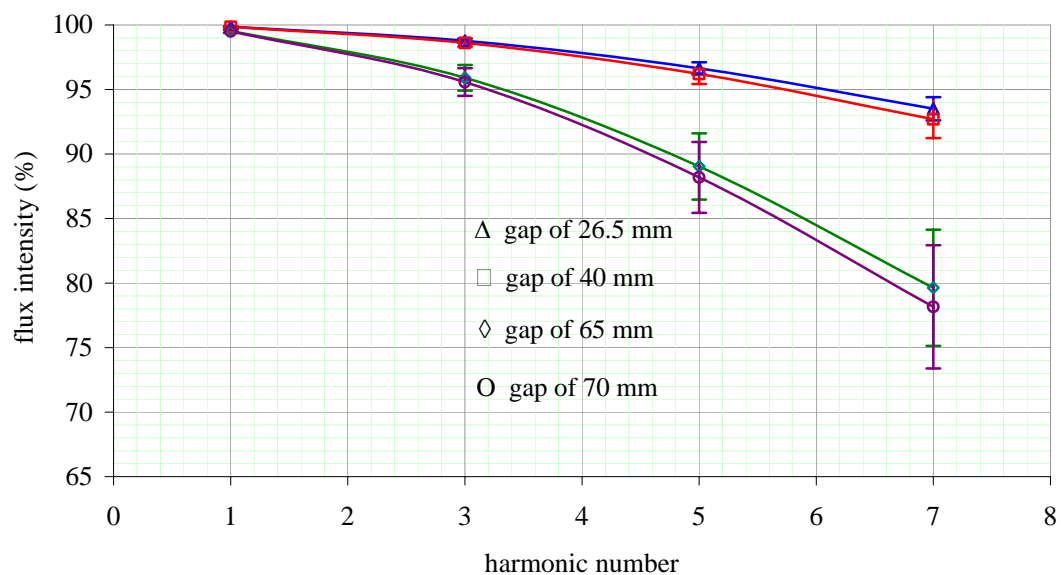


Figure 5.9 The percentage of the obtained flux intensities of undulator radiation as function of harmonic number.

These results confirm that as far as the phase errors are concerned, the quality of this device is quite good at gaps of 26.5 to 70 mm, which will give us the photon energy covering 40-1000 eV.

5.3 Effects on Closed Orbit Distortion

While an electron moves inside the undulator, it is acted on by the undulator field. Magnetic field errors cause it to move out of the device with the deviated angle and transverse position respect to the point entering the undulator. By assigning upper limit of the integration $z' = L$, the undulator's magnetic length, in the Equations (5.1) and (5.3), the deviated angles and transverse positions of the electron at the exit of the undulator can be evaluated. These are, respectively,

$$\Delta x' = x'(z' = L) \quad (5.9)$$

and

$$\Delta x = x(z = L). \quad (5.10)$$

The deviated angles and transverse positions of the electron at the exit of the undulator, measured by flipping coil, are respectively illustrated in Figures 5.10 and 5.11.

By considering the deviated angle in Figure 5.10, the horizontal component is quite constant for all gaps. The averaged value and the standard deviation are respectively 0.026 mrad and 9.43×10^{-4} mrad.

The orbit displacements of an electron after passing the undulator are shown in Figure 5.11. The average of horizontal displacement and the standard deviation are respectively found to be 41.91 μm and 3.82 μm . For the vertical component, the

average displacement and the standard deviation are $-14.64 \mu\text{m}$ and $5.42 \mu\text{m}$, respectively.

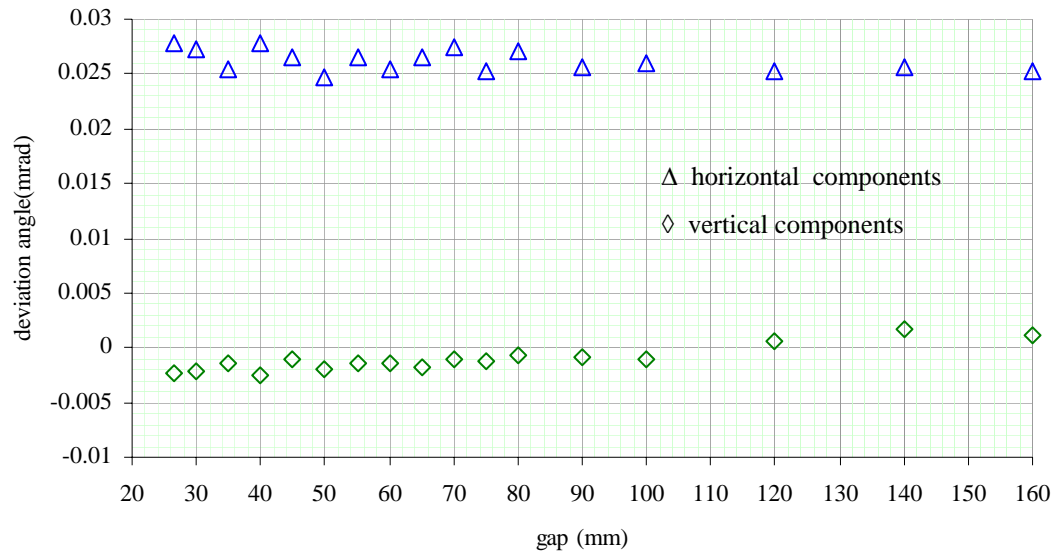


Figure 5.10 Deviated angle of an electron at the exit of the undulator as function of gap.

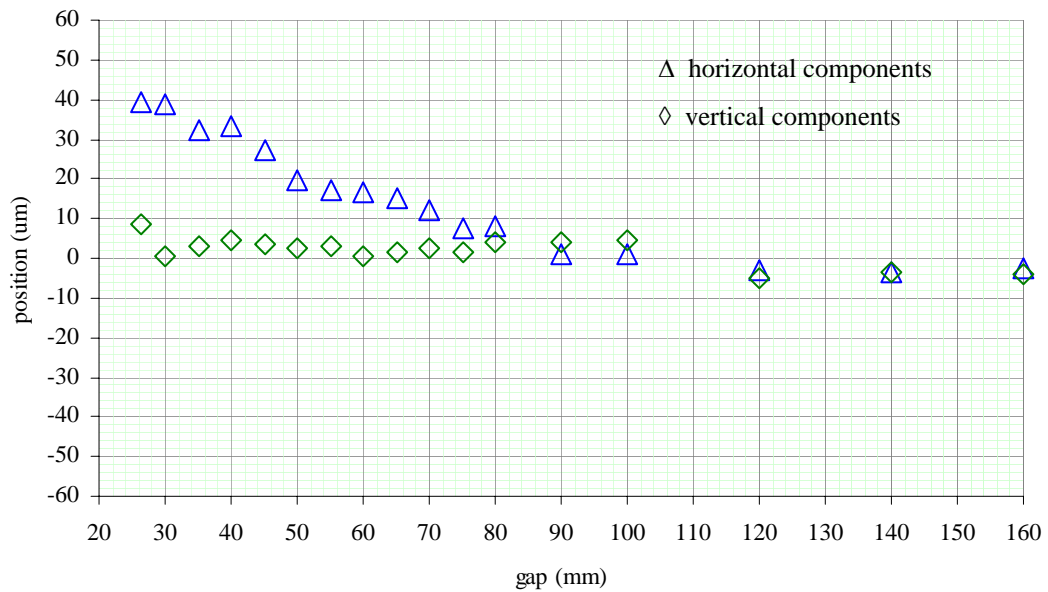


Figure 5.11 Off-axis position of an electron at the exit of the undulator.

From the deviated electron angle at the exit of the undulator, we get the closed orbit distortion (COD) in the BPM numbered j

$$\Delta = \frac{\theta \sqrt{\beta_i \beta_j}}{2 \sin \pi \nu} \cos(|\mu_i - \mu_j| - \nu \pi), \quad (5.11)$$

where θ is the kicked electron angle, μ is the phase advance and ν is the betatron tune. Subscript i and j indicate the positions at the exit of an undulator and BPMs. The horizontal and vertical COD are, respectively, shown in Figures 5.12 and 5.13. The experimental predictions are compared with the COD measurements, shown in Figure 5.14. However, the BPMs are calibrating because there is more noise.

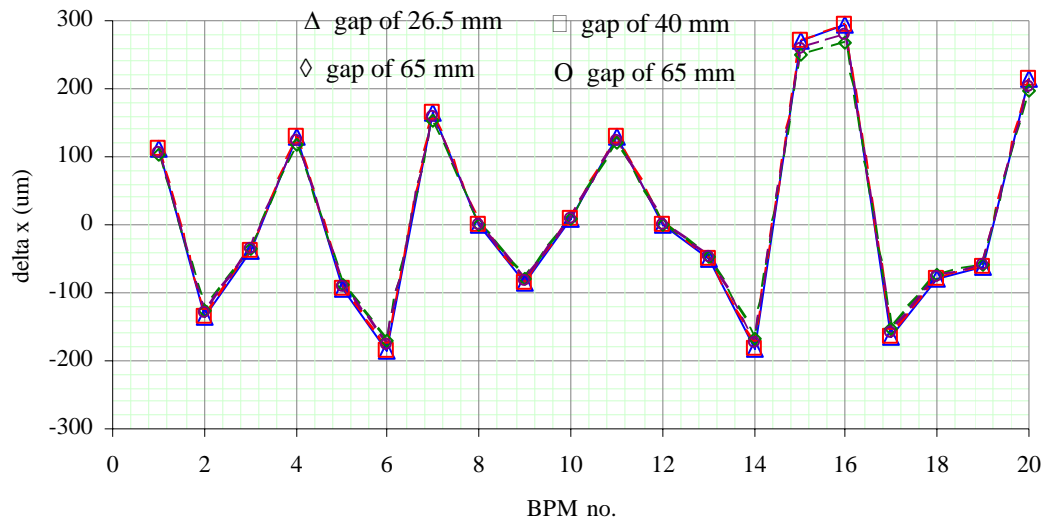


Figure 5.12 Predicted horizontal COD as function of a BPM number.

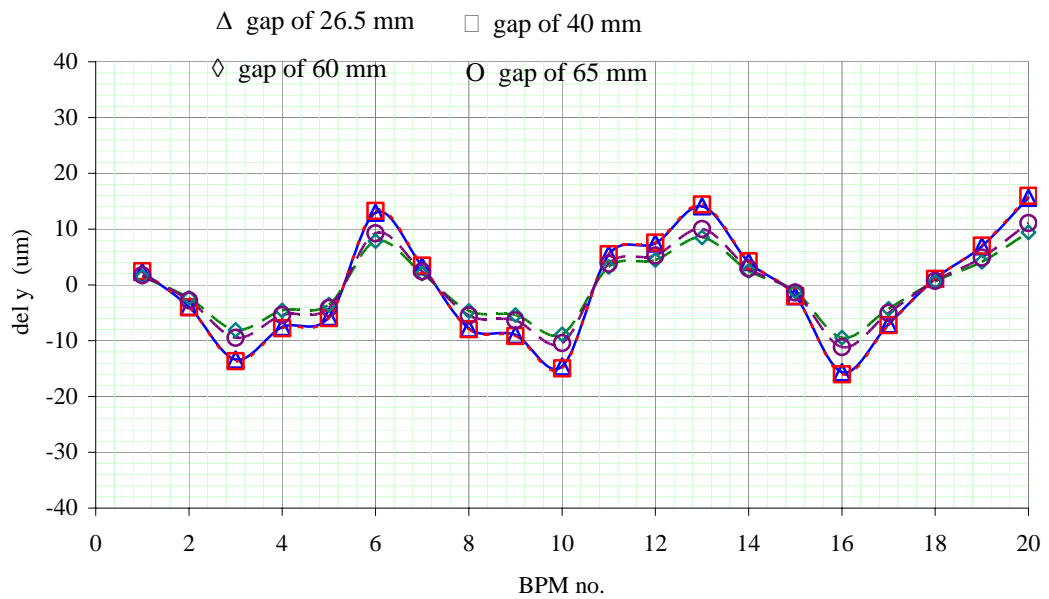
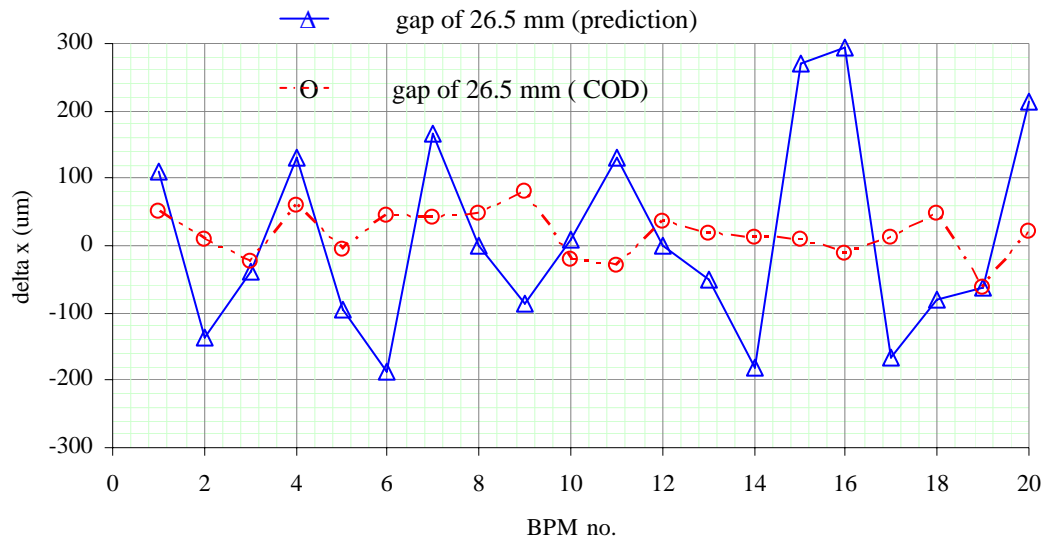
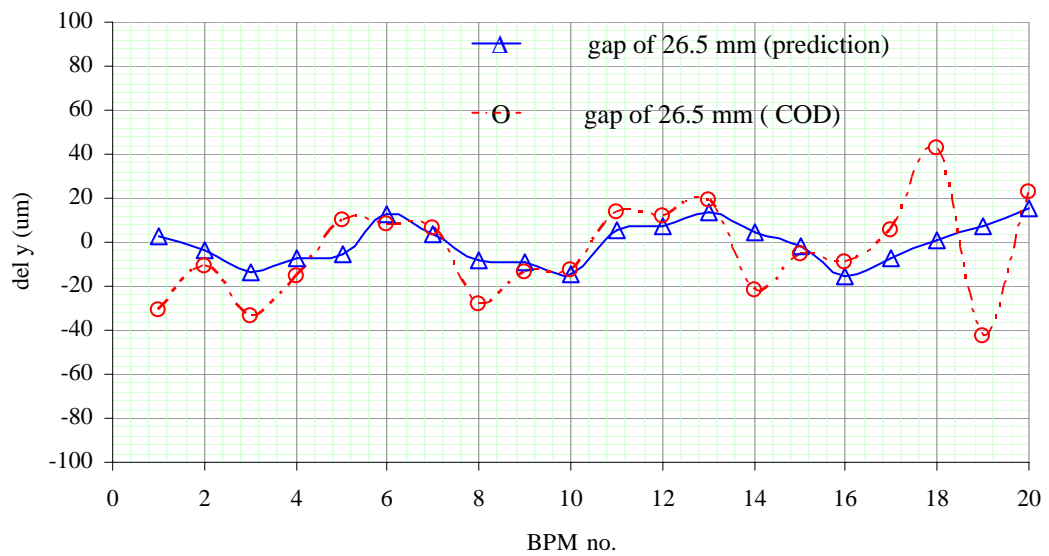


Figure 5.13 Predicted vertical COD as function of a BPM number.



(a)



(b)

Figure 5.14 Comparison between the experimental prediction and COD measurement: (a) horizontal COD and (b) vertical COD.

5.3.1 Effects on the Betatron Tunes and Betatron Function

The U60 undulator was inserted in the straight section located between the QF12 and QF13. This is illustrated in Figure 5.15. Insertion of the undulator into the storage ring causes the betatron tune shifts. The betatron tune shifts are calculated using Matlab programming with accelerator toolbox (AT) (Terebilo, 2001). The undulator magnet model is constructed as the series of hard edge dipoles, using the measured peak field. The dipole model representing the undulator magnet blocks is a rectangular dipole, shown in Figure 5.16. A transfer matrix of the rectangular magnet is given by

$$M_{rect} = \begin{pmatrix} 1 & 0 \\ \frac{\tan(\delta)}{\rho} & 1 \end{pmatrix} \begin{pmatrix} \cos \theta & \rho \sin \theta \\ -\frac{1}{\rho} \sin \theta & \cos \theta \end{pmatrix} \begin{pmatrix} 1 & 0 \\ \frac{\tan \delta}{\rho} & 1 \end{pmatrix}. \quad (5.12)$$

For $\theta \ll 1$, $\delta = \frac{\theta}{2}$, where $\theta = \frac{l_h}{\rho_h}$, l_h is an effective length and ρ_h is a radius of curvature. The l_h and ρ_h are respectively defined for a hard-edge model magnet as (Wiedemann, 1995)

$$l_h = \frac{2}{\pi^2} \lambda_u, \quad (5.13)$$

$$\rho_h = \frac{4}{\pi} \rho_o, \quad (5.14)$$

where $\rho_o = \frac{E[\text{GeV}]}{0.299B_0[\text{T}]}$ is the radius of curvature related to the undulator peak field

and λ_u is a periods length. By modeling all peaks of undulator magnetic field and later substituting them into AT, the tune shifts are finally obtained. The calculated tunes shifts are shown in Figure 5.17. The graph shows that they are exponentially

decreased as a function of gap. The maximum vertical tune shift produced at the gap of 26.5 mm is 0.0038, while the horizontal tune shift is negligibly small.

The tunes shift can also be calculated by a linear perturbation method (Rugmai, 2005; Walker, 1995). By evaluating the focusing strength of the undulator in Equation (2.3)

$$K_y = \left(\frac{0.3}{E(\text{GeV})} \right)^2 \frac{1}{L} \int_0^L B_y^2(z) dz, \quad (5.15)$$

and phase advance in Eq. (2.64)

$$\mu_y = \cos^{-1} \left(\frac{1}{2} \text{Tr}(M_C M_{F,\text{eff}}) \right), \quad (5.16)$$

the tunes shift can be eventually calculated by

$$\Delta \nu_y = \frac{\mu_u - \mu_y}{2\pi}, \quad (5.17)$$

where M_C is the one turn matrix without an undulator :

$$M_C = \begin{pmatrix} \cos \mu_y + \alpha_y \sin \mu_y & \beta_y \sin \mu_y \\ -\gamma_y \sin \mu_y & \cos \mu_y - \alpha_y \sin \mu_y \end{pmatrix},$$

$M_{F,\text{eff}}$ is defined by (Bassetti, Cattoni, Luccio, Preger and Tazzari, 1977)

$$M_{F,\text{eff}} = \begin{pmatrix} 1 & -\frac{L}{2} \\ 0 & 1 \end{pmatrix} \begin{pmatrix} \cos \sqrt{K_y L} & \frac{1}{\sqrt{K_y}} \sin \sqrt{K_y L} \\ -\sqrt{K_y} \sin \sqrt{K_y L} & \cos \sqrt{K_y L} \end{pmatrix} \begin{pmatrix} 1 & -\frac{L}{2} \\ 0 & 1 \end{pmatrix},$$

and $M_C M_{F,\text{eff}}$ is therefore the one turn matrix in presence of the undulator given by

$$M_C M_{F,\text{eff}} = \begin{pmatrix} \cos \mu_u + \alpha_y \sin \mu_u & \beta_u \sin \mu_u \\ -\gamma_u \sin \mu_u & \cos \mu_u - \alpha_u \sin \mu_u \end{pmatrix}. \quad (5.18)$$

The calculated results are also shown in Figure 5.17. The analytical calculation gives larger vertical tune shift, with the value of 0.0064 at the minimum gap.

Tunes shifts in Figure 5.17 are only produced from the intrinsic focusing of the undulator magnet. However, the tune shifts are also produced from undulator field errors. Effects from the field error alone can be evaluated by performing polynomial fits on the measured field integrals along the horizontal position. The multipole expansion of the field integral are obtained by

$$I_i(x) = \int_{z'=0}^L B_i(z')dz = B_{o,i}L + (B'_iL)x + \left(\frac{1}{2}B''_iL\right)x^2 + \dots,$$

or

$$I_i(x) = a + bx + cx^2 + \dots \quad (5.19)$$

where L is the length of the long coil, $a = B_{o,i}L$, $b = B'_iL$, and $c = \frac{B''_iL}{2}$ are the dipole, quadrupole and sextupole components, respectively. Subscript i is a component x or y . The quadrupole strength is therefore given by

$$\Delta k[\text{m}^{-2}] = \frac{b}{B\rho} \quad (5.20)$$

The obtained quadrupole components are shown in Figure 5.18. By using Equation (5.20), the quadrupole strength can be calculated. The results are shown in Figure 5.19. By substituting quadrupole strength in the undulator matrix $M_{F,eff}$ and using Equations (5.16)-(5.18), the tune shift due to the quadrupole component can be calculated. The vertical strength gives the vertical tune shift and the horizontal strength gives the horizontal tune shift. The results are shown in Figure 5.20. The graph shows that the tunes shift due to the undulator field errors are small.

Tune shifts calculated by AT are approximated by using the peak of magnetic field in each magnetic field pole, whereas tune shifts obtained by using

analytic calculation are straightforwardly calculated from all points of the measured field. Therefore, the tune shifts obtained from analytical calculation, are reasonable choice for obtaining the compensation scheme. The tune shifts due to field error from multipole fit is also used to obtain the compensation scheme. Therefore, the summation of vertical tune shifts due to intrinsic field using the analytical calculation and field error, shown in Figure 5.21, will be used to obtain the compensation scheme. The result shows that at the undulator gap of 26.5 mm the tune shift is 0.0066. The result from experiment at the same gap is 0.0065, shown in Figure 5.22.

The theoretical betatron functions calculated before and after the inserting the U60 undulator in the SPS storage ring are illustrated in Figures 5.23 a. and 5.23b. The graph in Figure 5.23b is the result at the gap of 26.5 mm.

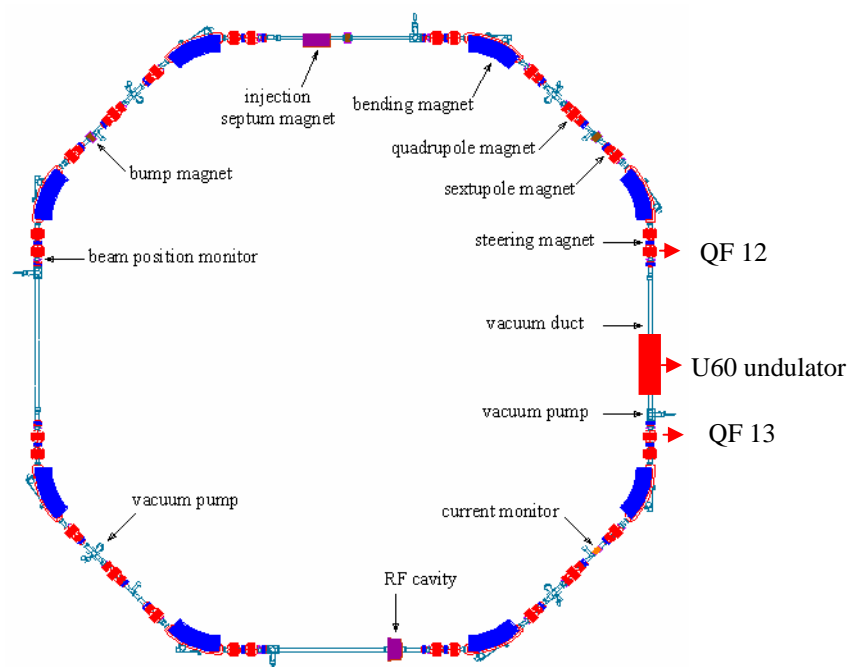


Figure 5.15 The location of the U60 in the SLRI storage ring.

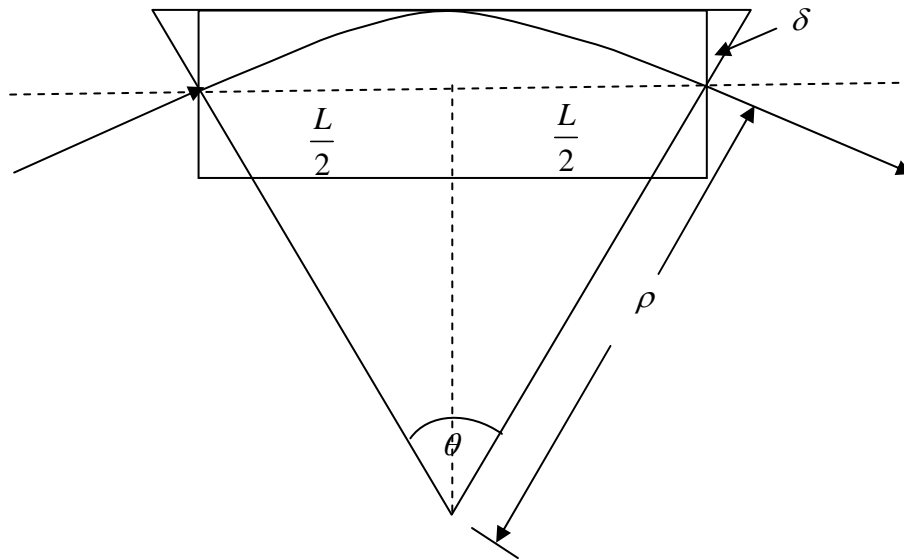


Figure 5.16 Rectangular dipole model.

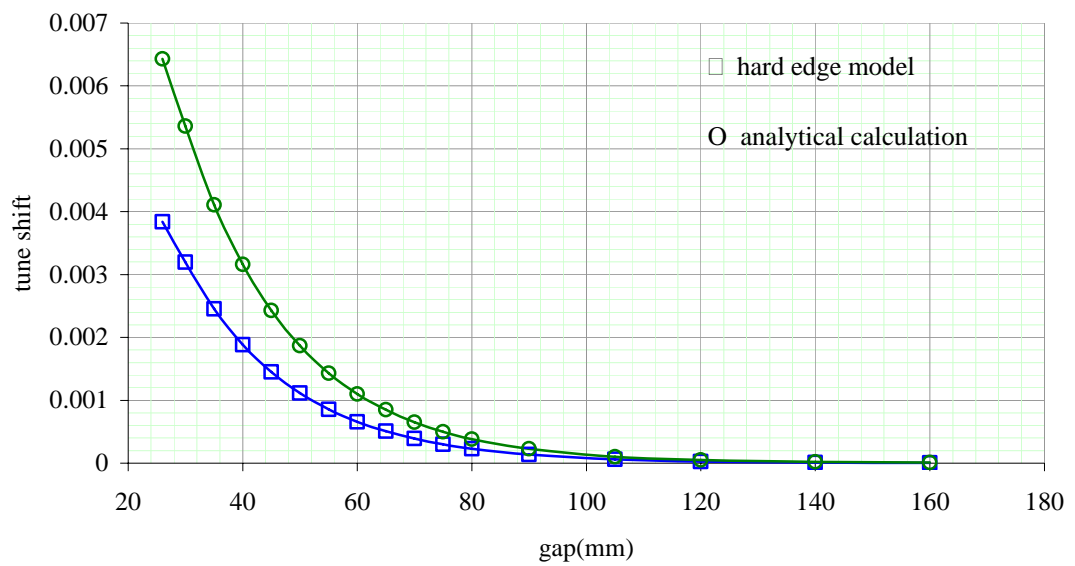


Figure 5.17 The tunes shift as function of the undulator gap.

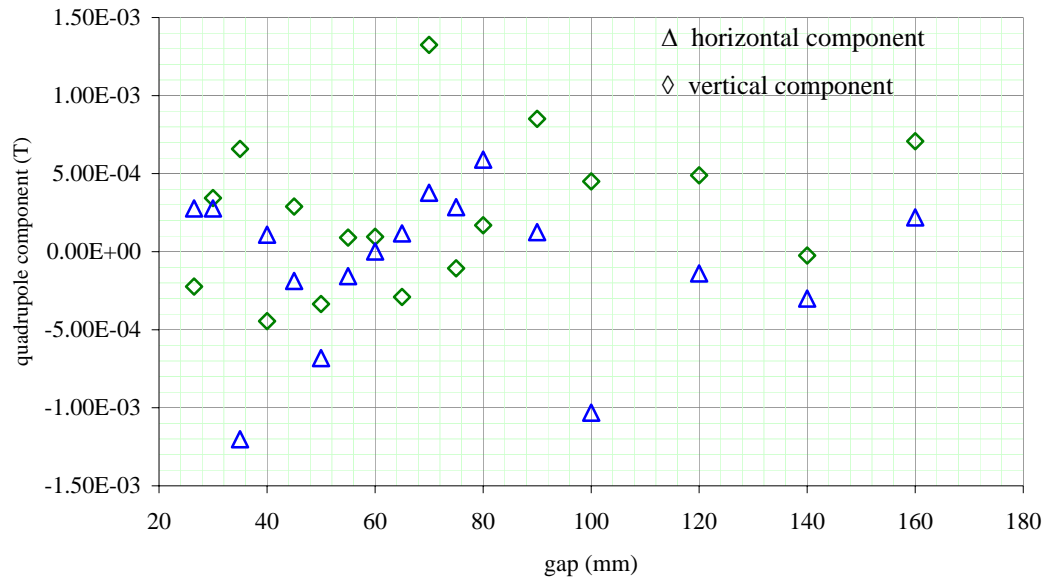


Figure 5.18 The quadrupole component as of function of the undulator gap.

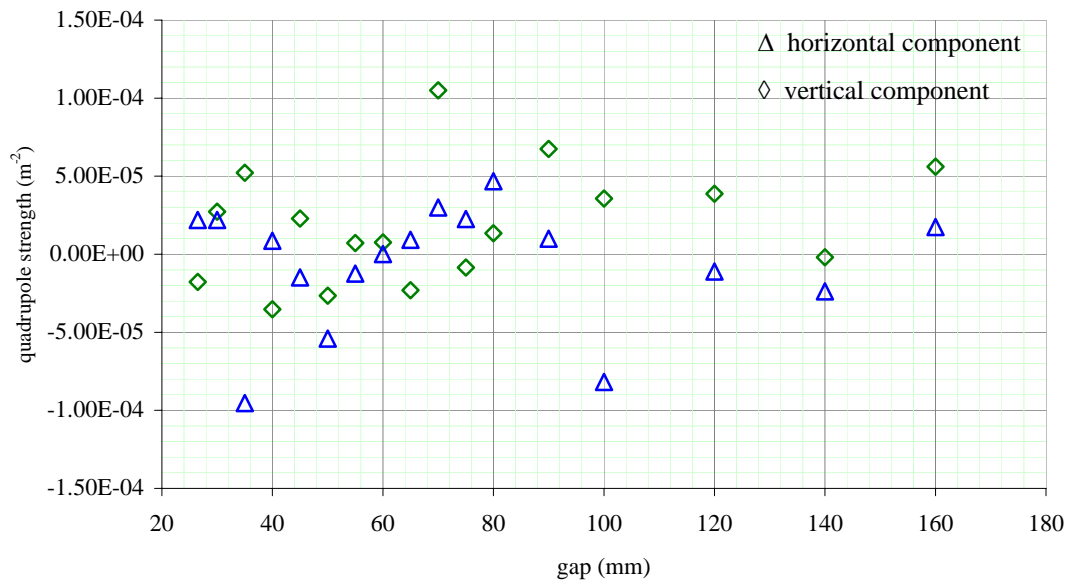


Figure 5.19 The quadrupole strength as function of the undulator gap.

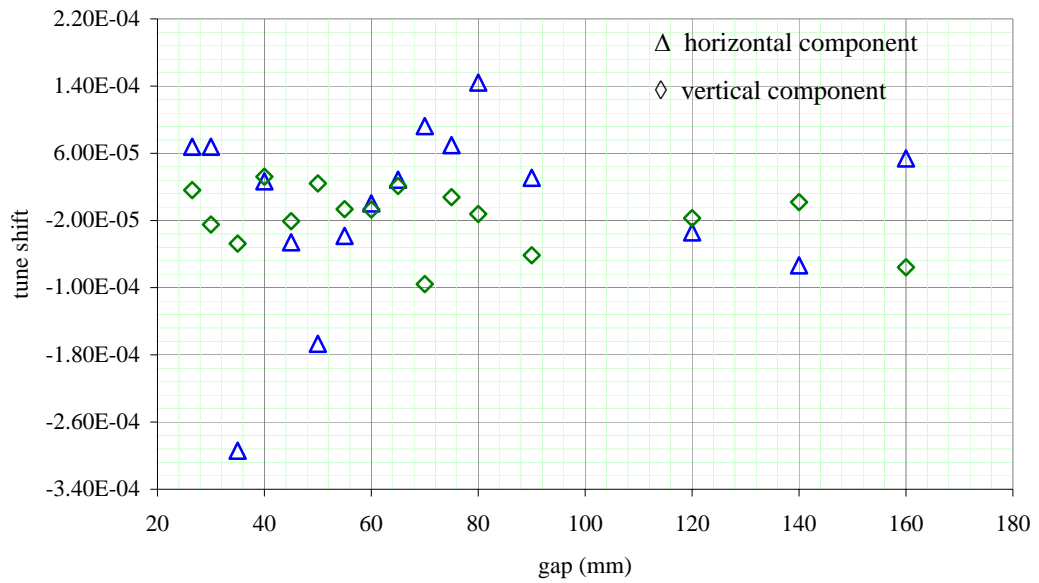


Figure 5.20 The tunes shift due to the undulator field error.

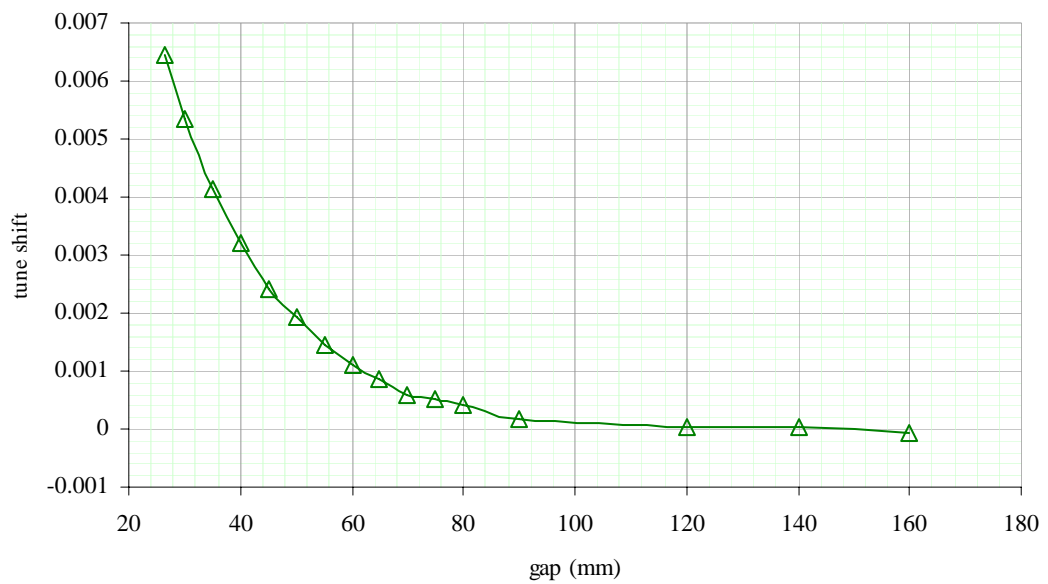
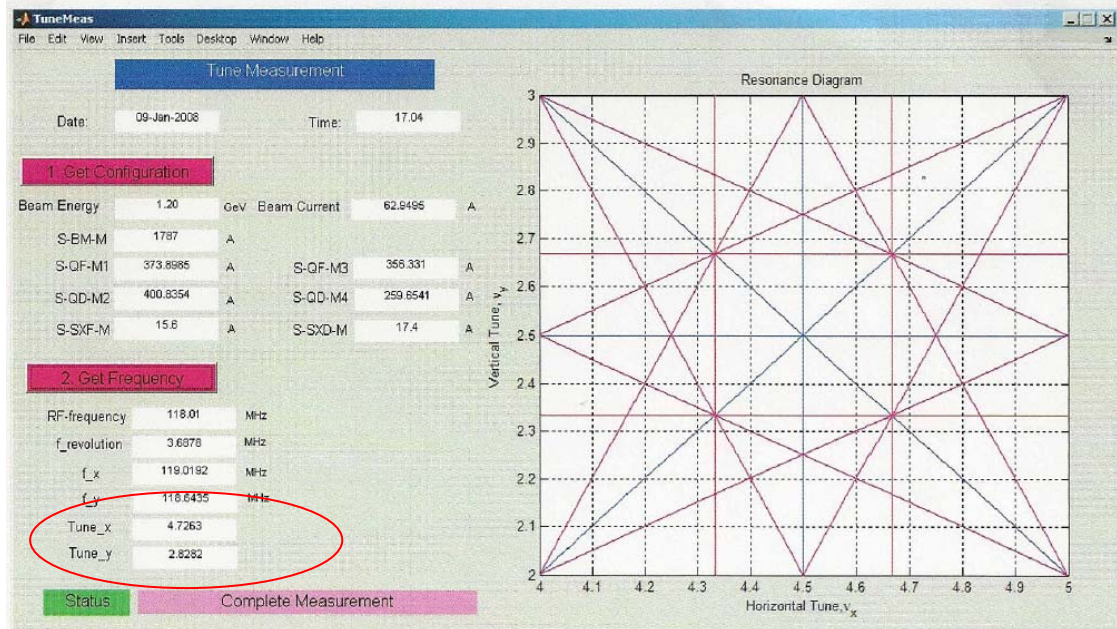
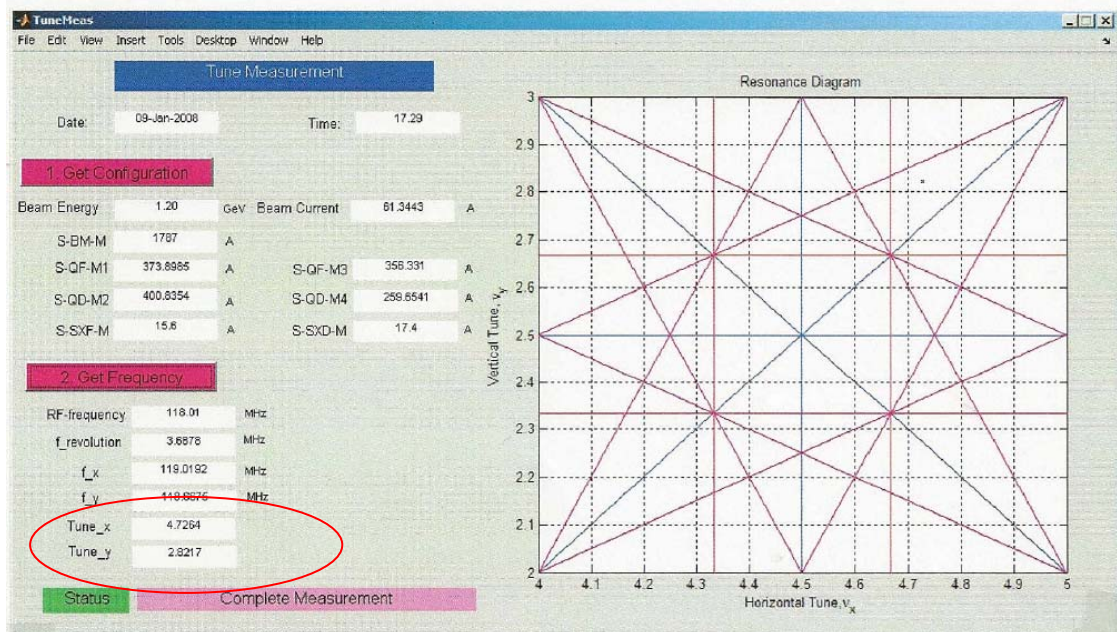


Figure 5.21 The vertical tune shift due to the U60 undulator that is summation of intrinsic field and field error.

Close gap



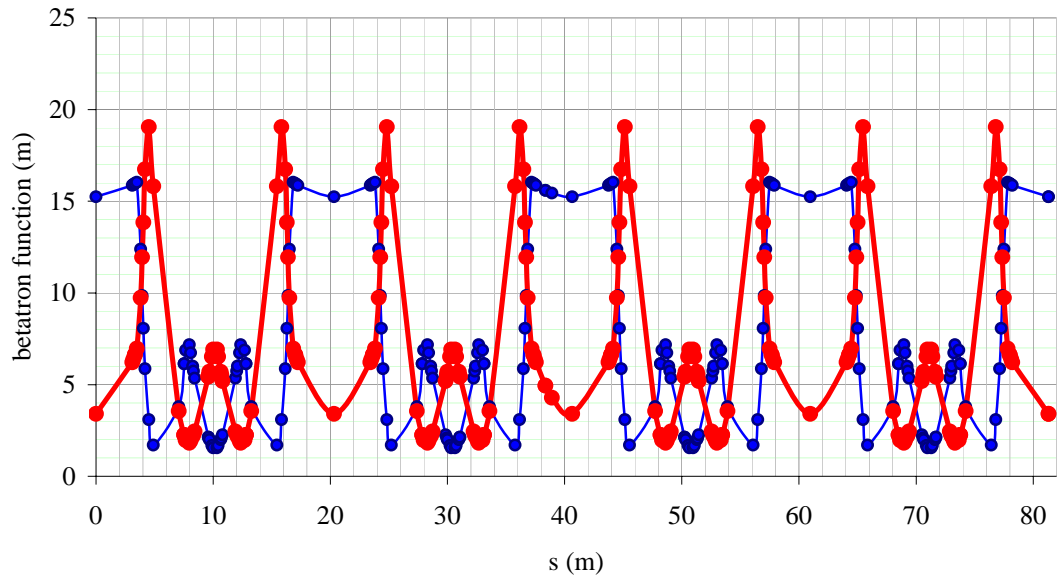
Open gap



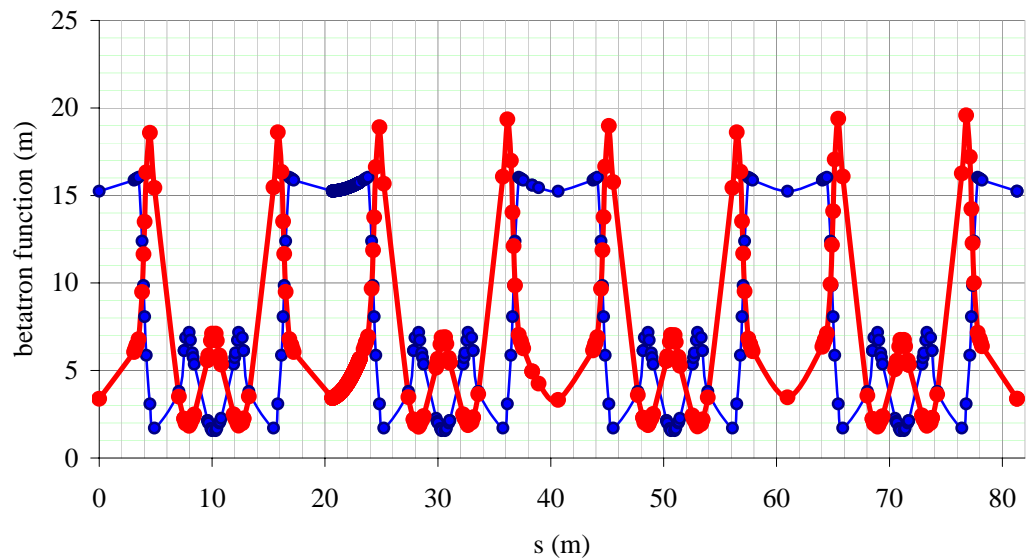
(a)

(b)

Figure 5.22 The tunes shift from the measurement when (a) close the undulator gap of 26.5 mm and (b) open the undulator gap, marked by the ellipticities. The device shifts the vertical betatron tune by 0.0064.



(a)



(b)

Figure 5.23 The betatron function of (a) without undulator (b) with the undulator at gap of 26.5 mm. The thin lines are β_x and thick lines are β_y .

5.4 Higher Order perturbations

From the polynomial fits in Equation 5.22, the sextupole components can be calculated from $c = \frac{B_i'' L}{2}$ and shown in Figure 5.24. The largest horizontal sextupole

component is found to be $0.38 \frac{\text{T}}{\text{m}}$ at the undulator gap of 50 mm. The largest vertical

sextupole component is $0.25 \frac{\text{T}}{\text{m}}$, found at the gap of 35 mm. These sextupole

components give the sextupole strength through

$$k_{sex} [\text{m}^{-3}] = \frac{c}{B\rho} \quad (5.21)$$

The obtained sextupole strengths are shown in Figure 5.25.

To obtain the effects on the chromaticity, two special sextupoles are constructed at the both ends of the undulator. Strengths of the special sextupoles are obtained by equating the integrated strength to that of the undulator. The strength of each special sextupole can then be found from

$$k_{sp} = \frac{k_{sex} l_{und}}{2l_{sp}}, \quad (5.22)$$

where l_{sp} is special sextupole length, 0.01 m, l_{und} is the U60 undulator length of

2.5 m and k_{sex} is undulator sextupole strength obtained from Equation (5.21). The

changes of the horizontal chromaticity are obtained by using the horizontal sextupole

strengths and the changes of the vertical chromaticity are obtained by using the

vertical sextupole strengths. The results are shown in Figure 5.26.

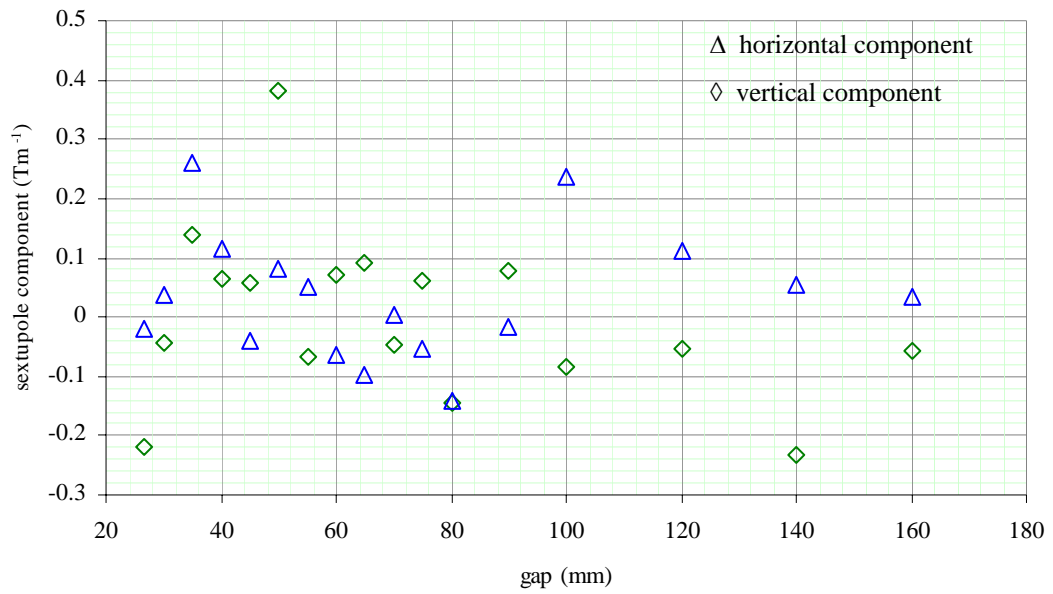


Figure 5.24 The sextupole component as function of the undulator gap.

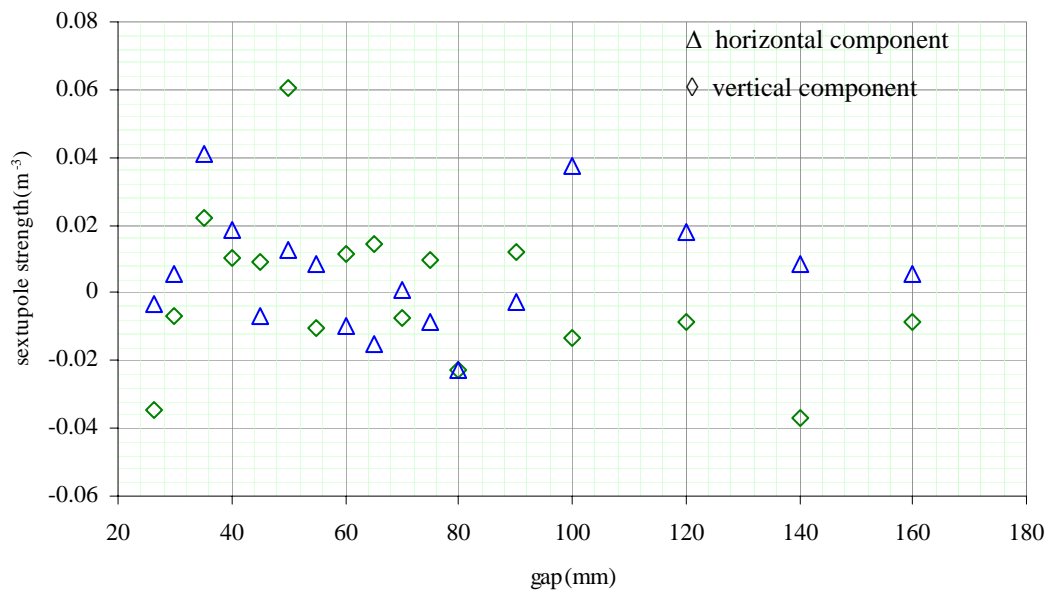


Figure 5.25 The sextupole strength as function of the undulator gap.

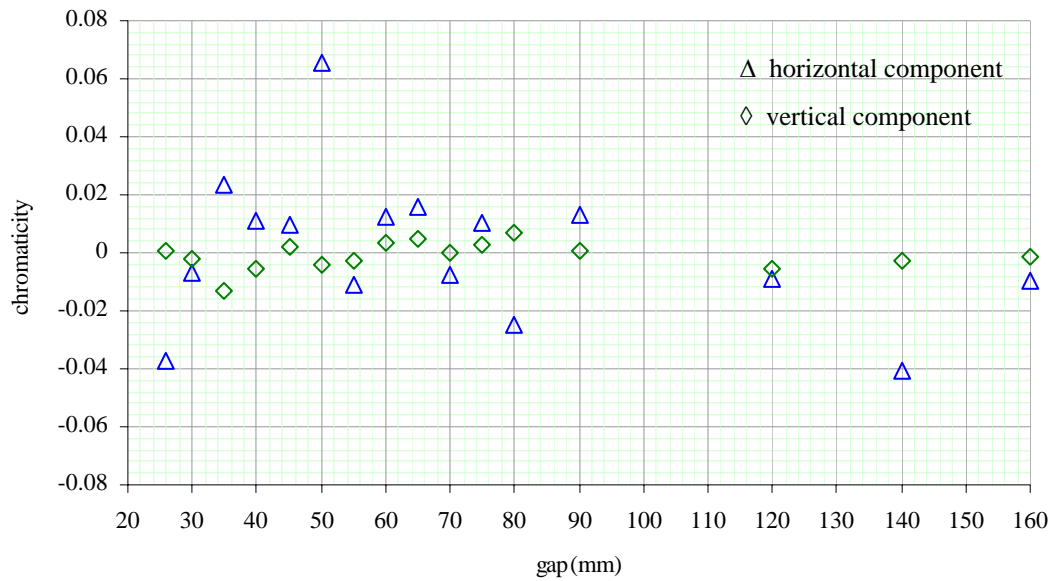


Figure 5.26 Chromaticity due to undulator field error as function of the undulator gap.

The maximum horizontal chromaticity produced at the gap of 50 mm is 0.065 while the vertical chromaticity produced also at the gap of 140 mm is -0.04. These are quite small compared with natural chromaticities.

The next chapter will discuss the compensation method for obtaining the maximum performance on the photon flux and decreasing the effects on the electron beam.

CHAPTER VI

COMPENSATION OF FIELD ERRORS

This chapter discusses the methods to compensate the effects from the previous chapter. These are divided four parts, i.e. the correction of the electron trajectory, the compensation of orbit distortion, the compensation of the tune shift and the chromaticity correction.

6.1 Correction of Trajectory

Moving through the undulator, the electron is gradually kicked out from the undulator axis. To correct the trajectory, the second field integrals calculated from the measured magnetic field, are considered. The quadratic component of the second field integral are evaluated by making the polynomial fits as discussed in the previous chapter. Compensation of the related constant magnetic field component can be achieved by using a long coil.

The long coil field is simulated from two-turns rectangular coils, using a square-shape wire with $2.8 \times 5.0 \text{ mm}^2$ cross-section wounded to have a coil of $160 \times 2520 \text{ mm}^2$ size. The geometries of the coil are shown in Figure 6.1. The coil is assumed to be installed immediately above the undulator vacuum chamber. The

distance of 12.5 mm below the coil which is the vertical center of the undulator, is the position of the evaluated field. The simulation is done by Radia code (Chubar, Elleaume, and Chavanne, 1998) executed in Mathematica version 5.2. The second field integral is then calculated from the obtained field. The quadratic component of the second field integral is then evaluated by fitting the polynomial. By varying the current in the simulation, the various fields and various quadratic components of the second field integral are obtained.

The long coil having the same configuration as the simulated one was constructed. The coil fields are measured by Hall probe scan, illustrated in Figure 6.2. The applied currents to obtain the required field are obtained from the simulation. Examples of the simulated and measured fields are shown in the Figure 6.3a.

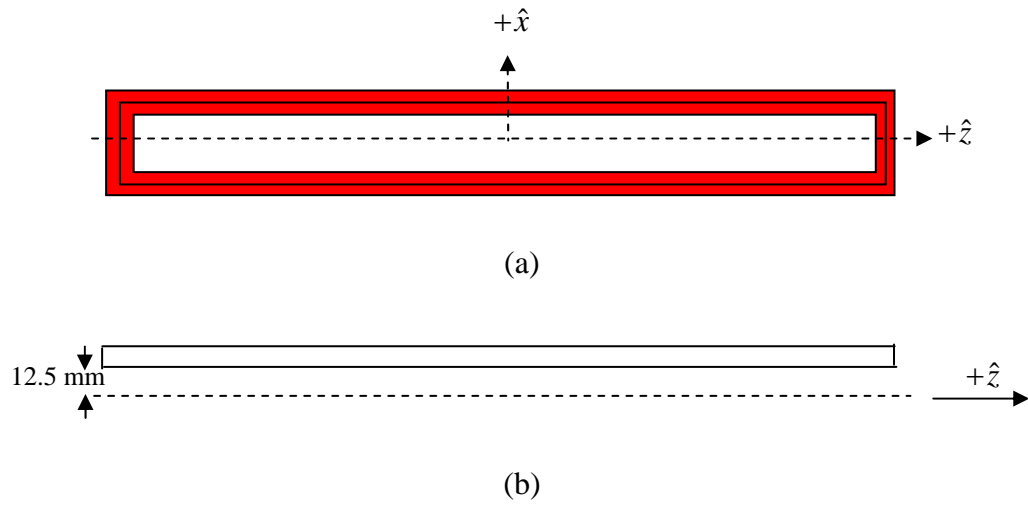


Figure. 6.1 The geometry of the two-turn rectangular coil, (a) top view and (b) side view. The dash line is the position of the evaluated field.

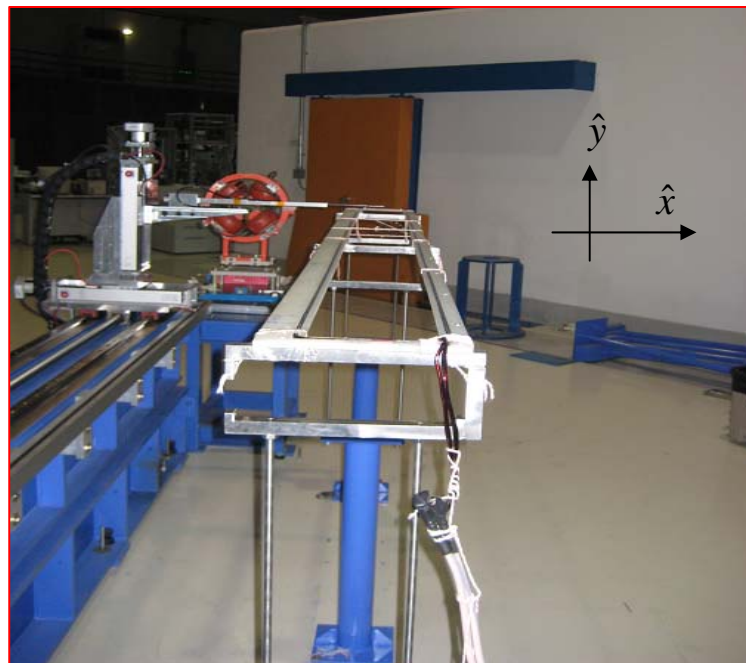
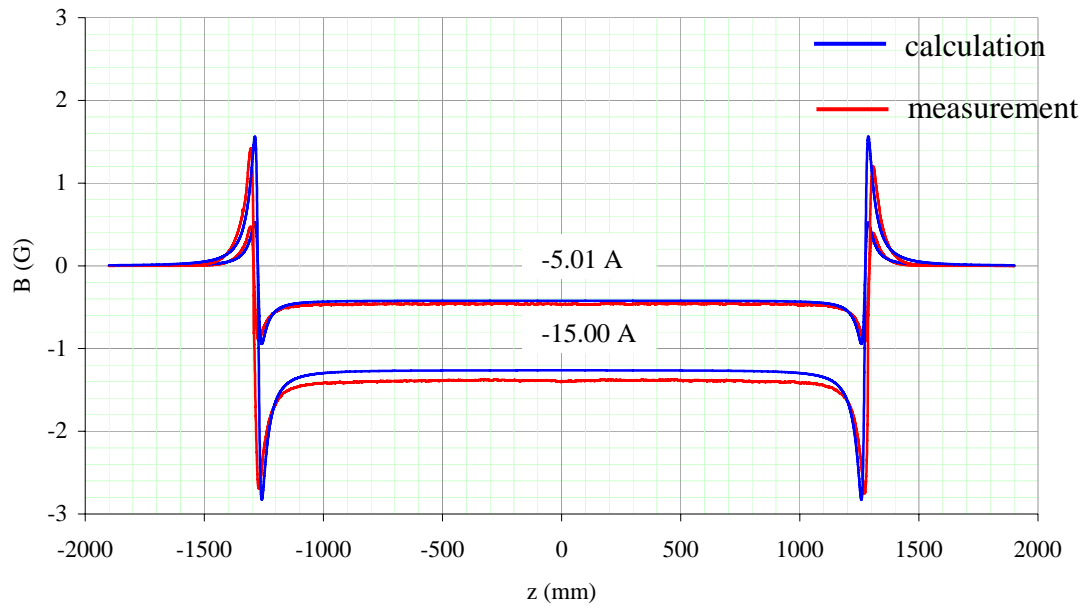
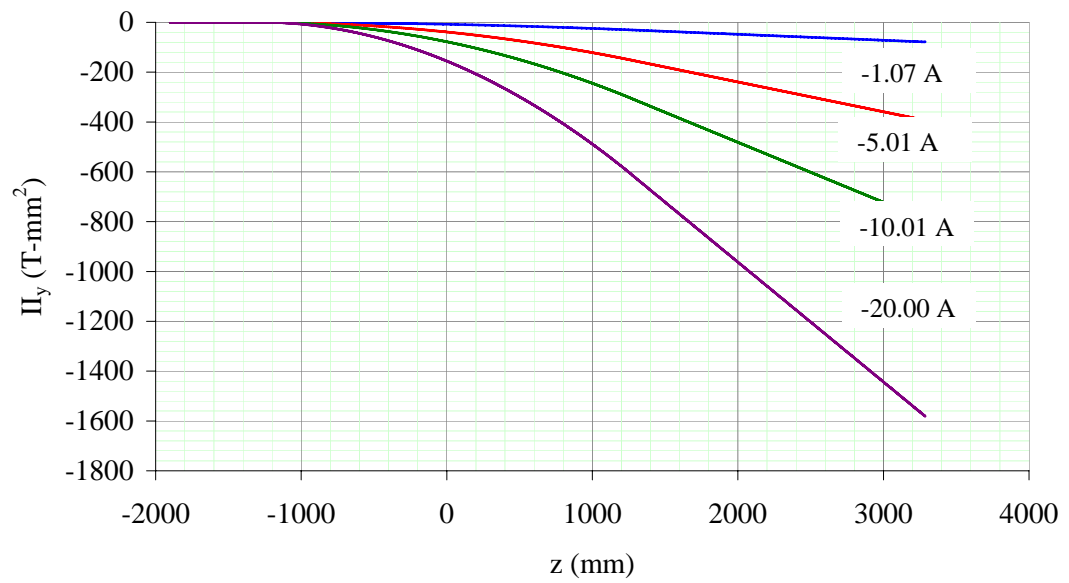


Figure. 6.2 The rectangular coil field measurement by Hall probe scan.



(a)



(b)

Figure. 6.3 (a) Examples of the long coil field and (b) the second field integral calculated from the measured field at various applied currents.

By using the measured field, the second field integrals are then calculated. The examples of the obtained results are shown in the Figure 6.3b. By fitting the polynomial up to quadratic term of these second field integrals, the various quadratic components are then obtained. The results are shown in the Figure 6.4. The graphs are also compared with the quadratic components that calculated from the theoretical field. The relations in this graph will be used to correct the electron trajectory.

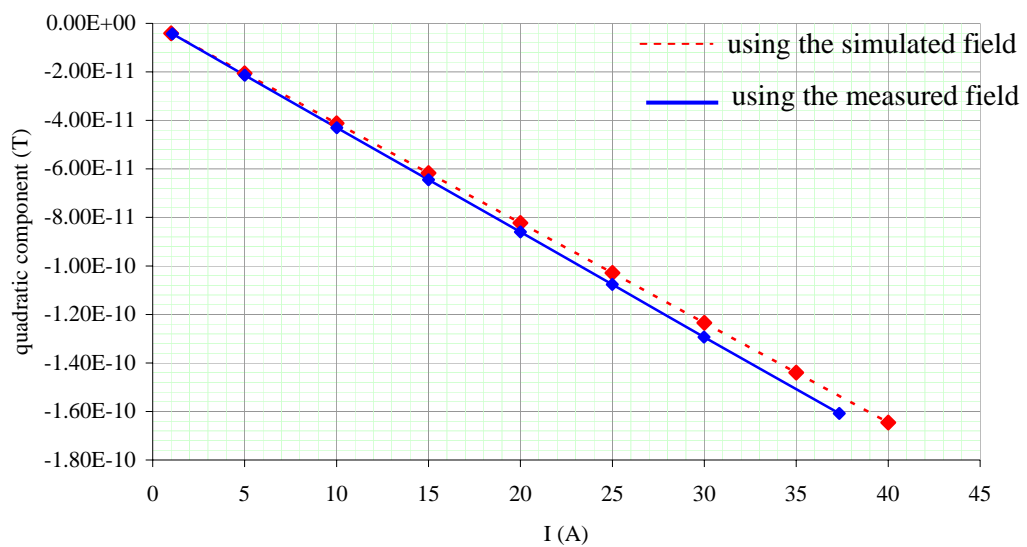


Figure. 6.4 The relation between the quadratic component and the applied current. The dashed line and thin line are respectively obtained from the polynomial fits of the second field integral of the calculated and measured fields.

The electron trajectory compensation will be illustrated. For the actual operation the undulator gap must be opened and closed to obtain the required photon energy.

According to Figure 6.5, the quadratic component can be then evaluated. By using the relation in Figure 6.5 and 6.4, the relation between the applied current and the undulator gap are therefore obtained, shown in Table 6.1 and Figure 6.6.

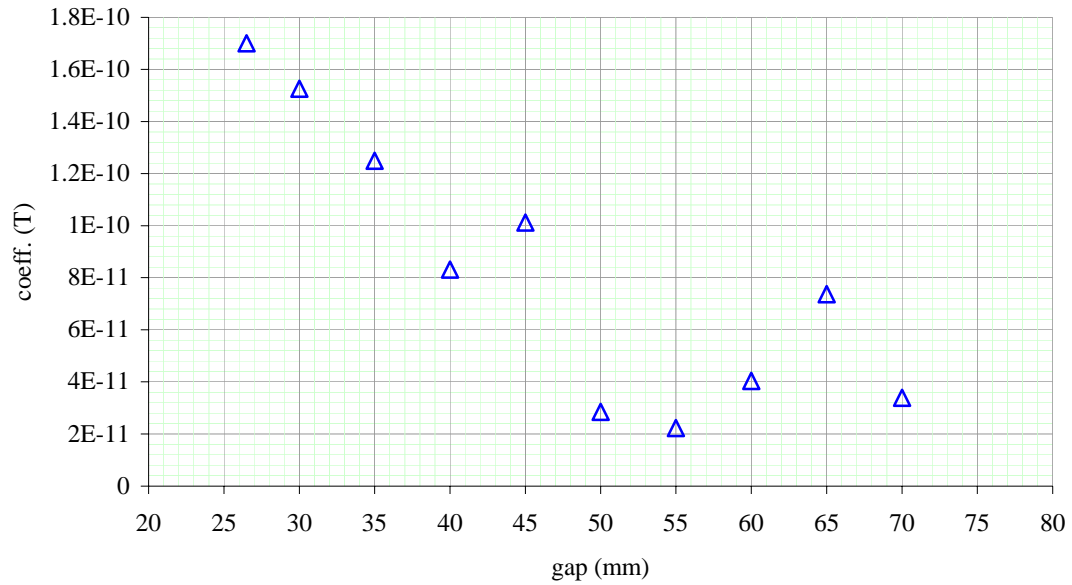


Figure. 6.5 The relation between quadratic component as function of the undulator gap.

Table 6.1 The relation between undulator gap and compensated current for correcting the electron trajectory.

Gap (mm)	Compensated Current (A)
26.5	-44.7067
30	-39.2598
35	-31.1516
40	-19.9254
45	-24.6618
50	-6.5675
55	-5.1067
60	-9.3900
65	-17.5439
70	-7.8543

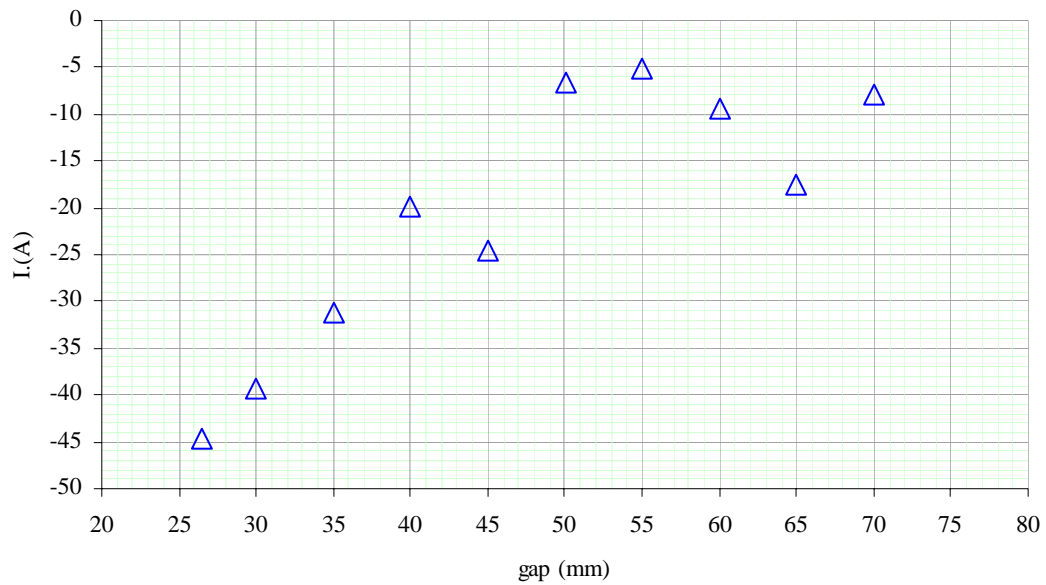


Figure. 6.6 The relation between compensated current and undulator gap for correcting of an electron trajectory.

The graph in Figure 6.6 is used for correcting the electron trajectory. While the gap is opened by users, the electron trajectory must be compensated to improve the photon intensity. This can be done by applying the correlated current to the long coil.

Our next section is how to compensate the electron's angle and position at the exit of the undulator.

6.2 Compensation of Orbit Distortion

We know that the inserting of the U60 undulator will introduce both changes in angle and position of the electron beam. The results were already shown in previous chapter. The orbit distortions are compensated by means of the corrector

magnets located at both ends of the U60 undulator, shown in Figure 6.7. Both the corrector magnets C_1 and C_2 function as a vertical and horizontal corrector magnet.

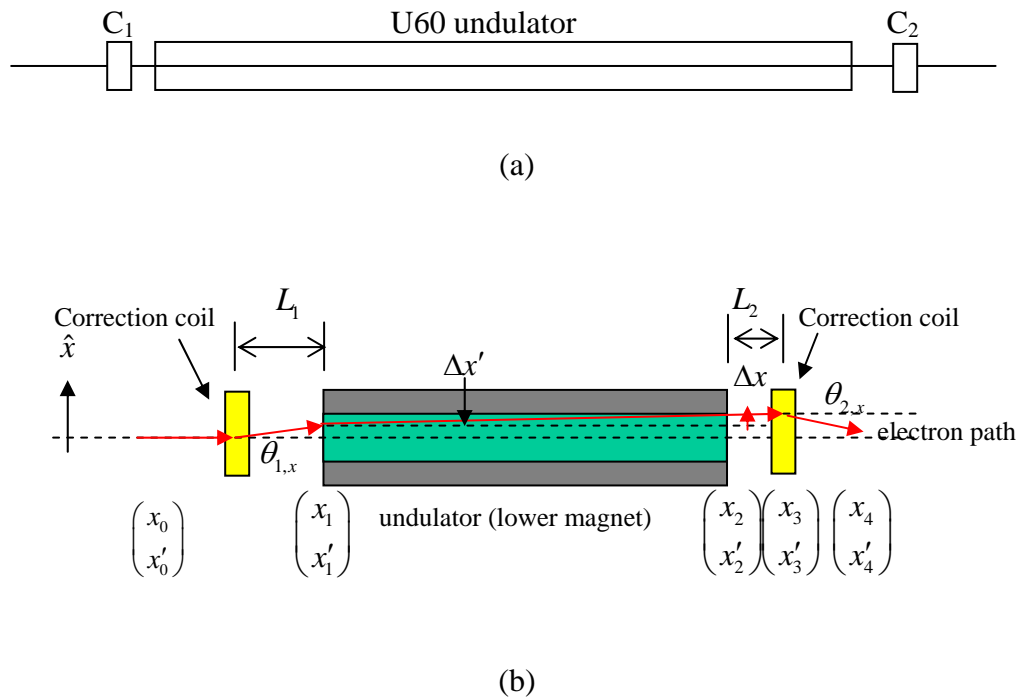


Figure. 6.7 (a) The layout of the corrector magnet (C_1 , C_2) in the U60 undulator straight section. (b) The layout for the deviated angle and position of the electron (top view).

The deviated angle and position of the electron shown in the previous chapter are used to evaluate the kick angles required for the correction magnets to compensate the orbit. By assuming that an electron moves on ideal orbit into an undulator, after that it exits from the device with the deviated angle of $\Delta x'$ and deviated position Δx , illustrated in Figure 6.7b for horizontal component. Also in vertical component, an electron moves out from the device with the deviated angle $\Delta y'$ and position Δy . The horizontal component will be discussed to illustrate the compensation procedure.

Starting with the electron angle x'_0 and position x_0 , shown in the Figure 6.7(b), before moving into the correction coil that is installed at the entrance of an undulator. When this electron later moves out from the first correction coil, it is acted on to deflect with angle $\theta_{1,x}$. After that, it arrives the undulator with the angle of x'_1 and position of x_1 .

The x'_1 and x_1 are thus obtained in term of x_0 and x'_0 by

$$\begin{aligned}x_1 &= x_0 + \theta_{1,x}.L_1, \\x'_1 &= x'_0 + \theta_{1,x}.\end{aligned}\quad (6.1)$$

Later, it moves into the undulator of length L . After that, it exits the device with the angle $\Delta x'$ and position Δx . At this point, the angle x'_2 and position x_2 are therefore obtained in term of $\Delta x'$ and Δx with:

$$\begin{aligned}x_2 &= x_1 + \Delta x = x_0 + \theta_{1,x}.L_1 + \Delta x, \\x'_2 &= x'_1 + \Delta x' = x'_0 + \theta_{1,x} + \Delta x'.\end{aligned}\quad (6.2)$$

Next, this electron moves to the second corrector coil with the distance L_2 . At this point, the angle x'_3 and x_3 are obtained with:

$$\begin{aligned}x_3 &= x_2 + \Delta x'.L_2 = x_0 + \theta_{1,x}.L_1 + \Delta x + \Delta x'.L_2, \\x'_3 &= x'_2 = x'_0 + \theta_{1,x} + \Delta x'.\end{aligned}\quad (6.3)$$

Finally, this electron moves out from the second correction coil with the angle x'_4 and position x_4 . So, x_4 and x'_4 are respectively obtained with:

$$\begin{aligned}x_4 &= x_3 = x_0 + \theta_{1,x}.L_1 + \Delta x + \Delta x'.L_2, \\x'_4 &= x'_3 + \theta_{2,x} = x'_0 + \theta_{1,x} + \Delta x' + \theta_2.\end{aligned}\quad (6.4)$$

Because we want the angle $x'_4 = x'_0$ and the position $x_4 = x_0$. This means after an electron exits the undulator, it should return exactly to its nominal orbit. Therefore, the required angle for orbit compensation by the correction coils are

$$\theta_{1,x} = -\frac{(\Delta x + \Delta x' \cdot L_2)}{L_1},$$

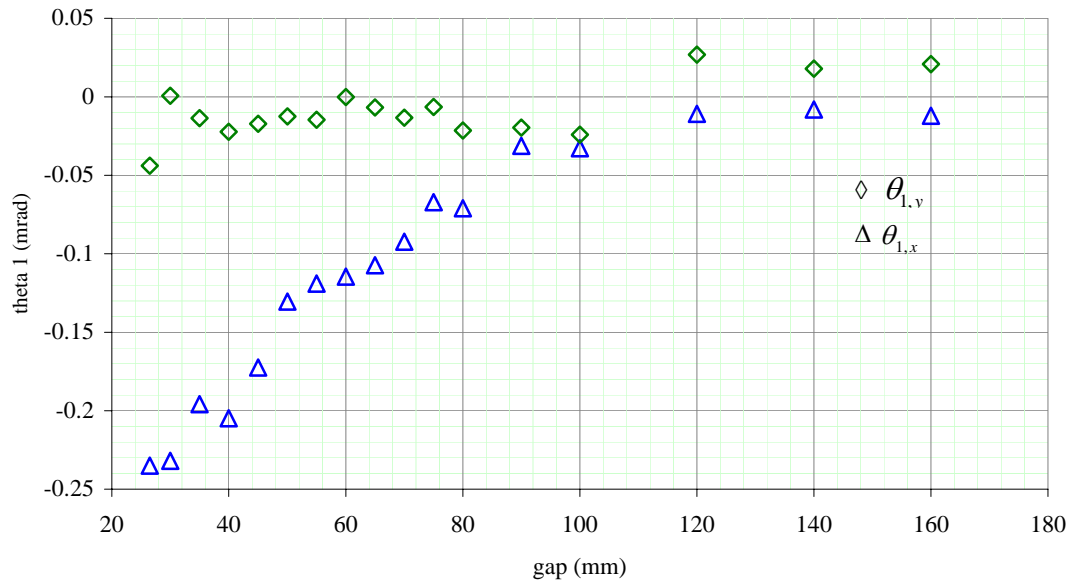
$$\theta_{2,x} = -(\theta_{1,x} + \Delta x'), \quad (6.5)$$

where $\theta_{1,x}$ and $\theta_{2,x}$ are compensated angle by first and second horizontal correction coil, respectively.

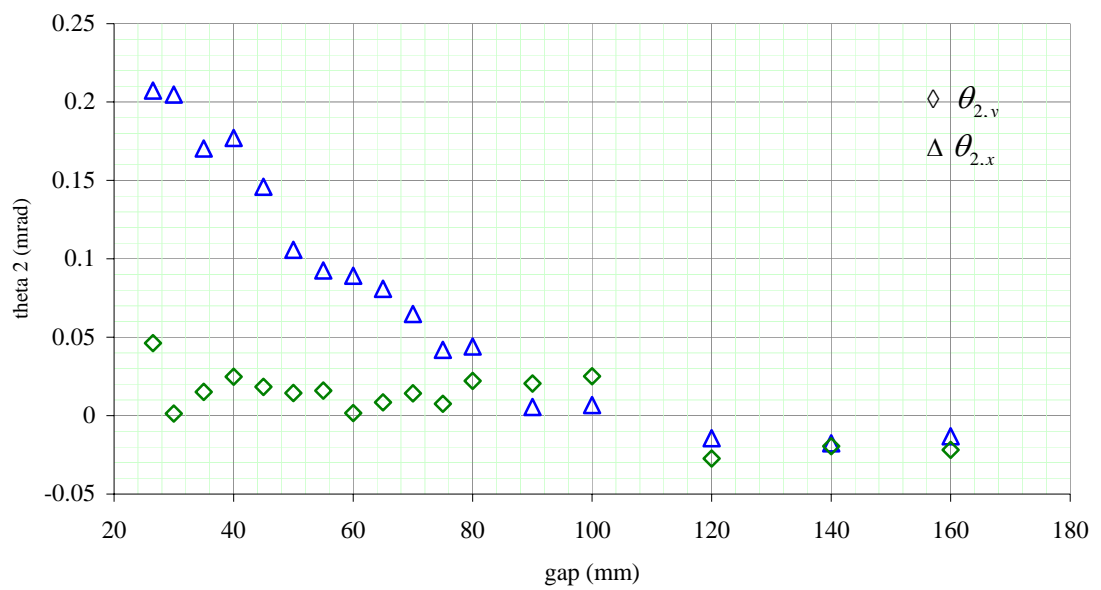
For the horizontal component, by substituting the deviated positions Δx and deviated angles shown in Figure 5.10 and 5.11, the angle $\theta_{1,x}$ and $\theta_{2,x}$ thus can be calculated. The results are shown in Figure 6.8. The angle $\theta_{1,x}$ in Figure 6.8a will be generated by the horizontal corrector magnet C_1 . And the angle $\theta_{2,x}$ in Figure 6.8b will be generated by the horizontal corrector magnet C_2 . In the part of vertical component, the $\Delta y'$ and Δy obtained from the flipping coil are used to calculate the $\theta_{1,y}$ and $\theta_{2,y}$. By substituting $\Delta x'$ with $\Delta y'$ and Δx with Δy in Equation (6.5), the angle $\theta_{1,y}$ and $\theta_{2,y}$ can be calculated. These results are also shown in Figure 6.8. The angle $\theta_{1,y}$ will be generated by the vertical corrector magnet C_1 . Whereas the $\theta_{2,y}$ will be generated by the vertical corrector magnet C_2 . The represented angle θ_y is the angle must be compensated. The field for correcting is given by

$$B_{x,y} = \theta_{y,x} \frac{\left(\frac{P}{e}\right)}{L}, \quad (6.6)$$

where $\frac{P}{e} = B\rho = \frac{E[\text{GeV}]}{0.299}$ is magnetic rigidity and L is corrector magnet effective length. By substituting the obtained θ_x and θ_y in (6.6), the compensated magnetic fields by correction magnet are so obtained. Due to the deviated angle and position are related with the undulator gap. The compensated fields generated by correction magnets as a function of undulator gap are obtained, shown in Figure 6.10. However, to obtain these fields, the current must be applied. By using the relation the $B - I$ curve, measured by Danfysik Inc., the applied currents are therefore calculated. The applied currents for the corrector magnets are shown in Table 6.2, 6.3 and Figure 6.10. Figure 6.10a shows the applied currents for the corrector magnet C_1 , and Figure 6.10b shows the applied currents for the corrector magnet C_2 .

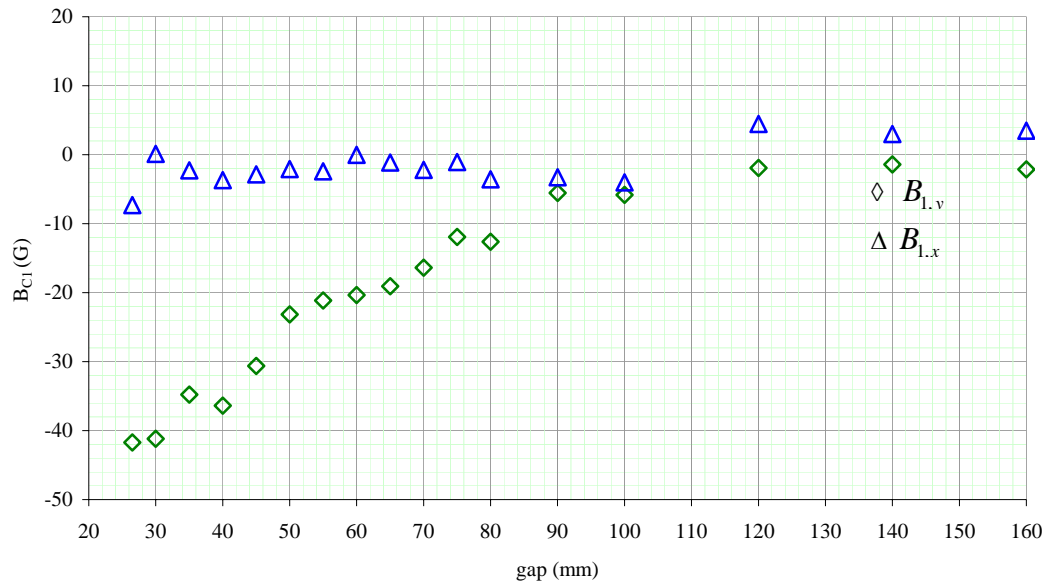


(a)

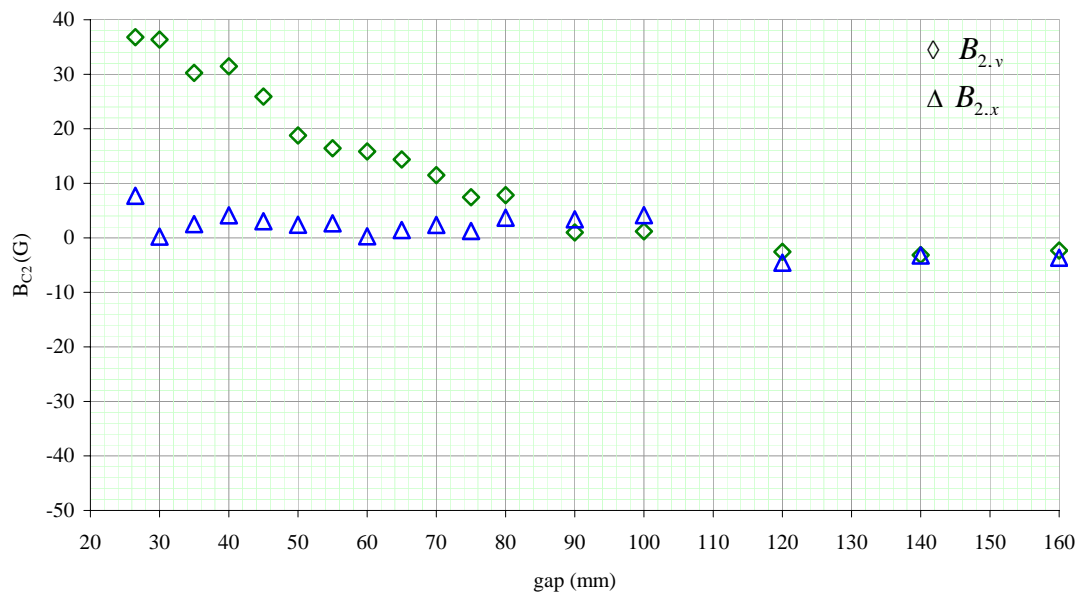


(b)

Figure. 6.8 Deviated angle must be corrected by (a) corrector magnet C_1 and (b) corrector magnet C_2 .



(a)



(b)

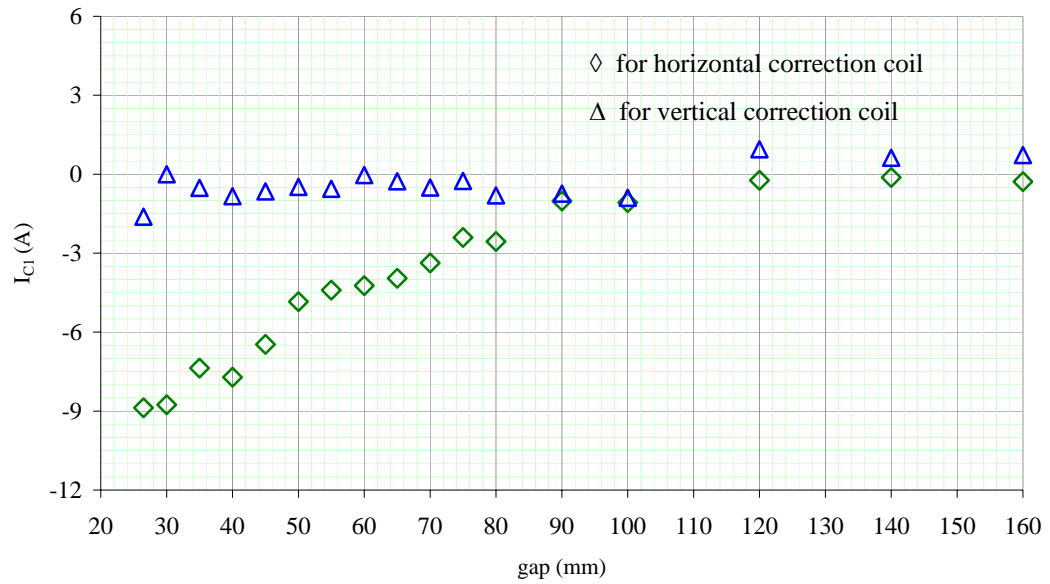
Figure. 6.9 Compensated magnetic field generated by (a) corrector magnet C_1 and (b) corrector magnet C_2 .

Table 6.2 The relation between undulator gap and applied current for vertical correction coil.

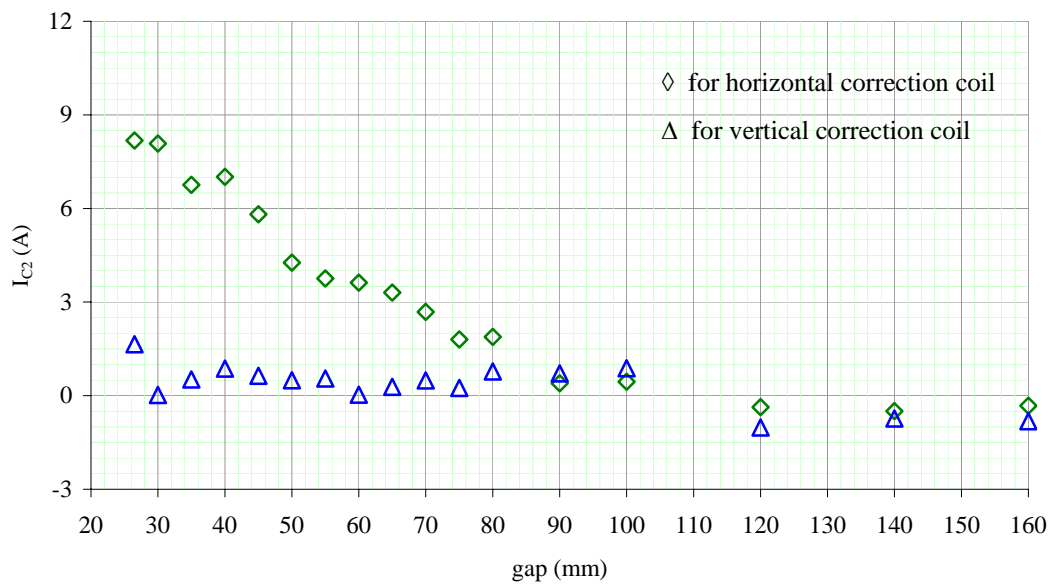
gap (mm)	compensated current for vertical correction coil (A)	
	C ₁	C ₂
26.5	-1.61645839	1.64866174
30	-0.00095064	0.02119849
35	-0.52048841	0.520448152
40	-0.83236095	0.868187176
45	-0.64977175	0.63596455
50	-0.48010668	0.494195638
55	-0.55431274	0.550649602
60	-0.03282433	0.032059495
65	-0.27236708	0.281384008
70	-0.50616279	0.488370433
75	-0.26035438	0.247996333
80	-0.80461352	0.774141093
90	-0.73696487	0.713738193
100	-0.89821151	0.878607715
120	0.94383285	-1.021764981
140	0.62364486	-0.734907457
160	0.72749369	-0.820641897

Table 6.3 The relation between undulator gap and applied current for horizontal correction coil.

gap (mm)	compensated current for horizontal correction coil (A)	
	C ₁	C ₂
26.5	-8.87618491	8.17860785
30	-8.76003618	8.08174382
35	-7.36626351	6.75546762
40	-7.71321161	7.01563454
45	-6.46434219	5.81497689
50	-4.84372658	4.26185775
55	-4.40357855	3.75421325
60	-4.23517841	3.62438252
65	-3.95628097	3.30691567
70	-3.3738585	2.68592379
75	-2.40388856	1.80273502
80	-2.5548127	1.88616269
90	-1.01839411	0.39795587
100	-1.07646949	0.4463889
120	-0.23129799	-0.36985555
140	-0.12379895	-0.4966393
160	-0.27922353	-0.32193001



(a)



(b)

Figure. 6.10 The applied currents of (a) corrector magnet C_1 and (b) corrector magnet C_2 .

The graph in Figure 6.10 is used for correcting the electron orbit distortion. Figure 6.10a and 6.10b are the applied current for correction coil C1 and C2 magnets, respectively. By using undulator gap together with the relation between applied currents and undulator gap in Figure 10, the orbit distortion of electron beam can be compensated.

6.3 Compensation of Tune Shift

The compensation of tune shifts will be discussed in this section. The tune shifts will be compensated by using two pairs of the quadrupole magnets adjacent to the U60 undulator. The quadrupole magnets are the pair of QF12 and QF13 and pair of QD22 and QD23, shown in the Figure 6.11. By simulating with AT, the compensated quadrupole strengths can be calculated. The results are shown in Figure 6.12. The results are summation of intrinsic field and field error. These compensated quadrupole strengths are strength that must be decreased or increased from the original quadrupole strength. The compensated currents corresponding to the strengths can be calculated by using the following equation

$$\Delta I[\text{A}] = \frac{1}{\frac{\Delta g}{\Delta I} \left[\frac{\text{T}}{\text{mA}} \right]} \times B\rho[\text{Tm}] \times \Delta k_q [\text{m}^{-2}], \quad (6.7)$$

where Δk_q is the change of focusing strength of quadrupole magnet, $\frac{\Delta g}{\Delta I}$ are

0.02636807 and -0.02613686 $\frac{\text{T}}{\text{mA}}$ for QF1 and QD2, respectively (Kaewprasert,

2006), $B\rho = \frac{E[\text{GeV}]}{0.29979}$ is the magnetic rigidity. The results are shown in Table 6.3 and

Figure 6.13. The figure consists of the applied current for QF, I_{QF} , and QD, I_{QD} .

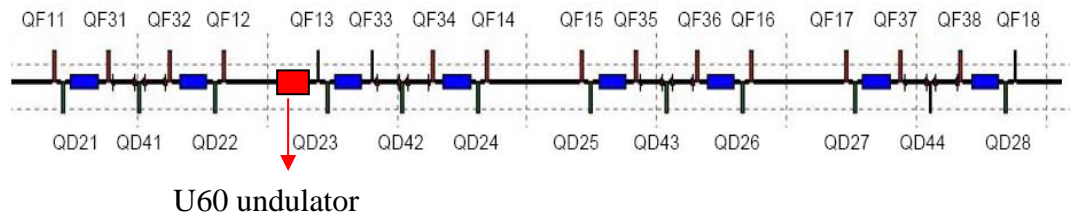


Figure. 6.11 Position of the U60 undulator in the SPS storage ring. It is located between QF12 and QF 13.

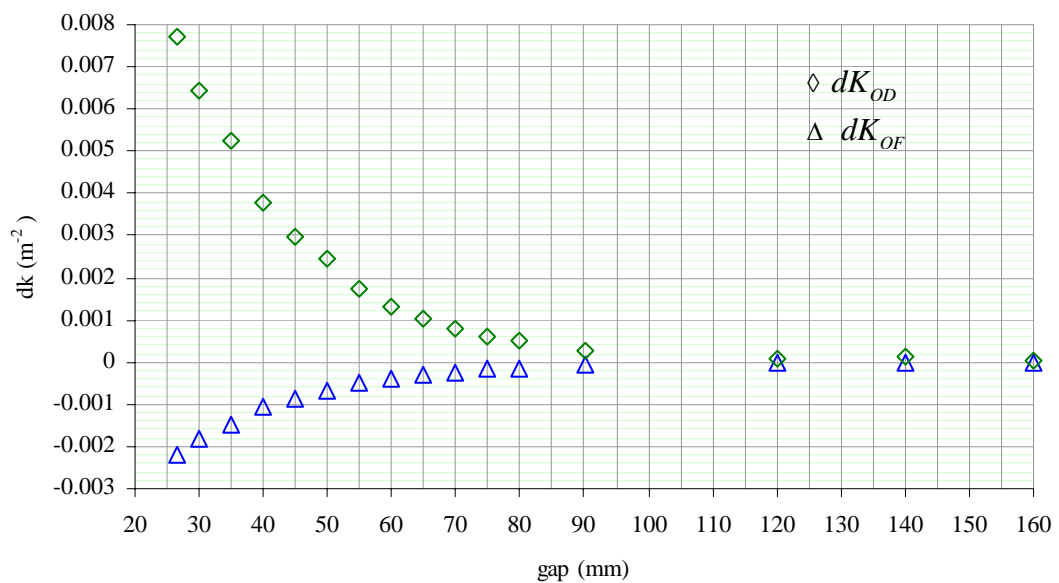


Figure. 6.12 Compensated quadrupole strength as a function of the undulator gap.

Table 6.4 The relation between undulator gap and applied current for tune shifts compensation.

Gap (mm)	Compensated Current (A)	
	QF	QD
26.5	-0.3337	-1.18322
30	-0.27832	-0.98687
35	-0.22711	-0.8053
40	-0.16389	-0.58112
45	-0.128	-0.45389
50	-0.10494	-0.37213
55	-0.07587	-0.26904
60	-0.05691	-0.2018
65	-0.04436	-0.15732
70	-0.0349	-0.12377
75	-0.02682	-0.09513
80	-0.02165	-0.0768
90	-0.0123	-0.04365
120	-0.00425	-0.01511
140	-0.00463	-0.01644
160	-0.00124	-0.00443

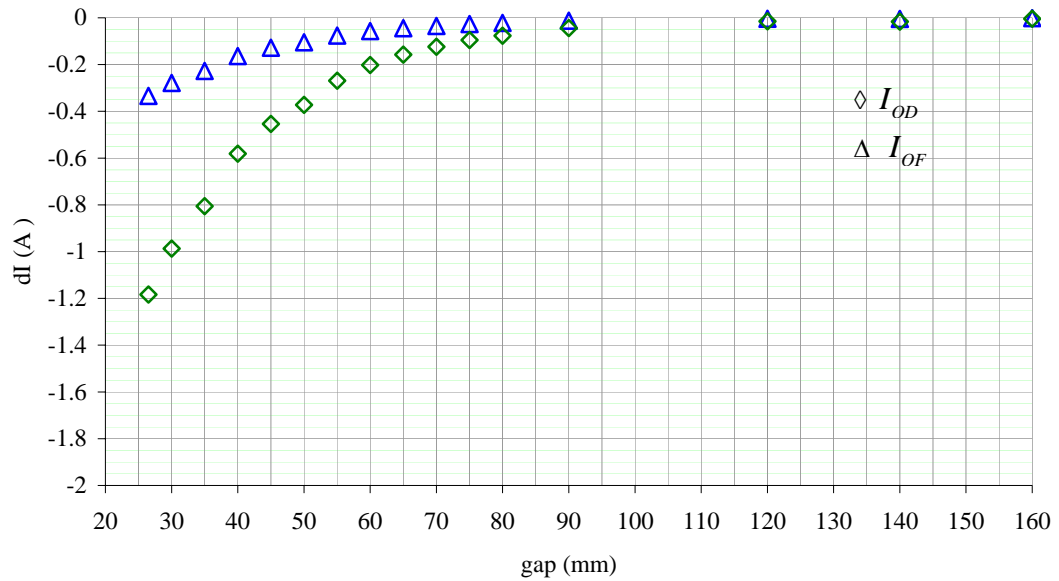


Figure. 6.13 Compensated currents as a function of the undulator gap for compensating tune shifts.

The graph in Figure 6.13 is used for compensating tune shift. By using undulator gap together with the relation between applied currents and undulator gap in Figure 6.13, the tune shift can be therefore compensated. For example of tune shift compensation, when the undulator gap is opened by 26.5 mm. At this gap, the undulator will shift the vertical and horizontal tune by 0.0064 and 1.5×10^{-5} , respectively. From Figure 6.13, the applied currents for compensating so are -0.33 A for the pair of QF magnets and -1.18 A for the pair of QD magnets, respectively. Finally, the betatron tunes will be pulled to the original tunes.

Now, we can compensate the tunes shift by using the pairs of quadrupole magnets adjacent to the U60 undulator, i.e. pair focusing quadrupole magnets (QF12 and QF13) and pair defocusing quadrupole magnets (QD22 and QD23). The tune

shifts are generated from the intrinsic field and field errors. The last we will discuss the chromaticity compensation.

6.4 Correction of Chromaticity

Above section the betatron tunes shift are compensated. This section the compensation of chromaticity will be discussed. The chromaticity perturbed by U60 undulator was already shown in Figure 5.23. The two families of sextupole magnets are required to compensate the chromaticity in both planes. For two sextupole magnets families, the focusing sextupoles S_F having the strength k_F located at s_i and the defocusing sextupoles having the strength k_D located at s_j , where $i, j = 1, 2, 3, \dots, 8$, the chromaticities in both planes are respectively (Dugan, 2002)

$$\xi_x = (\xi_{x,natural} + \xi_{x,undulator}) + \frac{k_F}{4\pi} \beta_x(s_i) \eta_x(s_i) + \frac{k_D}{4\pi} \beta_x(s_j) \eta_x(s_j), \quad (6.8)$$

and

$$\xi_y = (\xi_{y,natural} + \xi_{y,undulator}) + \frac{k_F}{4\pi} \beta_y(s_i) \eta_y(s_i) + \frac{k_D}{4\pi} \beta_y(s_j) \eta_y(s_j). \quad (6.9)$$

In Eq. (6.15) and (6.16), $\xi_{natural}$ is the natural chromaticity, $\xi_{undulator}$ is the chromaticity due to the U60 undulator, $\beta(s_i)$ is the betatron function located at s_i and $\eta(s_i)$ is the dispersion function located at s_i . To get zero total of chromaticities in Equation (6.10) and (6.11), we need to evaluate the sextupole strengths of k_F and k_D . By substituting the $\xi_{undulator}$ and programming with the AT, the k_F and k_D can be evaluated. The results are shown in Figure 6.14. Later, the applied sextupole currents will be

calculated to obtain the compensated sextupole strength. These calculating can be done by using the relation of

$$\Delta I = \frac{2 * B \rho * k_{sex}}{\frac{\Delta g'}{\Delta I}}, \quad (6.10)$$

where the slope $\frac{\Delta g'}{\Delta I}$ of the focusing sextupole and defocusing are 5.4733 and -5.4885

$\frac{T}{m^2 A}$, respectively (Kaewprasert, 2006). The results are shown in Table 6.5 and

Figure 6.15.

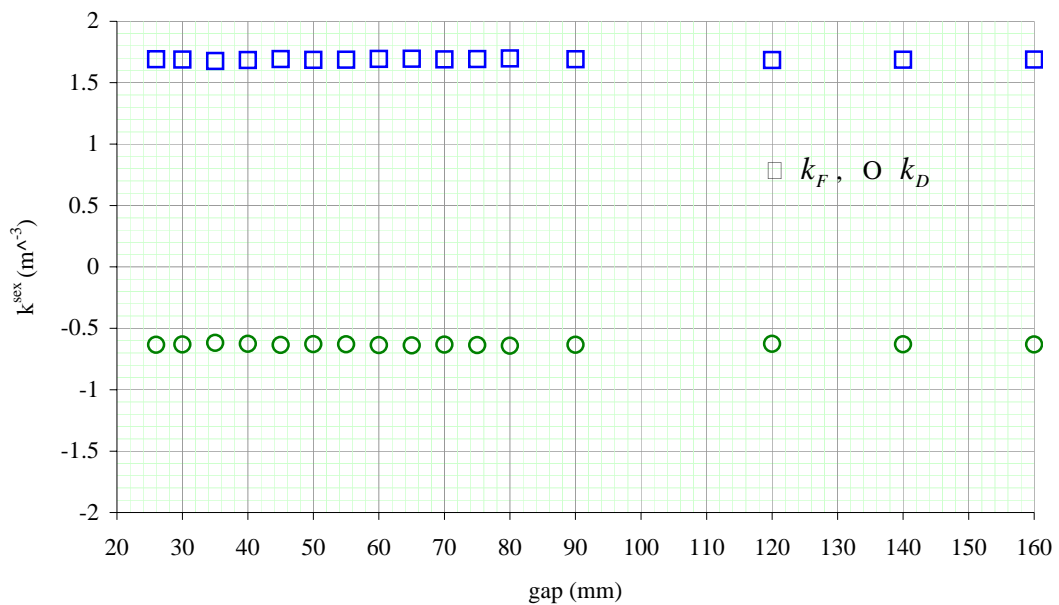


Figure. 6.14 The required sextupole strength as function of the undulator gap.

Table 6.5 The relation between undulator gap and applied current for chromaticities compensation.

gap (mm)	compensated Current (A)	
	SF	SD
26.5	2.4726	0.92373
30	2.4685	0.91894
35	2.4523	0.89988
40	2.4627	0.91203
45	2.4742	0.92555
50	2.4653	0.91511
55	2.4673	0.91747
60	2.4758	0.92745
65	2.4782	0.93033
70	2.4709	0.92169
75	2.4751	0.92666
80	2.4815	0.93431
90	2.4723	0.92343
120	2.4629	0.91232
140	2.4672	0.91734
160	2.4687	0.91911

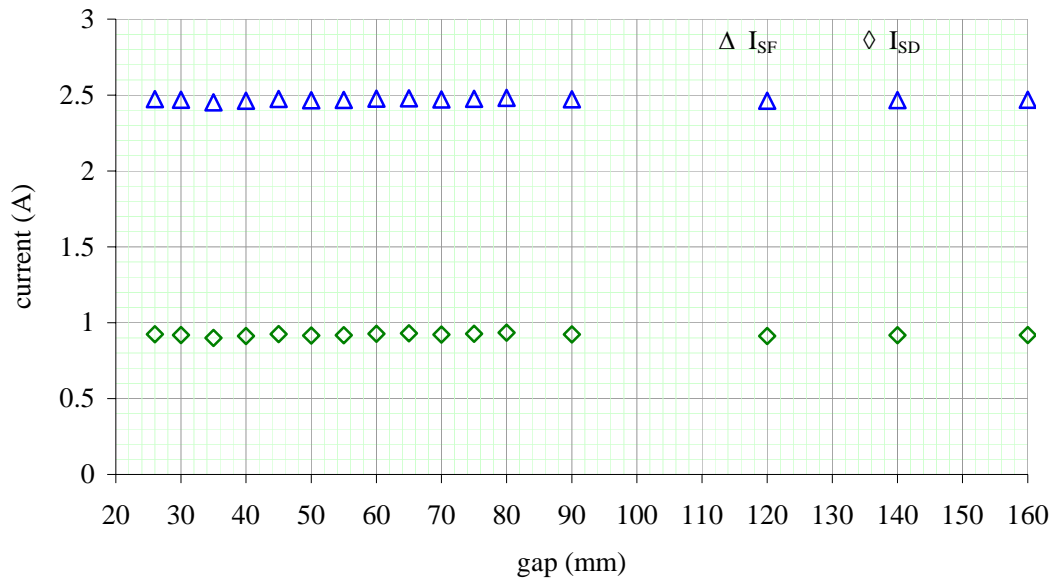


Figure. 6.15 The compensated current as function of the undulator gap. (a) SF and (b) SD magnets.

The graph in Figure 6.15 is used for compensating chromaticity. I_{SF} and I_{SD} are the applied current for SF and SD magnets, respectively. By using undulator gap together with the relation between applied currents and undulator gap in Figure 6.15, the chromaticity can be therefore compensated.

Finally, these compensations will restore the electron beam in the SPS storage ring to the conditions without the U60 undulator.

CHAPTER VII

CONCLUSIONS

The following conclusions have been reached during the course of this thesis work.

7.1 Results of the undulator magnetic field and analysis

By measuring the undulator magnetic field and analysis, we obtained the following results.

- The characterization of U60 undulator magnetic field by Hall probe scanning, the magnetic field mapping at various undulator gaps were obtained. The obtained magnetic fields are sinusoidal field consisting of 81 full poles each of approximately 30 mm length. The maximum peak magnetic field obtained at the minimum gap of 26.5 mm is 0.55 T. This field gives the photon energy at the 1st harmonic of 39.81 eV .
- The magnetic fields were used to calculate tune shifts by using AT and analytical calculation. The maximum tune shifts obtained at 26.5 mm of undulator gap, the first method gives 0.004, whereas the analytical calculation gives 0.0066 whereas the experiment gives 0.0065.
- The magnetic fields were also used to predict the performance of the undulator radiation by using the phase error of the magnetic fields. At the

- gap of 26.5 mm, the phase error is 2.12° . The predicted photon flux intensity is 99.86%, compared with the ideal device.
- Moreover, the magnetic fields were used to calculate the trajectories and angle of electron throughout the undulator. The results show that the electron is gradually kicked out from the on-axis throughout the undulator. Eventually, it moves out from the undulator with the deviated angle and position, compared with the angle and position before moving into the device.
- The field integrals were measured by the flipping coil. The on-axis first and second field integrals were obtained. At the gap of 26.5 mm, the vertical and horizontal deviated angle are respectively -0.0024 and 0.028 mrad. The vertical and horizontal deviated positions are respectively 8.81 and $39.09 \mu\text{m}$. The field integral for $|x| \leq 25$ mm were also measured to obtain the multipole components. At the gap of 26.5 mm, we found that the horizontal and vertical dipole field at the gap of 26.5 mm are respectively -9.6×10^{-6} and 1.11×10^{-4} Tm. The horizontal and vertical quadrupole field are respectively 2.77×10^{-4} T and -2.23×10^{-4} T. The horizontal and vertical sextupole field are respectively -0.02 and $-0.22 \frac{\text{T}}{\text{m}}$.
- At the gap of 26.5 mm, we found that the vertical and horizontal tune shifts due to field error are respectively 1.61×10^{-5} and 6.77×10^{-5} .
- At the gap of 26.5 mm, we found that the vertical and horizontal chromaticities due to sextupole field error are respectively 0.001 and -0.036 .

7.2 Compensation scheme

The compensation schemes, we found the following results.

- The electron trajectory will be compensated by dipole field, generated by a long coil system.
- The deviated angle and position of an electron beam at the exit of the device will be compensated by means of the correction magnets located at both ends of the U60 undulator.
- Tune shifts due to intrinsic field will compensate by the local quadrupole magnets, consisting of the pair of QF12 and QF13 and pair of QD22 and QD23. The tune shift, obtained from analytical calculation, will be used for compensating.
- Tune shifts due to magnetic field errors, obtained from the flipping coil, will be also compensated by the local quadrupole magnets.
- Chromaticity due to magnetic field errors will be also compensated by the two families sextupole magnets in the ring.

REFERENCES

REFERENCES

- Alp, E. E., and Viccaro, P. J. (1988). The effect of random field errors on the radiation spectra of selected APS undulators. **Nucl. Instr. and Meth. A** 266: 116-119.
- Bassetti, M., Cattoni, A., Luccio, A., Preger, M., and Tazzari, S. (1977). A transverse wiggler magnet for ADONE, **Laboratori Nazionali Frascati Technical Notes LNF-77/26(R)**.
- Bobbs, B. L., Rakowsky, G., Kennedy, P., Cover, R.A., and Slater, D. (1990). In search of a meaningful field-error specification for wiggler. **Nucl. Instr. and Meth. A** 296: 574-578.
- Borovikov, V., *et al.* (1998). Proposal of superconducting 7 Tesla wiggler for LSU-CAMD. **Nucl. Instr. and Meth. A** 405: 208-213.
- Chubar, O., Elleaume, P., and Chavanne, J., (1998). A three-dimensional magnetostatics computer code for insertion devices. **J. Synchrotron Rad.** 5: 481-484.
- Dasri, T., Siriwattanapaitoon, S., Chachai, W., and Rugmai, S. (2007). Characterization of soft X-ray undulator for the Siam Photon Source. **Nucl. Instr. and Meth. A** 582: 40-42.
- Duke, P. J. (2000). **Synchrotron Radiation Production and Properties** (1st ed.). Oxford University Press.

- Dejus, J. R., Vasserman, I., Moog, R. E., and Gluskin, E. (1994). Phase errors and predicted spectral performance of a prototype undulator. **Rev. Sci. Instrum.** 66: 1875-1878.
- Diviacco, B., and Walker, R. P. (1996). Recent advances in undulator performance optimization. **Nucl. Instr. and Meth. A** 368: 522-532.
- Diviacco, B., and Walker, R. P. (1998). Phase variation in a segmented undulator. **ST/M-88/9**.
- Dugan, G. (2002). Introduction to Accelerator Physics: Lecture 8. **USPAS Jan 2002 Accelerator school Phys 450B**.
- Elleaume, P. (1991). Insertion device for the new generation of synchrotron source: A review. **Rev. Sci. Instrum.** 63: 321-326.
- Isoyama, G. (1989). Simulation of a magnetic field correction scheme for Halbach-type undulator. **Rev. Sci. Instrum.** 60: 1826-1829.
- Jacob, J. M. (1982). **Applications & Design with Analog Integrated Circuits** (1st ed.). US: Reston.
- Kaewprasert, C. (2006). Measurement of the chromaticity for the beam service configuration 1.2 GeV. **NSRC-TN-2006-1**.
- Kaewprasert, C. (2006). Local betatron and dispersion function. **NSRC-TN-2006-2**.
- Kim, D. E., *et al.* (2001). 6 cm period Apple-II type elliptically polarized undulator at PLS. **Nucl. Instr. and Meth. A.** 467-468: 157-160.
- Kincaid, B. M. (1985). Random errors in undulators and their effects on radiation spectrum. **J. Opt. Soc. Am. B** 2: 1294-1306.
- Kincaid, B. M. (1990). Analysis of field errors in existing undulators. **Nucl. Instr. and Meth. A** 291: 363-370.

- Klysubun, P., Rugmai, S., Klysubun, W., and Prawatsri, P. (2007). A 6.4 superconducting wavelength of hard X-rays at the Siam Photon Source. **Nucl. Instr. and Meth. A.** 582: 47-50.
- Krinsky, S. (1980). An undulator for the 700 MeV VUV-ring of the national synchrotron light source. **Nucl. Instr. and Meth.** 172: 73-76.
- Khruschev, S. V., *et al.* (2007). Superconducting 63-pole 2T wiggler for Canadian light source. **Nucl. Instr. and Meth. A.** 575: 38-41.
- Mezentsev, N. A. (2005). Survey of superconducting insertion devices for light source. In **Proceeding of Particle Accelerator Conference** (pp 256-260).
- Marechal, X. M., *et al.* (1990). Magnetic field generated by parallelepiped permanent magnet block. **European Synchrotron Radiation Facility Technical Notes ESRF-SR/ID-90-37.**
- Ortega, J. M., *et al.* (1983). Realization of the permanent magnet undulator NOEL. **Nucl. Instr. and Meth.** 206: 281-288.
- Prawanta, S., (2007). Sextupole magnet with current rating of 20 amperes for the Siam Photon Source. **M. Sc. Dissertation**, Suranaree University of Technology, Thailand.
- Rugmai, S., *et al.* (2007). Soft X-ray undulator for the Siam photon source. **Synchrotron Radiation Instrumentation: Ninth International Conference.** CP879: 335-338.
- Rugmai, S. (2004). Magnetic simulation of 6.4 T wavelength shifter from MAX-lab and its effects on the SPS. **NSRC-TN-2004/05.**
- Rugmai, S. (2005). Effects of high field permanent magnet insertion device on the Siam photon source storage ring. **ScienceAsia** 31: 159-165.

- Sasaki, S. (1994). Analyses for a planar variably-polarizing undulator. **Nucl. Instr. and Meth. A** 347: 83-86.
- Shih, C. C., and Coponi, M. Z. (1982). Theory of multicomponent wiggler free electron lasers in the small regime. **Phys. Rev. A** 26: 438-448.
- Suller, V. P. (1980). The interaction of wigglers and undulators with stored electron beam. **Nucl. Instr. and Meth.** 172: 39-44.
- Schwinger, J. (1949). On the classical radiation of accelerated electrons. **Phys. Rev.** 75: 1912-1925.
- Tanaka, T., *et al.* (2001). SPECTRA: a synchrotron radiation calculation code. **J. Synchrotron Rad.** 8: 1221-1228.
- Terebilo, A., (2001). Accelerator Toolbox for MATLAB. **SLAC-PUB-8732**.
- Wallen, E., LeBlanc, G., Eriksson, M. (2001). The MAX-Wiggler wiggler, a cold bore superconducting wiggler with 47 3.5 T poles. **Nucl. Instr. and Meth. A** 467-468: 118-121.
- Walker, R. P. (1993). Interference effects in undulator and wiggler radiation source. **Nucl. Instr. and Meth. A** 335: 328-337.
- Walker, R. P., and Diviacco, B. (1994). Initial operation devices in Elettra. **Rev. Sci. Instrum.** 66: 2708-2712.
- Walker, R. P., (1995). Wigglers. **CERN Accelerator School Proceeding**: 807-835.
- Wiedemann, H. (1995). **Particle Accelerator Physics II Nonlinear and higher-order beam dynamics** (1st ed.). Springer-Verlag Berlin Heidelberg.
- Winick, H., J. (1994). **Synchrotron Radiation Source A Primer** (1st ed.). World Scientific Publishing Co. Pte. Ltd.

Winick, H., and Helm, R. H. (1978). Standard wiggler magnet. **Nucl. Instr. and Meth.** 152: 9-15.

Yonehara, H., Kasuga, T., Hasumoto, M., and Kinoshita, T. (1989). Orbit distortion due to UVSOR wiggler. **Rev. Sci. Instrum.** 60: 1849-1850.

APPENDIX

Soft x-ray undulator for the Siam Photon Source

S. Rugmai ^{a,b}, T. Dasri ^b, S. Prawanta ^a, S. Siriwattanapaitoon ^a, A. Kwankasem ^a, V. Sooksrimuang ^a, W. Chachai ^a, N. Suradet ^a, N. Juthong ^a and S. Tancharakorn ^a

^a National Synchrotron Research Center, P.O. Box 93, Nakhon Ratchasima, 30000, Thailand.

^b School of Physics, Suranaree University of Technology, 111 University Avenue, Muang District, Nakhon Ratchasima, 30000, Thailand.

Abstract. An undulator for production of intense soft x-rays has been designed for the Siam Photon Source. The construction of the undulator has been completed. It is now being characterized and prepared for installation. The device, named U60, is a pure permanent magnet planar undulator, consisting of 41 magnetic periods, with 60 mm period length. Utilization of the undulator radiation in the photon energy range of 30 - 900 eV is expected. The design studies of the magnetic structure, including investigation of perturbations arising from the magnetic field of the device, their effects on the SPS storage ring and compensation schemes are described. A magnetic measurement system has been constructed for magnetic characterization of the device. Partial results of magnetic measurements are presented.

Keywords: Insertion Device, Undulator, Soft X-rays

PACS: 07.85.Qe

INTRODUCTION

The U60 is a permanent magnet planar undulator containing 41 magnetic periods, with 60 mm period length. The total length of the undulator was designed to be 2500 mm, which will occupy approximately half the space in one of the straight sections. The undulator was constructed by Danfysik, and now being characterized and prepared for installation at the Siam Photon Laboratory. The device was designed to generate intense photons for soft x-ray beamline. The magnetic structure was designed to give the minimum photon energy of 28 eV at 1.0 GeV beam energy, or 40 eV at 1.2 GeV beam energy. Utilization of up to 900 eV photons from the 7th harmonic, at 1.2 GeV beam energy, is expected. The undulator minimum gap was decided to be 26 mm. This will give comfortable space of 24 mm for the vertical size of the vacuum chamber. A stainless steel chamber with 2 mm thick will then give vertical aperture of 20 mm for the electron beam.

MAGNETIC SIMULATION

In order to obtain the specified minimum photon energy the magnetic designs require the maximum wiggler strength of $K = 3.05$. This corresponds to the peak magnetic field of at least 0.54 Tesla at the undulator minimum gap. In order to determine the size of magnet blocks which gives the required peak magnetic field, we assume the rectangular magnet blocks. With this assumption the generated magnetic field can be given analytically [1]. Minimum width and height of the magnet blocks which give the required undulator peak magnetic field can then be determined. A FORTRAN code to simulate undulator magnetic field from arrays of rectangular magnet blocks arranged in Halbach configuration, based on the above analytical expressions, was written to carry out the design calculations. The code is equipped with an option to include random errors for magnetization direction and amplitude of each magnet block. Simulations by the code Radia [2] were also performed and gave similar results.

NdFeB was chosen for magnet material. Practical remanent field of 1.25 Tesla is assumed in the calculations. The magnet block size of around 95 mm in width and 40 mm in height is obtained from the simulations. Apart from giving the required peak magnetic field from the undulator, the obtained size also gives small field roll-off of 0.09%

at the transverse position of $x = \pm 5$ mm. This value is expected to be small enough to ensure negligible effects on the electron beam.

The calculated peak magnetic field as a function of undulator gap is shown in Fig. 1. The 900 eV photon of the 7th harmonic radiation corresponds to the undulator peak magnetic field of 0.12 Tesla, obtained at the undulator gap of 55 mm. The calculation from an analytical expression of gap-dependent undulator field, after Halbach [2] is also given for comparison.

The magnetic field of the undulator is terminated by end magnets. Sophisticated end structures have been proposed by various laboratories. SPring-8 adopted the end structure design which includes an additional horizontally magnetized block, installed at the distance of half-period from the half-pole end of each magnet array. The size of the additional magnet blocks is optimized to shift the electron trajectory to the undulator magnetic center [4]. Another similar design has been proposed by ESRF. In this design an additional horizontally magnetized block of size approximately 3/20 of the period length is added at each end of the magnet arrays. This modification reduces the field integral variation with gap by a factor of 4 to 5 [5]. By discussion with the manufacturer the ESRF end-structure design has been chosen for the U60, since the manufacturer is familiar with such design. The total length of the constructed device is 2510 mm.

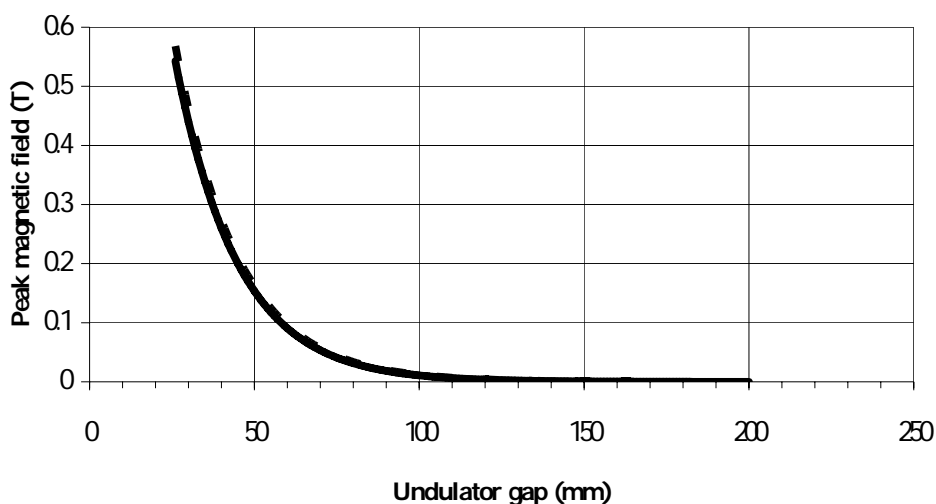


FIGURE 1. Calculated undulator peak magnetic field as a function of undulator magnetic gap (thick blue line). The dotted line is from analytical expression of gap dependent undulator peak magnetic field after Halbach [2], given for comparison.

U60 SPECTRUM CALCULATIONS

Photon spectra of U60 are calculated by the program SPECTRA [6]. The gap-dependent magnetic field input for SPECTRA is simulated by The Fortran code explained above. Magnetization direction and amplitude errors of 2 degrees and 2%, respectively, for each magnet block are included. The calculated peak brilliance of the undulator light is shown in Fig. 2. The calculations are for the operation at 1.2 GeV beam energy with 41 nm-rad emittance.

EFFECTS ON STORAGE RING BEAM DYNAMICS

Effects of U60 on the storage ring beam dynamics are calculated using linear perturbation method [7]. The calculated vertical tune shift from effects of the undulator at the minimum gap is 0.011, and the stop band width of 0.02. The maximum perturbed vertical beta function, β_y , is obtained with $\Delta\beta_y / \beta_y = 0.07$. The perturbations are also studied by constructing an undulator comprising series of hard-edge bending magnets at the magnet pole positions for input to MAD8 [8]. This hard-edge model is to give equivalent focusing property as the sinusoidal magnetic field of the device [9]. Since effects of perturbations are stronger at lower beam energy, the calculations

are carried out for 1.0 GeV beam energy operation. For simplicity the calculations are performed by inserting 42 periods of magnetic structure, in the middle of one of the straight sections of the SPS storage ring. Results from MAD give the vertical tune shift of 0.013. The calculated tune shift is significant and has to be compensated. The compensations can be done by adjusting the quadrupoles in the storage ring. Detailed studies will be carried out when magnetic measurements of the constructed device are completed.

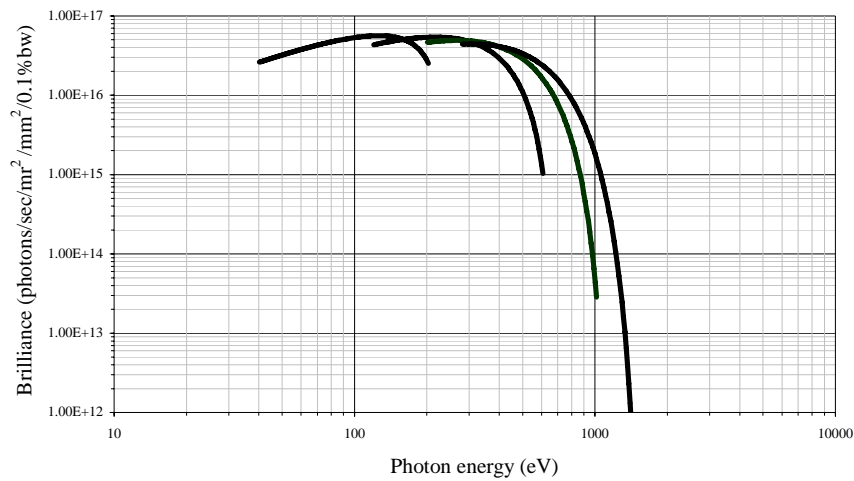


FIGURE 2. Calculated peak brilliance of the undulator radiation, up to the 7th harmonic, for the 1.2 GeV beam energy with 41 nm-rad emittance of the Siam Photon Source.

CHARACTERIZATION OF U60

To prepare for installation, U60 is now being characterized. A magnetic measurement bench has been constructed for the purpose, and also for general magnetic measurements and future insertion device developments. A Hall probe scan system has been completed and a flip coil system for field integral measurements is being constructed. The trajectory calculated from measured magnetic field, using the Hall probe scan, at the undulator minimum gap is shown in Fig. 3.

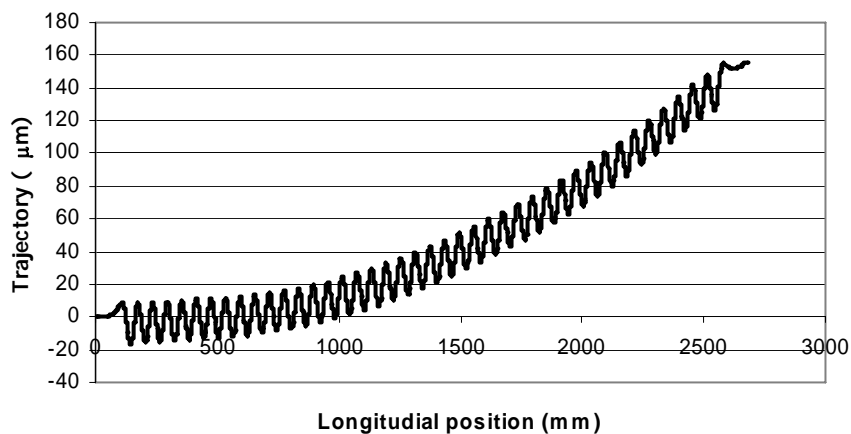


FIGURE 3. Uncompensated electron trajectory inside the undulator, calculated from the measured magnetic field at the minimum gap.

CONCLUSIONS

U60, a pure permanent magnet planar undulator, has been designed and constructed for the soft x-ray beamline at the Siam Photon Laboratory. The 2.5 m length undulator contains 41 periods, with 60 mm period length. Utilization of the undulator radiation in the photon energy range of 40 – 900 eV, for 1.2 GeV beam energy, is expected. Effects of the perturbations to the electron beam are calculated and found significant. The device is now being characterized and prepared for installation. A magnetic measurement system is being constructed for magnetic measurements.

ACKNOWLEDGEMENT

The authors are grateful to Prof. T. Ishii, Prof. G. Isoyama, Prof. H. Kitamura, Prof. H. Ohkuma and Dr. T. Tanaka for discussion in the design stage of the undulator, and Prof. H. Wiedemann for discussion on the beam dynamics studies.

REFERENCES

1. J.M. Ortega *et. al.*, *Nucl. Instr. Meth.* **206**, 281 (1983).
2. O. Chubar, P.Elleaume and J. Chavanne, *J. Synchrotron Rad.* **5**, 481-484 (1998).
3. K. Halbach, *Nucl. Instr. Meth.* **187**, 109 (1981).
4. T. Hara, T. Tanaka, T. Tanabe, X.-M. Marechal, S. Okada and H. Kitamura, *J. Synchrotron Rad.* **5**, 403 (1998).
5. J. Chavanne, P. Elleaume and P. Van Vaerenbergh, *Proceedings PAC99*, New York, 1999.
6. T. Tanaka and H. Kitamura, *J. Synchrotron Rad.* **8**, 1221 (2001).
7. Walker RP, "Wigglers", in *Cern Accelerator School Proceedings*, 1995, pp 807-835.
8. H. Grote and F.C. Iselin FC, *CERN/SL/90-13 (AP)*, 1996.
9. H. Wiedemann, *Particle Accelerator Physics Vol. II*, Berlin, Springer, 1995.

Characterization of soft X-ray undulator for the Siam Photon Source

T. Dasri^a, S. Siritwattanapitton^b, W. Chachai^b, S. Rugmai^{a,b,*}

^a*School of Physics, Suranaree University of Technology, 111 University Avenue, Muang District, Nakhon Ratchasima 30000, Thailand*

^b*National Synchrotron Research Center, P.O. Box 93, Nakhon Ratchasima 30000, Thailand*

Available online 10 August 2007

Abstract

An undulator for production of intense soft X-rays has been constructed for the Siam Photon Source (SPS). The device, named U60, is being characterized and prepared for installation. It is a pure permanent magnet planar undulator, consisting of 41 magnetic periods, with 60 mm period length. Utilization of the undulator radiation in the photon energy range of 30–900 eV is planned. Magnetic field mapping of the undulator has been carried out using a Hall probe. The measured magnetic fields are used to estimate field errors and perturbations of the undulator on the electron beam dynamics in the storage ring. Compensation schemes for the perturbation are investigated.

© 2007 Elsevier B.V. All rights reserved.

PACS: 07.85.Qe

Keywords: Insertion device; Undulator; Soft X-rays

1. Introduction

The U60 is designed for an intense soft X-ray source for the Siam Photon Source (SPS) [1]. It is a pure permanent magnet planar undulator containing 41 magnetic periods, with 60 mm period length. The total length of the undulator is 2523 mm, which will occupy approximately half the space in the straight section number three of the SPS. It is designed to generate intense photons for soft X-ray beamline. The magnetic structure was designed to give the minimum photon energy of 28 eV at 1.0 GeV beam energy, or 40 eV at 1.2 GeV beam energy. Utilization of up to 900 eV photons from the seventh harmonic, at 1.2 GeV beam energy, is expected. Construction of the U60 has been completed by Danfysik. The device is now being characterized and prepared for installation at the Siam Photon Laboratory. Magnetic field mapping using a Hall probe has been carried out. Results of the measurements and analyses are reported. Construction of a flip coil system for field integral measurements is also in progress.

2. Magnetic field mapping by Hall probe scans

A magnetic measurement bench has been constructed for general purpose magnetic field measurements including insertion devices. The bench is equipped with four-axis stage, controlled by stepping motors. A Hall probe arm is installed on the stage and has been used for magnetic field mapping of the undulator. The vertical magnetic field has been measured, at various undulator gaps and horizontal positions, to characterize the undulator.

Photon energies, calculated from averaged measured peak magnetic fields, as a function of the undulator gap is shown in Fig. 1. Orbit displacements, calculated from the measured magnetic field, along the undulator axis are shown in Fig. 2. Polynomial fits of the orbit displacements are also shown. The quadratic components in the fits indicate that there is a dipole component mixed in the undulator magnetic field. The origin of this dipole component is not clear. However, it is expected to originate from the undulator structure, since it appears to vary with the undulator gap. This dipole component can be compensated by a long coil. Fig. 2 also shows the measured orbit displacement at the minimum gap of 26 mm compensated by a long coil, simulated using Radia [2].

*Corresponding author. National Synchrotron Research Center, P.O. Box 93, Nakhon Ratchasima 30000, Thailand.

E-mail address: supagorn@nsrc.or.th (S. Rugmai).

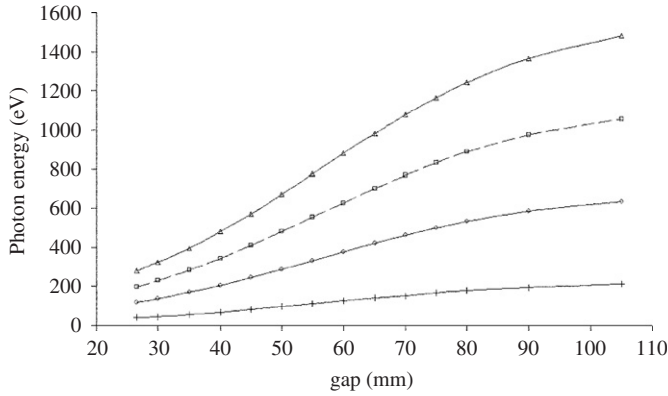


Fig. 1. Photon energy as function of gap at first (plus), third (circles), fifth (squares) and seventh (triangles) harmonics.

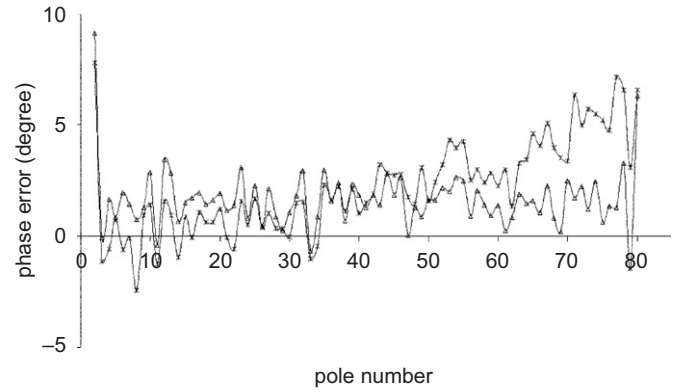


Fig. 3. Phase errors at 26 mm (triangles) and 60 mm (asterisks) gaps.

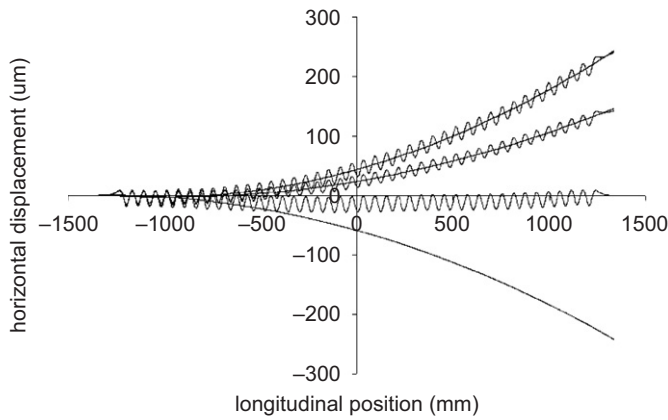


Fig. 2. Electron trajectories at 26 mm (top graph) and 35 mm (second graph from top) gaps. Trend lines are polynomial fits up to quadratic term. Long coil compensated trajectory (third graph from top) and long coil trajectory (bottom graph) are also shown.

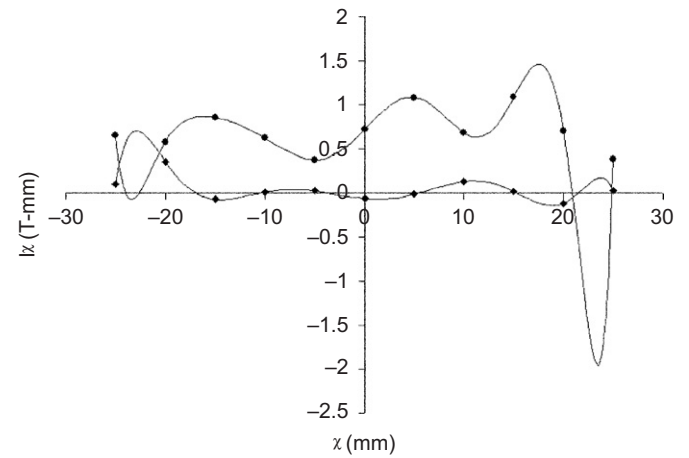


Fig. 4. Field integrals as a function of horizontal position at 26 mm (circles) and 60 mm (diamonds) gaps. Lines are multipole fits up to decapole terms.

The long coil is simulated from a one-turn rectangular coil, with $2.8 \times 5.0 \text{ mm}^2$ cross-section wire and $160 \times 2520 \text{ mm}^2$ coil size, supplied with 33 A current. The remaining angular deflection and orbit displacement at the end of the device can be compensated by steering magnets at both ends of the undulator. These magnets will be used as part of the global orbit correction of the SPS [3] after the undulator is installed.

3. Phase errors

Phase errors calculated from the measured magnetic fields are shown in Fig. 3. It is seen that the phase errors are quite small. The 900 eV photons from the seventh harmonic are obtained at the undulator gap of 60 mm. At this gap, the RMS phase error is 2.15° . The expected photon flux from the seventh harmonic with regards to that from an ideal undulator is 93.35% [4].

4. Effects on the electron beam dynamics

The betatron tune shifts caused by the undulator are calculated using accelerator toolbox (AT) [5]. The undulator magnet model is constructed as a series of hard-edge dipoles, using the measured peak magnetic field. The calculation gives the vertical tune shift of 0.005 at 26 mm gap, while the horizontal tune shift is negligibly small. Calculations by a linear perturbation method [6,7] are also performed to verify the result. This analytical calculation gives similar vertical tune shift of 0.006. It is seen that the tune shift caused by the undulator is quite small. By varying two pairs of quadrupoles adjacent the undulator, the tune shift may be compensated. The calculations show that only 0.5% maximum variation of quadrupole currents is needed to compensate the tune shift.

Integrated multipole components arising from the undulator magnetic field are investigated by calculating the field integrals along the horizontal positions of the undulator using the measured magnetic field. Polynomial fits are then performed to obtain the integrated multipole components. Integrated field integrals are shown in Fig. 4.

The largest sextupole component is found to be 3.27 T m^{-1} at the undulator gap of 60 mm.

5. Conclusions

Magnetic field mapping of the U60 using Hall probe scans have been carried out. The measurement results are used to characterize the device to prepare for the installation. The measurements show a dipole component mixed in the undulator field. A long coil has been simulated to correct the error. The undulator phase errors are found from the analyzes to be small indicating usability of high harmonic photons. Tune shifts and multipole component resulting from perturbation of the undulator are also found to be small.

Acknowledgments

The authors would like to thank the staff of the Accelerator Technology Division and Technical and Engineering Division of the National Synchrotron Research Center for technical supports.

References

- [1] S. Rugmai, et al., AIP Proc. 879 (2007) 335.
- [2] O. Chubar, P. Elleaume, J. Chavanne, J. Synchrotron Radiat. 5 (1998) 481.
- [3] S. Rugmai, P. Klysubun, C. Keawprasert, in: Proceedings of APAC, 2007.
- [4] B. Diviacco, et al., Nucl. Instr. and Meth. A 368 (1996) 522.
- [5] A. Terebilo, SLAC-PUB-8732.
- [6] R.P. Walker, in: CERN Accelerator School Proceedings, 1995, p. 807.
- [7] M. Bassetti, et al., Laboratori Nazionali Frascati Technical Notes LNF-77/26(R).

CURRICULUM VITAE

Mr. Thananchai Dasri

Date of birth: 12 June 1976

Place of birth: Surin, Thailand

Nationality: Thai

Education

Academic year

1995-1999 Khon Kaen University, Khon Kaen, Thailand.

Bachelor of Science (Physics)

1999-2003 Khon Kaen University, Khon Kaen, Thailand.

Master of Science (Physics)

Academic Experience

2004 Nongkhai Campus, Khon Kaen University, Nongkhai,
Thailand.